8-2007

Mapping the Martian Geologic Record: Studies of the Gusev Crater Spirit Landing Site and Plagioclase Feldspar Compositions on Mars

Keith Alan Milam
University of Tennessee - Knoxville

To the Graduate Council:

I am submitting herewith a dissertation written by Keith Alan Milam entitled "Mapping the Martian Geologic Record: Studies of the Gusev Crater Spirit Landing Site and Plagioclase Feldspar Compositions on Mars." I have examined the final electronic copy of this dissertation for form and content and recommend that it be accepted in partial fulfillment of the requirements for the degree of Doctor of Philosophy, with a major in Geology.

Harry Y. McSween, Jeffrey E. Moersch, Major Professor

We have read this dissertation and recommend its acceptance:

Larry A. Taylor, John B. Rehder

Accepted for the Council:
Dixie L. Thompson

Vice Provost and Dean of the Graduate School

(Original signatures are on file with official student records.)

To the Graduate Council:

I am submitting herewith a dissertation written by Keith Alan Milam entitled "Mapping the Martian Geologic Record: Studies of the Gusev Crater Spirit Landing Site and Plagioclase Feldspar Compositions on Mars." I have examined the final electronic copy of this dissertation for form and content and recommend that it be accepted in partial fulfillment of the requirements for the degree of Doctor of Philosophy, with a major in Geology.

Harry Y. McSween, Jr. Major Professor

Jeffrey E. Moersch, Major Professor

We have read this dissertation
and recommend its acceptance:

Larry A. Taylor

John B. Rehder

Acceptance for the Council:

Carolyn R. Hodges, Vice Provost
and Dean of the Graduate School

(Original signatures are on file with official student records.)

Mapping the Martian Geologic Record: Studies of the Gusev Crater Spirit Landing Site and Plagioclase Feldspar Compositions on Mars

A Dissertation
Presented for Doctor of Philosophy
Degree
The University of Tennessee, Knoxville,

Keith Alan Milam

August, 2007

Dedication

This dissertation is dedicated to

Kerry and the rest of my family,

whose patience, love, understanding, and support,

have allowed me to follow my dream.

Acknowledgments

This journey would not have been possible without the encouragement and support of Harry Y. McSween, Jr. ("Hap") during my time at the University of Tennessee. Hap has taught me what it means to be a professional and polished scientist. He is the academic standard by which I judge myself. Both Hap and Jeff Moersch have made it possible for me to sail to Mars and back on several missions . . . every boy's dream. Thanks also to my other committee members Larry Taylor and John Rehder for their support and mentoring along the way. I really appreciate the Larry's "tough love" – it was just what the doctor ordered for the overly confident undergrad that walked through the front door of the geology department several years ago.

I also want to thank those currently or formerly at the University of Tennessee upon whose shoulders I have rested. To Mike Wyatt, my academic sibling, I have been and continued to be inspired by the quality of your research and appreciate all you have done for me. Karen Stockstill, we spent a great deal of time in the trenches together. To Bill Deane, our friendship and mutual interest in caving and impact cratering has been one exciting adventure. I appreciate the friendship and laughter that I experienced with others along the way: Dan Britt, Josh Cahill, Tabbatha Cavendish, Josh Chamot, Mike DeAngelis, Tasha Dunn, Jonathan Evenick, Heather Gastineau, Amitabha Ghosh, Eddy Hill, Linda Kah, Penny King, Nick Lang, Pascal Lee, Rachel Lentz, Rhiannon Mayne, Jeff Nettles, Jen Piatek, Kathy Ocker-Stone, Michael Rampey, Valerie Reynolds, Patrick Schunneman, Cara Thompson, Livio Tornabene, Tomohiro Usui, Chris Whisner and so many others who are too numerous to mention. I am deeply grateful to "the girls" in the office who, over the years, have taken great care of me and all of my fellow graduate students: Melody Branch, Teresa Parrott, Diane Pealor, and Denise Stansberry. Your concern, care, and help have made this an easier experience. And to Ray Mowry and the staff at "Ray's Place": not only do you provide the best cup of sweet tea on the hill, but your

friendship and friendly conversation have always brightened many a dreary day.

To my many friends in Knoxville outside the university: thanks for opportunity to have a life beyond campus. My family and I will miss you all: Tom, Lisa, Emily, Nick, Noah, Luke, Mitzi, A.C., Robert, Lisa, Tim H., Becky, Phoenix, John, Joel, Shonda, Joe, Hanna, Mike, Caleb, Josh, Diane, Hunter, Carolyn, Tim W., Alaura, Sarah, Alicia, J. C., and Mildred. I hope that our paths cross many times again. To my boys, the Cub Scouts: grow up strong and well and continue to "do your best". Make yourselves, your family, and community proud of who you are and the things you do.

Last but most definitely not least, I would not have made it this far without the love and support of my family. To my beautiful wife, Kerry, I really could not have done this without you. I appreciate your patience and understanding through the ups and downs of graduate school. I am glad you were there to share in my triumphs and were willing to listen to my problems. You are everything a Kentucky girl is and should be. I love you babe. To my son, Zacary, I have enjoyed our adventure so far. I am glad you share my enthusiasm in science and "doing experiments" and cannot wait to see what's around the corner for you. If you keep your nose to the grindstone, you'll go far. To my baby girl Emily, you're the apple of your daddy's eye. Keep those hugs and giggles coming.

Abstract

The flurry of activity involved in the scientific study of Mars has resulted in multiple new data sets from several missions (Mars Global Surveyor (MGS), Mars Odyssey (MO), Mars Exploration Rovers (MER), Mars Reconnaissance Orbiter (MRO), and Mars Express) that provide information for unlocking the planet's geologic and climatic history.

This three part study utilized both orbital data and laboratory experiments to examine Mars for morphologic and mineralogic evidence of aqueous activity and magmatic evolution.

The first study examined Gusev Crater, landing site for the Spirit MER rover. This work began during final landing site selection and was published just prior to Spirit's January 2004 landing. In this work, I examined the paradigm that Gusev once held a paleolake and that it contains detrital sediment from the northern highlands. Analyses involved using the most current data then available. I produced thermophysical, morphological, and surface unit maps showing the spatial distribution and stratigraphic relationships of materials on the floor of Gusev. Orbital analyses found no unambiguous evidence of paleolake deposits. This study offered alternative hypotheses explaining floor units, one of which, volcanic deposition, has since been verified by Spirit on the ground.

The second and third studies address our ability to accurately derive plagioclase compositions on Mars and to use thermal emission spectroscopy to map

the distribution of plagioclase compositions on Mars. Plagioclase is the most abundant mineral in the martian crust and may provide information about the igneous evolution and subsequent alteration of the Martian surface. The second study focuses on mixtures more complex in nature than the two-component (composition) plagioclase sand mixtures used in previous work. Linear deconvolutions of laboratory spectra from mixtures involving additional components and phases were used to calculate average plagioclase compositions whose accuracies were found to be comparable to previous studies. The final project carried results from previous laboratory studies one step further to map the global distribution of plagioclase compositions on Mars. Maps reveal a world dominated by labradorite and bytownite, with lesser amounts of other plagioclase. Localized variations are difficult to discern at the scale of individual MGS Thermal Emission Spectrometer (TES) observations.

Table of Contents

List of Tables

Part 2

Part 3

Part 4

List of Figures

Part 2

Part 3

Part 4

Part 1

Introduction

1. Overview

Mars Exploration has experienced rapid growth in the past decade, leading to additional discoveries and questions with each new data set. What is emerging is a picture of a planet where water, climate, and geologic processes produced a more Earth-like world in the ancient past, possibly with the ingredients for life. What remains today, however, is essentially a polar desert where some geologic processes continue to shape the surface. The work that follows utilizes some of those new data sets to examine the geologic and potentially aqueous past of Mars.

2. Characterization of the MER-A (Spirit) Gusev Crater Landing Site

One emphasis for NASA's Mars Exploration Program has been to identify sites that have a high preservation potential for biomarkers or evidence of aqueous activity in the Martian past. Such sites may serve to address the question of past life on Mars. During 2002-2003, NASA held a series of workshops for the selection of high-priority landing sites that met specific engineering and scientific criteria [*Golombek et al.,* 2003]. Final selection considered sites (1) with minimal landing hazards that would increase chances of mission success and (2) that possibly held evidence of past aqueous activity and climatic evolution on Mars. This work on Gusev Crater using the most recent orbital data sets (Part 2 of this dissertation, already published as [*Milam et al.,* 2003]), in addition to other studies, was considered by NASA in the final selection of Gusev as one of two landing sites for the Mars Exploration Rovers (MERs).

Gusev Crater was initially considered because it was postulated as the site of

an ancient paleolake basin during the Hesperian period [*Schneeberger*, 1989; *Cabrol et al.,* 1993, 1998; *Grin et al.,* 1994; *Grin and Cabrol*, 1997a]. Gusev is a 150 km diameter crater located near the boundary between the Amazonian-aged northern lowlands and Noachian southern highlands. Intersecting the southern crater rim is Ma'adim Vallis, a 900 km, south-to-north trending valley that was presumably carved by water and may have facilitated transported sediment from the Noachian terrain into Gusev [*Schneeberger*, 1989; *Irwin et al.,* 2002]. Interpretations of visual imagery suggested that various landforms were evidence of a standing body of water in Gusev [*Cabrol et al.,* 1994; *Cabrol et al.,* 1997; *Schneeberger*, 1989; *Grin and Cabrol*, 1997a].

This study focused on using new data sets that were available prior to landing to map the geologic history of Gusev and to examine multiple working hypotheses to explain deposits on the crater floor. I utilized MGS Thermal Emission Spectrometer (TES) data to examine albedo differences and thermal inertia variations across the floor of Gusev. These, in addition to relative brightness temperatures from MO Thermal Emission Imaging System (THEMIS) thermal infrared multispectral images, were used to map thermophysical variations among the floor deposits. THEMIS and MGS Mars Orbital Camera (MOC) visible wavelength images were utilized to examine textural differences between units and to age-date various units using crater counting techniques. MGS Mars Orbiter Laser Altimeter (MOLA) data were used to correlate thermophysical and morphologic units and to construct a better stratigraphy for Gusev than previous studies [*Landheim et al.,* 1994; *Grin and Cabrol*, 1997b;

Kuzmin et al., 2000].

This study resulted in thermophysical and morphologic unit maps that were similar enough to warrant their merging into a "surface unit" map for Gusev crater. Crater-counting and elevation data also allowed me to produce a stratigraphic column for Gusev that spanned much of the Martian geologic record (Noachian to Amazonian). This study examined the hypothesis of lacustrine deposition, but could find no conclusive evidence for such an interpretation. Equally viable alternatives involved volcanism or a combination of volcanic and sedimentary deposition.

Since landing, the Spirit rover has yet to find definitive evidence of a lacustrine setting. Volcanic materials (basalts) have been found to cover the floor of Gusev [*Squyres et al., 2004; McSween et al.* 2004, 2006], confirming one of our hypotheses. These rocks show only a limited amount of weathering that may have involved water. The geologic diversity in our maps, discernible from orbit, bore the scrutiny of scientific investigation, as Spirit traversed into new and different terrains [*McSween et al.,* 2006]. This study was also the first to identify temporal variations in the low albedo material of Gusev from orbital data and offered aeolian activity as the cause. Dust devil observations by the rover have since confirmed our hypothesis [*Greeley et al.,* 2004].

3. Modeling Plagioclase Compositions in Multi-Component and Multi-Phase Mixtures

Another means of assessing geologic processes (including aqueous activity) at work on Mars is to extract compositional information from major mineral phases in the

Martian crust using thermal emissivity spectra. Mars is a world dominated by basalt [*Christensen et al.,* 2000; *Bandfield et al.,* 2000, *McSween et al.,* 2003] and possibly andesite [*Bandfield et al.,* 2000] although the latter interpretation has been challenged [e.g. *Wyatt and McSween*, 2002]. Orbital remote sensing data indicate that plagioclase feldspar is the dominant phase in the Martian crust [*Bandfield et al.,* 2000; *Hamilton et al.,* 2001; *Wyatt and McSween*, 2002]. This is supported by rover observations [*Christensen et al.,* 2004; *McSween et al.,* 2004], but not Martian meteorites (for a review see e.g. [*McSween and Treiman* 1998]). These meteorites are not likely to be representative of the bulk Martian crust [*Hamilton et al.,* 2003].

Some previous studies [e.g. *Feely and Christensen*, 1999; *Wyatt et al.,* 2001] have addressed our ability to derive modal mineralogies using thermal emission spectra. At thermal infrared wavelengths (5-50 μm), the emissivity spectrum of a rock (or any natural coarse-grained sample) represents a linear mixture of its constituent mineral spectra. Thus, unmixing such a spectrum in a linear fashion reveals the modal mineralogy of a sample [Ramsey and Christensen, 1998], as long as an appropriate spectral library is used. The derived mineral abundances are thought to be fairly accurate for most minerals present in abundances >5-10% of a given sample.

While mineral abundances prove important for constraining the petrogenesis of igneous rocks, so too are mineral compositions. In particular, the composition of feldspars, the most abundant mineral in the Martian and terrestrial crusts, can provide insights into the magmatic evolution and possible subsequent alteration of the Martian

surface. Two earlier studies examined our ability to derive plagioclase compositions in terrestrial volcanic rocks (though to be analogous to those found on Mars). *Wyatt et al.* [2001] and *Milam et al.,* [2004] suggested that compositions could be derived within 10-15 An (An=Ca/(Ca+Na+K) of normative or calculated weighted average values. These conclusions, however, were subject to our inability to accurately determine average plagioclase compositions in complex natural samples.

In order to study samples with controlled average plagioclase compositions, *Milam et al.*[2004] examined two-component (referring to specific plagioclase compositions) coarse sand mixtures. That study determined that plagioclase compositions could be derived to within 12 An (overall) and 6 An (1 σ standard deviation) using emissivity spectra degraded to the varying spectral resolutions of thermal emission spectrometers in orbit or roving on Mars. Although mixtures represented varying proportions of each plagioclase component and were produced over varying ranges of, two-component sand mixtures are not truly representative of natural samples that have multiple grain sizes, numerous coexisting plagioclase compositions, and other minerals like pyroxene and olivine.

In an attempt to better simulate the complexity of natural samples while controlling the average plagioclase composition for comparison to a spectrally-derived average, Part 3 involves the use of multi-component and multi-phase coarse sand mixtures. Fifteen multi-component coarse plagioclase sand mixtures were produced with varying proportions of components used. Three multi-phase sand mixtures were also made that were analogous to three observations or samples from

Mars (TES Surface type 1 [*Bandfield et al.,* 2000], Shergotty [*Stolper and McSween*, 1979], and Mazatzal [*McSween et al.,* 2004). Thermal emissivity spectra were collected and modeled using a technique described by *Ruff and Christensen* [1998]. Average plagioclase composition were accurately derived to 6 An (1σ) of measured values. This accuracy is unaffected by the number of plagioclase compositions or number of other phases and also applies to data collected at spectral resolutions of thermal emission spectrometers at Mars. Results are directly comparable to those from *Milam et al*. [2004] and to deconvolutions of spectra of coarse-grained homogeneous plagioclase sand. Our results suggest that more complex mixing of plagioclase components (i.e. chemically-zoned plagioclase grains or mechanical mixtures of plagioclase compositions) and added phases appear to have minimal effect on our plagioclase compositions derived from thermal emission spectra of the Martian surface.

4. The First Plagioclase Compositional Maps of Mars

Part 4 is an effort to apply our ability to accurately deconvolved plagioclase compositions [*Milam et al.,* 2004; Part 3 of this dissertation] to Mars. This study involved use of MGS-TES spectra to derive average plagioclase compositions across Mars. Variations in plagioclase composition, in consideration with other mineralogic data, may provide key insights into the magmatic, geologic, and aqueous evolution of the Martian crust.

TES spectra were selected from low albedo regions on Mars, collected at

surface temperatures > 265 K to avoid the potential effects of random and systematic noise in the data which could affect the fidelity of spectral deconvolutions. Data were also selected to avoid atmospheric phenomena and areas with a high surface dust component [as described by *Ruff and Christensen,* 2002]. Emissivity spectra were deconvolved as in *Ramsey and Christensen* [1998] and a new computer algorithm calculated the average plagioclase composition (expressed as anorthite content or An) from the plagioclase spectral endmembers used in each deconvolution. Spectra were color-coded and binned by plagioclase solid solution ranges in six maps that highlighted the distribution of plagioclase compositions across Mars.

The study revealed that the average plagioclase composition on Mars is labradorite (An_{61}). The majority of TES pixels modeled as labradorite (An_{50-70}) to bytownite (An_{70-90}) with lesser percentages of other plagioclase types. Plagioclase compositions vary little between the two dominant surface types: ST1 (An_{62}) and ST2 (An_{59}), and this variation is within the margin of error of the technique [*Milam et al.,* 2004; Part 3 of this study].

5. Summary

These three studies, although unique in their foci and individual approaches, address fundamental questions about the evolution of the Martian crust over time. They also highlight difficulties in interpreting remote sensing data. Visual and thermophysical data unveiled a complex geologic history that occurred at Gusev crater, but because of significant dust cover, revealed little about rock compositions

and modal mineralogies from orbit. Average global plagioclase compositions, calculated from orbital data, show little or no correlation with terrains that vary by morphology or age, suggesting that plagioclase compositions in igneous units have remained constant by emplacement episodes or have been globally-homogenized over geologic time.

References

Bandfield, J.L., V.E. Hamilton, and P.R. Christensen (2000), A global view of Martian surface compositions from MGS-TES, *Science, 287,* 1,626-1630.

Cabrol, N.A., E.A. Grin, A. Dollfus, and G. Dawidowicz, An ancient inner lake in Ma'adim Vallis, Lunar and Planetary Science Conference, 24th, 241-242, 1993.

Cabrol, N.A., R. Landheim, R. Greeley, and J.D. Farmer, Fluvial processes in Ma'adim Vallis and the potential of Gusev crater as a high priority site, Proceedings of the Lunar and Planetary Science Conference, 25th, 213-214, 1994.

Cabrol, N.A., and E.A. Grin, Hydrogeology and exobiology significance of martian large crater lakes, in Conference on early Mars; geologic and hydrologic evolution, physical and chemical environments, and the implications for life, edited by S.M. Clifford, A.H. Treiman, H.E. Newsom, and J.D. Farmer, pp. 14-15, Lunar and Planetary Institute, Houston, 1997.

Cabrol, N.A., E.A. Grin, R. Landheim, R.O. Kuzmin, and R. Greeley, Duration of the Ma'adim Vallis/Gusev crater hydrogeologic system, Mars, Icarus, 133, 98-108, 1998.

Christensen, P.R., J.L. Bandfield, M.D. Smith, V.E. Hamilton, and R.N. Clark (2000), Identification of a basaltic component on the Martian surface from Thermal Emission Spectrometer data, *J. Geophys. Res., 105*, 9,609-9,621.

Christensen, P. R., M. B. Wyatt, T. D. Glotch, A. D. Rogers, S. Anwar, R. E. Arvidson, J. L. Bandfield, D. L. Blaney, C. Budney, W. M. Calvin, A. Fallacaro, R. L. Fergason, N. Gorelick, T. G. Graff, V. E. Hamilton, A. G. Hayes, J. R. Johnson, A. T. Knudson, H. Y. McSween, Jr., G. L. Mehall, L. K. Mehall, J. E. Moersch, R. V. Morris, M. D. Smith, S. W. Squyres, S. W. Ruff, M. J. Wolff, Mineralogy at Meridiani Planum from the Mini-TES experiment on the Opportunity rover, *Science, 306,* 1733 – 1739, 2004.

Feely, K.C., and P.R. Christensen (1999), Quantitative compositional analysis using thermal emission spectroscopy: Applications to igneous and metamorphic rocks, *J. Geophys. Res., 104,* 24,195-24,210.

Golombek, M. P., J. A. Grant, T. J. Parker, D. M. Kass, J. A. Crisp, S. W. Squyres, A. F. C. Haldemann, M. Adler, W. J. Lee, N. T. Bridges, R. E. Arvidson, M. H. Carr, R. L. Kirk, P. C. Knocke, R. B. Roncoli, C. M. Weitz, J. T. Schofield, R. W. Zurek, P. R. Christensen, R. L. Fergason, F. S. Anderson, and J. W. Rice, Jr., Selection of the Mars Exploration Rover landing sites, *J. Geophys. Res., 108*, doi:10.1029/2003JEE002074, 2003.

Greeley, R., S. W. Squyres, R. E. Arvidson, P. Bartlett, J. F. Bell III, D. Blaney, N. A. Cabrol, J. Farmer, B. Farrand, M. P. Golombek, S. P. Gorevan, J. A. Grant, A. F. C. Haldemann, K. E. Herkenhoff, J. Johnson, G. Landis, M. B. Madsen, S. M. McLennan, J. Moersch, J. W. Rice, Jr., L. Lichter, S. Ruff, R. J. Sullivan, S. D. Thompson, A. Wang, C. M. Weitz, P. Whelley, and the Athena Science Team, Wind-related processes detected by the Spirit rover at Gusev crater, Mars, *Science, 305*, 810-821, 2004.

Grin, E.A., N.A. Cabrol, and G. Dawidowicz, Proposal for a topographic survey of

Gusev Crater, Lunar and Planetary Science Conference, XXV, 483-484, 1994.
Grin, E.A., and N.A. Cabrol, Antarctic analog for a perennial ice-covered paleolake in Gusev Crater (Mars), Proceedings of the Lunar and Planetary Science Conference, 28th, 473-474, 1997a.
Grin, E.A., and N.A. Cabrol, Limnologic analysis of Gusev crater paleolake, Mars, Icarus, 130, 461-474, 1997*b*.
Hamilton, V.E., M.B. Wyatt, H.Y. McSween, Jr., and P. R. Christensen, Analysis of terrestrial and Martian volcanic compositions using thermal emission spectroscopy II: Application to Martian surface spectra from the Mars Global Surveyor Thermal Emission Spectrometer, *J. Geophys. Res., 102*, 14,733-14,746, 2001.
Hamilton, V. E., P.R. Christensen, H.Y. McSween, Jr., and J.L. Bandfield, Searching for the source regions of Martian meteorites using MGS TES: Integrating Martian meteorites into the global distribution of igneous materials on Mars, *Meteorit. Planet. Sci., 38,* 871-885, 2003.
Irwin, R.P. III, T.A. Maxwell, A.D. Howard, R.A. Craddock, and D.W. Leverington, A large paleolake basin at the head of Ma'adim Vallis, Mars, 296, 2209-2212, 2002.
Kuzmin, R.O., R. Greeley, R. Landheim, N.A. Cabrol, and J.D. Farmer, Geologic map of the MTM-15182 and MTM-15187 quadrangles, Gusev Crater - Ma'adim Vallis Region, Mars, in Geologic Investigative Series, pp. 8, 1-sheet, U. S. Geological Survey, Reston, VA, 2000.
Landheim, R., N.A. Cabrol, R. Greeley, and J.D. Farmer, Strategic assessment of Gusev crater as an exobiology landing site, Proceedings of the Lunar and Planetary Science Conference, 25th, 769-770, 1994.
McSween, H. Y., Jr., and A. H. Treiman, Martian meteorites, in *Reviews in Mineralogy, Volume 36: Planetary Materials (J. J. Papike ed.)*, Mineralogical Society of America, Washington, D. C, 1998.
McSween, H. Y., R. E. Arvidson, J. F. Bell III, D. Blaney, N. A. Cabrol, P. R. Christensen, B. C. Clark, J. A. Crisp, L. S. Crumpler, D. J. Des Marais, J. D. Farmer, R. Gellert, A. Ghosh, S. Gorevan, T. Graff, J. Grant, L. A. Haskin, K. E. Herkenhoff, J. R. Johnson, B. L. Jolliff, G. Klingelhoefer, A. T. Knudson, S. McLennan, K. A. Milam, J. E. Moersch, R. V. Morris, R. Rieder, S. W. Ruff, P. A. de Souza Jr., S. W. Squyres, H. Wänke, A. Wang, M. B. Wyatt, A. Yen, J. Zipfel, Basaltic rocks analyzed by the Spirit rover in Gusev Crater, *Science, 305*, 842-845, 2004.Milam, K. A., K. R. Stockstill, J. E. Moersch, H. Y. McSween, Jr., L. L. Tornabene, A. Ghosh, M. B. Wyatt, and P. R. Christensen, THEMIS characterization of the MER Gusev crater landing site, *J. Geophys. Res., 108*(E12), 8078, doi:10.1029/2002JE002023, 2003.
McSween, H. Y., R. E. Arvidson, J. F. Bell III, D. Blaney, N. A. Cabrol, P. R. Christensen, B. C. Clark, J. A. Crisp, L. S. Crumpler, D. J. Des Marais, J. D. Farmer, R. Gellert, A. Ghosh, S. Gorevan, T. Graff, J. Grant, L. A. Haskin, K. E. Herkenhoff, J. R. Johnson, B. L. Jolliff, G. Klingelhoefer, A. T. Knudson, S. McLennan, K. A. Milam, J. E. Moersch, R. V. Morris, R. Rieder, S. W. Ruff, P. A. de Souza Jr., S. W. Squyres, H. Wänke, A. Wang, M. B. Wyatt, A. Yen, J. Zipfel,

Basaltic rocks analyzed by the Spirit rover in Gusev Crater, *Science, 305*, 842-845, 2004.

McSween, H. Y., S. W. Ruff, R. V. Morris, J. F. Bell III, K. Herkenhoff, R. Gellert, K. R. Stockstill, L. L. Tornabene, S. W. Squyres, J. A. Crisp, P. R. Christensen, T. J. McCoy, D. W. Mittlefehldt, and M. Schmidt, Alkaline volcanic rocks from the Columbia Hills, Gusev crater, Mars, *J. Geophys. Res., 111,* doi:10.1029/2006JE002698, 2006.

Ramsey, M. S. and P. R. Christensen, Mineral abundance determination: Quantitative deconvolution of thermal emission spectra *J. Geophys. Res., 103*, 579– 596, 1998.

Ruff, S. W., and P. R. Christensen, Bright and dark regions on Mars: Particle size and mineralogical characteristics based on Thermal Emission Spectrometer data, *J. Geophys. Res., 107*(E12), 5127, doi:10.1029/2001JE001580, 2002.

Schneeberger, D.M., Episodic channel activity at Ma'adim Vallis, Mars, Proceedings of the Lunar and Planetary Science Conference, 20th, 964-965, 1989.

Squyres, S. W., R. E. Arvidson, J. F. Bell, III, J. Brückner, N. A. Cabrol, W. Calvin, M. H. Carr, P. R. Christensen, B. C. Clark, L. Crumpler, D. J. DesMarais, C. d'Uston, T. Economou, J. Farmer, W. Farrand, W. Folkner, M. Golombek, S. Gorevan, J. A. Grant, R. Greeley, J. Grotzinger, L. Haskin, K. E. Herkenhoff, S. Hviid, J. Johnson, G. Klingelhöfer, A. Knoll, G. Landis, M. Lemmon, R. Li, M. B. Madsen, M. C. Malin, S. M. McLennan, H. Y. McSween, D. W. Ming, J. Moersch, R. V. Morris, T. Parker, J. W. Rice, Jr., L. Richter, R. Rieder, M. Sims, M. Smith, P. Smith, L. A. Soderblom, R. Sullivan, H. Wänke, T. Wdowiak, M. Wolff, and A. Yen, The Spirit Rover's Athena Science Investigation at Gusev Crater, Mars, *Science, 305,* 794-799, 2004.

Stolper, E. M., and H. Y. McSween, Jr. (1979), Petrology and origin of the shergottite meteorites, *Geochim. Cosmochim. Acta, 43*, 1475-1498.

Wyatt, M.B., V.E. Hamilton, H.Y. McSween, Jr., P.R. Christensen, and L.A. Taylor (2001), Analysis of terrestrial and Martian volcanic compositions using thermal emission spectroscopy: 1. Determination of mineralogy, chemistry, and classification strategies, *J. Geophys. Res., 106,* 14,711-14,732.

Wyatt, M.B., and H.Y. McSween, Jr. (2002), Spectral evidence for weathered basalt as an alternative to andesite in the northern lowlands of Mars, *Nature, 417*, 263-266.

Part 2

THEMIS Characterization of the MER Gusev Crater Landing Site

The chapter that follows is a reformatted (according to the University of Tennessee publication formatting standards) version of a paper originally published in the Journal of Geophysical Research – Planets in 2003 by Milam et al.:

Milam, K. A., K. R. Stockstill, J. E. Moersch, H. Y. McSween, Jr., L. L. Tornabene, A. Ghosh, M. B. Wyatt, and P. R. Christensen, THEMIS characterization of the MER Gusev crater landing site, *J. Geophys. Res., 108*(E12), 8078, doi:10.1029/2002JE002023, 2003.

Abstract

Gusev crater is a proposed landing site for one of the Mars Exploration Rovers (MER). Gusev has been interpreted as the depocenter for the Gusev-Ma'adim Vallis fluvio-lacustrine system. Here we use new remote sensing data from the Thermal Emission Imaging System (THEMIS), supplemented by data from the Thermal Emission Spectrometer (TES), Mars Orbiter Camera (MOC), and Mars Orbiter Laser Altimeter (MOLA) to characterize the geology of Gusev crater. Thermal infrared data from THEMIS and TES were used to map thermophysical units based on relative albedos and diurnal temperature variations. THEMIS and MOC visible images were used to map unit morphologies and to determine crater density ages. MOLA data was used to identify unit contacts and stratigraphic relationships. Various data sets were combined to construct a new surface unit map and stratigraphic column for Gusev. Eight surface units were identified in Gusev, mostly Hesperian in age, but two showing evidence of later modification and re-distribution. Six or more surface units and layering are present within the MER-A landing ellipse, attesting to the geologic diversity of this site. Various surface units show features that could be consistent with fluvio-lacustrine, aeolian, and/or volcanoclastic depositional regimes. The spatial

resolution of visible/infrared data does not allow the distinction of textures associated with each of the regimes or the identification of unambiguous evidence for a fluvio-lacustrine depocenter. However, a MER rover landing in Gusev may provide the opportunity to analyze multiple units within Gusev, distinguish between rock types, examine stratigraphic relationships, and shed light on the ancient depositional environment for Gusev crater.

1. Introduction

The focus of the Mars Exploration Program is the search for water, with the goal of identifying regions having the highest probability of capturing and preserving biomarkers. Under this plan, two rovers are set to launch toward Mars in 2003 with early 2004 landings. Each Mars Exploration Rover (MER) will carry the Athena science package [see *Squyres et al.*, this issue] with instruments suitable for gathering evidence of ancient water on Mars. Each MER rover will land at a site that has been considered for evidence of past water and the relatively low probability of hazards posed during landing. Prior to final landing site selection and mission operations, it is crucial that all available data sets from Mars orbiting spacecraft be analyzed to ascertain the potential scientific return of each site.

Gusev crater is a ~160 km diameter complex impact structure (Figure 1 – please note: all figures and tables appear in the appendix to each section), centered at 14.64°S 175.36°E, within the Aeolis Quadrangle of Mars (USGS M 5M-15/202 RN, 1984). The location of Gusev at the terminus of the 900 km-long Ma'adim Vallis

and geomorphic features within both landforms have led several researchers [*Schneeberger*, 1989; *Cabrol et al.,* 1993, 1998; *Grin et al.,* 1994; *Grin and Cabrol*, 1997a] to propose Gusev as a lacustrine depocenter for the Ma'adim drainage system. Interpretations by previous authors that are consistent with this hypothesis include: multiple terrace levels within Ma'adim Vallis [*Cabrol et al.,* 1994], evidence of stream migration [*Cabrol et al.,* 1997], debris lobes or 'deltaic' deposits at the mouth of Ma'adim [*Schneeberger*, 1989; *Grin et al.,* 1997a; *Grin and Cabrol*, 1997b], and curvilinear ridges within Gusev analogous to sedimentary structures formed in terrestrial ice-covered lakes by sub-glacial rotary currents [*Grin and Cabrol.,* 1997a; 1997c]. Recent studies have also proposed this hydrologic system to have been active for 2 Ga over the Noachian-Hesperian periods [*Cabrol & Grin*, 1997; *Grin and Cabrol*, 1997b].

Evidence of a paleolake in Gusev crater [*Masursky et al.,* 1988; *Landheim et al.,* 1993; *Cabrol et al.,* 1994; *Cabrol and Brack*, 1995; *Cabrol et al.,* 1996; *Cabrol & Grin,* 1997] makes it an attractive candidate for a MER landing [*Cabrol et al.,* 2002] for several reasons. First, potential lacustrine environments like Gusev may contain sedimentary structures (flow margins, shorelines, channels, ripple marks, etc.) or mineral deposits (evaporites, tufas, etc.) indicative of former aqueous activity [*Eugster and Hardie*, 1978]. Second, continuous settling of fine-grained sediment in terrestrial lacustrine environments leads to the burial and preservation of biomarkers. If life formerly existed on Mars, fluvio-lacustrine environments like Gusev would thus be a favored setting for fossil preservation [*Farmer and Des Marais*, 1999]. Also,

relatively flat 'lake beds' are devoid of many hazards posed to lander missions.

Although there is much that may suggest an ancient lacustrine environment at Gusev, no unequivocal evidence (such as evaporite deposits or shorelines) has been found to confirm the proposed hypothesis. With this in mind, we take a first look at new data from the Mars Odyssey Thermal Emission Imaging System (THEMIS) to provide insight into the geologic story of Gusev crater. This study also employs data from the Mars Global Surveyor (MGS) Thermal Emission Spectrometer (TES), Mars Orbiter Camera (MOC), and Mars Orbiter Laser Altimeter (MOLA) instruments to:

- map surface units by their thermophysical and morphological properties
- derive a stratigraphic sequence
- make comparisons with previous geologic surveys

with the ultimate aim of evaluating various depositional hypotheses for Gusev crater.

2. Methods

Data from the THEMIS, TES, MOC, and MOLA instruments were used to provide thermophysical, morphologic, topographic, and temporal perspectives of Gusev crater. Thermal infrared (TIR) data from the THEMIS and TES instruments was first used to identify and map units based on thermophysical properties (temperature and albedo). THEMIS visible and daytime TIR data, along with high-resolution MOC images, were then used to map units based on morphology and texture. These data were also used for crater counting/age determination, and to search for evidence of layering. MOLA data provided elevations of contacts between units, estimations of

strata thicknesses, and confirmation of unit boundaries.

Data collected from THEMIS include visible images in 5 bands at 20 m/pixel spatial resolution and TIR images at 100 m/pixel spatial resolution using 8 spectral bands from 6.8 to 12.6 μm (1563-690 cm^{-1}). Images were collected during the Martian day (~ 1600 local solar time) and night (~ 0400 local solar time) to observe diurnal changes in surface temperatures [*Christensen et al.*, submitted]. THEMIS TIR bands were chosen for their usefulness in detecting relevant geologic materials including silicates, carbonates, and sulfates. Currently, THEMIS has collected 12 visible, 17 daytime, and 6 nighttime TIR images for Gusev, producing ~50%, 100%, and 94% coverage for each dataset, respectively. Mosaics of each data type were produced for Gusev (Figures 1-2). Daytime and nighttime TIR images were used to compare and contrast the absolute and relative temperatures of surfaces within Gusev (by comparison of relative temperatures on gray-scale normalized TIR images). *Relative* temperatures were qualitatively characterized as 'hot', 'warm', and 'cold' based on the amplitude of diurnal temperature variations observed using daytime and nighttime TIR images. Visible and daytime TIR images were also used to measure crater densities for defined units (discussed later).

The TES instrument, on board the Mars Global Surveyor spacecraft, [*Christensen et al.*, 1992; *Christensen et al.*, 2001] is a Fourier transform Michelson interferometer that collects TIR spectra over 1709-200 cm^{-1} (5.8-50 μm) with 5 and 10 cm^{-1} spectral sampling and 3x5 km spatial resolution. During its initial mapping phase, which lasted approximately 1 martian year, the TES instrument collected

approximately $5x10^7$ spectra from Mars. Approximately 80% of Gusev crater has been mapped by TES. TES spectra were used to note the presence of surface types 1 and 2 [*Bandfield et al.,* 2000] in Gusev and a TES thermal inertia map by *Jakosky and Mellon* [2001] was used to determine thermal inertias of major units within Gusev. TES bolometric data were used to measure relative albedo variations across surfaces. Albedos were categorized as 'low' (<0.23), 'intermediate' (0.23-0.26), and 'high' (>0.26).

Narrow angle, high spatial resolution (1.46-5.68 m/pixel) MOC (Mars Global Surveyor) images were used to identify distinctive morphologies within Gusev. Surfaces that: (a) were laterally extensive, (b) had consistent morphologic characters, and (c) occur within a specific range of elevations were identified as distinctive morphologic units. Viking Orbiter and THEMIS data were also used with MOC data to track larger-scale modifications to surfaces within Gusev. For more on the MOC instrument, see *Malin et al.,* [1992] and *Malin and Edgett,* [2001].

The MOLA instrument is a laser altimeter on board Mars Global Surveyor that is used to collect high precision elevation data from the martian surface. MOLA fires 10 Hz (~8 ns) pulses toward the martian surface and measures return times to calculate surface elevations with a vertical accuracy of <1m. A description of MOLA data collection and processing can be found in *Zuber et al.* [1992] and *Smith et al.,* [2001]. The MOLA team has generated global topographic grids for Mars (at 1/128°, 1/64°, and 1/32° per pixel resolutions. Data from the (1/128° per pixel) v. 2.0 MEGDR topographic grid (between 0°-44° S, 90°-180°E) were used to generate a

topographic map for Gusev (Figure 3). This map, along with topographic profiles of key unit boundaries, was used to estimate the maximum and minimum elevations of floor units. Topographic relief was calculated as an indication of each unit's minimum thickness (assuming horizontality). Topographic profiles were used to identify prominent slope changes or 'benches' that occur at constant elevations. Such identifiable slope breaks, where present, are thought to represent unit contacts.

3. Identification of Units

3.1. Unit Nomenclature.

For this study, one of our objectives has been to identify and delineate units on the floor of Gusev crater. Our approach has been to map units based on thermophysical and morphological properties independently (explained later).

3.2. Thermophysical Properties

Eight *thermophysical* units were identified in Gusev crater by qualitative comparisons of albedos and relative temperature differences (Table 1) derived from THEMIS and TES observations as described above. As used here, a *thermophysical* unit is defined as rock or sediment that is laterally extensive, defining an area with similar albedos and thermal inertias. Thermophysical units are identified by a subscript "t" in their unit abbreviations.

The most obvious thermophysical unit is the Low Albedo (LA_t) unit (Figure 4a). As its name implies, LA_t has low albedos but is hot in THEMIS daytime and nighttime

TIR images (Figures 1-2). LA_t has a mean thermal inertia value of 240 $\pm$ 20 J m^{-2} K^{-1} $s^{-1/2}$, consistent with a surface covered by medium-grained sand [*Pelkey et al.,* 2001]. LA_t is presently split into two areas, a western area having sharp boundaries (as determined by visible and daytime TIR images) and an eastern area having more diffuse boundaries (visible and daytime/nighttime TIR). THEMIS nighttime TIR shows eastern LA_t extending farther southeast than is shown by daytime TIR imagery.

A High Thermal Inertia (HTI_t) unit has been identified in southeastern Gusev using THEMIS and TES data (Figure 4a). Visibly, this unit has intermediate to low albedos and is warm to cold in daytime TIR (Figures 1-2a). Nighttime TIR shows this as a very hot unit, occurring as eastern and western lobes (Figure 2b). Both lobes are centered around an irregular depression in southeastern Gusev. The eastern lobe appears as a THEMIS nighttime TIR hot unit with sharp, well-defined boundaries. Nighttime TIR images show that relative temperatures are more diffuse and boundary contacts less distinct for the western lobe. TES thermal inertia values for this area are ~400 $\pm$ 70 J m^{-2} K^{-1} $s^{-1/2}$. Such high thermal inertias are consistent with very coarse sand to granule particle sizes [*Pelkey et al.,* 2001].

The Ma'adim Vallis (MV_t) unit extends from Ma'adim Vallis, through 'Downe'* and 'New Plymouth'* craters (Figure 1) onto the floor of Gusev crater (Figure 4a). THEMIS and MOC visible imagery do not indicate noticeable albedo variations between MV_t and adjacent units. Daytime TIR images show this unit as having warm temperatures, also making it indistinguishable from surrounding units. Nighttime TIR data does show this cold nighttime unit extending into Gusev towards a small

unnamed crater (14.74°S, 174.82°E). Relative nighttime TIR temperatures show a discernible eastern boundary for the unit (Figure 5).

The Plains (PL_t) unit extends from the terminus of Ma'adim to the northwest breach in the crater rim near 'Zutphen' crater (Figure 4a). PL_t has intermediate albedos with warm daytime and nighttime TIR temperatures (Figures 1-2). Thermal inertia values for PL_t are 290 $\pm$ 70 J m^{-2} K^{-1} $s^{-1/2}$, consistent with a surface covered mostly by coarse sand [*Pelkey et al.,* 2001]. Nighttime TIR images reveal that PL_t can be distinguished by the presence of craters with hot nighttime TIR rim material and ejecta (Figure 6). Daytime TIR images show PL_t as warm material with craters containing cooler ejecta (Figure 2). These thermophysical characteristics are not common to other units within Gusev.

The Mesa (MS_t) unit is present just north of the Ma'adim terminus (Figure 4a) and has been previously interpreted by others [*Landheim et al.,* 1994; Grin *and Cabrol*, 1997a, 1997b, and 1997c] as deltaic sediment deposited by Ma'adim. The MS_t unit is composed of flat-topped positive relief features that are identifiable in visible images, have intermediate albedos (Figure 1), and are of warm temperatures in daytime TIR (Figure 2a). Mesas are separated by steep-walled valleys that are oriented in multiple directions. At night, MS_t mesas have relatively warm to cold tops and hot slopes (Figure 2b). Our observations are similar to those of other mesas on Mars [*Christensen et al.*, submitted]. A variety of scenarios could account for this, such as well-indurated, coarse-grained rock overlain by unconsolidated sediment cover, changes in grain size or porosity, or the contribution of nighttime radiative

heating from nearby lowlands reflected off MS_t slopes, thus contributing to their increased temperatures at night. While the origin of their thermophysical properties is presently unclear, nighttime TIR temperature variations between mesa tops and slopes make MS_t a distinct thermophysical unit.

The Etched (ET_t) unit occurs in the southeastern quadrant (Figure 4a) beyond the rim of Thira crater (14.46°S, 175.75°E). ET_t is intermediate in albedo, is relatively cold in daytime TIR, and in nighttime TIR has a 'mottled' (warm-cold) appearance (Figures 1-2). ET_t's 'mottled' nighttime TIR temperature correlates with its dissected nature. ET_t's landscape represents an erosional surface (warm nighttime TIR areas) superimposed upon distinctive underlying material (cold nighttime TIR areas). The northern and southwestern thermophysical boundaries of ET are gradational with adjacent units.

The Wrinkled (WR_t) unit occupies the northeastern quadrant of Gusev and the central region of the crater (Figure 4a). WR_t has intermediate albedos and warm daytime and nighttime TIR temperatures (Figures 1-2), with a thermal inertia of 200 $\pm$ 20 J m^{-2} K^{-1} $s^{-1/2}$, consistent with a surface covered mostly in fine-grained sand [*Pelkey et al.,* 2001]. A distinguishing thermophysical property of WR_t is the abundance of small (typically <2 km diameter) craters whose floors are cold in nighttime TIR (Figure 6).

The Thira Rim unit (TR_t,), located just to the northeast of Gusev's center (Figure 3), is comprised of rim material from this crater (~20 km diameter; 14.45°S 175.75°S) and associated collapse terrace blocks. Most TR_t material has high albedo and is hot

in daytime and nighttime TIR images (Figures 1-2); however, sections containing low albedo material that are very hot in nighttime TIR images exist along the southern part of the rim (Figure 7). It is unclear whether these low albedo areas are deposits along the rim, represent actual exposures of bedrock along Thira crater, and/or are wind-blown LA_t. Based on our method of defining thermophysical units, for now we consider the low albedo areas as LA_t.

3.3 Morphological Characteristics

3.3.1. Unit Descriptions.

An independent assessment of THEMIS and MOC visible images was used to identify *morphologic* units based on distinguishing morphologic characteristics (Table 1). As applied here, a *morphologic* unit is defined as a laterally extensive unit with a homogeneous surface texture that occurs within a specific range of elevations. To distinguish from thermophysical units, *morphologic* unit abbreviations are denoted by a subscript "m". Seven distinct *morphologic* units were identified, many corresponding to previously identified thermophysical units (Figure 4b).

MV_m (Figure 8a) can be identified within Ma'adim Vallis based on the presence of subdued ridges parallel to longitudinal axis of the valley. This morphological expression, however, does not appear to extend into Gusev Crater. In fact, the area within Gusev that was previously defined (thermophysically) as MV_t has surface textures very similar to PL_m. Despite this, an escarpment, corresponding to the suggested thermophysical boundary for MV_t extends from Ma'adim into Gusev and to the east of

a small crater (Figure 9a). This indicates that MV_m may extend into Gusev as a localized unit.

PL_m (Figure 8b) is relatively flat (with a slight north-south slope) and has a lower crater density than MV_m. Most of the larger craters in PL_m appear degraded, while there is a population of small (<1 km diameter) craters with well-defined rims. West-northwest to east-southeast linear dust-devil tracks (Figure 9b), similar to those identified elsewhere in MOC data by *Malin and Edgett* [2001], are superimposed on PL_m, showing the effects of wind activity on this unit. PL_m terminates in the east along a steep escarpment (Figures 9c) and also contains several minor north-south oriented escarpments in the northern half of the unit that suggest it may be composed of sub-units.

MS_m occurs as flat-topped mesas, flanked by slope debris, with a population of small (< 1 km diameter) craters superimposed on mesa-tops (Figure 8c). Exposures of this unit are separated by narrow canyons, which suggest this unit was once continuous and subsequently eroded.

A new morphologic unit not distinguishable by its thermophysical properties is the Lobate Unit, LB_m. LB_m occurs to the east of PL_m in central Gusev and has thermophysical properties similar to WR_t. LB_m can be distinguished by its lobate margins along its eastern boundary (Figure 8d). LB_m extends from the PL_m unit boundary, is deposited against ET_m south of and within Thira crater, and overlies WR_m in central Gusev.

The distinctive morphologic characteristic of ET_m is a series of low knobs, small

mesas, and interspersed dunes superimposed upon a relatively flat underlying surface, giving it an 'etched' appearance (Figure 8e). Most of the knobs appear to be randomly oriented, while some in the southernmost part of this unit show a weak northwest-southeast orientation. In the northwestern parts of ET_m, channel-like features are present, suggesting some fluid modification (Figure 10).

WR_m (Figure 8f) consists of subdued, northeast-southwest and north-south oriented ridges (producing a 'wrinkled' appearance) with superimposed craters having degraded rims and infilled floors. The distinctive WR_m morphology is found in northeast and central Gusev and along the floor of the depression in southeast Gusev mentioned earlier. Some of the ridges appear to form longer 'fronts' that have been interpreted by *Grin and Cabrol* [1997c] as evidence for rotary currents under a glacier-covered Gusev paleolake. However, ridge orientations are mostly north-south, showing no evidence of changing 'rotary' orientations around Gusev.

The TR_m unit (Figure 8g), is exposed crater rim material from Thira crater, with ET_m, LB_m, and WR_m deposited against it. The degraded rim of TR_m lacks a sizeable crater population and has inward margins showing several slope breaks (variable elevation) around ~80% of the crater. Observations of the lack of ejecta superimposed upon adjacent units and termination of lateral deposition against TR_m also suggests that the Thira impact was one of the earliest events in Gusev and sampled distinctive strata from depth.

Examination of the area previously identified as HTI_t reveals that, morphologically, the eastern lobe coincides with and shares the same morphology as

ET_m. The western lobe shares the same surface textures as PL_m, LB_m, and WR_m, while the depression between the two lobes resembles WR_m with a thin mantling of low albedo material. Because surface textures for HTI_t vary greatly across this area, it is not a true morphologic unit but an area of PL_m, WR_m, ET_m, and LB_m that share similar nighttime TIR temperatures. A thin mantling of low albedo material or the mantling in combination with the rough landscape of this area in this region may be responsible for its nighttime TIR signature.

Additional scrutiny of THEMIS and MOC visible imagery (Figure 8h) of the low albedo areas (defined as the LA_t thermophysical unit) shows what appears to be the agglomeration of northwest-southeast oriented dust devil tracks, wind streaks, intracrater deposits, and possible blanketing material. Within the northwest-southeast prevailing wind pattern, track and streak orientations vary from due east to 50°SE, suggesting localized variations in wind direction. Western low albedo area occurs as a continuous exposure of material grading northward into agglomerated northwest-southeast dust-devil tracks/wind streaks. The low albedo material is somewhat ephemeral, having been observed to change position and orientations over the past 25 years (Figure 11). The low albedo patterns are spatially associated with and trending towards the southern and northwest breaks in Gusev's crater rim. This, coupled with the dust devil/wind streak phenomenon, suggests that this material is associated with the aeolian processes of scouring and/or deposition. It is unclear whether deposition, erosion, or both are being represented. Although the low albedo material does appear to correspond with morphologic features in Gusev, I do not

consider it as a *morphologic* unit as defined in this paper. While laterally extensive in some parts of Gusev, this unit does occur at a variety of elevations corresponding to the PL_m, WR_m, LB_m, and possibly TR_m units. This could suggest that either these units are being blanketed by material or are being eroded to reveal underlying lower albedo material. Low albedo material thus represents aeolian processes rather than a coherent unit.

3.3.2. Morphologic Unit Contacts.

Morphologic unit contacts in Gusev were delineated by differences in morphology and were often found to correspond with marked changes in elevation (Figure 3b). The boundary between the ET_m and WR_m in northeastern Gusev corresponds to a gradual change in slope and morphology, grading from ET_m to WR_m northward (Figure 12a). In southeastern Gusev, however, the boundary between ET_m and WR_m is marked by a steep escarpment and a pronounced change in morphology (Figure 12b). At the westernmost extent of ET_m, to the southwest of Thira crater, lobe margins for LB_m terminate at ET_m.

The exact eastern boundaries of the PL_m unit are less distinguishable visibly because of the presence of low albedo material. However, the boundary is defined by a noticeable slope break (~ -1880 m to –1939 m) along an east-west transect (Figure 12c). Unit boundaries for TR_m and MS_m are also distinguished by their respective morphologies and topographic relief along unit boundaries; however, some contacts are more difficult to define.

Nighttime TIR data gives the appearance that MV_t truncates a small crater's ejecta (Figure 5). Analysis of crater ejecta patterns, however, reveals that this crater was likely formed by an oblique impact from the southwest. This style of impact resulted in a 'forbidden zone' of ejecta on the uprange side of the crater rim (Figures 12d & 5), which is typical of oblique impacts [*Pierazzo & Melosh*, 2000]. MOLA profiles show an asymmetric profile to the crater, further indicating an oblique impact (Figure 12d). This suggests that the northernmost boundary for MV_t does not truncate the crater ejecta. Linear margins, one of which corresponds to MV_t eastern boundary, do suggest that MV_m does extend onto the floor of Gusev to the northeast of the crater (Figure 10a).

3.3.3. Layering Within Morphologic Units.

Of the 8 identified morphologic units within Gusev, four show evidence of layering. For this discussion, the term *layering* denotes layering within the major morphologic (and later surface) units. Most layers are exposed at constant elevations, possibly indicating horizontal to subhorizontal strata, and each appears to be of uniform thickness. Because exposures are not abundant in Gusev, most layering is observed along the steep slopes of crater walls and escarpments (Figure 13). An unnamed, 3.8 km-diameter impact crater within the ET_m in southeastern Gusev (14.83°S, 176.08°E), exposes several layers within its wall (Figure 13a). Some layers form cliffs while others form shallow slopes. Elevations of exposed layering in the western crater wall are between –1671 and –1789m below datum, coinciding with

ET_m elevations. This indicates that the uppermost ET_m is composed of several layers. Layers appear to be approximately horizontal, corresponding to given elevations along the crater wall.

Three craters expose layering within the PL_m unit. The first crater (Figure 13b), 6.5 km in diameter (14.54°S, 174.57°E), shows layers exposed along its southeastern wall between -1899 and –1939 m (corresponding to PL_m elevations). A second crater (Figure 13c), at 14.32°S 175.13°E, shows layers exposed along the entire crater wall at elevations between –1884 and –1898 m. The third crater (Figure 13d) at 14.68°S 175.07°E shows several layers exposed approximately between –1843 and –1926 m.

At least 4 craters in northeastern Gusev expose layering within the WR_m unit to the northeast of Thira crater. An example is a < 0.8 km diameter crater (14.04°S 176.08°E), exposing several layers between –1850 and –1900 m within its crater wall (Figure 13e). Layers are highlighted by shadowing and, in this case, slight albedo differences. Weathering profiles are also accentuated by shadowing effects.

MS_m shows some evidence of indistinct, sub-horizontal layering. One mesa (15.23 °S, 175.04°E) shows layers between –1800 and –1875 m, along eastward-facing exposures (Figure 13f).

4. Discussion

4.1 Proposal of Surface Units.

Comparison of thermophysical and morphologic unit properties shows a strong spatial correlation between many of the 2 unit types. This supports our approach of

using these properties independently to identify prominent units. However, it is important to note that the thermophysical properties of a given unit can vary laterally depending on a variety of factors such as grain size, facies changes, extent of cementation, degree of erosion/weathering, etc. Also, TIR data from the Martian surface is only representative of the top few centimeters of exposed material. If units are mantled by aeolian dust, TIR data cannot be used to map units. Thus, when observing discrepancies between thermophysical and morphologic units and trying to determine true unit boundaries, final morphologic delineation is, at the moment, preferred. In many cases, sudden slope changes also correspond more closely with morphologic changes rather than thermophysical ones, further supporting use of morphology as the deciding factor for delineating unit boundaries.

Recognizing the correlations between thermophysical and morphologic units, we propose 8 *surface* units within Gusev crater. Here the term *surface unit* defines rocks or sediments that (1) are laterally extensive or mappable, (2) express similar surface morphologies, (3) possess similar thermophysical qualities, and (4) occur over consistent elevation ranges across the mapped area. Surface unit abbreviations are indicated by the absence of a subscript. A surface unit map for Gusev crater is shown in Figure 14a. Proposed surface units are named using earlier designations and include Thira Rim (TR), Wrinkled (WR), Etched (ET), Lobate (LB), Plains (PL), Mesa (MS), and Ma'adim Vallis (MV).

4.2. Surface Unit Elevations and Thicknesses.

MOLA data (Figure 3) provide a means of measuring the maximum and minimum elevations of exposed units within Gusev. Elevation data allows comparison the relative vertical positions of different surface units (Figure 15). For example, Figure 15 shows that the highest exposed surface unit within Gusev is MS, while the lowest exposed units are WR and LB. Topographic relief (calculated from maximum and minimum unit elevations) was assumed to represent minimum unit thicknesses (Figure 15). Marked slope breaks at constant elevations also provided a means of further delineating suspected unit boundaries and identifying exposures of underlying units (Figure 3b).

4.3. Crater densities.

In an effort to determine relative and absolute ages of identified units, crater density measurements were made according to methods from previous studies *Crater Analysis Technique Working Group* [1979]. Results of crater counts, measurements of surface areas, populations of craters $\geq$ 1, 2, 5, and 16km, and age estimates are reported in Table 2 and summarized in Figure 16. Crater density measurements identify many of the units as Late Noachian to Late Hesperian in age, with WR Early Amazonian in age. Because no craters or ejecta are superimposed on low albedo material and due to their very recent (< 25 yrs.) redistribution within Gusev, this material is obviously Late Amazonian in age. Ages are mostly consistent with age estimates by *Kuzmin et al,* [2000].

4.4. Gusev Crater Stratigraphy

The combination of surface unit mapping (Figure 14), elevation data (Figure 15), and crater density ages (Figure 16) provides a means of determining the stratigraphy (Figure 14a) and thus the depositional/erosional history of Gusev crater. Ages based on crater densities for Gusev units should be considered with caution. Planetary surfaces that undergo modification by processes other than impact cratering give problematic crater ages. Factors such as erosion by wind or water, infilling, and the duration of exposure can lead to the obliteration of craters and therefore influence age estimates for such surfaces. With the presence of drainage and aeolian features within the Aeolius Quadrangle, age dating surface units is problematic and should only be considered within the context of topographic and other data.

The lowest (elevation) stratigraphic units within Gusev appear to be TR and WR. Exposed TR lies between –1625 and –1900 m, whereas WR is exposed between –1875 and –1975 m. From these elevations, it appears that WR lies below TR. However, WR is deposited against Thira's rim to the north (Figure 17). This indicates that TR existed prior to WR deposition, making TR the oldest unit within Gusev. No crater density data exists for TR due to a variety of factors. First, the high elevation of TR has led to prolonged erosion, modifying smaller craters superimposed upon the crater rim. Secondly, several collapsed terrace blocks lie along the rim, indicating further modification by crater wall collapse. The limited TR exposures also provide a statistically insignificant area for crater counting.

Both WR and LB lie at comparable elevations, but LB appears to have an older

relative age. This gives the first order appearance that LB may be older than WR. A comparison of the state of crater rims within both units (Figure 8) shows WR rims to be more degraded than those of LB, suggesting that WR is actually older than LB. If WR craters had been modified or even obliterated over time, crater density ages would represent the period during which modification took place, rather than deposition of WR. Additional support for an older WR comes from north central Gusev (Figure 18). Here LB has been deposited against WR ridges and in the valleys in between. This confirms that WR was first deposited and later modified prior to LB deposition.

While TR and WR have been demonstrated to be the oldest units within Gusev, the relationship between WR and other units is less clear. Crater density data also suggests that WR deposition post-dated that of ET. Based on the above discussion, an Early Amazonian age for WR is suspect. While WR lies at lower elevations within Gusev, its mean elevation is near –1905 m. When topographic profiles across ET-WR unit contacts in the north and southeast are considered (Figures 12a-b), a noticeable slope break at ~ -1900 m is observed. This slope break appears to be the topographic expression of WR underlying ET in southeastern Gusev.

Conflicting age data also exist between WR and PL. Crater densities suggest a Late Noachian to Late Hesperian age for PL compared to the derived Early Amazonian age for WR. Based on the above discussion, however, modification of WR gives a younger apparent age. Insight into the WR-PL relationship is provided by a broad 'window' (topographic depression) in northwestern Gusev. This 'window' shows smaller ridges at the bottom of the depression that corresponds to WR elevations. This

suggests that WR underlies PL, but could have resulted from erosion of PL and subsequent deposition of WR within basins. Comparison of the mean elevations for WR (-1905 m) and PL (-1865 m) supports the former hypothesis of WR underlying PL. This also suggests that PL may be relatively thin (<40 m). Based on this, 'Crivitz' crater, to the northwest of the landing ellipse, corresponds to WR elevations and has been mapped as WR (Figures 4b and 14). LB overlies WR in central Gusev and PL occurs at higher elevations than LB, further supporting the proposed WR-PL age relationship. It is certain that PL is present within western Gusev, but its easternmost extent is unclear. An escarpment near the southeastern PL boundary and the lack of PL exposure in eastern Gusev implies that PL does not extend into the eastern half of Gusev. However, an indistinct slope break near –1874 m in the ET-WR escarpment of northeastern Gusev may represent the topographic expression of PL in this area, suggesting PL deposition in eastern Gusev prior to ET. Lack of PL deposition in eastern Gusev would imply that ET directly overlies WR. The overlap in Late Noachian and Late Hesperian ages between ET and PL could support coeval deposition. If ET and PL were syndepositional, then a facies change may exist between these units. In either case, deposition of ET is contemporaneous with or post-dates PL deposition.

Although PL overlies LB and WR, the age relationship between PL and MS is less clear. Observations suggest that MS had been dissected. However, elevation data are not clear as to whether or not the PL depositional/erosional event was responsible. Crater densities (Figure 16) however, suggest a relatively younger age for PL indicating that PL deposition may post-date MS deposition. Because MV is at

higher elevations than PL both within Ma'adim Vallis and Gusev, we propose that MV post-dates PL. Crater densities show that MV deposition happened near the time of PL deposition.

Finally, with the low albedo material showing re-distribution during previous Mars missions (Figure 9), it is clear that this material represents the last stratigraphic event in Gusev.

Thira's calculated excavation depth (-3884 $\pm$413 m) does not extend to the initial estimated excavation depths of Gusev crater (-9326 $\pm$2848 m elevation respectively). Within minutes of most impact events (for complex craters), crater wall collapse sends target rock down toward the center of the transient crater, enlarging the crater diameter and infilling the transient cavity, reducing the crater depth. Gusev's initial modified crater depth is uncertain. The relationship of final crater depth, d, to final crater diameter, D, for martian craters (7 to 100 km diameter) was determined by *Smith et al.* [2001] to be $d = 0.33D^{0.53\pm0.03}$. This relationship was determined from measurements made by MOLA data of modified craters that are in various stages of exhumation and burial. If for the moment, we assume that this morphometric relationship holds for the 150 km-diameter Gusev crater and that d represents the initial modified crater depth (between – 4582 and – 3092 m) for Gusev, then it is possible that Thira may have excavated slumped target rock material from an infilled Gusev. If this relationship does not hold for larger craters, it is still possible that Thira excavated basement material. Soon after the formation of complex craters, a central uplift forms (although Gusev shows no evidence of such a central

peak). Thira crater, due to its proximity to Gusev's center, might have sampled basement in the central uplift. Such exhumation may have provided a means of sampling the oldest strata within Gusev.

The stratigraphic column and surface unit map (Figure 14) provide a basis for inferring the depositional/erosional history for units within Gusev crater. Following the Noachian impact event that formed Gusev [*Kuzmin et al.,* 1997; 2000], the Thira impact event exposed deep strata or basement. After Thira, WR was deposited (possibly across the entire floor of Gusev and perhaps preceded by deposition of older strata). Layering suggests multiple WR depositional episodes. Following WR deposition, ET was deposited and subsequently eroded. Lack of detection of ET beyond southeastern Gusev suggests that ET may represent localized deposition; however, exposed ~horizontal layering suggests that ET was laterally extensive and occurred in multiple episodes. The high degree of modification of the ET surface suggests extensive post-depositional erosion, with some areas resembling relict 'channels' suggestive of fluid movement (Figure 11). LB deposition occurred and was concentrated in southwestern and central Gusev, as demonstrated by its terminal lobate margins (Figure 8e). This unit was deposited at some of the lowest crater elevations. PL deposition then followed in multiple depositional events. Subsequent MV deposition then represented the last depositional event related to Ma'adim Vallis. During the Early Amazonian, modification of the WR surface occurred. Long after this, low albedo material was deposited and redistributed/re-exposed across Gusev.

4.5. Comparisons to Previous Work.

Analysis of THEMIS data, in context with TES, MOC, MOLA, and Viking Orbiter camera data sets has, for the first time, provided a new means of identifying local surface units on Mars and re-constructing their stratigraphic relationships and depositional/erosional histories. This approach can be compared to earlier studies [*Landheim et al.,* 1994; *Grin and Cabrol*, 1997b; *Kuzmin et al.,* 2000] that mapped surface units using Viking visible images and estimated elevations using photoclinometric and radar-based techniques. Newer Mars Odyssey and MGS instruments provide data related to thermophysical, morphological, topographic, crater density, and temporal relationships among units.

The first geologic map of Gusev [*Landheim et al.,* 1994] identified 6 geologic units. This map was followed by the *Grin and Cabrol* [1997b] sedimentologic map, which included 7 Gusev sedimentologic units. The USGS map [*Kuzmin et al.*, 2000] of Gusev was, like previous editions, based on analyses of Viking imagery and age calculations from crater density measurements. A distinction between our *surface unit* map and other 'geologic' maps is that presently, no compositional data presently exists for surface units, which are necessary for use of the term *geologic unit*. Forthcoming analyses of THEMIS spectra may allow some compositional inferences to be drawn. Here we compare our surface unit map with that of *Kuzmin et al.* [2000].

Although there is a rough correspondence between surface units from this study (Figure 14a) and the previously mapped 'geologic' units of *Kuzmin et al*. [2000] (Figure 14b), some differences are apparent. TR corresponds to a distinct geologic

unit of Moderately Degraded Crater Material (c_2). ET, in southeastern Gusev, corresponds to the southern half of Basin Floor Unit 1 $AHbm_1$, whereas WR correlates with both Gusev Crater Formation Member 1 $AHgf_1$ and $AHbm_1$. One of several WR outliers near the middle of the landing site ellipse was recognized as $AHbm_1$ on the geologic map. LB corresponds to $AHgf_1$. PL corresponds mostly with Gusev Crater Formation Member 2 ($AHgf_2$). MS mesas are distinctive in their thermophysical and morphological properties and thus are assigned to a distinct surface unit, but were correlated with $AHbm_1$ on the geologic map. MV is equivalent to Young Channel Floor Material ($AHch_3$) within Ma'adim Vallis, but with the extension of MV basinward, MV is shown to correlate with $Ahgf_2$ and Low Albedo Smooth Material as well. The two parallel bands of low albedo material now covering parts of $Ahgf_1$ and $AHgf_2$ were represented by a larger band of low albedo smooth material in previous geologic mapping (derived from Viking imagery), demonstrating temporal changes in the distribution of these units.

Several different stratigraphic sequences have been proposed for Gusev [*Landheim et al.*, 1994; *Cabrol et al.*, 1998; *Kuzmin et al.*, 2000]. The various stratigraphic models are compared with ours in Figure 17. Comparisons are complicated by different unit definitions. In comparing our stratigraphic column to that of *Kuzmin et al.* [2000], there is general agreement in the overall depositional sequence, with the exception of the timing of ET, LB, and MS depositional events. *Kuzmin et al.* [2000] considered ET, WR, and MS as a single unit, $AHbm_1$. Our model also correlates well with the depositional sequence of *Landheim et al.* [1994], with the

exception of low albedo material deposition (or exhumation). The *Cabrol et al*. [1998] model considers units outside of Gusev and does not subdivide the floor of Gusev into separate units.

4.6. Depositional Models.

Was Gusev truly a fluvio-lacustrine depocenter for much of martian history, as interpreted by others [*Schneeberger*, 1989; *Cabrol et al.,* 1993, 1998; *Grin et al.,* 1994; *Grin and Cabrol*, 1997b]? Could volcanic or aeolian deposition be plausible depositional models for Gusev, or could all of these have contributed? Here we consider 3 hypotheses for unit deposition within Gusev crater: (1) sedimentary, (2) volcanoclastic, or (3) volcanoclastic-sedimentary deposition.

The first model involves deposition of strata entirely by sedimentary processes, either in fluvial and/or lacustrine settings as proposed by others [*Schneeberger*, 1989; *Cabrol et al.,* 1993, 1998; *Grin et al.,* 1994; *Grin and Cabrol*, 1997b]. Surface units within Gusev appear as horizontal to sub-horizontal units that show basin-wide or localized deposition. Original horizontality, while not unique to sedimentary regimes, does appear to occur within Gusev and may suggest sedimentary deposition. While horizontal units in Gusev may represent deposition under a lacustrine regime, present data sets (MOC and THEMIS) do not provide the resolution needed to identify uniquely lacustrine features.

Under a fluvio-lacustrine regime, changing lacustrine base levels could account for varying geographic extents of geologic units. Initially, deposition of the

basin-wide WR would represent normal, quiet water deposition of silt and clay across the basin. A rising base level would have then led to deposition of ET across Gusev, filling it to levels of at least –1710 m below datum. Base level in Gusev would then have dropped and LB would have been subaerially deposited within western and central Gusev. *Cabrol* [2002] interpreted LB's lobate margins as terraced shorelines. The morphology and changing elevations over which LB is deposited does not agree with this. Rather, it appears that the lobate margins represent the termination of flow against ET (in the southeast) and WR (in central Gusev). The morphology of this unit is possibly consistent with deposition by sub-lacustrine turbidity currents. The lobate nature of LB's terminal margins is more consistent with deposition by debris flow or as a 'slurry' of material. Though the relative timing of PL and MS deposition is unclear, crater ages and the dissected nature of MS suggest that MS was deposited prior to PL. A rising base level (to at least –1500 m) would then account for the later deposition of MS at the terminus of Ma'adim. The sudden change from the higher energy regime of Ma'adim to the lower energy regime of standing water in Gusev would result in dumping of sediment as 'deltaic' deposits at the interface. In terrestrial deltas, deposition of sediment along slopes results in foreset bedding. Weakly exposed layering in MS appears to be horizontal, with a lack of dipping strata, suggesting that MS may not be deltaic in origin. An alternative to this could be that MS was a basin-wide deposit, subsequently eroded away from most of Gusev. Depending upon the true lateral extent of PL, deposition may have been more localized (suggestive of fluvial settings) or basin-wide (suggesting a somewhat higher base levels between –

1865 and –1905 m). Either scenario would represent a reduced base level from the time of MS deposition. Subsequent, very localized, deposition of MV would have resulted from even lower base levels under a fluvial setting. Under a fluvio-lacustrine regime, the changing morphology of MV from Ma'adim to Gusev could be accounted for. The linear ridges parallel to the long axis of Ma'adim Vallis continue until the breach in Gusev's southern rim. Once inside Gusev the characteristic MV texture is lost. This could indicate constrained valley flow towards the crater rapidly changing into flow across the broader plan of the crater floor. Another moderate rise in base level could account for sub-lacustrine modification of WR during the Early Amazonian. Eventual evacuation of water from Gusev would have led to the present-day aeolian regime. Under this model, fluvio-lacustrine activity would have dominated during the Hesperian, suggesting a period of hydrologic activity of <1 Ga, as opposed the <2 Ga period proposed by *Grin and Cabrol* [1997b] and *Cabrol et al.* [1998]. However, standing lake levels as late as the Early Amazonian may have occurred, modifying WR, extending this period to <2 Ga. Thermal inertia values for surface units, under a fluvio-lacustrine regime, should be expected to correlate with values expected from sediment or sedimentary rock. Interpretations of surfaces covered by $\leq$ sand-sized particles for 2 surface units (PL and WR) and low albedo material are consistent with this. However, these thermal inertias are from the uppermost regolith and may not be representative of the entire surface unit. Also, under this model, thermal inertias of units (such as MV or PL) extending from Ma'adim into Gusev should consistently change as depositional energies (and thus particle size distribution) change. This

trend is not readily observable in TES data, but also may be masked by dust covering surface units.

Our consideration of the fluvio-lacustrine hypothesis should not preclude the role of aeolian deposition within Gusev. Aeolian erosion and deposition are the only processes that presently occur within Gusev. Wind streaks, dust-devil tracks, and small dune fields have been observed superimposed on surface units, indicating more recent activity. However, we have not yet observed 'fossil' aeolian bedforms within surface units or their layers; however, current data sets lack the resolution to identify and distinguish between 'fossil' aeolian and fluvio-lacustrine sedimentary structures.

A volcanoclastic model may account for the distribution and orientation of units and layering within Gusev. Horizontal layering occurs in many terrestrial and martian lava flows and ash deposits. Apollinaris Patera, to the northeast, would be a candidate source area for such material. Surface types 1 and 2, thought to represent volcanic lithologies [*Bandfield et al.,* 2000; *Hamilton et al.,* 2001; *Minitti et al.,* 2002; *Wyatt & McSween,* 2002], have been detected in low albedo material in Gusev; however, visible imagery and TES thermal inertia data suggest that these are likely aeolian sand. While Apollinaris lava flows did not extend as far as Gusev, explosive volcanic episodes during the Hesperian may have deposited ash within Gusev [*Robinson et al.*, 1993]. Surface unit ages do correspond to the timing of Apollinaris volcanic activity. Prevailing winds at the time of eruption could have carried ash fall southeastward toward Gusev. Under this model, variability in layering weathering profiles could be explained by ash compositional variability or the degree

of induration of ash falls. However, comparisons of slope angles for Apollinaris Patera with other martian phreatomagmatic and shield volcanoes, suggest less energetic explosive activity and thus fewer distal fall deposits [*Thornhill* et al., 1993]. This model alone cannot account for the localized deposition of units such as LB, MS, MV, and potentially ET and PL, but may account for deposition of WR and the low albedo material. Because this model considers Apollinaris Patera the most likely volcanic source area, volcanoclastic deposits would thus thicken northwestward across Gusev. Presently, there is no indication that such thickening occurs. If such thickening once existed, it may have been subsequently modified by erosional processes inside Gusev.

Because neither of the above models provides a unique solution for deposition within Gusev, a third volcanoclastic-sedimentary model is considered. This model proposes syndepositional and/or alternating volcano-sedimentary deposits within Gusev. It evokes fluvial and/or aeolian processes for localized deposition, while lacustrine and ash-fall activity could account for basin-wide deposition. Pronounced weathering profiles could also be explained by changes in rock type or other factors mentioned above.

With the limitations placed on the volcanoclastic model, it is the least favored of the three. The volcanoclastic-sedimentary model is the most preferred because it accounts for both localized and widespread deposition within Gusev and recognizes the potential influx of ash-fall deposits from nearby Apollinaris Patera. Even if explosive activity were less energetic, leading to lower plume heights, prevailing wind

patterns could serve to transport ash over 350 km to Gusev crater. With such minimal activity and long transport distances, the role of volcanic deposition is diminished as compared to sedimentary processes. While the results of our study are consistent with Gusev as a fluvio-lacustrine depocenter, we have yet not identified features that are uniquely lacustrine (i.e. shorelines, evaporites, etc.).

4.7. MER testable hypotheses.

Regardless of the exact depositional/erosional history of Gusev crater, this study has demonstrated the geologic variability of the site (6 or more of the 8 surface units mapped in this study lie within the MER-A landing ellipse). With such heterogeneity, the possibility of sampling materials transported from proximal units (by aeolian, fluvial, or impact processes) during MER rover traverses (<600 m) is high relative to other candidate landing sites.

A MER rover in Gusev would provide an opportunity to calibrate remote sensing data collected by the orbiting THEMIS and TES instruments. Mini-TES will have the ability to measure albedo, thermal inertia, and temperature, as well as the capability of collecting spectra from dust-free surfaces, which could be used to compare surface compositions derived from the THEMIS and TES instruments. The ability to "ground-truth" remote sensing data may lead to more accurate interpretations of Gusev geology.

Instruments on MER provide a means of testing depositional models and determining stratigraphic relationships of units within Gusev. Spectral analyses from

Mini-TES and APXS may provide data with which to identify rock types and thus clarify depositional regimes. Pancam and Microscopic Imager could reveal textures within strata indicative of depositional parameters (i.e. energy of environment). Pancam, APXS, and Mini-TES could discriminate rock types, thus noting contributions from various depositional sources (fluvio-lacustrine, aeolian, volcanoclastic). In addition, imaging instruments may be used to determine the true nature of some unit contacts (i.e. stratigraphic position, conformable vs. non-conformable) within Gusev.

MER traverses will occur within only a limited portion of the MER-A landing ellipse (Figure 1). Considering this, we take a closer look at the geology of the landing ellipse (Figure 14) from east to west, examining previous hypotheses and how MER might test them.

A landing near the rim of Thira crater provides an opportunity to examine the TR and LB units. Is TR different spectrally (and thus compositionally) from LB, or did the Thira impact event sample a lower portion of WR? Analyses of rim material may also determine whether dark patches along the Thira rim is aeolian drifts of low albedo material or exposed bedrock.

Traverses farther west would likely encounter exposures of LB, PL, and low albedo material. Analyses of low albedo material in this area may indicate whether or not it overlies PL and LB or simply represents a scouring of the PL and LB surfaces. A landing on the eastern side of the escarpment between LB and PL/low albedo material exposures could provide an opportunity to examine further the stratigraphic relationships and note the presence of additional strata not measured in this study.

The center of the landing ellipse is dominated by the PL unit, which, if determined to represent fluvial deposition, provides a means of analyzing sediment from Ma'adim source regions [*Irwin et al.*, 2002]. Although PL is the dominant unit here, there are several craters that likely sampled sub-surface strata (below the inferred 40 m thickness for PL). The measured depth (>-1900 m) of an unnamed crater (Figure 13c) indicates that it likely excavated LB and WR strata, providing a means for MER to sample these units. Elevation measurements from another crater northwest of the landing ellipse (Figure 13b) also indicate that this impact event sampled WR, ejecting material into the landing ellipse.

Two isolated areas within the landing ellipse (Figure 14) may provide access to other units. Each exposes material that morphologically, has an 'etched' appearance, suggestive of ET. They also have nighttime TIR temperatures comparable to western ET. In daytime TIR, each window has thermophysical properties consistent with LB, ET, or the material immediately underlying PL. MOLA data show elevations consistent with PL and ET. MER traverses in this area may allow for the distinction between PL and ET for these areas. The presence of ET within the landing ellipse would further add to the geologic diversity of the ellipse, with 7 of the 8 units exposed.

Quasi-Circular Depressions (QCDs), first identified on Mars by *Frey et al.* [1999], may also provide a means of sampling from Gusev's sub-surface strata within the landing ellipse. A Quasi-Circular Depression (QCD) within the southwestern portion of the landing ellipse has been detected (at 14.96°S, 175.04°E) from MOLA data (Figure 4b). This QCD, first identified by *Kuzmin et al.* [2000], is thought to

represent a buried crater. Its rim has yet to be noted in visible or TIR data; however, a circular positive relief feature (-1820 to –1860 m) has been detected using MOLA data and is thought to represent the surficial expression of the crater rim. Measured rim diameters and heights have allowed us to calculate the transient crater diameter [*Croft*, 1985] and excavation depth for this QCD. This crater would have penetrated to depths of –3300 to –4000 m, well below the lowest exposed WR. Like Thira crater, this QCD may have sampled WR strata or older units. A landing near the center of the ellipse provides MER a means of sampling sub-surface stratigraphy to address the following questions: (1) What are the stratigraphic relationships between PL, LB, WR, and potentially older units? (2) Are these units spectrally (and perhaps compositionally) distinct from each other? (3) Has Gusev's depositional environment changed from its early history?

MER traverses within the western portion of the landing ellipse would also permit the examination of low albedo material and PL, but more importantly, could allow the nature of MV to be determined. Is MV a real surface unit within Gusev, or does it represent a thermophysically distinct area within the PL unit? If it is a distinctive surface unit, how does it compare spectrally with PL? Does it represent a final stage of fluvial deposition? Answers to these questions would provide insight into Gusev's late-stage depositional environments.

It is clear that the MER-A landing ellipse lies within a geologically heterogeneous area of Mars and of Gusev itself. If this heterogeneity represents changes in a single or multiple depositional environments, then direct analyses of

Gusev surface units by MER may provide insight into changing geologic/climatic conditions over a significant interval of Martian geologic history. More importantly, MER would provide a means of examining the geologic and climatic record of Mars over an extended and important (Noachian-Hesperian) interval of martian history.

5. Summary

Gusev crater is a candidate site for MER because of its suspected former fluvio-lacustrine environment. This study has used high spatial-resolution data from THEMIS, supplemented by TES, MOC, and MOLA data, to re-examine units comprising the floor of Gusev and Ma'adim Vallis. Thermophysical and morphologic unit maps show broad correlations, supporting the validity of the 7 proposed surface units, as follows:

- Ma'adim Vallis (MV) – THEMIS nighttime cold material (occurring as parallel ridges in the valley) from Ma'adim Vallis appearing to extend into Gusev
- Plains (PL) – unit trending from Ma'adim to northwest breach in Gusev's rim with hot nighttime TIR craters
- Mesa (MS) – dissected mesas with cold nighttime tops and hot TIR slopes
- Lobed (LB) – flat, freshly-cratered surface with distinctive lobate margins
- Etched (ET) – unit with a 'mottled' daytime/nighttime TIR appearance and apparently eroded surface

- Wrinkled (WR) – unit with low, north-south oriented ridges that contains cold nighttime TIR craters
- Thira Rim (TR) – unit exposed along Thira crater rim; hot nighttime TIR material; strata exhumed from depth

Observations of the surface unit map and MOLA topography data allowed us to define Gusev's stratigraphy and thus infer a depositional/erosional history for the crater interior. The stratigraphic order (top to bottom), is as presented above. The existence of 8 surface units, and layering within these units, suggests multiple depositional and erosional events. Observations are consistent with deposition by fluvial, lacustrine, volcanoclastic, and/or aeolian processes. Landing a MER rover in Gusev would probably allow sampling of multiple surface units, would provide ground truth for orbital remote sensing measurements, and would test a number of hypotheses about surface and geologic units in the interior of Gusev offered in this and previous papers.

* = Crater names denoted by quotation marks are pending approval by the International Astronomical Union

Acknowledgments

This work was partly supported by NASA subcontract 01-082 from Arizona State University (HYM), JPL-1241129 (JEM), and the 2001 Mars Odyssey Science Office (PRC). Thanks also to Victoria E. Hamilton, Melissa Lane, and Jim Rice for their insightful review of our work.

References

Bandfield, J.L., V.E. Hamilton, and P.R. Christensen, A global view of martian surface compositions from MGS-TES, *Science, 287* (5458), 1626-1630, 2000.

Cabrol, N.A., and A. Brack, Episodic oasis for water-dependent life on Mars, *Proc. of the Lunar and Planet. Sci. Conf., 26th*, 201-202, 1995.

Cabrol, N.A., E.A. Grin, A. Dollfus, and G. Dawidowicz, An ancient inner lake in Ma'adim Vallis, *Lunar and Planet. Sci. Conf., 24th*, 241-242, 1993.

Cabrol, N.A., R. Landheim, R. Greeley, and J.D. Farmer, Fluvial processes in Ma'adim Vallis and the potential of Gusev crater as a high priority site, *Proc. of the Lunar and Planet. Sci. Conf., 25th*, 213-214, 1994.

Cabrol, N.A., E.A. Grin, V.C. Gulick, C.P. McKay, R. Greeley, M. Sims, and G. Briggs, Rover mobility and sampling strategy on Mars: The case for Gusev crater, *Proc. of the Lunar and Planet. Sci. Conf., 26th*, 189-190, 1996.

Cabrol, N.A., and E.A. Grin, Hydrogeology and exobiology significance of martian large crater lakes, *In Conference on early Mars; geologic and hydrologic evolution, physical and chemical environments, and the implications for life, edited by S.M. Clifford, A.H. Treiman, H.E. Newsom, and J.D. Farmer*, pp. 14-15, Lunar and Planetary Institute, Houston, 1997.

Cabrol, N.A., E.A. Grin, R. Landheim, R.O. Kuzmin, and R. Greeley, Duration of the Ma'adim Vallis/Gusev crater hydrogeologic system, Mars, *Icarus, 133*, 98-108, 1998.

Cabrol, N.A., E.A. Grin, and D. Fike, Gusev Crater: A landing site for MER. *In Lunar and Planetary Science Conference XXXIII*, Abstract #1142, Lunar and Planetary Institute, Houston, (CD-ROM), 2002.

Cabrol, N. A., Gusev crater (MER A): Overview of relevance, science, and testable hypotheses, Mars Exploration Rover Landing Site Workshop, March 26-28, 2002, Pasadena, California (presentation).

Christensen, P.R., D.L. Anderson, S.C. Chase, R.N. Clark, H.H. Kieffer, M.C. Malin, J.C. Pearl, and J. Carpenter, Thermal emission spectrometer experiment; Mars Observer mission, *J. of Geophys. Res., 97 (5)*, 7719-7734, 1992.

Christensen, P.R., J.L. Bandfield, V.E. Hamilton, S.W. Ruff, H.H. Kieffer, T.N. Titus, M.C. Malin, R.V. Morris, M.D. Lane, R.N. Clark, B.M. Jakosky, M.T. Mellon, J.C. Pearl, B.J. Conrath, M.D. Smith, R.T. Clancy, R.O. Kuzmin, T. Roush, G.L. Mehall, N. Gorelick, K. Bender, K. Murray, S. Dason, E. Greene, S. Silverman, and M. Greenfield, Mars Global Surveyor Thermal Emission Spectrometer experiment: Investigation description and surface science results, *J. of Geophys. Res., 106 (E10)*, 23823-23871, 2001.

Christensen, P. R., J. L. Bandfield, J. F. Bell III, N. Gorelick, V. E. Hamilton, A. Ivanov, B. M. Jakosky, H. H. Kieffer, M. D. Lane, M. C. Malin, T. McConnochie, A. S. McEwen, H. Y. McSween, Jr., G. L. Mehall, J. E. Moersch, K. H. Nealson, J. W. Rice, Jr., M. I. Richardson, S. W. Ruff, M. D. Smith, T. N. Titus, and M. B. Wyatt, Morphology and composition of the surface of Mars: Mars Odyssey THEMIS results, *Science, 300*, 5628, 2056-2061, 2003.

Crater Analysis Technique Working Group, Standard techniques for presentation and analysis of crater-size frequency data, *Icarus, 37*, 2, 467-474, 1979.

Croft, S.K., The scaling of complex craters, *J. of Geophys. Res., 90*, C828-C842, 1985.

Eugster, H.P., and L.A. Hardie, Saline lakes, *In Lakes; chemistry, geology, physics, edited by A. Lernam*, pp. 237-293, Springer-Verlag, New York, 1978.

Farmer, J.D., and D. Des Marais, Exploring for a record of ancient martian life, *J. of Geophys. Res., 104* (E11), 26977-26995, 1999.

Frey, H., S.E.H. Sakimoto, and J.H. Roark, Discovery of a 450km diameter, multi-ring basin on Mars through analysis of MOLA topographic data, *Geophys. Res. Lett., 26*, 12, 1657-1660, 1999.

Grin, E.A., N.A. Cabrol, and G. Dawidowicz, Proposal for a topographic survey of Gusev Crater, *Lunar and Planet. Sci. Conf., XXV*, 483-484, 1994.

Grin, E.A., and N.A. Cabrol, Antarctic analog for a perennial ice-covered paleolake in Gusev Crater (Mars), *Proc. of the Lunar and Planetary Sci. Conf., 28th*, 473-474, 1997*a*.

Grin, E.A., and N.A. Cabrol, Limnologic analysis of Gusev crater paleolake, Mars, *Icarus, 130*, 461-474, 1997*b*.

Grin, E.A., and N.A. Cabrol, Subglacial rotary currents in Gusev Crater paleolake (Mars), *Proc. of the Lunar and Planetary Sci. Conf., 28th*, 475-476, 1997*c*.

Hamilton, V.E., M.B. Wyatt, H.Y. McSween, Jr., and P.R. Christensen, Analysis of terrestrial and martian volcanic compositions using thermal emission spectroscopy, 2. Application to martian surface spectra from the Mars Global Surveyor Thermal Emission Spectrometer, *J. Geophys. Res., 106* (E7), 14733-14746, 2001.

Irwin, R.P. III, T.A. Maxwell, A.D. Howard, R.A. Craddock, and D.W. Leverington, A large paleolake basin at the head of Ma'adim Vallis, Mars, *Science, 296*, 2209-2212, 2002.

Jakosky, B.M., and M.T. Mellon, High-resolution thermal inertia mapping of Mars: Sites of exobiological interest, *J. of Geophys. Res., 106* (E10), 23887-23907, 2001.

Kuzmin, R.O., R. Greeley, R. Landheim, and N. Cabrol, Geologic mapping of Gusev crater-Ma'adim Vallis region, Mars, *Lunar and Planet. Sci. Conf. XXVIII*, 779-780, 1997.

Kuzmin, R.O., R. Greeley, R. Landheim, N.A. Cabrol, and J.D. Farmer, Geologic map of the MTM-15182 and MTM-15187 quadrangles, Gusev Crater - Ma'adim Vallis Region, Mars, in Geologic Investigative Series, pp. 8, 1-sheet, U. S. Geological Survey, Reston, VA, 2000.

Landheim, R., R. Greeley, D. Des Marais, J.D. Farmer, and H. Klein, Mars exobiology landing sites for future exploration, *Proc. of Lunar and Planet. Sci. Conf., 24th*, 845-846, 1993.

Landheim, R., N.A. Cabrol, R. Greeley, and J.D. Farmer, Strategic assessment of Gusev crater as an exobiology landing site, *Proc. of Lunar and Planet. Sci. Conf., 25th,* 769-770, 1994.

Malin, M.C., G.E. Danielson, A.P. Ingersoll, H. Masursky, J. Veverka, M.A. Ravine, and T.A. Soulanille, Mars Observer Camera, *J. of Geophys. Res., 97*, 7699-7718, 1992.

Malin, M.C., and K.S. Edgett, Mars Global Surveyor Mars Orbiter Camera: Interplanetary cruise through primary mission, *J. of Geophys. Res., 106 (E10)*, 23429-23570, 2001.

Masursky, H., A.L.J. Dial, M.E. Strobell, and D.J. Applebee, Recent progress in the study of MRSR (Mars Rover Sample Return) candidate landing sites, *Proc. of Lunar and Planet. Sci. Conf., 19th*, 730-731, 1988.

Minitti, M.E., J.F. Mustard, and M.J. Rutherford, Effects of glass content and oxidation on the spectra of SNC-like basalts: Applications to Mars remote sensing, *J. of Geophys. Res., 107 (E5),* 10.1029/2001JE001518, 2002.

Pelkey, S.M., B.M. Jakosky, and M.T. Mellon, Thermal inertia of crater-related wind streaks on Mars, *J. of Geophys. Res., 106 (E10)*, 23909-23920, 2001.

Pierazzo, E. and H.J. Melosh, Understanding oblique impacts from experiments, observations, and modeling, *Annu. Rev. Earth Planet. Sci., 28*, 141-167, 2000.

Robinson, M.S., P.J. Mouginis-Mark, J. Zimbleman, and S.S.C. Wu, Chronology, Eruption duration and atmospheric contribution of Apollinaris Patera, Mars, *Lunar and Planet. Sci. Conf., 24th,* 1209-1210, 1993.

Schneeberger, D.M., Episodic channel activity at Ma'adim Vallis, Mars, Proceedings of the *Lunar and Planet. Sci. Conf., 20th*, 964-965, 1989.

Smith, D.E., M.T. Zuber, H.V. Frey, J.B. Garvin, J.W. Head, D.O. Muhleman, G.H. Pettengill, R.J. Phillips, S.C. Solomon, H.J. Swally, W.B. Banerdt, T.C. Duxbury, M.P. Golombek, F.G. Lemoine, G.A. Neumann, D.D. Rowlands, O. Aharonson, P.G. Ford, A.B. Ivanov, C.L. Johnson, P.J. McGovern, J.B. Abshire, R.S. Afzal, and X. Sun, Mars Orbiter Laser Altimeter: Experimental summary after the first year of global mapping of Mars, *J. of Geophys. Res., 106 (E10)*, 23689-23722, 2001.

Tanaka, K. L., The stratigraphy of Mars, Proceedings of the 17th Lunar and Planetary Science Conference, Part I, *J. of Geophys. Res., 91 (B13)*, E139-E158, 1986.

Thornhill, G.D., D.A. Rothery, J.B. Murray, A.C. Cook, T. Day, J.P. Muller, and J.C. Iliffe, Topography of Apollinaris Patera and Ma'adim Vallis: Automated extraction of digital elevation models, *J. of Geophys. Res., 98* (E12), 23581-23587, 1993.

Wyatt, M.B., and H.Y.J. McSween, Spectral evidence for weathered basalt as an alternative to andesite in the northern lowlands of Mars, *Nature, 417 (6886)*, 263-266, 2002.

Zuber, M.T., D.E. Smith, S.C. Solomon, D.O. Muhleman, J.W. Head, J.B. Garvin, J.B. Ashire, and J.L. Bufton, The Mars Observer Laser Altimeter investigation, *J. Geophys. Res.,* 97, 7781-7797, 1992.

Appendix for Part 2

Table 1: THEMIS Units* within Gusev Crater

Units	Thermophysical Properties: Vis.	Day IR	Night IR	Morphologic Properties	Equivalent USGS Geologic Units**
Ma'adim Vallis (MV)	High	Warm	Cold	low ridges parallel to Ma'adim; length (apparent flow direction) but do not extend into Gusev; smaller perpendicular ridges nearer to Gusev	$AHch_3$, $AHgf_2$
Plains (PL)	High	Warm	Warm Craters: hot	Smooth w/ moderately dense, small crater population	$AHgf_2$
Mesa (MS)	High	Warm	Tops: cold Slopes: hot	Flat-topped surrounded by steep slopes	$AHbm_1$
Etched (ET)	High	Cold	Knobs: hot Underlying: cold	Small knobs w/ rare 'channelized' areas largely devoid of craters	$AHbm_1$, $AHgf_1$
Wrinkled (WR)	High	Warm	Warm Craters: cold	Low, subdued ridges trending NE-SW and N-S; older, degraded craters present	$AHbm_1$, $AHgf_1$
Thira Rim (TR)	High	Warm	Warm	Crater rim with collapsed terrace	c_2
Low albedo (LA_t and low albedo materials)	Low	Hot	Hot	Overlapping wind streaks, tracks; multiple prevailing/local wind patterns; variable distribution with time	$AHgf_2$
High Thermal Inertia (HTI_t)	High/ low	Warm/ cold	Hot	Rough terrain w/ high thermal inertia (TES) and low albedo deposits	$AHbm_1$, $AHgf_2$

* = the first six units occur as both thermophysical and morphological units, the second 2 units occurs only as thermophysical units; ** = *Kuzmin et al.* [2000]

Table 2. Crater Density/Age Determination

		Crater Density (N = no. craters > (x)km diam./10^6 km^2)			
Unit Name	Unit Area (km^2)	N(1)	N(2)	N(5)	Age Range
PL	3230	2167	1238	310	UN-UH
WR	2945	111	185	0	LA-UA
ET	1249	1600	800	0	LH-UH
MS	439	2277	2277	0	UH
TR	~163	0	0	0	
MV	549	3644	1822	0	LH
low albedo	~518	0	0	0	
LB	1152	3473	0	0	LH

UN = Upper Noachian; LH = Lower Hesperian; UH=Upper Hesperian;
LA = Lower Amazonian; UA = Upper Amazonian

Figure 1. (a) Current THEMIS visible coverage overlain on MOC-MGS mosaic of Gusev crater. Black ellipse shown represents the MER-A landing ellipse (a 3-sigma probability of actual MER-A landing). (b) Reference map showing the locations of detailed figures described later.

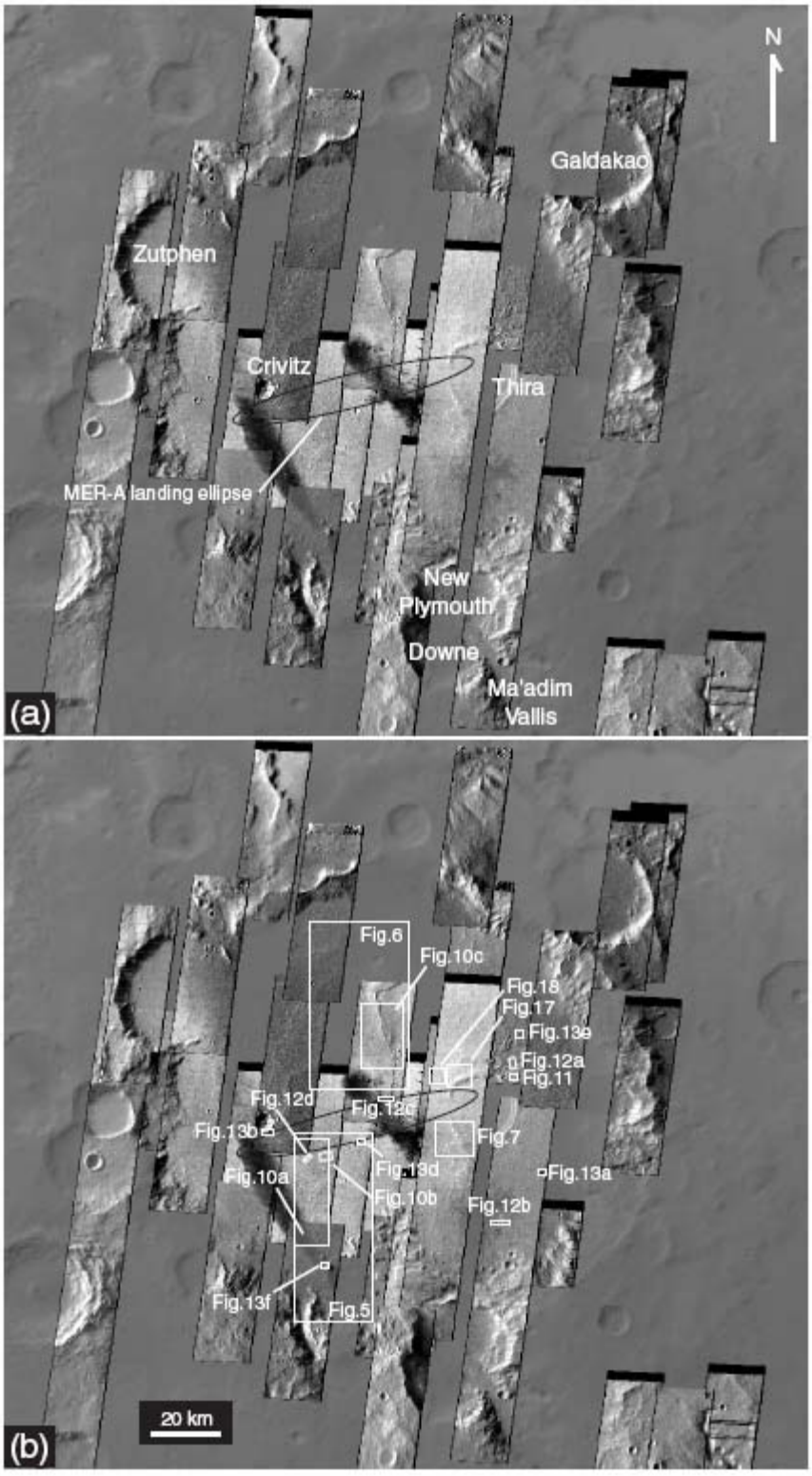
N
Galdakao
Zutphen
Crivitz
Thira
MER-A landing ellipse
New Plymouth
Downe
Ma'adim Vallis
(a)
Fig.6
Fig.10c
Fig.18
Fig.17
Fig.13e
Fig.12a
Fig.11
Fig.12d
Fig.12c
Fig.13b
Fig.7
Fig.13d
Fig.10a
Fig.13a
Fig.10b
Fig.12b
Fig.13f
Fig.5
20 km
(b)

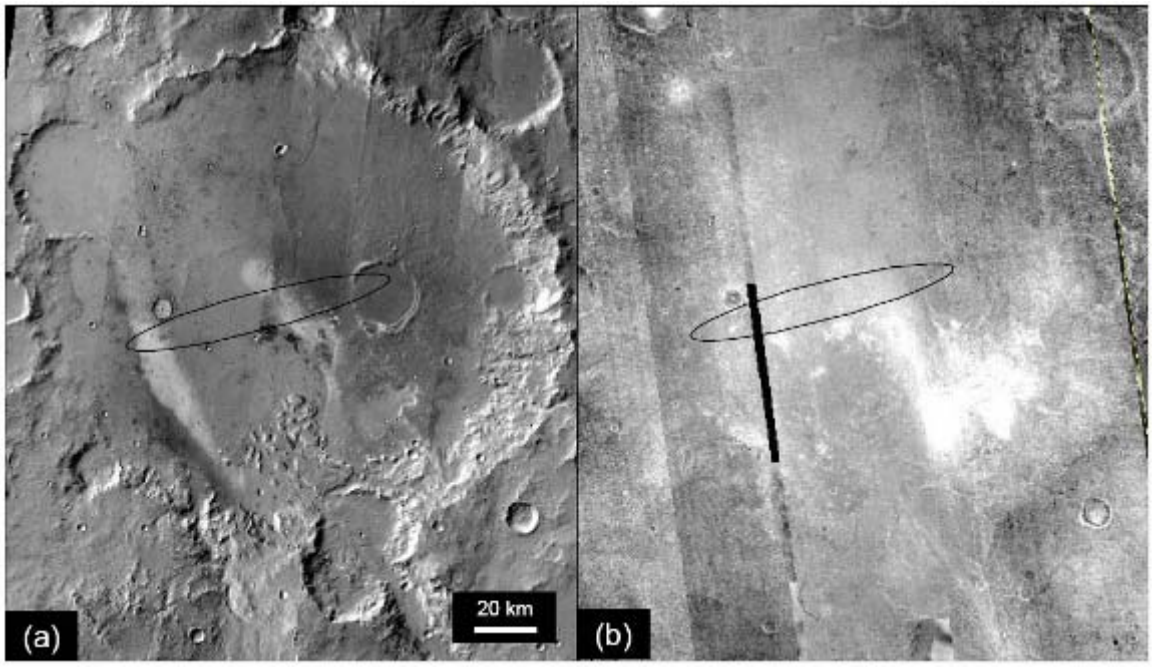

Figure 2. THEMIS (a) daytime TIR and (b) night TIR image mosaics (Band 9) for Gusev crater. Black ellipse shown represents the MER-A landing ellipse.

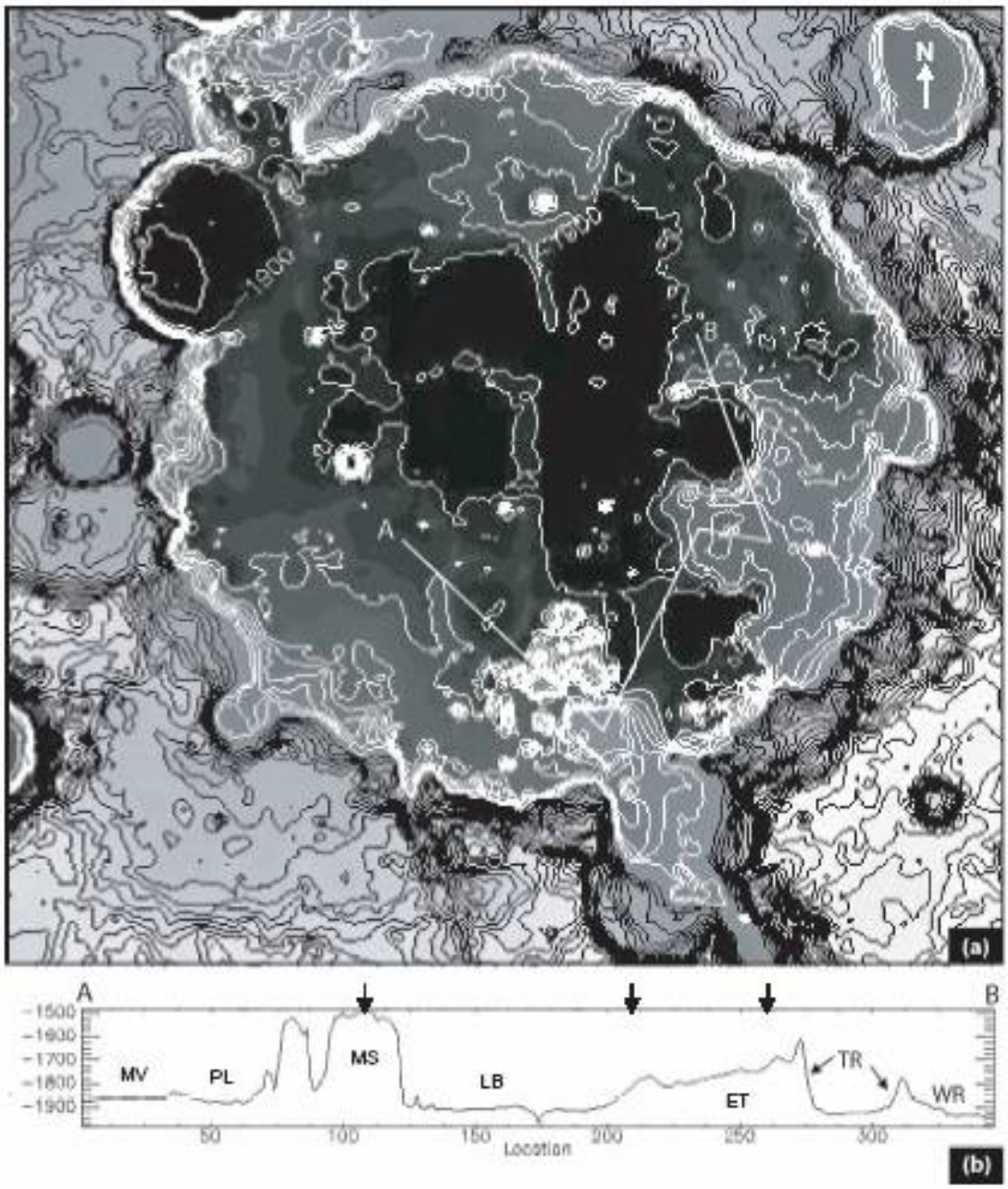

Figure 3. (a) Topographic map of Gusev crater generated from v.2.0 MEGDR MOLA global topographic grid. For clarity, the contour interval (white contours) inside the crater (between -200 and -1500 m below datum) is 50 meters; from the base of the rim outward (between -1500 and -2500 m), contour intervals of 100 m are used (black contours). (b) MOLA profile across most units within Gusev profile line is shown in (a). Unit abbreviations are given in Table 1 and defined later. Arrows above profile indicate a change in profile orientation in (a).

Figure 4. Maps of (a) thermophysical units and (b) morphologic units in Gusev Crater (overlain on THEMIS day IR image mosaic). Black ellipse represents MER-A landing ellipse.

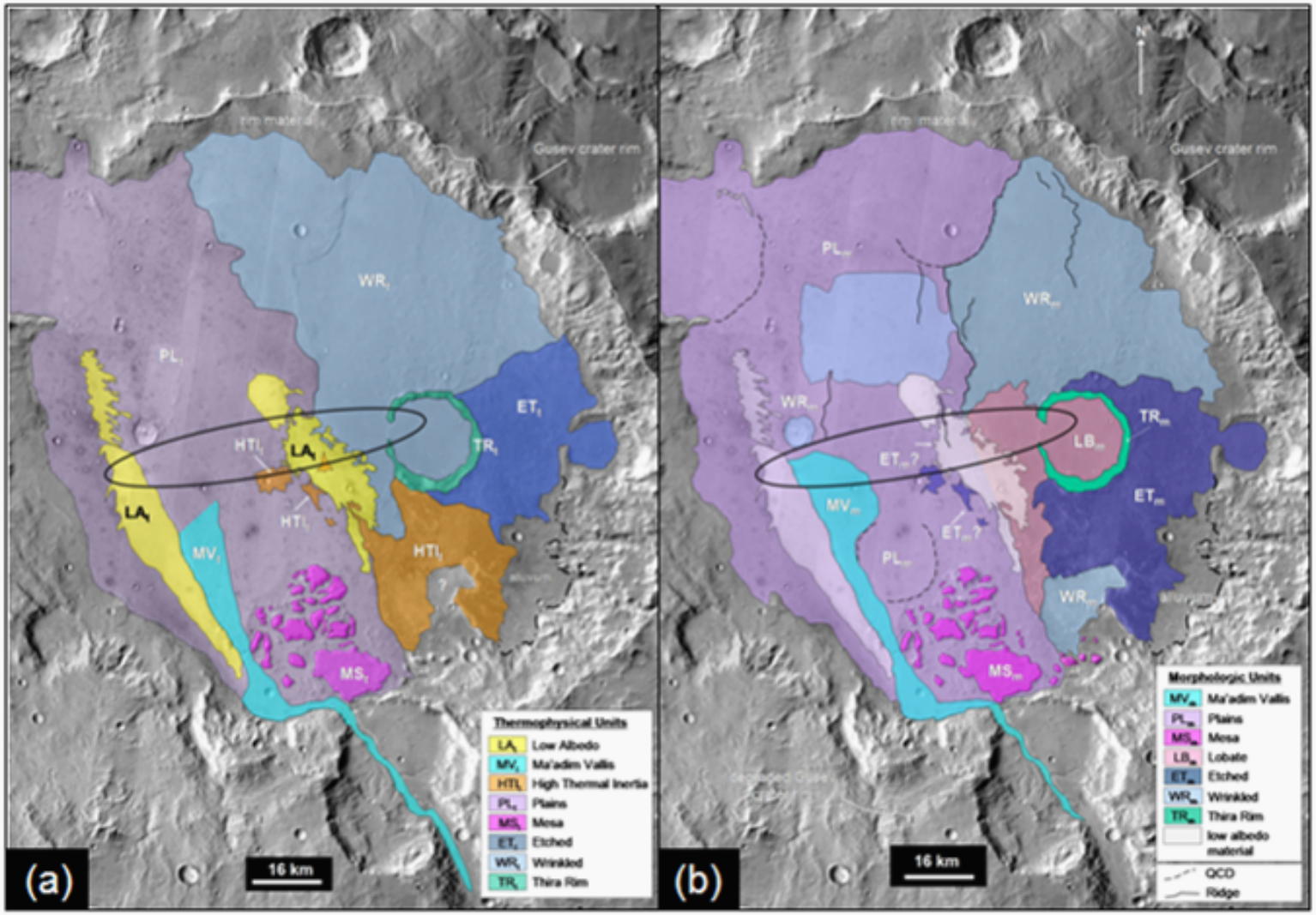
rim material
Gusev crater rim
WR
PL
ET
TR
HTI
LA
MV
MS
Thermophysical Units
LA Low Albedo
MV Ma'adim Vallis
HTI High Thermal Inertia
PL Plains
MS Mesa
ET Etched
WR Wrinkled
TR Thira Rim
16 km
(a)
(b)
N
Morphologic Units
MV Ma'adim Vallis
PL Plains
MS Mesa
LB Lobate
ET Etched
WR Wrinkled
TR Thira Rim
low albedo material
QCD
Ridge

Figure 5. THEMIS night IR image (I01873002) showing eastern boundary (arrows of Ma'adim Vallis thermophysical (MV_t) unit in Gusev Crater. 'Forbidden zone' of missing crater ejecta can be seen to the southwest of unnamed r.

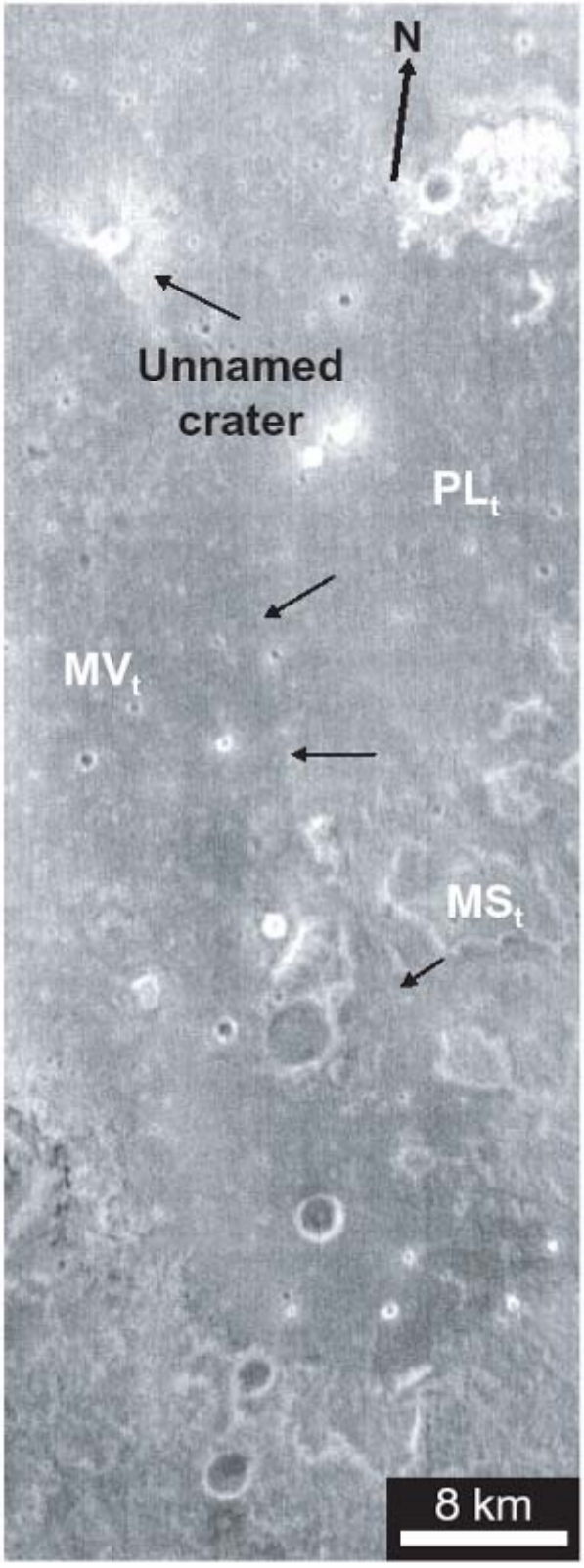
N
Unnamed crater
PLt
MVt
MSt
8 km

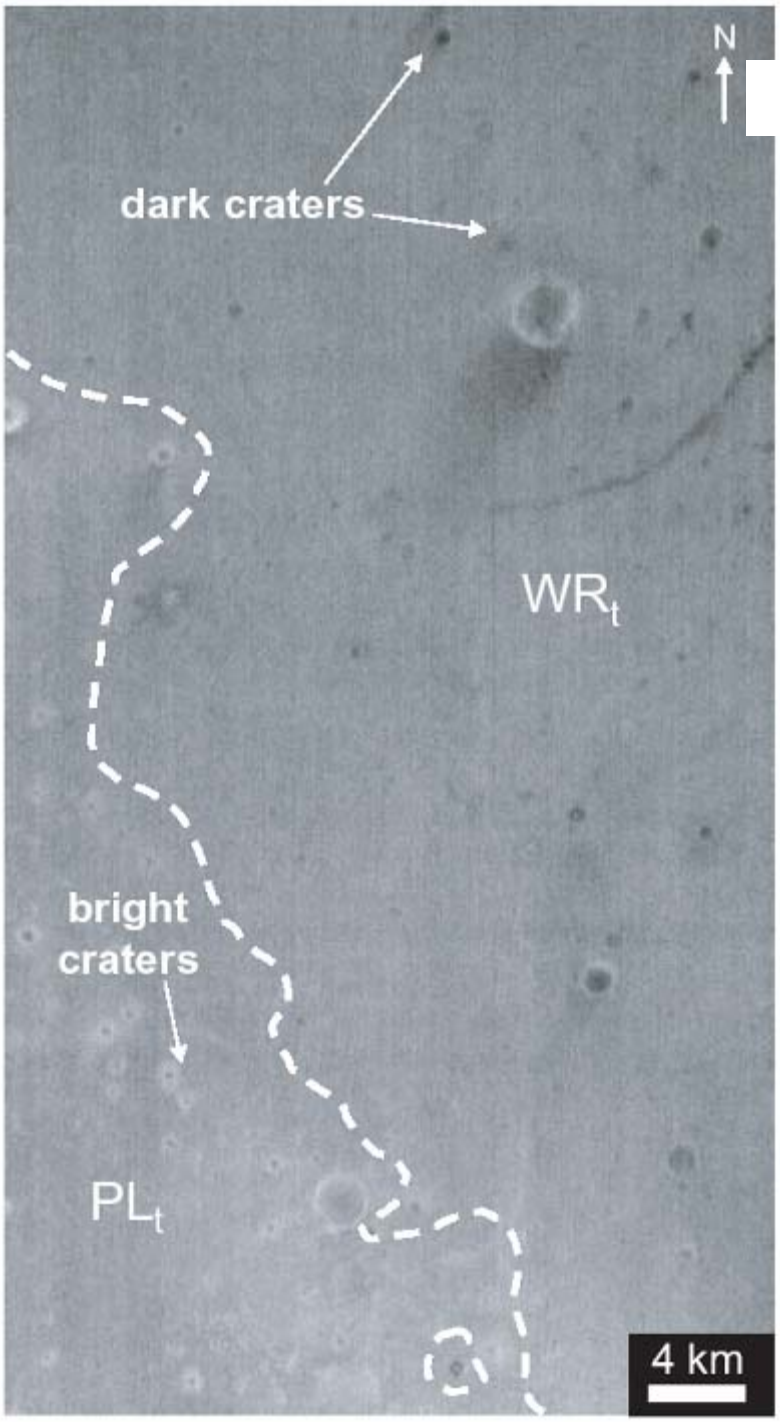

Figure 6. THEMIS night IR image (I01511006) showing dark craters distinctive of WR_t and bright-rimmed craters of PL_t.

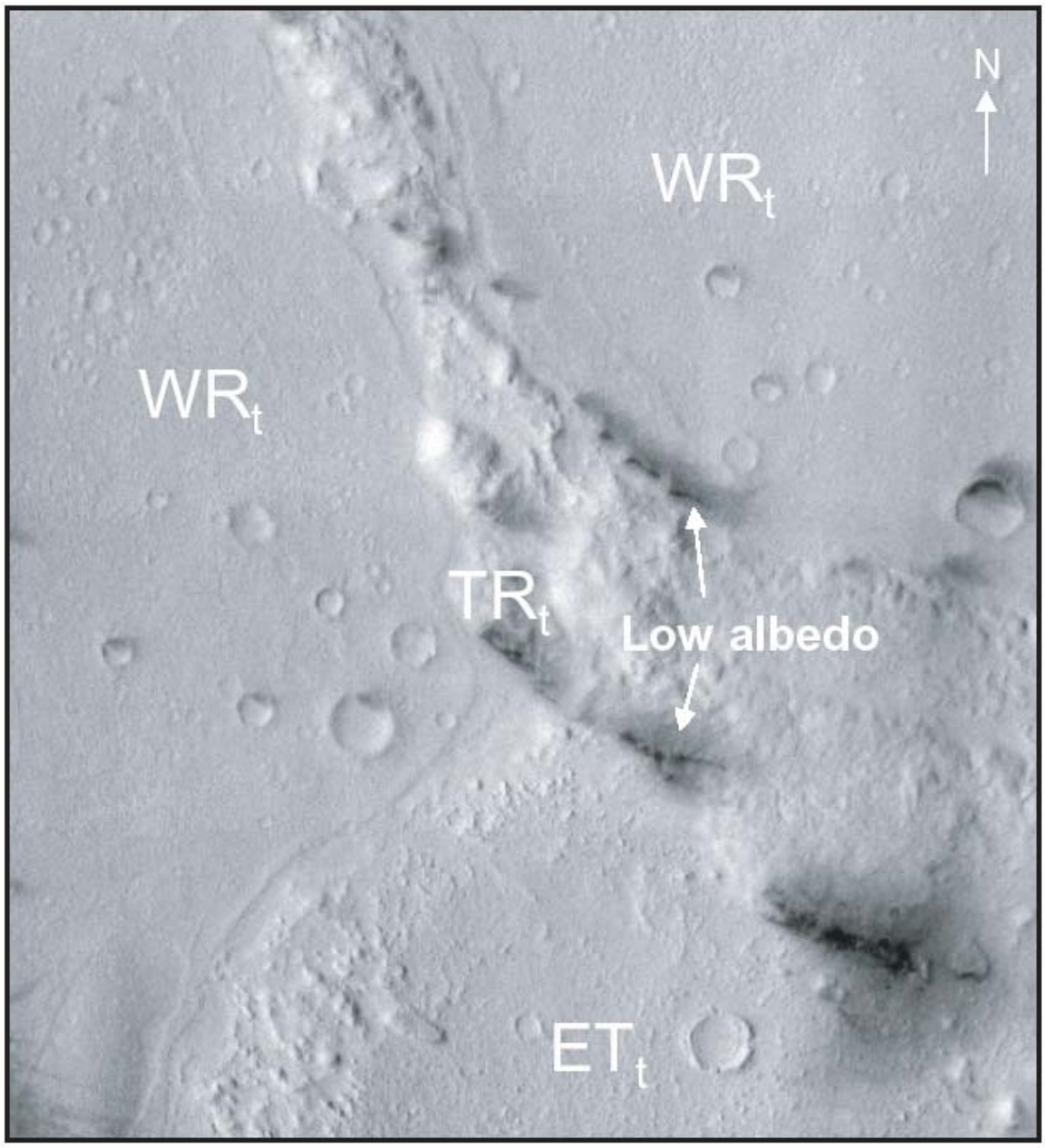

Figure 7. THEMIS visible image (V01580003) showing TR_t, associated low-albedo areas, and the contact between TR_t, WR_t, and ET_t units.

Figure 8. Characteristic textures of Gusev morphologic units and low-albedo materials. Units are as follows: (a) MV_m-Ma'adim Vallis (THEMIS-V02304003), (b) PL_m-Plains (THEMIS-V01243002), (c) MS_m-Mesa (MOC-E0300012), (d) LB_m-Lobed (THEMIS-V01580003) (e) ET_m-Etched Terrain (MOC-E0501350), (f) WR_m-Wrinkled (THEMIS-V02060002), and (g) TR_m-Thira Rim (MOC-E0201453). Also shown (f) is low-albedo material (THEMIS-V00881003).

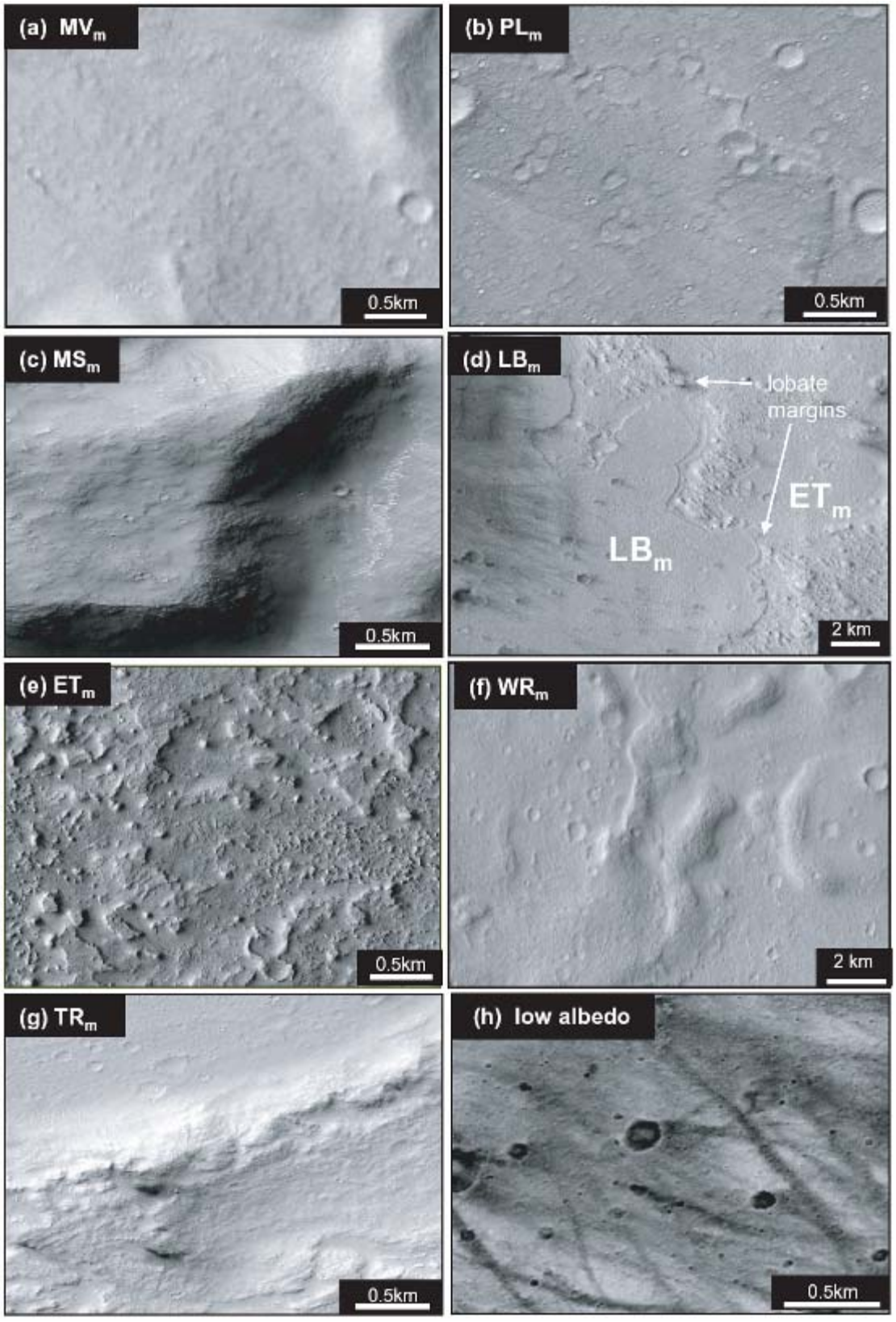
(a) MVm
0.5km
(b) PLm
0.5km
(c) MSm
0.5km
(d) LBm
Jobate margins
ETm
LBm
2 km
(e) ETm
0.5km
(f) WRm
2 km
(g) TRm
0.5km
(h) low albedo
0.5km

Figure 9. Selected features of morphologic units within Gusev: (a) MV_m unit boundary (arrows) (THEMIS-V02691003), (b) linear tracks superimposed on PL_m (MOC -E1103034-03), and (c) eastern boundary of PL_m (THEMIS-V03415003).

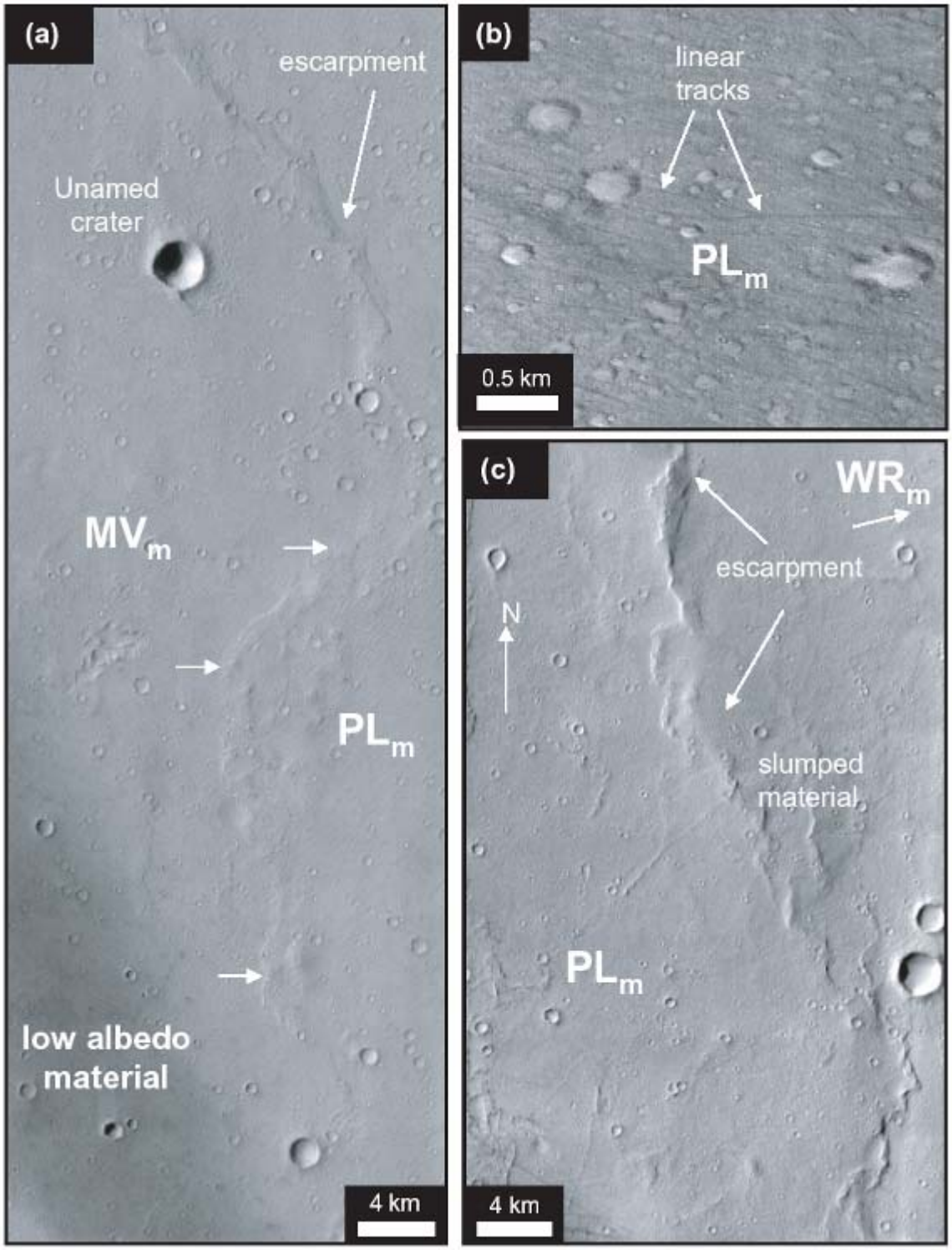
(a)
escarpment
Unamed
crater
MV$_m$
PL$_m$
low albedo
material
4 km
(b)
linear
tracks
PL$_m$
0.5 km
(c)
WR$_m$
escarpment
N
slumped
material
PL$_m$
4 km

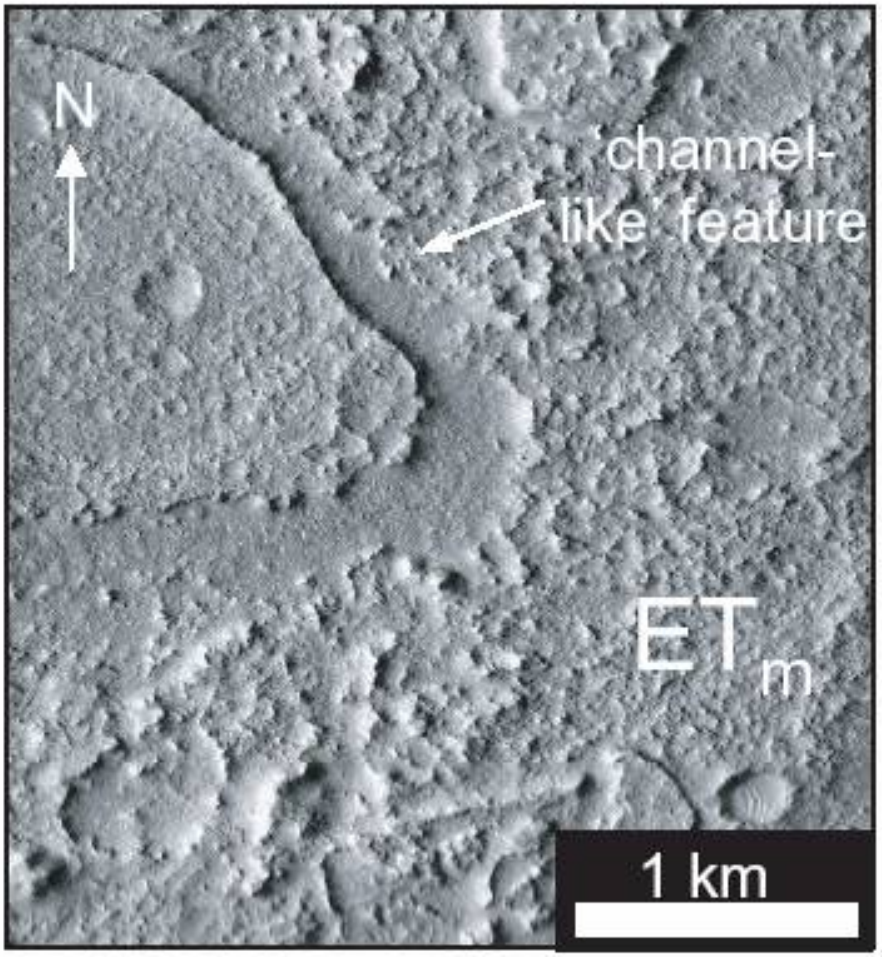

Figure 10. 'Channelized' areas in northern ET_m (MOC-E051350).

Figure 11. Viking Orbiter, MGS-MOC, and Mars Odyssey-THEMIS visible image mosaics of Gusev showing the redistribution of low-albedo materials during the past 25 years.

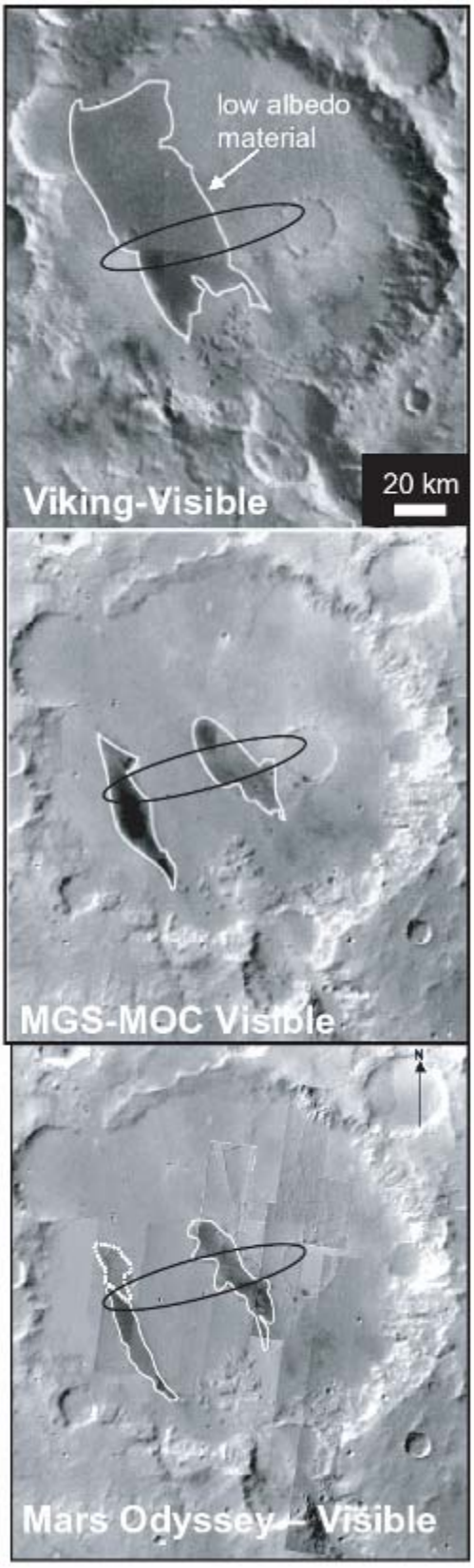
low albedo
material
20 km
Viking-Visible
MGS-MOC Visible
N
Mars Odyssey – Visible

Figure 12. MOLA profiles of select features in Gusev crater: (a) North-south topographic profile across the WR_m-ET_m unit boundary in northeastern Gusev with THEMIS visible image (VO2666002) showing the gradual change from ET_m (in the south) to WR_m (in the north), (b) East-west topographic profile across the WR_m-ET_m boundary in southeastern Gusev; profile shown on MOC visible image (E03-01511) showing the unit boundaries between WR_m and ET_m (c) Topographic profile across the contact between PL_m and WR_m (THEMIS-V03415003) (d) Topographic profile across unnamed crater (THEMIS-V02691003).

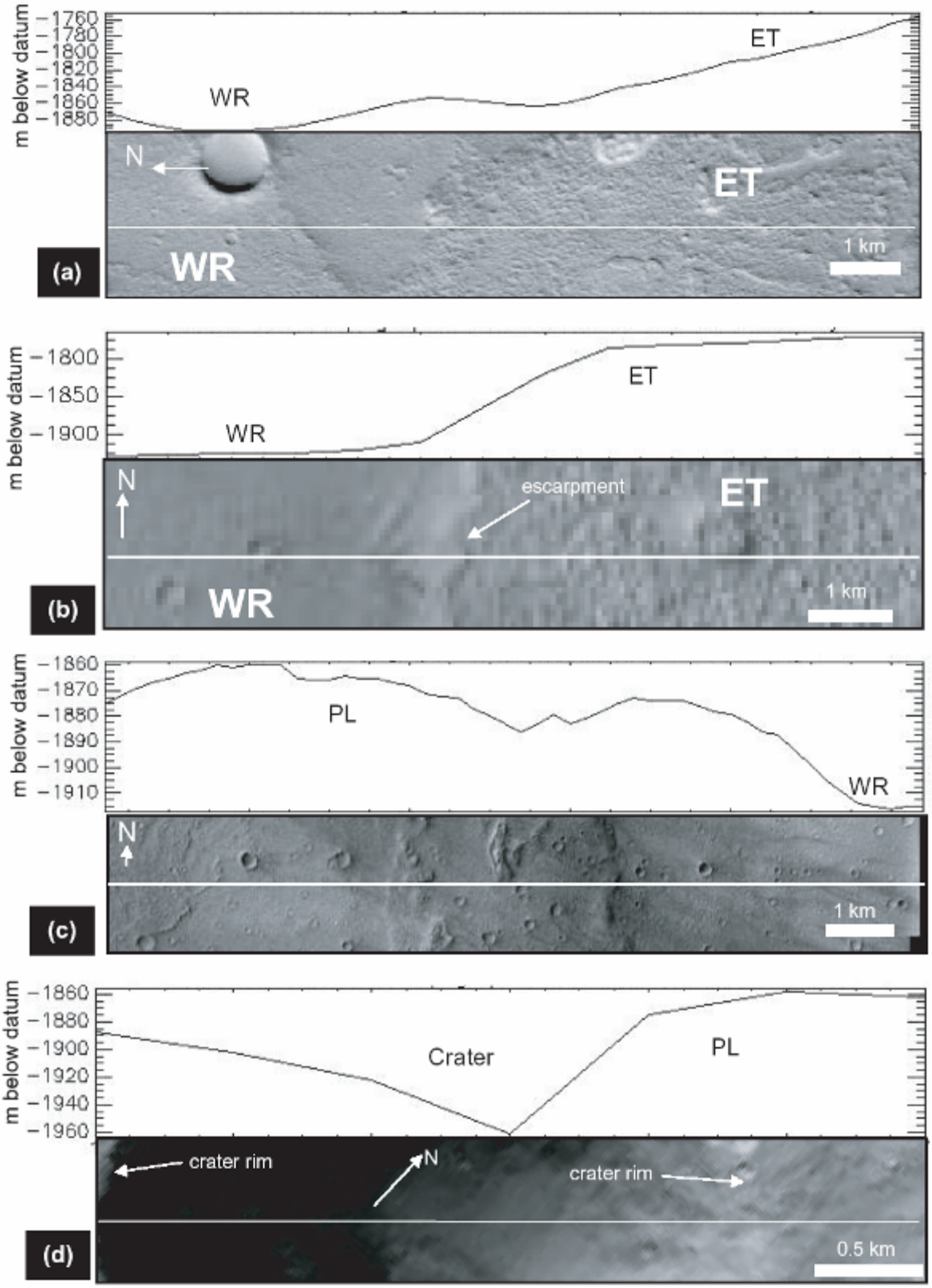
m below datum
−1760
−1780
−1800
−1820
−1840
−1860
−1880
WR
ET
N
ET
WR
1 km
(a)
m below datum
−1800
−1850
−1900
WR
ET
N
escarpment
ET
WR
1 km
(b)
m below datum
−1860
−1870
−1880
−1890
−1900
−1910
PL
WR
N
1 km
(c)
m below datum
−1860
−1880
−1900
−1920
−1940
−1960
Crater
PL
crater rim
N
crater rim
0.5 km
(d)

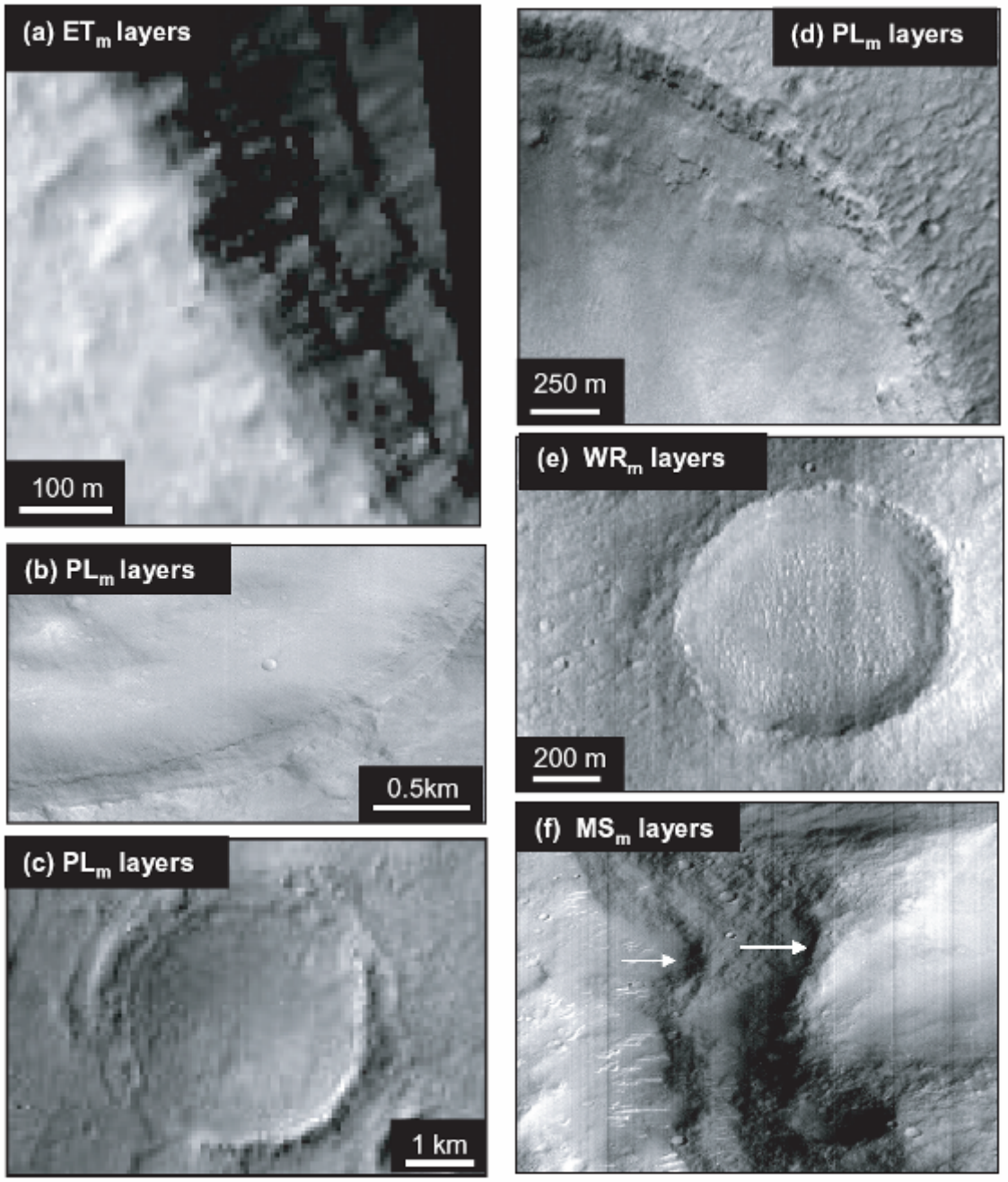

Figure 13. Evidence of layering within Gusev crater in (a) ET_m (MOC-M0202129), (b-d) PL_m (MOC-E1002768, E0503287, E1700827), (e) WR_m (THEMIS-V02666002), and (f) MS_m units (MOC-M0306211).

Figure 14. (a) Surface unit map of Gusev crater based on thermophysical, morphologic, topographic, and crater density data and (b) geologic map of Gusev crater from *Kuzmin et al.* [2001].

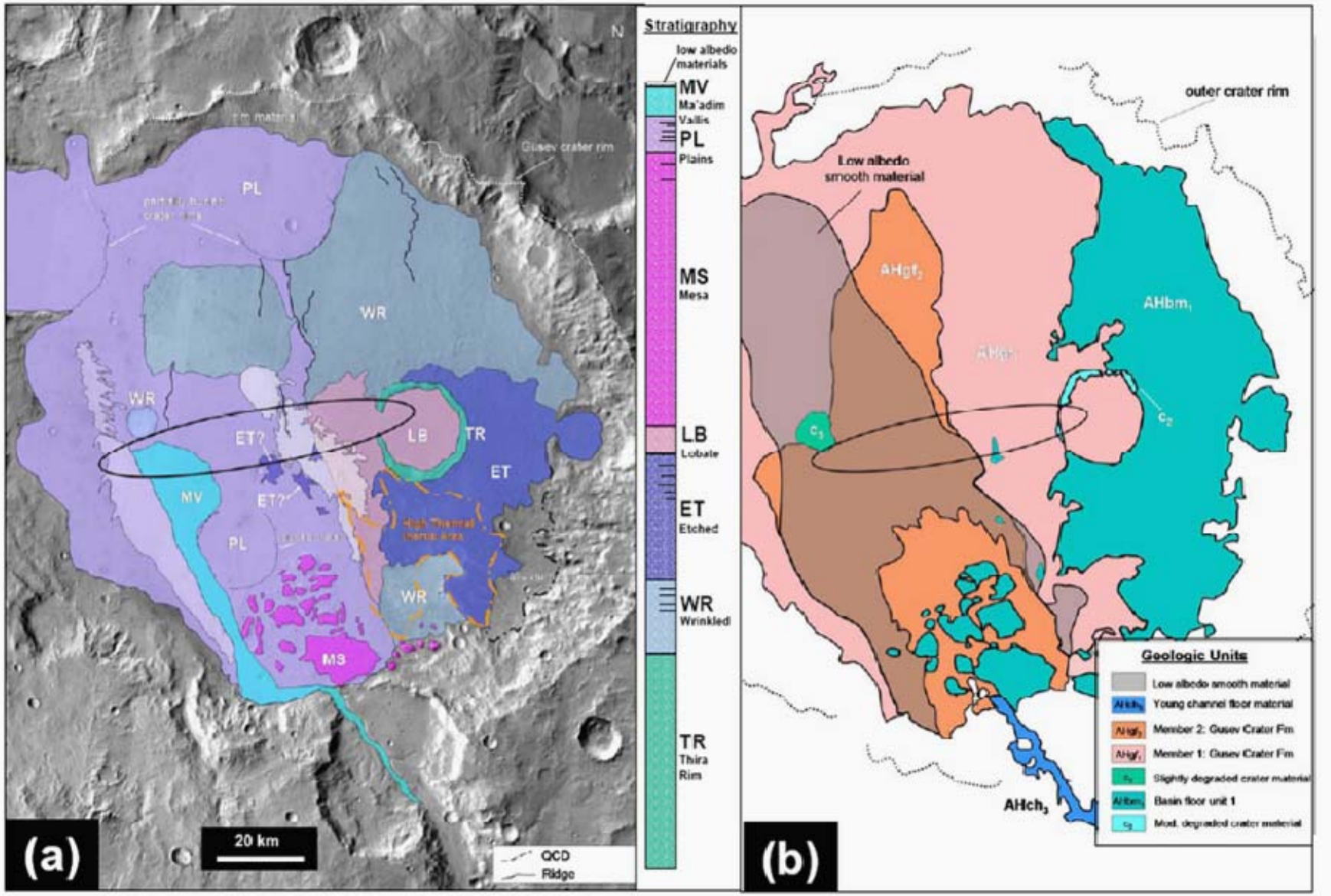
(a)
20 km
QCD
Ridge
Gusev crater rim
PL
WR
ET?
LB
TR
ET
MV
MS
Stratigraphy
low albedo materials
MV
Ma'adim Vallis
PL
Plains
MS
Mesa
LB
Lobate
ET
Etched
WR
Wrinkled
TR
Thira Rim
(b)
outer crater rim
Low albedo smooth material
Geologic Units
Low albedo smooth material
Young channel floor material
Member 2: Gusev Crater Fm
Member 1: Gusev Crater Fm
Slightly degraded crater material
Basin floor unit 1
Mod. degraded crater material

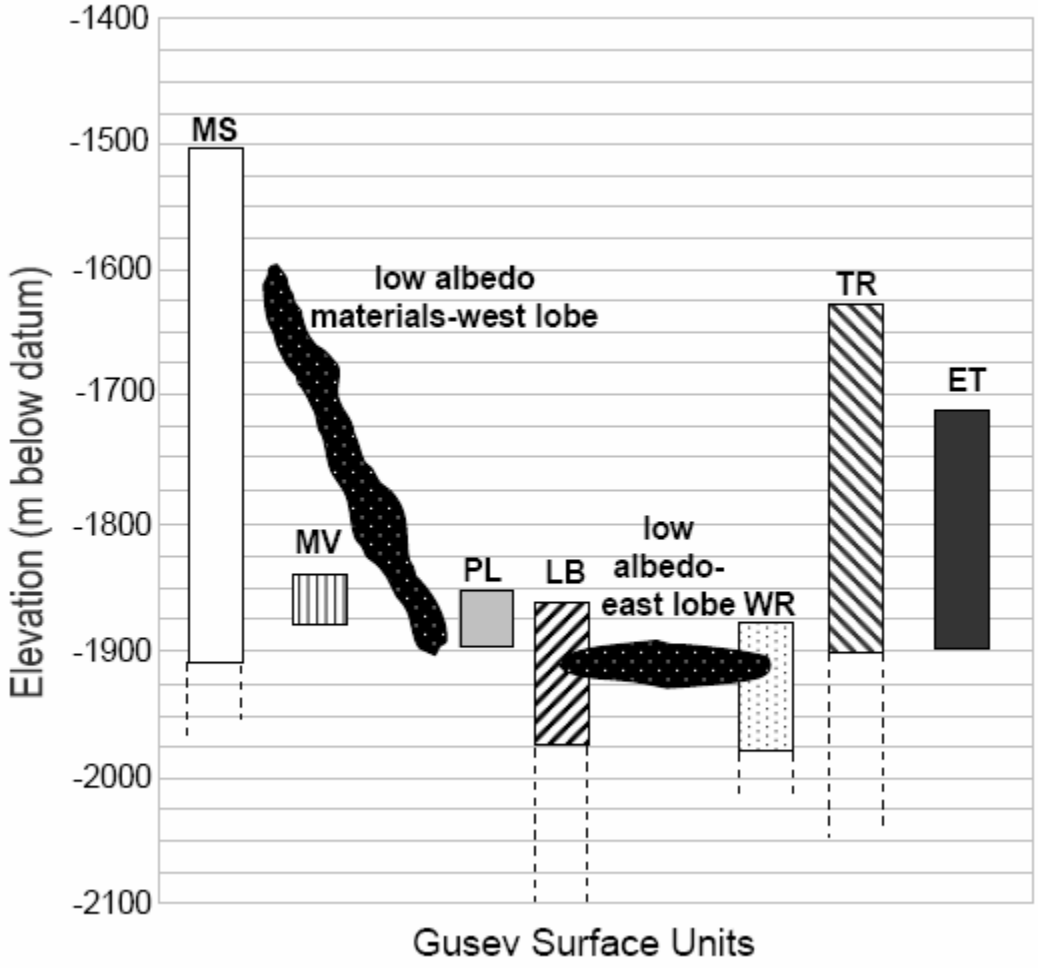

Figure 15. MOLA elevations of surface units within Gusev. Low-albedo materials are shown to illustrate their elevations and which units they overlie. The western low-albedo lobe overlies MV and PL, while the eastern lobe overlies LB and WR.

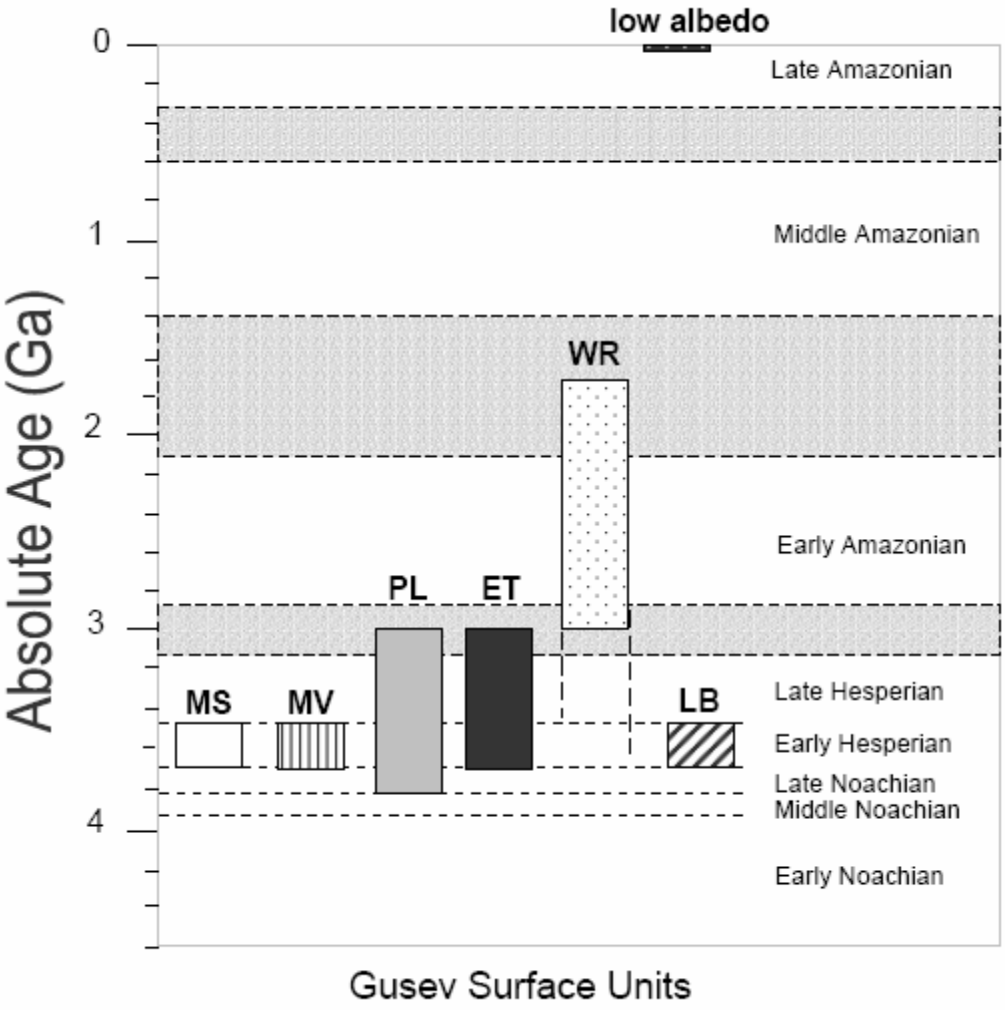

Figure 16. Age estimates for units based on crater density calculations. Bars represent the range in age estimates for 1, 2, and 5 km-diameter craters. Age boundaries for epochs are from *Tanaka et al.* [1986].

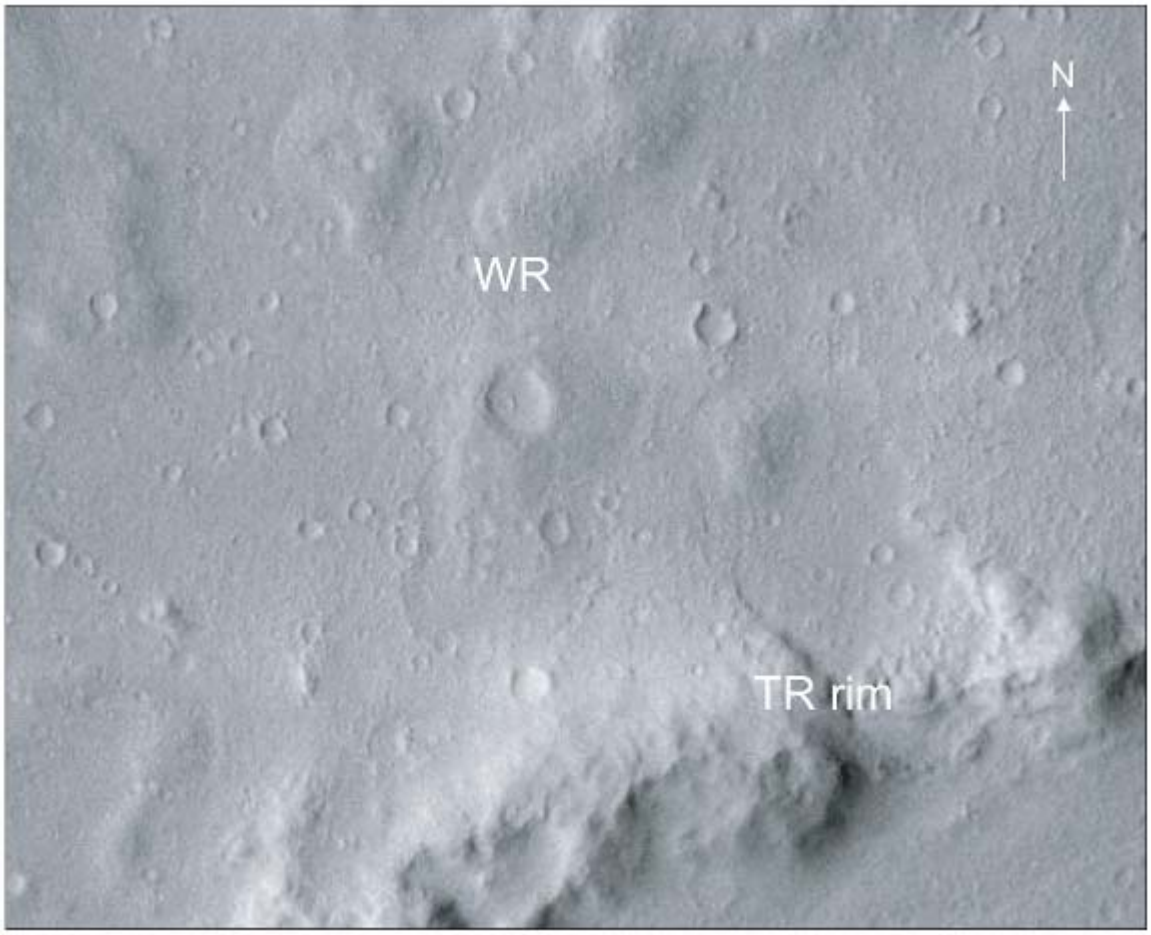

Figure 17. THEMIS day TIR view of WR deposited against TR northwest of the crater rim (V01580003).

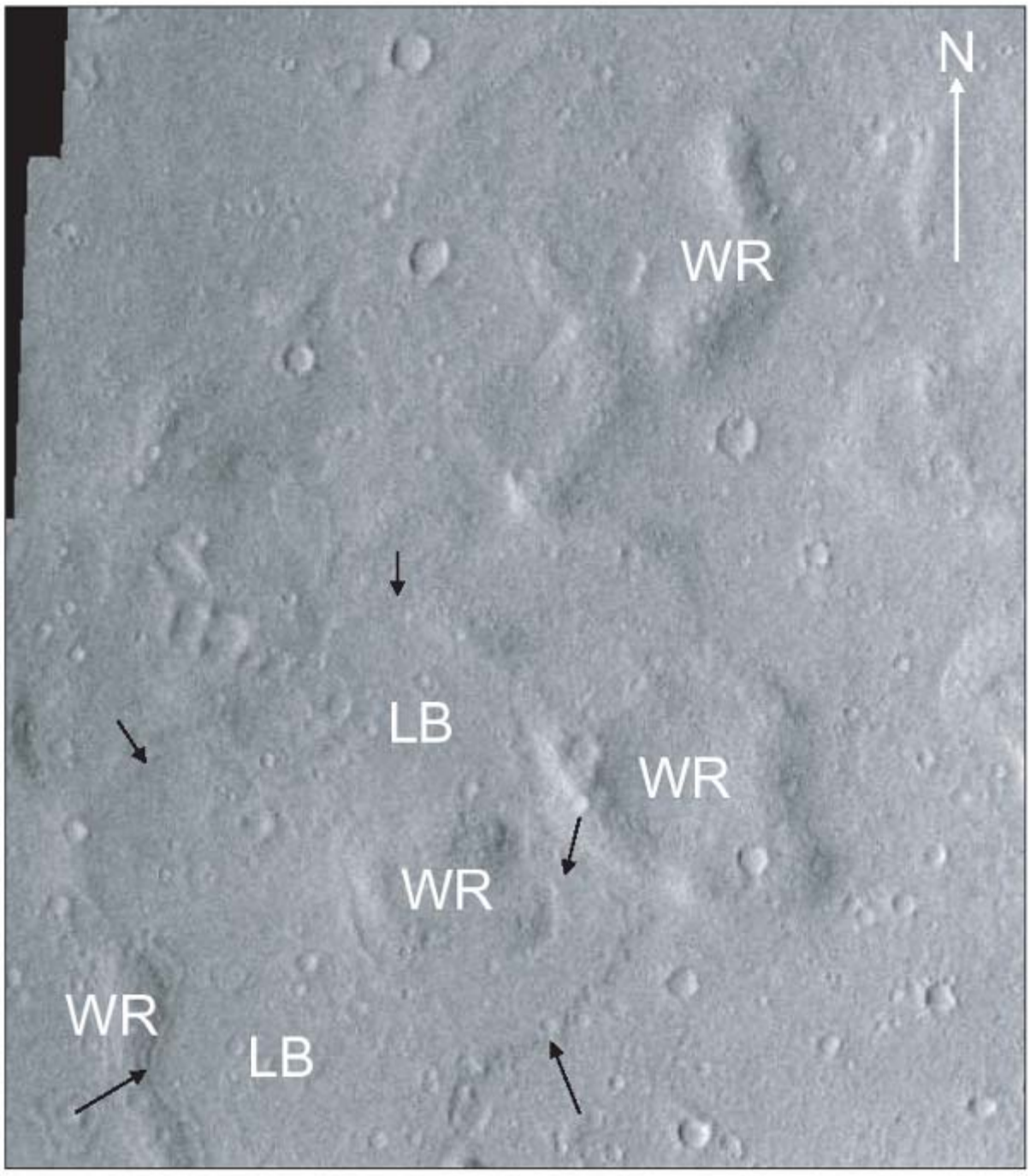

Figure 18. LB deposited against and between ridges of WR in north central Gusev (THEMIS-V-01580003).

Figure 19. Comparisons of the *Landheim et al.* (1994), *Cabrol et al.* [1998], and *Kuzmin et al.* [2000] stratigraphic models to that proposed in this study.

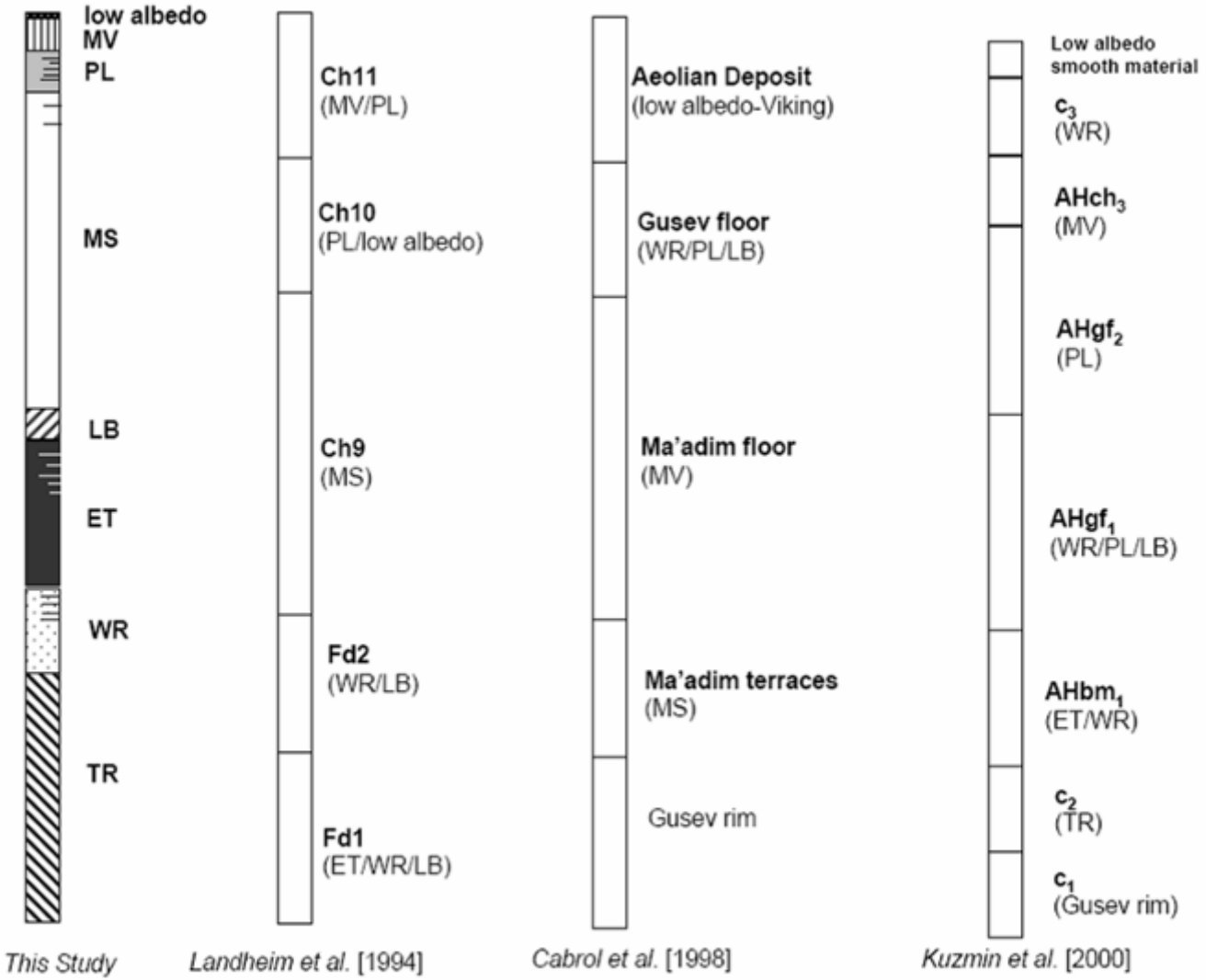
low albedo
MV
PL
MS
LB
ET
WR
TR
Ch11
(MV/PL)
Ch10
(PL/low albedo)
Ch9
(MS)
Fd2
(WR/LB)
Fd1
(ET/WR/LB)
Aeolian Deposit
(low albedo-Viking)
Gusev floor
(WR/PL/LB)
Ma'adim floor
(MV)
Ma'adim terraces
(MS)
Gusev rim
Low albedo
smooth material
c3
(WR)
AHch3
(MV)
AHgf2
(PL)
AHgf1
(WR/PL/LB)
AHbm1
(ET/WR)
c2
(TR)
c1
(Gusev rim)
This Study
Landheim et al. [1994]
Cabrol et al. [1998]
Kuzmin et al. [2000]

Part 3.

Plagioclase Compositions Modeled from Thermal Emission Spectra of Compositionally Complex Mixtures: Implications for Martian Feldspar Mineralogy

This paper is a reformatted version of a paper by the same name submitted to the Journal of Geophysical Research – Planets in December, 2006 by Milam et al. and is currently in final review

Milam, K. A., H. Y. McSween, Jr., J. E. Moersch, and P. R. Christensen (2007-in review), Plagioclase compositions from thermal emission spectra of compositionally complex mixtures: Implications for Martian Feldspar Mineralogy.

Abstract

The compositions of plagioclase, the most abundant mineral in the Martian crust, reflect changing conditions during magmatic evolution. Plagioclase contains spectral features at thermal infrared wavelengths that permit its detection by thermal emission spectrometers (TES, THEMIS, and Mini-TES) on Mars spacecraft. Previous studies have determined the accuracy with which average plagioclase compositions can be modeled in simple two-component sand mixtures and terrestrial volcanic rocks. Studies of terrestrial rock analogs suffer from difficulties in accurately determining the average plagioclase composition for comparison with the spectrally-modeled composition. Sand mixtures, however, provide a means of controlling plagioclase compositions for direct comparison to those modeled by linear deconvolution. This has allowed us to address how compositional complexity may affect our ability to derive average plagioclase compositions from thermal emission data. In this study, we examine the accuracy with which average plagioclase compositions can be modeled from emission spectra of complex mixtures of 3, 4, and 5 compositions of coarse (500-850 μm) plagioclase sand. Additionally, we examine multi-phase mixtures of plagioclase with pyroxene, olivine, magnetite, and ilmenite that are analogous to selected Martian surface materials. Increasing the number of plagioclase compositions or introducing additional mineral phases does not

affect the accuracy previously reported for modeling average plagioclase compositions. Plagioclase can be modeled to within $\pm$6 An of measured compositions at laboratory, TES, THEMIS, and Mini-TES resolution (within 1σ standard deviation), similar to previous work.

1. Introduction

The spatial distributions, abundances, and compositional ranges of mineral phases on Mars have important petrogenetic implications for the Martian mantle and crust. Previous studies of thermal emission spectra from the Mars Global Surveyor-Thermal Emission Spectrometer (MGS-TES) have shown the most abundant rock types in the Martian crust are basalt [*Christensen et al.,* 2000; *Bandfield et al.,* 2000] and andesite [*Bandfield et al.,* 2000] and/or partly weathered basalt [*Wyatt and McSween*, 2002; Michalski et al., 2005], referred to as surface types 1 and 2 respectively. Plagioclase feldspar is commonly modeled as the most abundant phase [*Bandfield et al.,* 2000; *Hamilton et al.,* 2001; *Wyatt and McSween*, 2002].

Plagioclase comprises a solid solution series ranging from anorthite $CaAl_2Si_2O_8$ to albite $NaAlSi_3O_8$, with compositions commonly expressed in terms of anorthite content ((An) = (Ca/Ca+Na) x100). In terrestrial basalts and andesites, unaltered plagioclase compositions typically range from $\sim An_{40\text{-}75}$ and reflect changing conditions during fractional crystallization. In low temperature settings (< approximately 200°C), plagioclase alters to a variety of clay minerals (e.g. montmorillonite, scapolite, prehnite, and various zeolites) [*Deer et al.*, 1996], whereas at higher temperatures, plagioclase is hydrothermally altered to more sodic compositions ($<An_{30}$) [*Hardie*, 1983; *Alt and Emmerman*, 1985; *Stakes and Schiffman*, 1999]. Our ability to determine plagioclase compositions accurately from remote sensing data can affect our identification and interpretation of crustal evolution and alteration on Mars.

At thermal infrared (TIR) wavelengths, most minerals have characteristic spectral

absorptions from which mineral abundance and compositional information can be extracted. In the TIR wavelength region, a rock spectrum is an approximately linear combination of its constituent mineral spectra [*Lyon*, 1965]. Several studies have addressed modeling of mineral abundances (including feldspars) using TIR spectra [*Thomson and Salisbury,* 1993; *Hamilton et al.,* 1997; *Feely and Christensen*, 1999; *Hamilton and Christensen*, 2000; *Wyatt et al.,* 2001]. Fewer have addressed modeling of mineral compositions (including plagioclase). Plagioclase has distinct spectral signatures in the mid-IR (4-15 μm; 2500-667 cm^{-1}), making it discernible from other phases [*e. g. Lyon et al.,* 1959; *Nash and Salisbury,* 1991]. Shapes and positions of band features vary with changing plagioclase compositions (Figure 20), making it possible to model compositional information from infrared spectra [*Ruff,* 1998]. For more information about the spectral signature of plagioclase, see *Illishi et al.* [1971], *Ruff* [1998], and *Milam et al.* [2004].

The average plagioclase composition modeled from linear deconvolution of a rock thermal emission spectrum is thought to represent the numerical average of plagioclase compositions in that sample, weighted by their areal abundances on the observed surface of the rock. To assess the accuracy of the modeled average plagioclase composition, previous studies [*Hamilton and Christensen*, 2000; *Wyatt et al.,* 2001] compared modeled compositions to normative plagioclase and averages calculated from multiple microprobe analyses (hereafter referred to as weighted averages). The complexity of natural samples, however, limits our ability to accurately measure or calculate true average plagioclase compositions. Mesostasis grains in volcanic rocks often approach the smallest beam size (1-2 μm) of an electron microprobe, making measurement challenging. Even if every grain in a

rock could be accurately measured, weighting analyses according to their relative areal proportions in order to calculate an average plagioclase composition would be difficult. For a *single* plagioclase grain, measured vs. weighted average plagioclase compositions can vary by as much as 4 An [*Milam et al.*, 2004]. Compounded for an entire sample, weighted average estimates could differ significantly from the true average composition. Comparison of spectrally-modeled and normative plagioclase compositions is also problematic. Normative mineralogy applies only to slowly-cooled igneous rocks that have crystallized under equilibrium conditions and is thus not applicable to many volcanic rocks. CIPW-NORM calculations also do not take into account intermediate solid solution series compositions, but only calculate anorthite and albite endmembers. A comparison of normative and weighted average plagioclase further calls into question which is the appropriate standard for comparison with spectrally-modeled compositions. Normative and weighted average plagioclase compositions may vary by as much as 20 An [*Milam et al.* 2004]. Thus, it is unclear whether either the weighted average or normative plagioclase represents the true average for a given sample that should be used to compare with spectrally-modeled compositions.

Physical mixtures of particulates allow for precise control of the average plagioclase compositions in complex samples. Knowledge of the exact compositions and proportions of mixture constituents allows for a more accurate determination of the true average composition for comparison to spectrally-modeled compositions. In a first attempt, *Milam et al.* [2004] produced several two-component physical mixtures of plagioclases (the term *component* is used to denote a pure plagioclase composition (< 5 An variation), collected

their emission spectra, resampled spectra to various instrumental resolutions of Mars spacecraft, and derived average plagioclase compositions. Results from this study, reported as *An variation* (ΔAn), the variation between measured and modeled compositions from deconvolution results, showed that plagioclase compositions could be modeled to within 12 An of the average plagioclase composition and to within 4-6 An (1σ standard deviation) in all deconvolutions at the various instrument resolutions. When presenting modeled An, we are referring to positive and negative values. In other words, 12 An indicates that plagioclase compositions can be modeled to within +/- 12 An of average plagioclase compositions. Results are comparable and perhaps improved, depending on the endmember set used, over those reported for volcanic rocks [*Wyatt et al.,* 2001; *Hamilton et al.,* 2001; *Milam et al.,* 2004].

Two-component mixtures, however, are not representative of the complexity of natural samples. Plagioclase phenocrysts are commonly zoned and mesostasis in terrestrial volcanic rocks contains plagioclase with multiple compositions [*Wyatt et al.,* 2001; *Milam et al.,* 2004]; moreover, these plagioclases coexist with other minerals that may have competing spectra. Building on the previous experiment, we have produced increasingly complex mixtures of plagioclase compositions, some of which include additional phases and have began to approach the *compositional and mineralogical* complexity of mafic-intermediate volcanic rocks.

2. Methods

For this study, we produced two types of physical mixtures. The first type included mixtures of multiple (three, four, and five) plagioclase feldspars of known composition. We use this set to assess the potential effects of multiple plagioclase compositions (such as in rocks with zoned or solid solution plagioclase) on our ability to model the average plagioclase composition from thermal emission spectra. For our other type, we produced three mixtures in which additional phases (pyroxene, olivine, magnetite, and ilmenite) were added to multi-component plagioclase mixtures. For this set, we assess if the addition of other common phases limits our ability to model the average plagioclase composition.

2.1. Homogeneous Plagioclase Used in Both Mixture Types

Samples of homogeneous plagioclase feldspars were selected according to the methods outlined in *Milam et al*. [2004]. We examined specimens for purity by optical microscope and analyzed using a CAMECA SX-50 electron microprobe using a wavelength dispersive spectrometer (WDS) at the University of Tennessee. We analyzed plagioclase compositions along core-to-rim traverses of representative grains and in fused glass beads produced from each feldspar. Selected samples were devoid of optical or compositional zoning (An variation <5 An), lacked accessory mineral inclusions ($<$ 5 vol. %), and displayed minimal or no signs of alteration/weathering. Five samples that met these criteria are listed in Table 5.

We ground selected individual plagioclases into finer particles by mortar and pestle, sieved the particulates, and separated a coarse sand (500-850 μm) portion for use. Visible

impurities were extracted by hand. Samples were washed and dried according to methods outlined in *Milam et al.* [2004] to remove clinging fine-grained particulates. Coarse sand was chosen because sand appears to be the dominant particle size contributing to thermal infrared spectra from Martian dark regions [*Christensen et al.,* 2001] and this size range allows us to avoid particle size effects [*Lyon*, 1965; *Salisbury and Wald,* 1992; *Moersch and Christensen*, 1995; *Mustard and Hays,* 1997; *Hamilton*, 1999].

2.2. Multiple Component Plagioclase Mixtures

In an effort to simulate the range of multiple plagioclase compositions that occur in natural samples, such as in volcanic rocks or aeolian deposits, we prepared fifteen physical mixtures of the pure plagioclase sand. Individual components, whose compositions ranged from An_{2-73}, were mixed in proportions (with a measured accuracy of 0.1 mg) ranging from 1 to 80% of the total mixture (Table 3). Representative reflected light photomicrographs of these mixtures are shown in Figure 21. Average mixture compositions ranged from An_{35-51}, similar to reported average plagioclase compositions from Martian samples and surface types [*McSween and Treiman*, 1998; *Wänke et al.*, 2001; *McSween et al.,* 2004; *Milam et al.,* 2004]. We produced three sets of mixtures, with each set using three, four, and five components. We refer to these as *multi-component mixtures*, again with the term *component* referring to a particular solid solution composition (An value) of plagioclase. This is in contrast with a *multi-phase mixture*, which involves the addition of separate mineral phases, such as pyroxene and olivine (see below).

2.3. Multiple Component, Multiple Phase Mixtures

Natural volcanic rocks contain phases other than plagioclase. In an effort to determine the potentially confounding effects of non-plagioclase components on the ability to model plagioclase compositions from thermal emission spectra, we also produced three multi-component, multi-phase mixtures. A portion of each mixture consisted of coarse multi-component plagioclase sand with average compositions known from geochemical analyses (Table 4). Compositional variation in each component plagioclase varied by no more than 5 An, and each component was weighed with a measured accuracy of 0.1 mg. We calculated average plagioclase compositions according to the mass percentage contribution of each component in a mixture. While volume percentages are more analogous to the field of view of a spectrometer, density differences between solid solution plagioclase members are so minor (2.61-2.76 g cm^{-3}) that average anorthite contents calculated using volume are identical those calculated with mass.

We designed mixtures to be roughly comparable in composition and modal mineralogies to TES surface type 1 [*Bandfield et al.,* 2000], Shergotty [*Stolper and McSween*, 1979], and Mazatzal rock at Gusev Crater [*McSween et al.,* 2004]. Surface type 1, dominated by feldspar (primarily plagioclase), clinopyroxenes, and sheet silicates, represents the Noachian-age basaltic southern highlands of Mars [*Bandfield et al.,* 2000; *Christensen et al.,* 2000]. Shergotty represents the basaltic shergottites, a class of meteorites thought to have originated on Mars. Shergottites are dominated by clinopyroxenes, maskelynite, and ilmenite. Mazatzal is a picritic basalt that was analyzed by the Spirit Mars Exploration Rover (MER) on the floor of Gusev Crater [*McSween et al.*, 2004; 2006]. Our multi-phase mixtures

reflect the major mineralogies measured or modeled for each of these Martian surface materials. Few accessory minerals (as modeled or measured in TES surface type 1, Shergotty, and Mazatzal) occur above the detectibility limit for most minerals at TIR wavelengths [*Ramsey and Christensen*, 1998]; therefore, we have only some of the less abundant phases in our mixtures. Although glass is quite common in the matrix of terrestrial volcanic rocks, it was not used in our mixtures. Glass grain sizes and compositional variability make it difficult to isolate and extract from natural samples and significant quantities of synthetic glass reflecting volcanic compositions is presently not available.

Mixture MP-1 (surface type 1 analog – Table 4) consists of 67% plagioclase and 33% augite (Tables 4 and 5). *Bandfield et al.* [2000] modeled surface type 1 as 50% feldspar (dominated by plagioclase), 25% clinopyroxene, and 15% sheet silicates. When sheet silicates are not considered, normalized abundances for feldspar and clinopyroxene are 67% and 33% respectively. In our mixtures, the plagioclase portion consists of a two-component plagioclase mixture of 25% albite (An_2) and 75% bytownite (An_{73}) used in [*Milam et al.,* 2004] that simulate the average plagioclase composition (An_{55}) similar to that modeled for surface type 1 [*Bandfield et al.,* 2000]. MP-2 (Shergotty analog) consists of four phases: augite, plagioclase, magnetite, and ilmenite (Tables 4 and 5). Modal mineralogies for these phases can be found in [*Stolper and McSween,* 1979]. We chose to use augite as the primary pyroxene phase in our mixture because its presence in Shergotty. Pigeonite is also present in Shergotty; however, significant quantities of pure pigeonite were not available for use in our physical mixtures. Pigeonite and augite can be distinguished by their spectral characteristics. Thus, the MP-2 mixture spectrum does differ somewhat from that of Shergotty. The

plagioclase portion includes a three-component mixture of 5% albite (An_2) and two labradorites (An_{51} and An_{53}; 15% and 80% respectively) that produce an average composition (An_{51}), within the reported range of maskelynite (shock melted plagioclase) values for Shergotty [*Stolper and McSween,* 1979, *Easton and Elliott,* 1977]. (For a discussion of the potential of shock effects on plagioclase thermal emission spectra see *Johnson et al.* [2002; 2003]). The third mixture, MP-3 (Mazatzal analog), contains plagioclase, diopside, olivine, magnetite, and ilmenite (Tables 4 and 5) similar to the norm for Mazatzal [*McSween et al.,* 2004, 2006]. MP-3 includes a four-component mixture of 30% albite (An_2) and 3 labradorites (An_{51}, An_{53}, and An_{63}; 30%, 20%, and 20% respectively) that produces an average plagioclase of An_{40}. It should be noted here that component plagioclases used in all mixtures were not chosen to reflect measured solid solution compositions, but were used to closely simulate the average plagioclase composition for a given analog.

2.4. Spectral Analysis and Processing

We collected TIR spectra of both multi-component and multi-phase mixtures using a Nicolet Nexus 670 spectrometer at Arizona State University. Each mixture spectrum is the average of 270 scans collected over 2000-200 cm^{-1} (2.5 – 50 μm) with 4 cm^{-1} spectral sampling. We then converted sample radiance to emissivity and calibrated each spectrum using techniques described by *Ruff* et al. [1997] and *Ramsey and Christensen* [1998]. As in *Milam et al.* [2004], we resampled laboratory spectra to TES/Mini-TES (10 cm^{-1} spectral sampling) and THEMIS (10 bands from 1480 – 796 cm^{-1}) resolution to simulate the effects of

lower spectral resolution collected by these instruments. The region between 825 – 507 cm^{-1} was excluded from use at TES and THEMIS spectral resolution due to a prominent atmospheric CO_2 absorption feature that occurs here in orbital data. Although TES and Mini-TES share the same spectral sampling, the atmospheric path length through which these instruments view varies significantly (from 400 km to > 1m respectively). Thus, the contribution from the 667 cm^{-1} CO_2 absorption in Mini-TES data is much less and so the number excluded bands at Mini-TES spectral resolution was limited to between 751 – 582 cm^{-1}. At THEMIS spectral resolution, band 10 is in a region of prominent atmospheric absorption and wavenumbers for bands 1 and 2 are identical and outside the wavenumber range for deconvolutions. So the effective number of bands in this work is seven, which restricts our deconvolutions to six or less spectral endmembers [*Ramsey and Christensen*, 1998].

We modeled mixture spectra using a linear deconvolution algorithm [*Ramsey and Christensen*, 1998] over 1300 – 400 cm^{-1} (1478-850 cm^{-1} for spectra at THEMIS resolution). This range includes most silicate absorption features and excludes wavenumbers <400 cm^{-1} in order to make direct comparisons to previous studies using similar ranges [*Hamilton and Christensen*, 2000; *Wyatt et al.,* 2001; *Milam et al.,* 2004]. Algorithm inputs include a measured spectrum, a spectral library, and a specified range over which a spectrum is to be deconvolved. For deconvolutions of multi-component mixtures, we used all available plagioclase spectral endmembers (Table 6) and excluded spectra of those endmembers actually used in the physical mixtures themselves. This method accounts for the low probability that a spectral library would contain endmembers with an exact match to those

present in a natural sample. Such spectral libraries represent expanded endmember sets that are equal to, if not superior than, constrained sets of endmembers, in their utility for deriving the average plagioclase composition for a complex mixture [*Milam et al.,* 2004; *Milam et al.,* 2006]. For spectral libraries used to model multi-phase mixtures, we included all available plagioclase except those actually used in the physical mixtures, as well as several common mafic-intermediate mineral phases (Table 6).

Because the linear deconvolution algorithm used here requires a spectral library with the number of endmembers being one less than the total number of bands in a spectrum [*Ramsey and Christensen,* 1998], we deconvolved THEMIS-resolution spectra using spectral libraries containing six endmembers. For multi-component mixture spectra at THEMIS resolution, we chose six plagioclase feldspar spectral endmembers based on those most reported in deconvolution results at TES resolution. For multi-phase mixture spectra at THEMIS resolution, we selected six total spectral endmembers of plagioclase and other mafic minerals (Table 6) based on their relative dominance in TES results. This resulted in libraries with 2-3 plagioclase spectral endmembers and 3-4 remaining phases. It should be noted, however, that practical application with laboratory and remote sensing data shows that spectral libraries containing more than 2/3 the number of bands in a deconvolution can result in instability and marginal degradation of model results.

We report deconvolution results as a modeled spectrum, normalized percentages of each endmember used, and a root-mean-square (RMS) error. The "goodness of fit" for an individual deconvolution was determined by qualitative comparison of measured vs. modeled spectra and by assessment of RMS values, a method utilized by previous studies [e.g.

Hamilton et and Christensen, 2000; *Wyatt et al.*, 2001]. We used plagioclase abundances modeled from each deconvolution to calculate average plagioclase compositions (average An) for each mixture to compare with average plagioclase compositions calculated from physical mixtures. We multiplied the percentage of each modeled plagioclase spectral endmember by its measured An and then summed each weighted value to produce an average modeled plagioclase composition.

3. Results

3.1. Multi-Component Mixtures

Representative examples of measured vs. modeled multi-component spectra at laboratory, TES, THEMIS, and Mini-TES resolution are shown in Figure 22. Variations between measured and modeled plagioclase compositions in each deconvolution are reported as ΔAn. *Average ΔAn* refers to the average ΔAn value calculated for all deconvolutions and, in this case, is depicted per the number of components or spectral resolution. *Maximum ΔAn* represents the absolute value of the maximum ΔAn observed from a set of deconvolutions. It thus represents the maximum variation that occurs in a given deconvolution and that variation may be positive or negative in actual value. In all deconvolutions at multiple spectral resolutions, ΔAn < 11; however, most results from multi-component mixtures indicate that plagioclase can be modeled to within ΔAn = 6 (1 σ standard deviation) of measured average plagioclase composition in mixtures at laboratory, TES, THEMIS, and Mini-TES resolutions. Below we further detail these results with ΔAn as a function of variation of the number of components and spectral resolution.

3.1.1. ΔAn as a Function of the Number of Components

Results indicate that the number of plagioclase components used in physical mixtures correlates with a slight increase in the maximum ΔAn and ΔAn from most deconvolutions (1σ standard deviation). In all deconvolutions at all spectral resolutions, ΔAn varied by as much as 5, 6, and 11 An for three, four, and five-component mixtures respectively (Table 7). However, ΔAn for most deconvolutions to within 1 σ standard deviation was much better, with

modeled plagioclase compositions for three, four, and five-component mixtures within ΔAn = 3, 4, and 6 respectively, of measured compositions (Table 7). ΔAn values here represent deconvolutions at all spectral resolutions. Average RMS errors were low (<0.0023), but maximum RMS errors ranged as high as 0.0084. There was no apparent trend in RMS errors that was correlative to the number of components.

3.1.2. ΔAn as a Function of Different Spectral Resolutions

Overall, plagioclase compositions were modeled with maximum ΔAn of 5, 8, 11, and 7 An of measured average compositions at laboratory, TES, THEMIS, and Mini-TES resolutions respectively in all sets of deconvolutions (Table 8). To within 1σ standard deviation, results varied less, ranging from ΔAn = 4 to 5 An. Values reported here represent deconvolutions of all three-, four-, and five- component mixtures. Average RMS errors ranged from 0.0017 to 0.0024 (Table 8). Maximum RMS errors were comparable for laboratory, TES, and Mini-TES spectral resolutions (with maximum ranges of 0.0030 – 0.0046), but ranged < 0.0084 in deconvolutions at THEMIS spectral resolution.

3.2. Multi-Component, Multi-Phase Mixtures

Measured vs. modeled spectra from deconvolutions of multi-phase mixtures at varying spectral resolutions are shown in Figure 23. Modeled plagioclase endmember percentages were used to calculate average anorthite contents for each mixture. ΔAn is reported as with the multi-component mixtures (Figure 23), with respect to the changing number of phases and components (Table 9), and by spectral resolution (Table 10). Neither ΔAn nor RMS errors

correlated with an increase in the number of phases or components per mixture (MP-1 to MP-3). ΔAn for all deconvolutions was less than 12 An. Overall, deconvolutions of MP-1, MP-2, and MP-3 mixture spectra produced average ΔAn values of 4, 10, and 8, with maximum ΔAn values of 8, 12, and 10 respectively (Table 9). Plagioclase modeled to within 6 An (1 σ std. dev.) of measured compositions at laboratory spectral resolution, 5 An at TES and Mini-TES resolutions, and 3 An at THEMIS resolution (Table 7).

4. Discussion

Modeled ΔAn values from multi-component coarse sand mixture spectra are comparable to results reported for two-component spectra in *Milam et al.* [2004]. This study, however, suggests that there may be a correlation between ΔAn and increased numbers of plagioclase compositions (components) used in coarse-grained sand mixtures. Maximum ΔAn values increases from 5 to 11 An, while most increase from 3 to 6 An (to within 1 σ std. dev.) in mixtures with more components. The average, maximum and 1σ RMS error values do not show the same behavior, however.

If the increase in ΔAn is real, one would surmise that lessened precision relates to the number of components themselves or limitations placed on spectral libraries in deconvolving these mixtures. More components would hypothetically introduce more error in calculating the average anorthite content for a given mixture. As mentioned in *Milam et al.* [2004], each homogeneous plagioclase feldspar component was chosen based on compositional variation < 5 An. With increasing numbers of components placed in mixtures, more error in determining average An is introduced. For example, assuming that each of the measured

compositions of the plagioclase components is +5 An or -5An of the actual values in mixtures such as III-, IV-, or V-A, the average plagioclase composition calculated for the mixture (An_{51} in the case of all three mixtures) may be off by as much as +5 An or -5 An (i.e. An_{46} – An_{56}). This error can get slightly worse (0.5 to 1 An) with increasing numbers of components (3 to 5 components in this case).

Increases in ΔAn per the number of components could possibly relate to limitations placed on spectral libraries used in this study. As mentioned above, libraries did not include spectral endmembers with compositions identical to those actually used in a given mixture. Thus, with an increasing number of components in a mixture, the number of total spectral endmembers available for modeling is decreased. However, when analyzing thermal emission spectra from orbiting or landed instruments, the number of spectral endmembers is limited by the number of bands in the spectral range under study [*Ramsey and Christensen,* 1998]. In such studies, ΔAn between the actual and modeled average plagioclase compositions might be further reduced. This is promising, when considering that the Martian surface is likely dominated by mixtures of multi-component plagioclase in aeolian deposits and volcanic source rocks. In fact, the majority of TES, THEMIS, and Mini-TES data are likely affected by multiple compositions within a given pixel (with variation in spatial resolutions from km to cm-scale).

Spectral libraries with more endmembers representing an increased number of compositional varieties may be more useful in modeling solid solution minerals, such as plagioclase [*Milam et al.,* 2004]. When considered as a binary solid solution series mineral, plagioclase represents 100 possible compositions. If potassium content is considered,

several hundred additional compositions are possible. Thus, deconvolutions with more restricted spectral libraries could be expected to yield larger ΔAn values. Larger spectral libraries provide more endmembers to the deconvolution algorithm for matching smaller variations in absorption features. As noted previously, however, larger libraries whose number of endmembers > ~2/3 the number of bands, may result in instability and marginal degradation of deconvolution results. Thus, the ideal size of spectral library for modeling solid solution minerals would range from n-1 to <2/3n (where n represents the number of bands over which a spectrum is deconvolved).

If ΔAn between measured and modeled plagioclase compositions does vary with the number of components or limitations in spectral libraries, then ΔAn values from deconvolutions of plagioclase mixture spectra with more or less components should follow predictable trends. ΔAn would be expected to decrease further in mixtures with more feldspar components (compositions) and should improve with fewer components. A comparison of data from this study to *Milam et al.* [2004] is shown in Table 11. The data from *Milam et al.* [2004] is from deconvolutions of two-component coarse sand mixture spectra with spectral libraries that included all available plagioclase spectra but without those used in the physical mixtures. In addition, we took individual coarse-grained sand plagioclase component (one-component 'mixture') spectra and deconvolved each with all other remaining endmembers. Deconvolutions in Table 11 represent those in which spectra were resampled to laboratory, TES, and Mini-TES spectral resolutions. Because spectral libraries for deconvolutions at THEMIS resolution could not include all other available plagioclase endmembers, those results are not directly comparable and so are not included in Table 11. When our results

are re-considered with one- and two-component mixture spectra, there are no apparent increases in ΔAn with the number of plagioclase components. Likewise, RMS errors show no trend. The lack of variation is also apparent in deconvolutions of multi-phase mixture spectra (Table 9). In mixtures MP-1, MP-2, and MP-3, the number of plagioclase components is 2, 3, and 4 respectively. ΔAn does not increase with increasing numbers of components. Thus, the number of plagioclase compositions within a given mixture does not appear to alter our ability to model average plagioclase compositions from complex sand mixtures.

Similarly, there is no discernible correlation between the number of phases present in a given mixture and ΔAn or RMS errors from each mixture deconvolution. In mixtures MP-1, MP-2, and MP-3, ΔAn is 4, 3, and 3 An (1 σ standard deviation), respectively. Similarly, there are no noticeable trends in the average ΔAn or maximum ΔAn values. There is only a slight difference (1 An) between the maximum ΔAn values modeled from deconvolutions of multi-component (11 An) and multi-phase mixture spectra (12 An). Anorthite variation ranges more widely in deconvolutions of multi-phase mixture spectra relative to spectra from multi-component mixtures. This may result from the limited number of spectral endmembers available for deconvolution of individual phases in a mixture spectrum. For plagioclase, there are 23 available spectral endmembers for use in each linear deconvolution and, as has been suggested previously [*Milam et al.,* 2004] larger spectral libraries may be more useful in deriving mineral compositions. For a mineral such as augite (present in mixtures MP-1 and MP-2), only four spectral endmembers were available for deconvolution. Augite and other pyroxenes have spectral features at bands that can overlap with those of plagioclase. If a suitable suite of augite spectral endmembers are not available for modeling the spectral

characteristics of that pyroxene, then plagioclase spectral endmembers may be utilized by the linear deconvolution algorithm to produce the 'best fit' modeled spectrum. The result would then affect the modeled An and thus the ΔAn for that deconvolution. The maximum ΔAn values for deconvolutions of multi-phase mixtures would of course be expected to widen. Variations in maximum ΔAn values between multi-component and multi-phase mixtures are minimal, however. This coupled with the result that the largest 1 σ ΔAn is actually less for multi-phase mixtures indicates that the potential effect of biased spectral libraries is likewise minimal.

In multi-component mixtures, maximum ΔAn values do increase with spectral resolution (Table 8), with laboratory ΔAn ranging to 5 An and THEMIS ΔAn ranging up to 11 An. Standard deviations of ΔAn, however, are virtually identical (ΔAn = 4 to 5 An) regardless of spectral resolution and similar to those reported for two-component mixtures [*Milam et al.,* 2004]. The opposite is true of multi-phase mixtures (Table 10), where ΔAn values are slightly better at the lowest spectral resolution. RMS errors do not correlate with spectral resolution. We currently do not understand the nature of this ΔAn variation with spectral resolution in multi-phase mixtures, but suspect it is of little significance. The overall values for ΔAn at all spectral resolutions are comparable to those reported from previous studies [*Hamilton and Christensen*, 2000; *Hamilton et al.,* 2001; *Milam et al.*, 2004]. Likewise, RMS errors do not support this correlation and results from this (multi-phase) part of the study (three mixtures) have less overall statistical bearing than those of the two- [*Milam et al.*, 2004] and multi-component mixtures (21 and 15 total mixtures studied respectively).

Generally, the results from multi-component and multi-phase mixtures are virtually

identical to those reported by *Milam et al.* [2004] for two-component plagioclase coarse sand mixtures and are also within the reported range of accuracy for volcanic rocks [*Hamilton and Christensen,* 2000; *Milam et al.,* 2004]. Thus, the number and overall range of plagioclase compositions and the addition of other major phases in complex coarse sand mixtures has no significant effect on our ability to model average plagioclase compositions in thermal emission spectra from the TES, THEMIS, and Mini-TES instruments.

From a petrologic standpoint, however, grain sizes in volcanic rocks are well below those of coarse-grained sand (500-850 μm). While some plagioclase phenocryst dimensions are that of coarse sand, most crystal sizes in rapidly-cooled volcanic rocks are smaller. Fractures may develop along inter- or intra-grain boundaries of a rock, resulting in mechanical disaggregation of individual grains or lithic fragments. In the former case, the resultant sediment will likely represent a variety of grain sizes, most of which are smaller than the size fraction used in this study. At grain sizes below ~65 μm, particle size effects can significantly affect our ability to linearly model thermal emission spectra [*e.g. Salisbury and Wald*, 1992; *Moersch and Christensen,* 1995; *Ramsey and Christensen,* 1998; *Hamilton*, 1999]. Future studies should focus on derivation of plagioclase compositions in increasingly-complex mixtures, including variable grain sizes.

It is also important to note, from an application standpoint, that these results do not take into account effects other than variations in spectral resolution and range in simulating the performance of different instruments at Mars. Atmospheric effects and lower signal-to-noise ratios in orbital spacecraft thermal emission spectra of Mars are important. Likewise, this study does not consider the potential effects of dust cover or surficial alteration on

primary igneous rocks or the contribution of up- and down-welling radiance in spectra collected by landed spectrometers (i.e. the Mini-TES instruments on board Spirit and Opportunity). Finally, our work does not address potential effects of shock from exposure to impacts. A discussion of the effects of shock on plagioclase spectra may be found in *Johnson et al.* [2002; 2003].

5. Summary

Our study has shown that average plagioclase compositions in spectra from compositionally complex mixtures of coarse-grained plagioclase sand can be accurately modeled to 6 An (1σ) of measured values. This accuracy is unaffected by the number of plagioclase compositions or number of phases and is reported for all spectral resolutions. These results are directly comparable to those from *Milam et al.* [2004] and to deconvolutions of spectra of coarse-grained homogeneous plagioclase sand. Our results suggest that increased numbers of components (compositions) additional mineral phases appear to have minimal effect on our ability to model plagioclase compositions from thermal emission spectra of the Martian surface.

This study supports the conclusion that average plagioclase compositions may be accurately modeled from thermal emission spectra of rocks, sand dunes, or other complex mixtures on the Martian surface. The capability of accurately deriving plagioclase compositions may afford the opportunity to track the global magmatic evolution of Mars, map distinct geologic units, and search for locations where the Martian crust has been altered by various aqueous processes. Additional work is needed to discern other potential

effects, such as grain size variation, inclusion of dust in physical mixtures, and shock effects in plagioclase of intermediate compositions.

Acknowledgments

This work was supported by a fellowship from the NASA Graduate Student Researchers Program and a research grant from the Mayo Educational Foundation to KAM, and by THEMIS grants to HYM (ASU subcontract 01-082), JEM (JPL contract # 1241129 and subcontract # 1282418), and PRC. We thank Vicky Hamilton, Jeff Johnson, and Anne Hofmeister for their insightful and thorough reviews. We thank Larry Taylor, Allan Patchen, and Colin Sumrall for their assistance with the electron microprobe and reflected light photomicrographs. We are also grateful to Tim Glotch and Deanne Rogers for their assistance in processing spectral data.

References

Alt, J.C. and R. Emmermann (1985), Geochemistry of hydrothermally altered basalts: Deep Sea Drilling Project Hole 504B, Leg 83, *Initial Reports of the Deep Sea Drilling Project, 83,* 249-262.

Bandfield, J.L., V.E. Hamilton, and P.R. Christensen (2000), A global view of Martian surface compositions from MGS-TES, *Science, 287,* 1626-1630.

Christensen, P.R., J.L. Bandfield, M.D. Smith, V.E. Hamilton, and R.N. Clark (2000), Identification of a basaltic component on the Martian surface from Thermal Emission Spectrometer data, *J. Geophys. Res., 105*, 9609-9621.

Christensen, P. R., et al. (2001), Mars Global Surveyor Thermal Emission Spectrometer experiment: Investigation description and surface science results, *J. Geophys. Res., 106*, 23823-23871.

Deer, W.A., R.A. Howie, and J. Zussman (1996), An introduction to the rock-forming minerals, Prentice Hall, 712 p.

Easton, A. J., and C. J. Elliott (1977) Analyses of some meteorites from the British Museum of Natural History collection, *Meteoritics, 12,* 409-416.

Feely, K.C., and P.R. Christensen (1999), Quantitative compositional analysis using thermal emission spectroscopy: Applications to igneous and metamorphic rocks, *J. Geophys. Res., 104,* 24195-24210.

Hamilton, V. E. (1999), The effect of particle size on rock spectra in the thermal infrared: Implications for TES data analysis, *Lunar Planet. Sci.* [CD-ROM], *XXX*, Abstract 2001.

Hamilton, V.E., and P.R. Christensen (2000), Determining the modal mineralogy of mafic and ultramafic igneous rocks using thermal emission spectroscopy, *J. Geophys. Res., 105*, 9717-9733.

Hamilton, V.E., P.R. Christensen, and H.Y. McSween, Jr. (1997), Determination of Martian meteorite lithologies and mineralogies using thermal emission spectroscopy, *J. Geophys. Res., 102,* 25593-25603.

Hamilton, V.E., M.B. Wyatt, H.Y. McSween, Jr., and P. R. Christensen (2001), Analysis of terrestrial and Martian volcanic compositions using thermal emission spectroscopy II: Application to Martian surface spectra from the Mars Global Surveyor Thermal Emission Spectrometer, *J. Geophys. Res., 102*, 14733-14746.

Hardie, L.A. (1983), Origin of $CaCl_2$ brines by basalt-seawater interaction: Insights provided by some simple mass balance calculations, *Contributions to Mineralogy and Petrology, 82*, 205-213.

Iiishi, K., T. Tomisaka, T. Kato, and Y. Umegaki (1971), Isomorphous substitution and infrared and far infrared spectra of the feldspar group, Neues Jahrb. Mineral., 115, 98–119.

Johnson, J.R., F. Hörz, P. G. Lucey, P. R. Christensen (2002), Thermal infrared spectroscopy of experimentally shocked anorthosite and pyroxenite: Implications for remote sensing of Mars, *J. Geophys. Res., 107*, E10, doi:10.1029/2001JE001517.

Johnson, J.R., F. Hörz, and M. I. Staid (2003), Thermal infrared spectroscopy and modeling of experimentally shocked plagioclase feldspars, *American Mineralogist, 88*, 1575-1582.

Lyon, J. P., W. M. Tuddenham, and C. S. Thompson (1959), Quantitative mineralogy in 30

minutes, *Economic Geology, 54*, 1047-1055.
Lyon, R. J. P. (1965), Analysis of rocks by spectral infrared emission (8 to 25 microns), *Economic Geology, 58,* 274-284.
McSween, H. Y., Jr., and A. H. Treiman (1998), Martian meteorites, in *Reviews in Mineralogy, Volume 36: Planetary Materials (J. J. Papike ed.)*, Mineralogical Society of America, Washington, D. C.
McSween, H. Y., Jr., R. E. Arvidson, J. F. Bell III, D. Blaney, N. A. Cabrol, P. R. Christensen, B. C. Clark, J. A. Crisp, L. S. Crumpler, D. J. Des Marais, J. D. Farmer, R. Gellert, A. Ghosh, S. Gorevan, T. Graff, J. Grant, L. A. Haskin, K. E. Herkenhoff, J. R. Johnson, B. L. Jolliff, G. Klingelhoefer, A. T. Knudson, S. McLennan, K. A. Milam, J. E. Moersch, R. V. Morris, R. Rieder, S. W. Ruff, P. A. de Souza Jr., S. W. Squyres, H. Wänke, A. Wang, M. B. Wyatt, A. Yen, J. Zipfel (2004), Basaltic rocks analyzed by the Spirit rover in Gusev Crater, *Science, 305*, 842-845.
Michalski, J. R., M. D. Kraft, T. G. Sharp, L. B. Williams, and P. R. Christensen (2005), Mineralogical constraints on the high-silica Martian surface component observed by TES, *Icarus, 174,* 161-177.
Milam, K. A., H. Y. McSween, Jr., V. E. Hamilton, J. M. Moersch, and P. R. Christensen (2004), Accuracy of plagioclase compositions from laboratory and Mars spacecraft thermal emission spectra, *J. Geophys. Res., 109,* E04001, doi:10.1029/2003JE002097.
Milam, K. A., H. Y. McSween, Jr., J. E. Moersch, and P. R. Christensen (2006), The accuracy of derived plagioclase compositions from multi-component, multi-phase sand mixtures: Implications for determining Martian plagioclase compositions, *Lunar Planet. Sci.* [CD-ROM], *XXXVII*, Abstract 1156.
Moersch, J. E., and P. R. Christensen (1995), Thermal emission from particulate surfaces: A comparison of scattering models with measured spectra, *J. Geophys. Res., 100,* 7465-7477.
Mustard, J. F., and J. E. Hays (1997), Effects of hyperfine particles on reflectance spectra from 0.3 to 25 μm, *Icarus, 125,* 145-163.
Nash, D.B., and J. W. Salisbury (1991), Infrared reflectance spectra (2.2 – 15 mm) of plagioclase feldspars, *Geophys. Res. Lett., 18,* 1151-1154.
Ramsey, M. S., and P. R. Christensen (1998), Mineral abundance determination: Quantitative deconvolution of thermal emission spectra, *J. Geophys. Res., 103,* 579-596.
Ruff, S. W., P. R. Christensen, P. W. Barbera, and D. L. Anderson (1997), Quantitative thermal emission spectroscopy of minerals: A laboratory technique for measurement and calibration, *J. Geophys. Res., 102,* 14899-14913.
Ruff, S. W. (1998), Quantitative thermal infrared emission spectroscopy applied to granitoid petrology, PhD dissertation, 234 pages, Arizona State University.
Salisbury, J. W., and A. Wald (1992), The role of volume scattering in reducing spectral contrast of restrahlen bands in spectra of powdered minerals, *Icarus, 96,* 121-128.
Stakes, D.S., and P. Schiffman (1999), Hydrothermal alteration within the basement of the sedimented ridge environment of Middle Valley, northern Juan de Fuca Ridge, *GSA Bulletin, 3,* 1294-1314.
Stolper, E. M., and H. Y. McSween, Jr. (1979), Petrology and origin of the shergottite meteorites, *Geochim. Cosmochim. Acta, 43*, 1475-1498.

Thomson, J.L., and J.W. Salisbury (1993), The mid-infrared reflectance of mineral mixtures (7-14μm), *Remote Sens. Environ., 45*, 1-13.

Wänke, H., J. Brückner, G. Dreibus, R. Rieder, and I. Ryabchikov (2001), Chemical composition of rocks and soils at the Pathfinder site, *Space Science Reviews*, 96, 317-330.

Wyatt, M.B., and H.Y. McSween, Jr. (2002), Spectral evidence for weathered basalt as an alternative to andesite in the northern lowlands of Mars, *Nature, 417*, 263-266.

Wyatt, M.B., V.E. Hamilton, H.Y. McSween, Jr., P.R. Christensen, and L.A. Taylor (2001), Analysis of terrestrial and Martian volcanic compositions using thermal emission spectroscopy: 1. Determination of mineralogy, chemistry, and classification strategies, *J. Geophys. Res., 106,* 14,711-14,732.

Appendix for Part 3

Table 3. Plagioclase multi-component mixtures used in this study. Numbers in superscript reference combinations of plagioclase samples used (see Table 4 and *Milam et al*. [2004] for more sample information). Sample percentages are listed respective of the sample order shown below.

Mixture	Percentages*	Average An
	Three Component[1]	
III-A	80-15-5%	51
III-B	60-25-15%	45
III-C	40-35-25%	40
III-D	33-33-33%	36
III-E	20-45-35%	35
	Four Component[2]	
IV-A	80-10-5-5%	51
IV-B	60-20-15-5%	46
IV-C	40-30-20-10%	44
IV-D	25-25-25-25%	44
IV-E	20-30-30-20%	40
	Five Component[3]	
V-A	80-10-5-4-1%	51
V-B	60-20-10-6-4%	50
V-C	40-30-15-10-5%	48
V-D	20-20-20-20-20%	50
V-E	10-15-25-30-20%	49

* = by mass

Compositions and samples (sample numbers in parentheses) used:

[1] = An_{53}(0022b) - An_{51}(4512A-L) - An_{2}(5851)

[2] = [1] + An_{68}(SS)

[3] = [2] + An_{73} (1382a)

Table 4. Multi-phase mixture information. "WAR" denotes samples from Ward's Scientific, Co. Bulk chemistries for all non-plagioclase phases may be found in Table 5.

Mixture	mass (g)	% of mixture	average An
MP-1 (surface type 1 analog)			
plagioclase feldspar (25% An_2 + 75% An_{73})	2.0003	66.67	55
augite (WAR-5858)	0.9998	33.33	
MP-2 (Shergotty analog)			
augite (WAR-5858)	2.1825	72.74	
plagioclase (5% An_2 + 15% An_{51} + 80% An_{53})	0.7401	24.67	51
magnetite (WAR-5906)	0.0621	2.07	
ilmenite (WAR-5946)	0.0157	0.52	
MP-3 (Mazatzal analog)			
plagioclase (30% An_2 + 30% An_{51} + 20% An_{53} +20% An_{68})	1.3797	45.98	40
diopside (WAR-5870)	0.4168	13.89	
olivine (U.T. collection)	1.0954	36.5	
magnetite (WAR-5906)	0.0810	2.70	
ilmenite (WAR-5946)	0.0278	0.93	

Table 5. Bulk compositions (from XRF analyses) of all non-plagioclase phases used in multi-phase mixtures

Sample	Mineral Name	SiO_2	Al_2O_3	Fe_2O_3	MnO	MgO	CaO	Na_2O	K_2O	TiO_2	P_2O_5	Cr_2O_3	LOI	Total
WAR-5858	Augite	51.02	1.2	10.66	0.243	12.02	22.34	0.56	0.05	0.05	0.01	0.03	0.082	98.27
UT-1	Olivine	40.33	0.07	8.57	0.107	50.84	0.04	< 0.01	0.04	0.02	0.01	0.34	0.201	100.5
WAR- 5870	Diopside	44.83	9.22	6.19	0.173	14.03	18.11	0.24	0.07	0.92	0.01	0.01	0.246	94.05
WAR-5946	Ilmenite	0.45	0.14	50.45	2.868	0.42	0.05	0.08	0.03	46.13	0.01	0.02	-4.121	96.53
WAR-5906	Magnetite	1.05	0.62	97.72	0.053	0.16	0.18	0.07	0.03	0.12	0.01	< 0.01	-3.1	96.91

Table 6. Spectral endmembers (and their bulk chemistries) used in this study. All non-plagioclase spectral endmembers were utilized in deconvolutions of multi-phase mixtures.

Sample	Mineral Name	Notes	Collection	SiO_2	Al_2O_3	FeO (Fe_2O_3)	MnO	MgO	CaO	Na_2O	K_2O	TiO_2	Total	An
WAR-0235	albite		ASU	68.3	20	(0.33)	0.01	0.04	0.01	11.5	0.02	0.00	100	<1
WAR-0244	albite		ASU	69.2	18.2	0.24	0.01	0.01	0.38	10.2	0.66	0.00	98.9	2
WAR-0612	albite		ASU	67.2	19	0	0.02	0.4	0.35	9.26	0.18	0.00	96.4	2
5851	albite	1,2,3,4,5,6	UT	67.9	19.9	0	0.02	0.02	0.63	9.71	0.27	0.00	98.5	2
WAR-5851	albite	7	ASU	63	19.7	5.51	0.02	0.47	1.37	8.5	0.22	0.00	98.8	8
BUR-060D	oligoclase	10	ASU	63.5	22.5	0.21	0.01	0.01	3.36	9.21	0.6	0.00	99.4	15
BUR-060	oligoclase		ASU	60.4	21.9	4.16	0.08	0.06	3.24	9.37	0.79	0.00	100	16
WAR-5804	oligoclase	7	ASU	62	24	0.04	0	0	4.74	9.03	0.5	0.00	100	22
BUR-3680	oligoclase		ASU	63.5	22.7	0.03	0.13	0.44	4.94	7.76	0.63	0.00	100	25
WAR-0234	oligoclase		ASU	60.8	22.1	0	0.02	0.85	5.37	6.71	0.91	0.00	96.8	29
BUR-240	andesine	7	ASU	53.9	27.1	0.53	0.01	0.07	9.51	5.55	0.34	0.00	97	48
BUR-3080A	andesine		ASU	53.4	26.3	(1.5)	0.03	0.65	9.62	4.94	1.2	0.00	97.6	48
WAR-0024	andesine		ASU	56.4	24.6	(0.06)	0.07	2.51	9.38	4.67	0.76	0.00	98.5	50
4512A-L	labradorite	1,2,3,5,6	UT	54.2	24.4	2.16	0.05	1.32	9.8	4.34	1.3	0.00	97.6	51
0022b	labradorite	1,2,3,5,6	UT	54.8	26.5	1.1	0.03	0.24	10.4	4.02	0.47	0.00	97.6	53
WAR-4524	labradorite	7, 8, 9	ASU	52.6	27.7	(2.5)	0.02	0.14	10.9	5.01	0.42	0.00	99.3	53
WAR-1384	labradorite	8,9,10	ASU	51.3	30.9	(0.32)	0.03	0.5	11.8	3.64	0.26	0.00	98.8	63
WAR-RGAND01	labradorite	7	ASU	49.9	28	3.09	0.03	0.68	13	3.46	0.22	0.00	98.4	67
SS	labradorite	2,3,6	UT	50.9	29.8	0.3	0.02	0.15	13.4	3.42	0.14	0.00	98.1	68
WAR-5859	bytownite		ASU	48.4	31.5	1.56	0.01	0.26	14.7	2.89	0.09	0.00	99.4	73
1382a	bytownite	3,4,10	UT	49.1	30.4	0.5	0.04	0.45	14.5	2.86	0.2	0.00	98.1	73
WAR-5759	bytownite	8	ASU	41.5	29.5	9.2	0.03	2.69	15.4	1.13	0.08	0.00	99.5	88
BUR-340	anorthite	7,10	ASU	43.2	35.6	0.54	0.01	0.39	17.6	0.84	0.01	0.00	98.2	92
BUR-4120	plutonic Quartz		ASU	100.00	0.00	0.00	0.00	0.00	0.00	0.00	0.00	0.00	100.00	
HS-115.4	magnesiohastingsite		ASU	44.97	11.17	7.14	0.06	17.28	12.33	2.24	0.83	0.29	96.31	
WAR-0354	magnesiohornblende		ASU	56.54	1.39	5.71	0.22	21.12	12.34	0.35	0.03	0.01	97.70	
HS-9.4	orthopyroxene Mg_{90}		ASU	57.87	0.99	6.88	0.17	34.86	0.67	0.00	0.00	0.02	101.46	
NMNH-93527	orthopyroxene Mg_{77}		ASU	51.84	5.28	13.79	0.23	26.76	1.46	0.07	0.00	0.35	99.79	
WAR-5780	diopside	9	ASU	54.14	0.51	2.56	0.06	17.54	24.25	0.45	0.00	0.02	99.54	
HS-119.4b	augite	8,9	ASU	52.87	0.92	10.20	0.29	11.91	24.08	0.65	0.00	0.02	100.94	

Table 6 (continued).

Sample	Mineral Name	Notes	Collection	SiO_2	Al_2O_3	FeO (Fe_2O_3)	MnO	MgO	CaO	Na_2O	K_2O	TiO_2	Total	An
DSM- HED01	hedenbergite	[9]	ASU	49.96	0.06	14.14	7.99	4.32	22.80	0.11	0.00	0.01	99.39	
WAR-6474	augite (low-Ca)		ASU	50.60	2.35	12.58	0.30	9.96	21.13	2.00	0.00	0.18	99.10	
BUR-620	augite (low-Ca)	[8,10]	ASU	50.51	1.69	16.20	0.73	7.58	21.51	1.91	0.00	0.11	100.24	
NMNH-9780	augite (low-Ca)		ASU	51.00	1.55	16.52	0.46	9.42	20.49	0.33	0.02	0.20	99.99	
None	pigeonite $Wo_{10}En_{36}Fs_{54}$	[8,9,*]	ASU	50.49			32.59	12.20	4.71					
HS-8.4	antigorite		ASU	42.28	1.21	3.79	0.06	38.50	0.04	0.02	0.02	0.02	85.94	
83-145B	lizardite		ASU	40.62	0.00	8.82	0.12	48.99	0.07	0.00	0.00	0.00	98.62	
AZ-01	forsterite	[10]	ASU	38.47	0.09	9.57	0.13	48.88	0.14	0.03	0.01	0.01	97.33	
WAR-RGFAY01	fayalite		ASU	31.11	0.00	59.75	1.30	7.71	0.09	0.00	0.00	0.06	100.02	
None	pure silica glass		ASU	99.99	0.00	0.00	0.00	0.00	0.00	0.00	0.00	0.00	99.99	
None	K-rich glass		ASU	77.87	12.55	0.00	0.00	0.00	0.00	3.90	5.67	0.00	99.99	
WAR-4119	ilmenite		ASU	0.01	0.01	48.05	0.21	3.13	0.01	0.00	0.01	47.81	99.24	
WAR-0384	magnetite		ASU	0.31	0.00	92.61	0.04	0.13	0.00	0.00	0.00	0.08	93.17	

[1] = excluded from use in 3-comp. mixture deconvolutions; [2]=excluded from use in 4-comp. mixture deconvolutions; [3] = excluded from use in 5-comp. mixture deconvolutions;
[4] = excluded from MP-1 deconvolutions; [5] = excluded from MP-2 deconvolutions; [6] = excluded from MP-3 deconvolutions; [7]= plagioclase used in decon. of multi-comp. mixtures at THEMIS resolution

[8]=used in MP-1 decon. @THEMIS resolution; [9]=used in MP-2 decon. @ THEMIS resolution; [10]=used in MP-3 decon. @ THEMIS resolution
[*]=synthetic sample with modeled chemistry from D. Lindsley (see Wyatt et al. [2001])

ASU = Arizona State University; UT = University of Tennessee

Table 7. Anorthite variations (ΔAn) and RMS errors reported from deconvolutions of multi-component mixture spectra as a compared to the number of components present in each mixture. Average ΔAn reflects the average of all deconvolutions for a given number of components at laboratory, TES, THEMIS, and Mini-TES spectral resolutions. The maximum ΔAn represents the maximum absolute value for all deconvolutions at all spectral resolutions.

Number of Components	II	III	IV
Anorthite Variation			
average ΔAn	< 1	-4	1
maximum ΔAn	5	6	11
ΔAn (1 σ standard dev.)	3	4	6
RMS Errors			
average	0.0018	0.0023	0.0020
maximum	0.0024	0.0084	0.0046
(1 σ standard dev.)	0.0042	0.0015	0.0011

Table 8. Anorthite variations (ΔAn) and RMS errors reported from deconvolutions of multi-component mixture spectra as a function of varying spectral resolution.

Spectral Resolution	Lab	TES	THEMIS	Mini-TES
Anorthite Variation				
average ΔAn	-2	-1	5	-2
maximum ΔAn	5	8	11	7
ΔAn (1 σ standard dev.)	4	5	4	4
RMS Errors				
average	0.0024	0.0020	0.0017	0.0022
maximum	0.0046	0.0030	0.0084	0.0037
(1 σ standard dev.)	0.0007	0.0004	0.0020	0.0006

Table 9. Anorthite variations (ΔAn) and RMS errors reported from deconvolutions of multi-phase, multi-component mixture spectra versus the number of phases and components.

Number of Components	MP-1	MP-2	MP-3
Mixture			
Number of Phases	3	6	8
Number of Components	2	3	4
Anorthite Variation			
average ΔAn	4	10	8
maximum ΔAn	8	12	10
ΔAn (1 σ standard dev.)	4	3	3
RMS Errors			
average	0.0027	0.0029	0.0034
maximum	0.0036	0.0033	0.0035
(1 σ standard dev.)	0.0006	0.0004	0.0002

Table 10. Anorthite variations (ΔAn) and RMS errors reported from deconvolutions of multi-phase, multi-component mixture spectra as a function of varying spectral resolution.

Spectral Resolution	Lab	TES	THEMIS	Mini-TES
Anorthite Variation				
average ΔAn	7	7	6	10
maximum ΔAn	12	10	8	12
ΔAn (1 σ standard dev.)	6	5	3	5
RMS Errors				
average	0.0029	0.0029	0.0032	0.0031
maximum	0.0028	0.0032	0.0036	0.0034
(1 σ standard dev.)	0.0007	0.0004	0.0007	0.0004

Table 11. Anorthite variations (ΔAn) reported from deconvolutions of multi-component mixture spectra at laboratory, TES, and Mini-TES resolutions as compared to the number of components present in each mixture. Column 2 (number of components =1) data is from unpublished deconvolutions of single coarse sand plagioclase spectral endmembers with all other plagioclase spectral endmembers using the same methods of this study. Column 3 (number of components = 2) data originates from *Milam et al*. [2004]. Deconvolutions using endmember set #5 from that study correspond to methods used in this study.

Number of Components	I	II	III	IV	V
Anorthite Variation					
average ΔAn	4	-1	< 1	-4	1
maximum ΔAn	19	9	5	6	11
ΔAn (1 σ standard dev.)	4	3	3	4	6
RMS Errors					
maximum	0.0110	0.0040	0.0024	0.0084	0.0046
(1 σ standard dev.)	0.0025	0.0007	0.0042	0.0015	0.0011

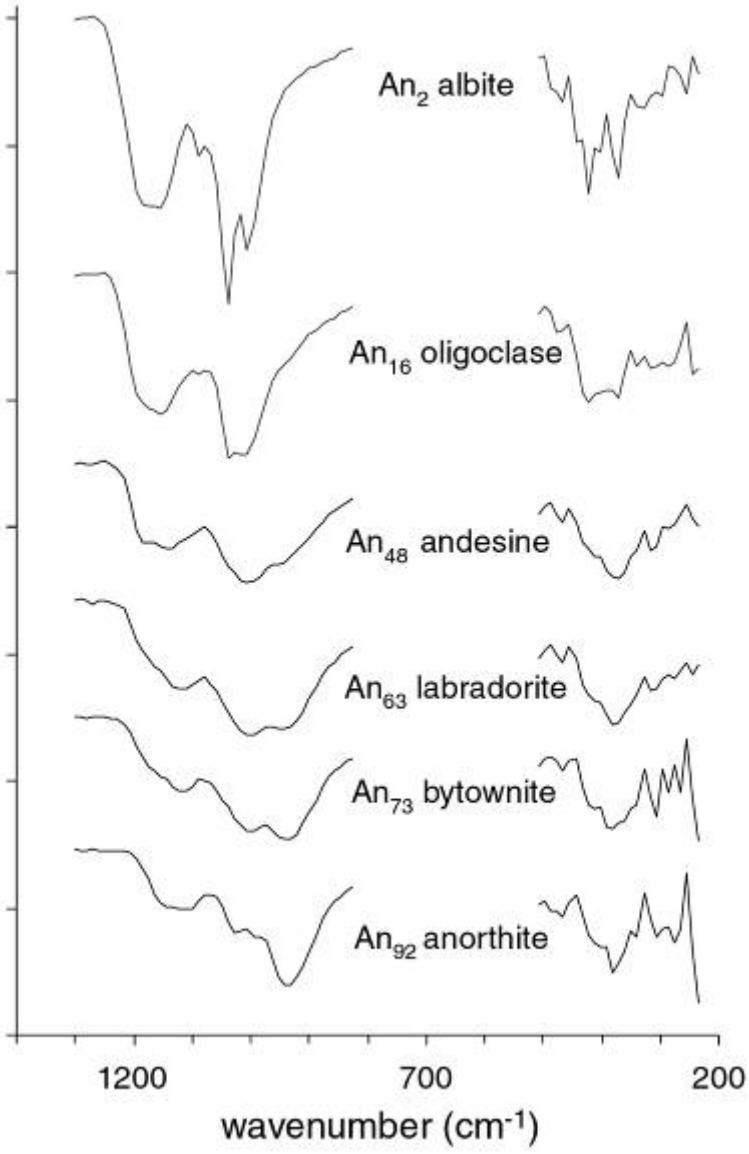

Figure 20. Representative solid solution series plagioclase feldspar thermal emission spectra from *Milam et al*. [2004] and this study. Spectra at the spectral resolution of the Thermal Emission Spectrometer (TES) instrument. The area between 507-825 cm^{-1} is excluded due to a prominent atmospheric CO_2 feature centered at 667 cm^{-1}. All spectra except that of albite have been offset for clarity. The Christiansen Frequency (a prominent reflectivity minimum/emission maximum between ~1234-1299 cm^{-1}) shows a shift to higher wavenumbers as plagioclase compositions change from albite to anorthite. Additional spectral features at 1200–900, 800–700, and 650–540 cm^{-1} result from various Si, Al, and O stretching/bending modes in plagioclase [*Iiishi et al.*, 1971; *Ruff*, 1998].

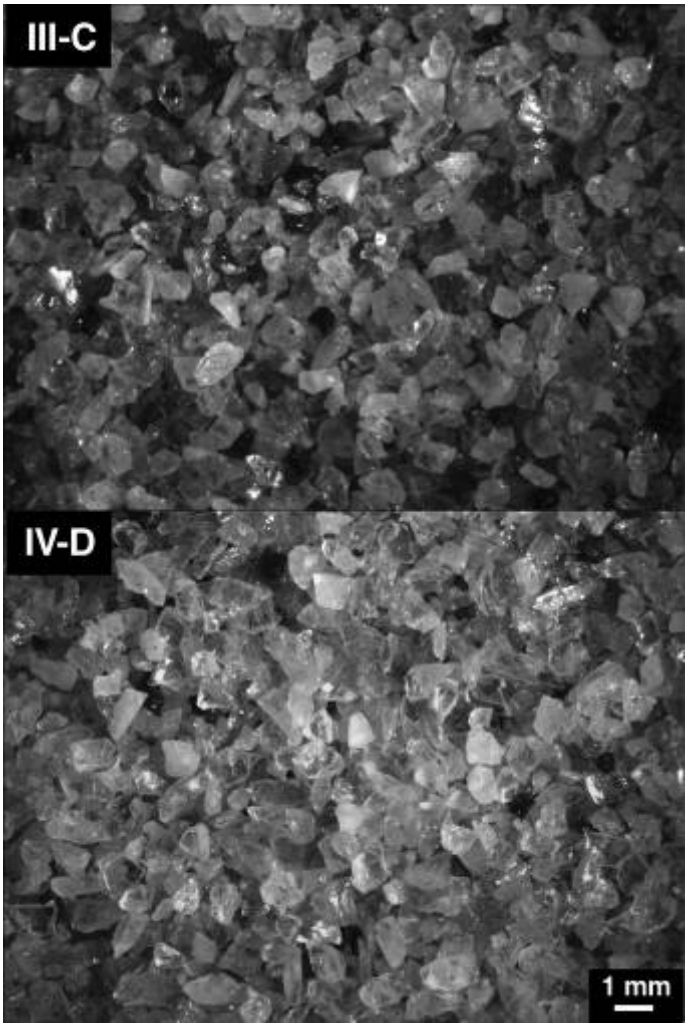

Figure 21. Reflected light photomicrographs of examples of three (III-C) and four (IV-D) multi-component mixtures.

Figure 22. Representative examples of measured (black) vs. modeled (magenta) thermal emission spectra of multi-component mixtures (III-A, IV-A, and V-A) at laboratory, TES, THEMIS, and Mini-TES resolution. Anorthite contents are reported as (ΔAn), measured (black), and modeled (magenta) along with root-mean-square (RMS) error and modeled endmember percentages.

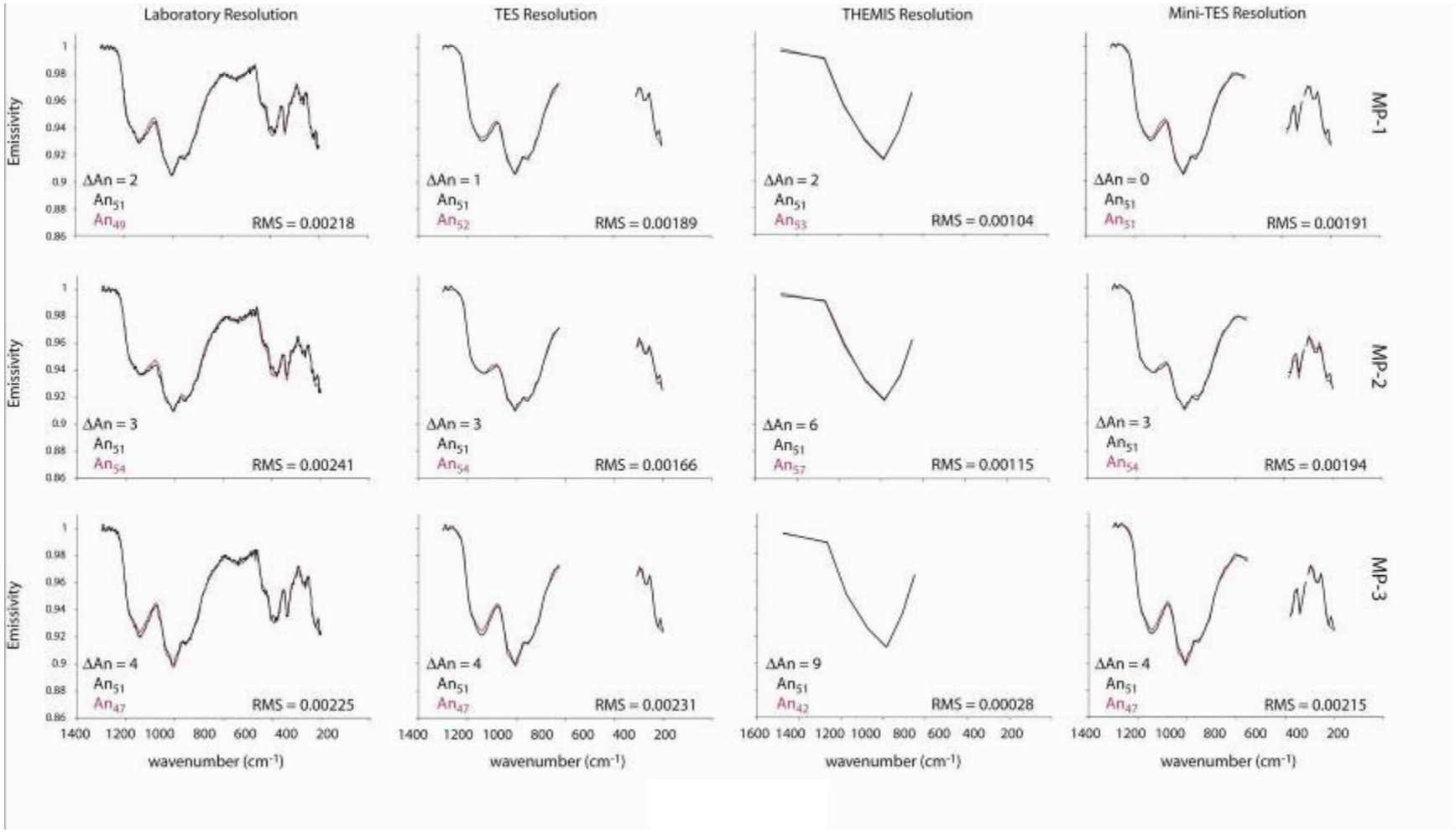
Laboratory Resolution
TES Resolution
THEMIS Resolution
Mini-TES Resolution
MP-1
MP-2
MP-3
Emissivity
ΔAn = 2
An51
An49
RMS = 0.00218
ΔAn = 1
An51
An52
RMS = 0.00189
ΔAn = 2
An51
An53
RMS = 0.00104
ΔAn = 0
An51
An51
RMS = 0.00191
ΔAn = 3
An51
An54
RMS = 0.00241
ΔAn = 3
An51
An54
RMS = 0.00166
ΔAn = 6
An51
An57
RMS = 0.00115
ΔAn = 3
An51
An54
RMS = 0.00194
ΔAn = 4
An51
An47
RMS = 0.00225
ΔAn = 4
An51
An47
RMS = 0.00231
ΔAn = 9
An51
An42
RMS = 0.00028
ΔAn = 4
An51
An47
RMS = 0.00215
wavenumber (cm-1)

Figure 23. Measured (black) vs. modeled (magenta) emission spectra of multi-phase mixtures at laboratory, TES, THEMIS, and Mini-TES resolution. Anorthite contents are reported as An variation (ΔAn), measured (black), and modeled (magenta) along with root-mean-square (RMS) error and modeled endmember percentages. Asterisk (*) indicates modeled endmember percentages below the reported detectibility limit for most mineral phases.

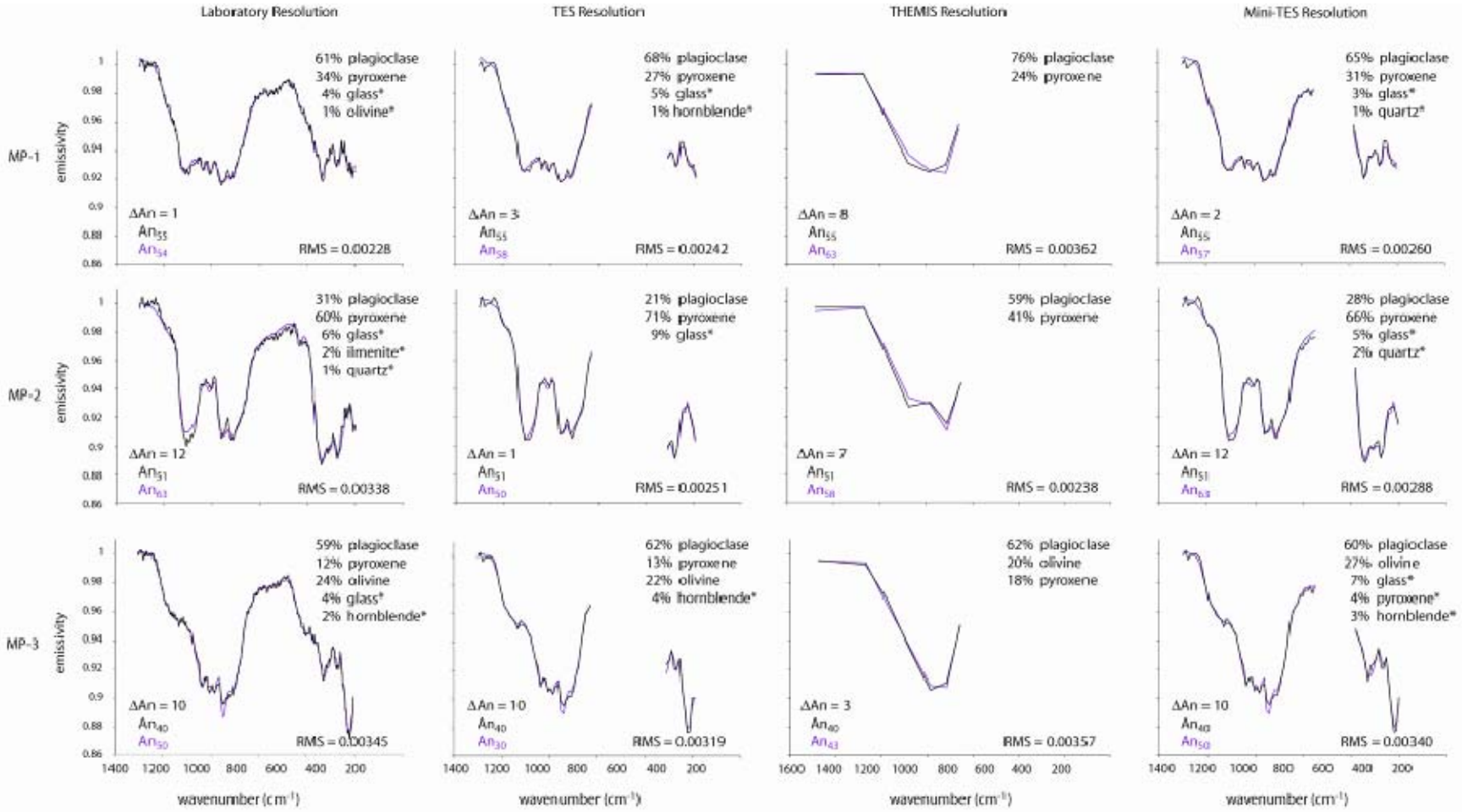
Laboratory Resolution
TES Resolution
THEMIS Resolution
Mini-TES Resolution
MP-1
MP-2
MP-3
emissivity
wavenumber (cm-1)
61% plagioclase
34% pyroxene
4% glass*
1% olivine*
ΔAn = 1
An55
An54
RMS = 0.00228
68% plagioclase
27% pyroxene
5% glass*
1% hornblende*
ΔAn = 3
An55
An58
RMS = 0.00242
76% plagioclase
24% pyroxene
ΔAn = 8
An55
An63
RMS = 0.00362
65% plagioclase
31% pyroxene
3% glass*
1% quartz*
ΔAn = 2
An55
An57
RMS = 0.00260
31% plagioclase
60% pyroxene
6% glass*
2% ilmenite*
1% quartz*
ΔAn = 12
An51
An63
RMS = 0.00338
21% plagioclase
71% pyroxene
9% glass*
ΔAn = 1
An51
An50
RMS = 0.00251
59% plagioclase
41% pyroxene
ΔAn = 7
An51
An58
RMS = 0.00238
28% plagioclase
66% pyroxene
5% glass*
2% quartz*
ΔAn = 12
An51
An63
RMS = 0.00288
59% plagioclase
12% pyroxene
24% olivine
4% glass*
2% hornblende*
ΔAn = 10
An40
An50
RMS = 0.00345
62% plagioclase
13% pyroxene
22% olivine
4% hornblende*
ΔAn = 10
An40
An30
RMS = 0.00319
62% plagioclase
20% olivine
18% pyroxene
ΔAn = 3
An40
An43
RMS = 0.00357
60% plagioclase
27% olivine
7% glass*
4% pyroxene*
3% hornblende*
ΔAn = 10
An40
An50
RMS = 0.00340

Part 4.

Distribution and Variation of Plagioclase Compositions on Mars

Abstract

This study presents the first global compositional maps of plagioclase, the most abundant mineral in the Martian crust. Linear deconvolutions of spectra from the Thermal Emission Spectrometer (TES) allowed calculation of average plagioclase compositions for dust-free areas on Mars $\pm$60° of the equator (approximately 40% of the surface for this range of latitudes). Surface type 1 and 2 terrains are virtually identical with respect to their average plagioclase compositions, An_{62} and An_{59}, with some variations in the percentages of TES spectra that model as particular compositions of plagioclase. The majority of TES observations were modeled as labradorite and bytownite (between An_{50-90}), with much lesser amounts of other plagioclase compositions that do not appear correlate with specific geologic terrains. The lack of diversity in average plagioclase compositions across multiple geologic units may represent an outer martian crust with minimal variation in plagioclase compositions. Alternatively, aeolian, fluvial, and/or impact activity may have redistributed heterogeneous crustal material forming a relatively homogeneous, global surface layer.

1. Introduction

Previous studies have addressed the abundance distribution of major minerals on the Martian surface [*Bandfield et al,* 2000; *Bandfield,* 2002], but few have examined the compositional variations that may occur in solid solution minerals, such as plagioclase, and the implications such variations may have for the crustal evolution of Mars. In this study, we build on previous, laboratory-based studies [*Milam et al.,* 2004; 2007 in review] to produce the first plagioclase compositional maps of Mars using thermal emission spectra from the Mars Global Surveyor (MGS) Thermal Emission Spectrometer (TES). With such maps, we are able to speculate on the magmatic evolution and alteration of a planet dominated by a basaltic (and possibly andesitic) crust.

2. Background

The Martian surface is composed of volcanic rocks that have been subjected to the effects of aeolian, impact, hydrologic, and mass-wasting processes. Interpretation of Mars Global Surveyor (MGS) Thermal Emission Spectrometer (TES) spectra shows that Mars can be generally divided into two primary surface types (ST) corresponding approximately to the planet's surface dichotomy [*Bandfield et al.,* 2000]. ST1 spectra represent a basalt-dominated southern highlands, whereas ST2 spectra suggests that andesite or weathered basalt comprises the northern lowlands and some high latitude regions of the southern highlands [*Christensen et al.,* 1999; *Bandfield et al.,* 2000; *Wyatt and McSween,* 2002]. While TES data indicate plagioclase as the dominant

mineral in the Martian crust [*Bandfield et al.,* 2000; *Hamilton et al.,* 2001; *Wyatt and McSween,* 2002; *Rogers and* Christensen, 2007], it has smaller abundance than pyroxenes in Martian basaltic meteorites [*McSween and* Treiman, 1998]. Martian meteorites, however, are likely not representative of the bulk Martian crust [for a discussion see e.g. *McSween,* 2002; *Hamilton et al.,* 2003]. Because plagioclase compositions in terrestrial rocks vary according to changing conditions during fractional crystallization and subsequent weathering/alteration, this prominent mineral has the potential to provide insights into the magmatic evolution and primary surface alteration processes on Mars.

2.1. Primary plagioclase compositions and alteration in terrestrial settings

On Earth, feldspar abundances and compositions reflect environmental conditions during their formation (*Deer et al.*, 1997). In metamorphic rocks, for example, plagioclase compositions (solid solutions of anorthite $CaAl_2Si_2O_8$ and albite $NaAlSi_3O_8$) are indicative of specific metamorphic grades and are dependent on bulk host rock compositions. In igneous rocks, the range of plagioclase compositions is indicative of the bulk chemistry of magmas, and varies systematically during fractional crystallization. In the granodioritic continental crust, feldspar is present as albite or intermediate plagioclase. Plagioclase in basalt and andesite is intermediate $\sim An_{50\text{-}75}$ ('An' refers to the molar anorthite content of the feldspar, specifically the ratio of [Ca/(Ca+Na+K)] x 100 in ternary feldspars) in composition. Primary sodic plagioclase ($<An_{30}$) is rarely found in unaltered mafic to intermediate volcanic rocks.

It does, however, occur in hydrothermally-altered basalts and andesites [e.g. *Alt and Emmerman*, 1985, see discussion below).

Plagioclase is prone to weathering in the presence of water. In low-temperature settings, it can alter to clay minerals (halloysite, kaolinite, montmorillonite, scapolite) prehnite, and various zeolites [e.g. *Robertson and Eggleton*, 1991; *Deer et al.,* 1997; *Jeong*, 1998; *Arslan et al.,* 2006] under low temperature (<200˚C), surface conditions at rates ranging from 1×10^{-19} to 2.8×10^{-16} mol m^{-2} s^{-1} [*White et al.,* 1996; *White et al.,* 2001]. Through aqueous alteration in sedimentary basins and hydrothermal environments, calcic plagioclase can become more sodic ($<An_{30}$) through a process known as albitization [*Cann,* 1969; *Hardie*, 1983; *Alt and Emmermann*, 1985; *Stakes and Schiffman*, 1999]. Albitization has been observed in materials from diagenetic, hydrothermal, and metamorphic settings [e. g. *Ramseyer et al.,* 1999; *Hunter et al.,* 1999; *Neuhoff et al.,* 1999]. In mid-ocean ridge basalts, albitization occurs by circulation of hydrothermal fluids near spreading centers by the reaction: $1.5CaAl_2SiO_2O_8 + Na^+ + 2H^+ = NaAlSi_3O_8 + 1.5Ca^{2+} + Al_2O_3 + H_2O$ [*Rosenbauer et al.,* 1983] and can alter plagioclase in several thousand meters of section [*Alt et al.,* 1996]. Experimental studies have demonstrated that albitization under hydrothermal conditions is primarily dependent upon pH [*Rosenbauer et al.,* 1983]. Empirical studies of low-temperature near surface conditions suggest that albitization is enhanced by increased temperatures [*Perez and Boles,* 2005], implying that hydrothermal rates for plagioclase alteration are much higher than those at lower temperature conditions mentioned previously.

In terrestrial sedimentary basins, albitization occurs by the diagenesis of plagioclase and/or K-feldspar under low-temperature conditions (<120ºC) [*Boles,* 1982; *Land,* 1984; *Morad et al.,* 1990; *Baccar et al.,* 1993]. On Earth, diagenetic albitization occurs within a relatively narrow range of burial depths (2500-3000m) and requires circulating pore fluids [*Boles*, 1982; *Morad et al.,* 1990]. Calcium and aluminum-rich products commonly become incorporated into carbonates, clays, and zeolites [*Boles,* 1982]. Preferential albitization of calcium-rich plagioclase has been noted for acidic conditions [e.g. *Ramseyer et al.,* 1992].

Albitization (also referred to in mid-ocean ridge settings as spilitization [*Deer et al.,* 1997]) may also occur when high-temperature (250-370°C) Na- and SiO_2-rich fluids interact with plagioclase at near-surface pressures to produce 'albitic' or sodium-rich feldspar. Oceanic crust has been hydrothermally altered by seawater along mid-ocean ridges, sites suggested as the birthplace of early terrestrial life forms [*Corliss et al.,* 1981]. If water was present on Mars in the vicinity of similar heat sources, thermal springs may have arisen and may hold record of the potential for biologic activity on Mars [*Walter and Des Marais,* 1993; *Farmer,* 1996, 1998; *Farmer and Des Marais,* 1999]. Thus, detection of sodium-rich feldspar in the basaltic Martian crust could lead to directed studies of high priority astrobiology sites.

2.2. Low- and High-Temperature Aqueous Alteration of Volcanic Terrains on Mars

Was the Martian surface wet enough to alter major minerals, such as plagioclase, or has Mars been dry over much of its history? Some evidence supports a dry past. Water is presently unstable at the Martian surface except under very limited and ephemeral environmental conditions [*Lobitz et al.,* 2001]. Morphologic features, such as shorelines and gullies, thought to have been formed by hydrologic processes, may have formed by non-aqueous means [*Carr and Head,* 2003; *Treiman*, 2003]. Unweathered minerals, such as olivine have been found in ancient Martian terrains [*Hoefen et al.,* 2002; *Christensen et al.,* 2003; *McSween et al.,* 2006] and in the Martian meteorites (for a review see *McSween and Treiman* [1998]). These observations seem to indicate that water may have played a limited role in altering the Martian crust.

Morphologic features (e.g. outflow channels, gullies, and some sedimentary deposits), however, provide evidence of fluvial modification of the Martian surface [e.g. *Carr*, 1996, *Malin and Edgett,* 2000; *Carr and* Head, 2003; *Malin and Edgett,* 2003; *Coleman,* 2003; *Mangold et al.,* 2004]. Aqueous minerals, such as hematite, phyllosilicates, and sulfates, have been detected, providing further support of a wet past [*Christensen et al.,* 2000, 2004; *Klingelhöfer et al.,* 2004; *Bibring et al.,* 2006] New data from the MER rovers confirm that processes such as leaching, mobilization, and precipitation of soluble salts has occurred at least locally [*Squyres et al.,* 2004; *Klingelhöfer et al.*, 2004; *Hurowitz et al.,* 2006].

If large reservoirs of water existed on the Martian surface in the past, it is possible that they may have co-existed with localized heat sources, resulting in hydrothermal alteration of crustal material (i.e. albitization of plagioclase). Some Martian terrains show that volcanism [*Carr*, 1984; *Strom et al.*, 1992; *Hartmann et al.,* 1999; *Hartmann & Berman*, 2000], impact bombardment [*Strom et al.*, 1992], and hydrologic activity were contemporaneous [*Tanaka et al.,* 1992; *Farmer,* 1998; *Farmer and Des Marais*, 1999]. Volcanic and impact generated landforms that may indicate interaction with water have been noted on Mars [e. g. *Carr et al.,* 1977; *Gulick*, 1998; *Christensen et al.,* 2000; *Farrand et al.,* 2001; *Fagents et al.,* 2001; *Lanagan et al.,* 2001].

In terrestrial settings, low-temperature (<150°C) alteration of MORBs produces spilites, or altered basalts, with distinctive secondary mineral assemblages of Fe-oxyhydroxides, saponite, celadonite, pyrite, and various silica-rich phases. Other secondary minerals (e.g. smectite, chlorite, actinolite, epidote, and zeolite) form from higher-temperature/pressure hydrothermal alteration [*Alt and Emmermann,* 1985; *Tanokura and Onuki*, 1990; *Shikazono et al.*, 1995; *Zierenberg et al.*, 1995; *Hunter et al.*, 1999; *Stakes and Schiffman,* 1999; *Larsson et al.,* 2002;]. Abundances of many alteration phases in terrestrial volcanics are often below detectibility limits of thermal infrared spectrometers that might be used to model mineral abundances on Mars. A better approach for locating either low-temperature diagenetic or hydrothermal sites (and by implication, high-priority astrobiology sites) from orbit would be to search for compositional variation of primary phases with more abundant

alteration products that might indicate altered rock. Because intermediate plagioclase appears to be the dominant phase in the mafic-intermediate Martian crust [*Zierenberg et al.,* 1995; *Bandfield et al.,* 2000; *Wyatt and McSween*, 2002], the identification of significant quantities (>10 vol %) of sodic plagioclase might indicate sites of diagenetic or hydrothermal alteration.

2.3. Accuracy in Determining Plagioclase Compositions on Mars

Several laboratory studies have demonstrated that plagioclase abundances and compositions can be accurately derived from thermal emissivity spectra of terrestrial, and, by inference, Martian volcanic rocks. At thermal infrared wavelengths, a rock spectrum is an approximately linear combination of its constituent mineral spectra [*Lyon*, 1965]. This allows numerical modeling of modal mineralogies and mineral compositions in a rock using thermal infrared spectra. Several studies have shown that most mineral abundances can be modeled to within 15 vol.% of measured values [*Thomson and Salisbury,* 1993; *Feely and Christensen*,1999; *Hamilton and Christensen*, 2000] *Hamilton et al.* [1997] and *Wyatt et al.* [2001] demonstrated that plagioclase abundances can be modeled to within 5-10 vol. % of measured abundances.

Compositions within the plagioclase solid solution series can also be modeled due to the variation of intrinsic characteristics of plagioclase TIR spectra with changing compositions. Plagioclase has distinctive spectral features at thermal infrared (TIR) wavelengths (4-15 μm; 2500-667 cm^{-1}), making it distinguishable from other phases

[e. g. *Lyon et al.,* 1959; *Nash and Salisbury,* 1991]. Absorption features that relate to vibrational and bending modes within the plagioclase crystalline lattice vary with changing plagioclase compositions (Figure 1) and make it possible to derive compositional information from infrared spectra. For more information about the spectral signature of plagioclase, see *Illishi et al.* [1971], *Ruff* [1998], and *Milam et al.* [2004; 2007, in review].

Average plagioclase compositions have been successfully modeled in complex mixtures of minerals that are thought to be analogous to those present on the surface of Mars. Average plagioclase compositions have been modeled to within 12 An (6 An 1σ standard deviation) in physical mixtures of coarse-grained plagioclase sand [Milam et al., 2004; 2007,in review] and more complex mixtures that include other phases common to terrestrial and Martian mafic volcanic rocks [Milam et al., 2007,review]. This reported accuracy applies to the spectral resolutions of thermal emission spectrometers flown to Mars. Similar results have been reported for terrestrial volcanic rock analogs [*Hamilton and Christensen*, 2000; *Wyatt et al.*, 2001; *Milam et al.*, 2004]. When processing thermal emission spectra collected from Mars, however, additional effects can influence our ability to model average plagioclase compositions. For example, lower signal-to-noise ratios in thermal emission spectra can result from data collection at specific times or latitudes corresponding to low surface temperatures. Modeled plagioclase compositions can vary by as much as 30 An from the additional noise at temperatures below 255 K (see Appendix A for a discussion). These and other effects, such as dust cover, shock metamorphism,

atmospheric effects, etc. must be taken into account when the results from laboratory-based studies are extrapolated to Mars.

3. Methods

Here we build on previous laboratory-based studies [*Milam et al.,* 2004; in review] by examining thermal emission spectra collected by the Thermal Emission Spectrometer (TES) onboard the Mars Global Surveyor (MGS) spacecraft to produce the first plagioclase compositional maps of the Martian surface. We then examine the degree to which these maps may be used to address such issues as: (1) mantle heterogeneity, (2) crustal evolution, (3) weathering/alteration processes.

3.1. Thermal Emission Spectrometer

MGS-TES provided the first high spatial resolution (~3 x 5 km pixel size) thermal infrared data of the Martian surface [*Christensen et al.,* 1992; 2001]. The TES instrument is a Michelson Fourier interferometer that collects thermal infrared spectra over 1709 – 202 cm^{-1} with 10 cm^{-1} and 5 cm^{-1} spectral sampling using a 3 x 2 array of detectors. TES also includes a visible/near-infrared bolometer that is sensitive over the 0.3 – 2.9-μm range. At the MGS mapping altitude of ~ 400 km, the TES instrument provides an instantaneous field of view of ~ 3 km, but because the TES image motion compensation is inactive, the down-track spatial resolution is approximately 5-8 km [*Christensen et al.,* 2000; *Bandfield,* 2002]. For a full description of the TES instrument and processing of spectral radiance data into

thermal emission spectra, see *Christensen et al.,* [1992] and *Christensen et al.* [2000].

3.2. Selection of TES spectra

Data used for this study were selected from those collected during the mapping phase of the mission prior to orbit 5317 (ocks 1683-7000, L_s 104° - 352°) because instrumental noise detected in TES spectra became progressively worse beyond this point. A minor spectral feature appears at ~1000 cm^{-1} occasionally from data taken after orbit 5317 that may correlate with spacecraft vibrations [*Bandfield*, 2002]. For this study, we have utilized data sampled at 10 cm^{-1} because this sampling represents >99% of the data collected over this orbit range and is directly comparable to results from previous studies [*Milam et al.,* 2004; 2007, in review]. This subset of the TES database was queried to search for spectra that met criteria specific to the Martian surface and was restricted using various quality parameters to avoid anomalous data. TES spectra were selected from a region centered $\pm$60° of the Martian equator. Higher latitudes correspond to TES data collected at lower surface temperatures, and contain the polar ice caps and geomorphic features suggestive of surface ice. This region encompasses a significant portion of the southern ST1-dominated highlands, the northern ST2-dominated lowlands, and areas covered by considerable surface dust, such as the Tharsis area [see *Bandfield et al.,* 2000]. This area also corresponds to dust- and ice-free regions on Mars demonstrated to have the highest abundance of plagioclase [*Bandfield,* 2002].

The spectra used in this study were also limited to those collected at surface brightness temperatures > 265 K. This constraint allowed us to focus on data with relatively high signal-to-noise ratios (>245 average SNR for 400 to 1300 cm^{-1}). As mentioned in Section 2.3, lower signal-to-noise ratios can potentially affect the accuracy of processing results. Appendix A highlights the potential errors introduced when modeling plagioclase compositions in thermal emission spectra whose signal-to-noise ratios worsen with decreasing surface temperatures (ranging from 140 – 300K). Most plagioclase compositions (to within 1 σ standard deviation) can be modeled with accuracies comparable to previous work (*Milam et al.,* [2004] and Part 3 of this volume) at T > 180-200K (SNR >23-45) in multi-component and multi-phase sand mixtures. However, average reported RMS errors, which are a quantitative measure of the overall spectral fit between measured and modeled spectra, degrade significantly when T < 255K (SNR ~ 200). So our selection of TES spectra > 265 K avoids most potential problems associated with lower signal-to-noise ratios.

Although deconvolutions of noisy multi-component TES (spectral) resolution spectra (at T > 265 K) model with accuracies comparable to previous work, (ΔAn =6, 1 σ standard deviation) it is important to note that anorthite variations in multi-phase mixtures are slightly worse (ΔAn = 10, 1 σ standard deviation). And while these values represent most (1 σ) results, ΔAn values from individual deconvolutions can vary by as much as 14 An and 30 An in multi-component and multi-phase mixtures respectively.

Dusty areas were eliminated by choosing TES spectra with Lambert albedos less

than 0.18. Higher albedo spectra correspond to dusty regions on Mars, where the true spectral signature of a primary surface (e.g. bouldered terrain, bedrock, etc.) can be spectrally masked by a mantle of dust [*Kieffer et al.,* 1973, 1977; *Ruff and Christensen*, 2002]. Because of our selection criteria, the area under study happened to correspond mostly to intermediate thermal inertias [*Mellon et al.,* 2000], regions on Mars dominated most by fine to coarse-grained sand [*Pelkey et al.,* 2001].

3.3. Atmospheric Correction and Unmixing

Atmospheric components were removed from TES spectra in a manner similar to previous studies [*Bandfield et al.*, 2000; *Christensen et al.* 2000; *Bandfield et al.,* 2002] using a linear deconvolution technique [*Ramsey and Christensen*, 1998]. TES spectra were modeled using a spectral endmember library [*Bandfield et al.*, 2000]. This endmember set includes 51 spectral endmembers representing primary igneous minerals common to mafic-intermediate volcanic rocks (including endmembers representing 23 different compositions of plagioclase), and common alteration weathering phases (Table 12), such as carbonates and clays. Hematite, sulfate, and carbonate spectral endmembers were also included due to their previous detection on Mars [e. g. *Christensen et al.,* 1999; *Christensen et al.,* 2004; *Bibring et al.,* 2006]. Four atmospheric spectral endmembers (moderate- and high-opacity dust and small and large particle size water ice cloud endmembers) and a high albedo surface dust spectral endmember [*Bandfield et al.,* 2000] were included to model atmospheric phenomenon and regions with a high surface dust component. A blackbody was also

included to model reduced spectral contrast in areas influenced by smaller grain sizes. Negative endmember percentages were initially allowed in modeled results to produce a linear least squares fit, but were later removed in an iterative fashion until all percentages were positive in order for the values to be geologically meaningful. The remaining modeled endmembers were re-normalized to 100 percent. This is technique that has been used previously and has the potential for eliminating lower endmember percentages from the result, but this rarely occurs [e.g. *Feely and Christensen,* 1999; *Bandfield et al.,* 2000; *Seelos and Arvidson*, 2003; *Rogers and Christensen,* 2005]. Each TES emissivity spectrum was modeled over 1300-825 cm^{-1} and 507-400cm^{-1}. Other channels observed by TES were excluded to eliminate random and systematic noise often observed in TES data and to avoid major CO_2 and H_2O-vapor absorptions. The spectral ranges used encompass all major absorption features in most common minerals (i.e. silicates, carbonates, sulfates, etc.) and are also comparable to previous studies of plagioclase compositions in sand mixtures [*Milam et al.,* 2004; in review] and volcanic rocks [*Hamilton and Christensen,* 2000; *Wyatt et al.,* 2001; *Milam et al.,* 2004;]. Outputs from this process include a modeled spectrum, a list of percentages in which each endmember was modeled, and a root-mean-squared (RMS) error that characterizes the difference between the actual spectrum and the modeled spectrum. Selected modeled spectra were compared to actual spectra to qualitatively ensure a good fit and RMS errors were examined globally to ensure that deconvolutions were providing a good fit. Ninety-nine percent of all RMS errors were less than 0.006 in study regions.

3.4. Plagioclase Feldspar Mapping

A computer algorithm was written in Interface Data Language (IDL) code (Appendix B) to review the output endmember percentages and retrieve only the percentages of plagioclase spectral endmembers used in deconvolutions of each TES spectrum. Plagioclase abundances were renormalized so that the sum of all plagioclase endmember abundances equaled 100%. These renormalized abundances were multiplied by the An content of each endmember (as determined from laboratory measurements [see *Christensen et al.,* 2000 and *Milam et al.,* 2004]) to get an appropriately weighted average plagioclase composition for each TES spectrum. This is the same technique used in previous studies [*Milam et al.,* 2004; 2007, in review]. Because we examined such a large portion of the Martian surface, TES observations were subdivided into scenes according to their geographic coordinates (mostly 10° x 10° regions). For each scene, a new data product was then constructed, with pixel values equal to average plagioclase compositions. In order to minimize potential visual effects that noisy data might introduce and to highlight potential compositional trends by region, each pixel was binned into one of the six fundamental plagioclase compositional ranges: albite (An_{0-10}), oligoclase (An_{10-30}), andesine (An_{30-50}), labradorite (An_{50-70}), bytownite (An_{70-90}), and anorthite (An_{90-100}). Pixels were then color-coded according to each of the plagioclase types. To better visually discern compositionally distinct regions on Mars, images for each plagioclase type for all scenes were mosaicked together in cylindrical projection covering the area $\pm$ 60° of the equator, to produce six plagioclase compositional maps.

4. Results

Deconvolutions resulted in modeled percentages of spectral endmembers similar to globally-averaged ST1 and ST2 spectra and atmospheric components [*Bandfield et al.,* 2000; *Hamilton et al.,* 2001; *Wyatt and McSween,* 2002]. In most cases, plagioclase and pyroxenes were the dominant mineral spectral endmembers, with lesser amounts of glass, sheet silicates, and clays, similar to previously modeled results for Mars [*Bandfield et al.,* 2000, *Hamilton et al.,* 2001, *Wyatt and McSween,* 2002]. RMS errors ranged up to 0.006 in most cases, with an average of 0.004 and occasional (< 1%) errors ranging up to 0.007 and 0.008. Lower RMS errors reflect better fits between actual and modeled spectra.

Plagioclase compositional maps are displayed in Figures 25-30. Map projections are cylindrical and extend $\pm$ 60° of the Martian equator. Gray areas on each lower map depict regions where TES data were either not available, not appropriate for use in this study, or where plagioclase did not model in deconvolutions. Less than 4% of the TES spectra used in this study were modeled as not having plagioclase and were randomly distributed across Mars. Because of our selection process, many of the gray areas largely devoid of TES spectra happened to correspond to regions at low- to mid-latitudes with lower thermal inertias ($\sim <$ 180 J $m^{-2}K^{-1}s^{-1/2}$) [see *Mellon et al.,* 2000; *Jakosky and Mellon*, 2001] and high amounts of dust cover (DCI (Dust Cover Index) < 0.96 per *Ruff and Christensen*, 2002]. Data used in this study show a strong spatial correlation to areas where ST2 is most abundant in the northern lowlands and ST1 is most abundant in the southern

highlands [*Bandfield et al.,* 2000].

Our compositional maps correspond to areas on Mars where abundant (exposed) plagioclase has been mapped in a separate study which also used TES spectra by [*Bandfield,* 2002]. The plagioclase abundance map of *Bandfield et al.* [2002] showed concentrations in the southern highlands and northern lowlands, with particularly high abundances in Syrtis Major, Solis Planum, and Acidalia Planitia. Sizeable regions on Mars (e.g. Tharsis) are devoid of concentrations of plagioclase exposed at the surface, likely due to a high surface dust component [*Ruff and Christensen*, 2002] that obscures the spectral signature of the underlying terrain.

4.1. Percentages of TES Spectra Modeled as Different Plagioclase Compositions

Compositional maps reveal a world with an apparent wide range of plagioclase compositions distributed randomly across the Martian surface (Figures 25-30). Plagioclase compositions ranging from albite (An_{1-10}) to anorthite (up to An_{92}) are modeled as the average compositions for individual TES spectra. A visual comparison of the maps reveals that in spite of the wide range of compositions, most TES spectra model as calcic plagioclase (labradorite and bytownite; An_{50-90}). Labradorite (49% of TES observations studied) and bytownite (25%) are the dominant plagioclase compositions (Table 13, Figure 31) in the Martian crust, with lesser amounts of anorthite or more sodic varieties. Anorthite is the average plagioclase composition in 7% of the TES pixels studied. Anorthite compositions are only modeled to An_{92}, the

anorthite content of our most calcic spectral endmember (Table 12). A Martian crust dominated by labradorite and bytownite is comparable to the most common plagioclase in terrestrial mafic-intermediate volcanic rocks, which dominate the Earth's crust. ST1 has a higher percentage of labradorite+bytownite (74%) compared to the global average (62%), while a lower percentage of ST2 (54%) emissivity spectra model as these two plagioclases. ST2 spectra also model higher percentages of more sodic varieties of plagioclase (albite – andesine) than ST1 or the global average.

4.2. Global Distribution of Plagioclase Compositions

The average global plagioclase composition for the portion of the Martian surface analyzed is An_{61} (labradorite) (Table 14). Averages for ST1 and ST2-dominated surfaces analyzed are An_{62} and An_{59} respectively, making them statistically indistinguishable in plagioclase composition. These values are comparable to derived plagioclase compositions [*Milam et al.,* 2004] from the model results of *Bandfield et al.* [2000] for averaged ST1 and ST2 spectra from Syrtis and Acidalia respectively. Calculations of average plagioclase compositions in the northern lowlands and southern highlands along the planetary dichotomy reveal no significant variations in composition (Table 14).

4.3. Regional Distributions of Plagioclase Compositions

Table 15 shows plagioclase compositional variation in selected regions on Mars. As with global ST1 and ST2 averages, plagioclase regional compositions,

taken as a whole, are only slightly more sodic in ST2 than in ST1. Again, it is important to note, that average plagioclase compositions presented are indistinguishable, based on the reported accuracy of the technique [*Milam et al.,* 2004; in review]. Variations within each surface type by region are likewise minimal. For example, plagioclase compositions in Syrtis Major are indistinguishable from those of Terra Sirenum. There are few regional-scale variations that show distinguishable variations from those of average ST1 and ST2 surface types.

4.4. Local Variations in Plagioclase Composition

A comparison of plagioclase compositional maps shows that spatial trends in localized variations in plagioclase compositions are difficult to discern. The most notable exception to this is Syrtis Major. Syrtis Major is a Late Noachian/Early Hesperian-age surface [*Hartman and Neukum* 2001; *Hiesinger and Head*, 2002] volcanic edifice to the west of Isidis Basin. Syrtis is the type locale for ST1 material, but variations in olivine abundance and composition of individual flows in Nili Patera (a caldera) have been detected in TES and THEMIS data [*Ruff and Hamilton*, 2001; *Christensen et al.,* 2005]. Our plagioclase compositional maps reveal a noticeable paucity of TES spectra that model as sodic compositions (albite and oligoclase) in southern and southeastern Syrtis Major (Figures 25 and 3). Closer examination of the Syrtis edifice supports this (Figure 32). Regional maps of average plagioclase composition show a subtle trend from NW to SE of increasingly calcic plagioclase and noticeably higher percentages of TES spectra modeling as calcium-rich plagioclase.

The terrain to the northwest of Syrtis, taken as a whole, is more sodic in composition (An_{61}) than Syrtis itself (An_{65}). The calcic compositions approximately coincide with Syrtis Major Planitia itself [*Scott and Carr*, 1978]. This might indicate that a compositional boundary exists between the Noachian-aged materials to the northwest and Late Noachian-Early Hesperian-aged volcanic terrain of Syrtis. However, average plagioclase compositions of these two areas are just within the margin of error (6 An, 1 σ standard deviation) for discriminating between plagioclase compositions [*Milam et al.,* 2004; in review], making this interpretation suspect.

4.5. "Ground-Truth" Verification of Technique

Geochemical data from several landed missions (Vikings 1 and 2, Mars Pathfinder, Spirit, and Opportunity) present the potential for providing a means of "ground-truth" for orbital derivations of plagioclase compositions. However, all but one of the lander/rover missions were deployed in areas where surface materials have a higher albedo (>0.18) or lower DCI value (< 0.96) than areas covered by our plagioclase compositional maps. Only the Opportunity landing site (1.95° S, 354.47°E) in Meridiani Planum has appropriate TES coverage with which to compare with ground data. Twenty TES emission spectra within a 30 km radius (mostly to the N and E) of Opportunity's Eagle Crater landing site were averaged and unmixed according to the methods above. These numbers of TES spectra were used to minimize potential effects of lower signal-to-noise ratios that can occur within a given TES observation. Figure 33 shows the average actual vs. the modeled TES thermal

emission spectrum. From this, an average derived plagioclase composition for this part of Meridiani Planum was calculated as An_{68}. For comparison, we averaged eight Alpha Particle X-ray Spectrometer analyses (sols 0 – 166) of the undisturbed basaltic sand that fills the floor of Eagle Crater and dominates the surrounding plains of Meridiani [*Soderblom et al.,* 2004]. Unlike the sulfate-rich outcrops exposed in limited areas of the landing site, basaltic sand (with hematite spherules) would be expected to provide the largest spectral contribution to TES spectra. These values, in addition to the appropriate Mössbauer Fe^{3+}/Fe_{Total} ratio for Meridiani basaltic soil [*Klingelhöfer et al.,* 2004], were used to calculate CIPW-NORM values, which resulted in an average APXS-derived plagioclase composition of An_{63}.

For an additional comparison, we derived an average plagioclase composition from an averaged Mini-TES spectrum representative of the basaltic, hematite-rich sands at Meridiani between Fram and Endurance craters. This Mini-TES spectrum is an average of 90 spectra from sol 90 (from *Christensen et al*. [2004]) and is representative of the plains in close proximity to the Eagle Crater landing site. Downwelling radiance, common in Mini-TES spectra, was removed according to the methods outlined in *Christensen et al*. [2004]. Modal mineralogy for this spectrum was derived by the same deconvolution technique [*Ramsey and Christensen*, 1998] used to unmix TES spectra. The same spectral library (Table 12) without TES-derived atmospheric endmembers was used to deconvolve the Meridiani spectrum over 1300-400 cm^{-1} and excluding the region between 825-507 cm^{-1} where a prominent atmospheric CO_2 absorption occurs. This excluded range is the same as that

excluded from TES spectra (as opposed to the region excluded from most Mini-TES observations, 739-589 cm^{-1}) in order to make a direct comparison with orbital observations . Results from this deconvolution are shown in Figure 34. The average plagioclase composition derived for the basaltic sands from Mini-TES data is An_{58}.

TES, APXS, and Mini-TES derived average plagioclase are very similar in composition, differing by only <10 An in composition. It is also interesting to note that our TES-derived abundance (23%) compares well with the APXS-derived normative plagioclase abundance (23 wt%/ 30 vol.%) and that estimated from deconvolution of Mini-TES data for basaltic sand (20% and 32% from *Christensen et al.,* 2004 and this study respectively]. Comparisons of modeled plagioclase abundances are mostly within the margin or error of modeling average mineral abundances using linear deconvolution [*Hamilton et al.,* 1997; *Wyatt et al.,* 2001].

Examination at a smaller scale reveals the inherent variability in average plagioclase compositions as derived on the scale of individual TES spectra. Of the 20 spectra used to produce the average landing site spectrum above, average plagioclase compositions ranged from An_{1-92}. Careful examination of emission spectra has not uncovered any anomalous absorption features or instances of relatively noisy spectra that are being inadequately modeled by the spectral deconvolution algorithm. Abundances of modeled atmospheric, surface dust, clay mineral, or sulfate endmembers showed no correlation to specific plagioclase compositions. RMS errors did not correlate to specific ranges of plagioclase compositions. There are no morphologic, textural, or geochemical observations

made by Opportunity that suggest any significant plagioclase compositional variability in the basaltic sands of Meridiani. Thus, at least on the scale of an single TES observation, it is quite unlikely that significant variation in plagioclase compositions is present. Noise within single TES observations may result in this variability. This assessment points to the necessity of averaging enough TES observations to reduce noise inherent to the TES data set in order to obtain a reasonable compositional estimate (See Section 5.3.3 below for a discussion).

5. Discussion

5.1. Global Patterns in Plagioclase Composition Distribution

Our plagioclase compositional maps provide some insight into geologic variations in the Martian crust. One would suspect that, for multiple terrains with a variety of morphologies and geologic ages, plagioclase compositions might vary because of magmatic fractionation and varying degrees of alteration or weathering. It is also reasonable to expect that compositional variability might correspond to specific regions or geologic units. Examination of plagioclase maps (Figures 25-30), however, reveals that the Martian crust is relatively homogeneous overall, with the majority of TES-derived plagioclase compositions modeling as labradorite (An_{50-70}) and bytownite (An_{70-90}) (Table 13). This range of plagioclase compositions is common in terrestrial mafic-intermediate rocks and, considered with mineralogies modeled in deconvolutions, is consistent with the interpretation that Mars is a world dominated by basalt and/or andesite [*Christensen et al.,* 2000; *Bandfield et al.,* 2001; *Hamilton et*

al., 2001; *Wyatt and McSween*, 2002].

The average global plagioclase compositions for ST1 and ST2 (An_{62} and An_{59} respectively; Table 14) are consistent with those modeled in standard ST1 and ST2 emissivity spectra [*Bandfield et al.,* 2000; *Milam et al.,* 2004]. Although average ST1 appears to be more calcic than ST2, the difference in their modeled average compositions is within the *minimal* margin of error of the technique [*Milam et al.,* 2004; 2007, in review]. Thus it is plausible that average ST1 and ST2 plagioclase compositions are identical.

These global similarities could represent multiple geologic units with minimal variation in plagioclase compositions (mostly labradorite). It is also plausible that average compositions are reflective of a relatively homogeneous surface layer derived from and superposed on a heterogeneous crust. On a world whose surface has been continually modified by active geologic processes, homogenization of the crust (as highlighted by the dominance of labradorite) could be explained by aeolian, fluvial, or impact re-distribution of materials [*Greeley et al.*, 1992, *Strom et al.*, 1992; *Malin and Edgett*, 2001]. In fact, low to moderate albedo material is often found in the form of aeolian deposits [*Cutts and Smith*, 1973, *Thomas and Weitz*, 1989]. Impacts eject material onto surrounding terrain and into the Martian atmosphere, where it would be re-distributed over larger regions. If impacts were the dominant factor for the re-distribution and homogenization of materials, then older terrains on

Mars might have experienced a higher degree of homogenization than younger geologic units. Thus, younger, volcanically-emplaced units might be expected to have more plagioclase variation by geologic unit if magmatic zoning or fractionation were the primary igneous processes at work on Mars. Unfortunately, some of the youngest volcanic terrain on Mars, such as the Tharsis Montes area, is spectrally-masked by surface dust, limiting regional comparisons [*Ruff and Christensen*, 2002]. Global comparisons of plagioclase compositions between the Noachian highlands and the predominantly Amazonian lowlands and specific regions on Mars (Table 15) do not show compositional heterogeneity within the error of technique.

5.2. Localized Investigations and Error Analysis

5.2.1. Plagioclase Heterogeneity in the Martian Crust?

While this work has revealed indistinguishable global-scale, and regional-scale variations in the range of plagioclase compositions, it was also intended to examine compositional variations on a much smaller scale (near that of individual TES observations (~ 3 x 8 km pixel or spatial footprint), that might, for instance, identify magmatically-evolved igneous rocks or a locale where hydrothermal fluids altered local bedrock. Figures 25-30 show a range of randomly-distributed plagioclase compositions everywhere on Mars (from albite to anorthite). Are plagioclase compositions in the Martian crust really this locally

heterogeneous? Plagioclase in Martian meteorites, rocks, and soils (Figure 35) make it clear that a variety of plagioclase compositions do occur, ranging from oligoclase (An_{13}) to bytownite (An_{77}). This variation, however, occurs on the scale of a single grain or sample and is thus not directly analogous to orbital-derived compositions. TES observations cover an approximately 3 x 8 km area on Mars. The plagioclase composition modeled from each TES spectrum represents the average of that area. So the variation that occurs on this scale would be expected to correlate with specific geologic (i.e. age) terrains or units. Plagioclase compositional maps, however, show a labradorite-rich Martian crust (with subtle variations) with an apparently random spatial distribution of most other plagioclase compositions. This random distribution does not correlate with specific terrains and can occur within a single orbit with near identical observational conditions from one TES spectrum to the next. Adjacent TES spectra in a single geologic terrain can produce different average plagioclase compositions as can overlapping TES observations from multiple orbits.

At this scale, however, the wide range of compositions and the random spatial distribution of less common plagioclase compositions (e.g. albite, oligoclase, andesine, and anorthite) suggest that the "noise" present in our results precludes an in-depth examination of most localized geologic features. Previous studies of global mineral or endmember abundances binned TES spectra in specific latitude-longitude

bins to avoid random and instrumental noise that is sometime present in emissivity spectra [e. g. *Bandfield,* 2002]. The noise in our results is apparent in our plagioclase compositional maps where co-registered TES spectra are modeled with widely different (up to 50 An) average plagioclase compositions. There is even variability in modeled average plagioclase compositions from adjacent TES spectra collected in a single orbit over a terrain of near-uniform elevation (Section 4.5. highlights an example). Likewise, there appear to be no correlated trends in derived plagioclase compositions within specific TES orbits. This suggests that such wide variation is not likely explained by atmospheric phenomenon, such as the presence of water-ice clouds, which would probably be confined to a single orbit over a given area.

5.2.2. Possible Errors Resulting from Selection of TES Spectra

To assess whether our procedures for selecting TES emissivity spectra resulted in the inclusion of data that systematically affected derivations of average plagioclase compositions, we compared variations in our modeled average plagioclase compositions to a variety of surface and atmospheric phenomenon. In selecting TES data, we conservatively selected TES spectra corresponding to avoid areas where surface dust and potential signal-to-noise effects might pose a problem. TES spectra influenced by significant proportions of atmospheric or surface dust or lower signal-to-noise ratios could induce additional errors in deriving average plagioclase compositions. We sampled several terrains on Mars and examined them for systematic variations in anorthite content, RMS errors, and variations of both thereof to

see if our modeling may have been affected by fine grain sizes (i.e. surface dust), atmospheric phenomenon, and temperature differences. Figure 36 shows a representative example of this for a relatively dust-free area between 0-10º N and 275-285º W on Mars in southeastern Syrtis Major (geologic unit Hprg-Ridged Plains Material from [*Scott and Carr*, 1978]). Ranges in albedo, the percentage of modeled atmospheric endmembers, modeled surface dust, DCI values, and temperature are compared to variations in modeled anorthite variations and RMS errors from deconvolution results. TES spectra which contain a finer-grained component would be expected to have higher albedo values, higher percentages of modeled surface dust, and lower DCI values. If our modeling were influenced by such a fine-grained component, variation in modeled anorthite content or RMS errors might be expected to show a positive correlation; however, this is not the case (Figures 36a-c). Thus, our selection criteria for TES spectra allowed us to avoid the potential effects of modeling dustier areas on Mars. Modeling spectra with relatively high percentages of atmospheric endmembers showed no identifiable trends in anorthite or RMS error variations. An example of this is shown in Figure 18d. Thus, atmosphere also appeared to have minimal influence on our ability to model average plagioclase compositions.

5.2.3. Potential Error Due to Signal-to-Noise Effects

Although our study purposely avoided TES observations collected at temperatures <265 K, an assessment was made to determine if derived plagioclase

compositions correlated with variations at higher temperatures, i.e. lower signal-to-noise (SNR) ratios (Appendix A). In some instances, such as is shown for Syrtis Major, variations in modeled plagioclase compositions did decrease with at lower temperatures (Figure 36e). This was variable, however, and In most cases the overall spectral fit did not worsen at lower temperatures. Trends in RMS error show this (Figure 36e). It is important, however, to note that even at temperatures > 265 K (SNR > 245), modeled plagioclase compositions typically vary by as much as 10 An and can vary by as much as 30 An in spectra that contain some noise (see Appendix A for a discussion).

5.2.4. Possible Effects of Shock

One way in which errors may have been introduced in deconvolutions of TES spectra relates to the impact history of the Martian surface. Like other solid bodies in the solar system, Mars has undergone extensive collisions that have resulted in a heavily cratered surface [for an overview see *Strom et al.* 1992]. The oldest, Noachian-aged, terrains on Mars have a high concentration of impact craters. Even the youngest regions on Mars appear to overlie terrain that has been heavily-cratered [*Frey et al.,* 2002]. It is thus reasonable to assume that most crustal materials on Mars have experienced varying degrees of shock metamorphism. Shock metamorphic features in Martian meteorites [*Nyquist et al.,* 2001] support this, as do shocked mineral phases, such as maskelynite [e.g. *Easton and Elliott*, 1977; *McSween*, 1994; *McSween and Treiman,* 1998]. Maskelynite is the glass form of plagioclase produced

at high shock pressures (> 29 GPa) [*Smith and Hervig*, 1979; *Stöffler et al.*, 1986] found not only in Martian (and other) meteorites, but also terrestrial impact craters [e.g. *Bunch et al.*, 1967; *Nayak*, 1993].

Thermal infrared spectral features in shocked plagioclase change with increasing shock pressure, as demonstrated in laboratory studies by *Johnson et al.* [2002, 2003]. Their deconvolution modeling of shocked albite (An_2) and shocked bytownite (An_{75}) spectra indicated that: (1) shocked albite could be modeled with low RMS errors using unshocked spectral libraries, likely due to the shared spectral similarities between shocked albite and clay minerals, and (2) that shocked bytownite could be modeled accurately to shock pressures ~ 20 – 25 GPa, above which the bytownite spectral shape changes significantly. Little is known about the spectral behavior of shocked plagioclase of other compositions. From these limited studies, however, it is possible that in highly shocked areas, such as might apply to the Noachian-aged highlands on Mars, shocked plagioclase spectral endmembers are required to better derive modal mineralogies [*Wright et al.* 2004; *Johnson and Staid*, 2005], but this suggestion is presently ambiguous [*Johnson et al.*, 2006]. These previous studies did not, however, address our ability to model plagioclase compositions.

To examine this, we deconvolved shocked albite and bytownite emissivity spectra (from *Johnson et al.* [2002; 2003]) with the unshocked

plagioclase (Table 12) and blackbody from the spectral library used in our global deconvolutions. A detailed description our methods and results is provided in Appendix C. Our results (Table 16) show that shocked, coarse calcic plagioclase (bytownite) can be modeled with similar accuracy to that of previous studies [*Milam et al.*, 2004; 2007], while results for shocked albite were worse. Because provinces with significant concentrations of sodic plagioclase have not been detected, it is not likely that the apparently random compositional variation in our TES data relates to shocked albite. This investigation does, however, suggest that shock metamorphism of crustal materials has little effect on our ability to model calcium-rich plagioclase compositions. For a full discussion, see Appendix C.

5.2.5. Possible Effects of Grain Size

Previous studies (e.g. *Moersch and Christensen*, 1995; *Mustard and* Hayes, 1997; Hamilton *et al.* 1999) have demonstrated significant degradation in modeling accuracy because of scattering effects as the grain size in unconsolidated samples approaches the wavelengths of the incident energy (typically < 60 μm). A large proportion of the surface is dominated by fine-grained material [*Kieffer et al.*, 1973, 1977; *Ruff and Christensen*, 2002]. Most of the finer particle sizes (i.e. surface dust) are concentrated in broad regions that spectrally mask underlying bedrock spectral signatures, such as the Tharsis area. However, we know from

lander/rover observations that even relatively dust-free areas have significant amounts of smaller grain size fractions and dust coatings. Because the size of the spatial footprint of a TES observation (~ 3 x 8 km) is quite large, it is possible, if not likely, that many our TES spectra were influenced by contributions by fine grain size fractions. For regions where this constituent comprises a significant proportion of the area under observation, our ability to model average plagioclase compositions would be degraded accordingly. The level of degradation is unclear. Ongoing work in plagioclase mixtures down to very fine-grain sand (~63 μm) sizes [*unpublished data*] indicates that compositions can be modeled with an accuracy comparable to that of coarse sand (500-850μm). Additional work with silt-clay size particulate mixtures and multi-grain size mixtures is the subject of future study.

Deconvolutions of shocked powders do provide some insight (Table 16). Our example above also examined spectra from "powders" of shocked albite and bytownite from *Johnson et al.* [2003] as a precursory demonstration of the effects of reduced grain size on our ability to derive plagioclase compositions. As shown in Table 16, average plagioclase compositions could not be modeled as well for samples with smaller grain sizes (< 30μm). Deconvolutions resulted in maximum ΔAn = 65 and 38 and ΔAn_{stdev} = 18 and 10 (for bytownite and albite respectively). Such variations in actual and modeled compositions in TES data would result in

misrepresentation of plagioclase in compositional maps. While we did examine areas of intermediate-low thermal inertia, low albedo, and low dust cover, it is still quite likely that many TES spectra are still influenced by a fine-grained component. This may partially account for the extreme pixel to pixel variation in modeled plagioclase compositions and is likely more of an influence than shock metamorphism.

Preliminary analysis of nine 10˚ x 10˚ regions on Mars indicates that some error may have been introduced from a fine-grained component present in some TES spectra. TES thermal inertia (TI) values < 420 J m^{-1} $s^{-1/2}$ K^{-1} decrease with decreasing grain size [*Pelkey et al.*, 2001]. Figure 37 shows that the 1σ standard deviations of An values are larger for lower ranges of thermal inertia (i.e. ranges corresponding to smaller grain sizes). This, coupled with laboratory studies of powdered plagioclase, suggests that fine-grained material may also account for large variations in plagioclase composition across Mars.

5.2.6. Localized Investigations Using Individual TES Observations

The dramatic range in plagioclase variations that can occur at the local scale may be explained by random noise in TES spectra even at higher temperatures and a fine-grained component that is likely present in various proportions across Mars. Atmospheric correction, systematic calibration, and other processing uncertainties also have the potential to

introduce additional errors [*Bandfield*, pers. comm., 2006]. These errors make interpretation of extreme compositional variations in local geology problematic.

6. Summary

The first plagioclase compositional maps of the Martian surface have provided new geologic insight into the evolution of the Martian crust. Maps show that:

(1) Mars is a planet dominated by calcic plagioclase (primarily labradorite and bytownite, with an average composition of An_{61});

(2) Surface types 1 and 2 are indistinguishable in terms of average plagioclase compositions (An_{62} and An_{59} respectively), but do show variations in the percentages of TES spectra that model as different plagioclase compositions (ST2 is more variable);

(3) the similarity in average plagioclase compositions between ST1 and ST2 may be explained by either a lack of variability in modeled plagioclase compositions during fractional crystallization of Martian magmas or aeolian, fluvial, or impact redistribution of primary igneous material; this redistribution likely resulted in a relatively homogenized (with respect to plagioclase compositions) surface layer.

Compositional variability at the scale of individual or overlapping TES

observations makes localized geologic investigations on this scale problematic. This is most likely results from grain size and signal-to-noise effects, even in the conservatively screened TES thermal emission spectra used in this study.

Acknowledgments

I thank the National Aeronautics and Space Administration Graduate Student Researchers Program (NASA-GSRP) for financially supporting this research. Jeff Johnson provided emissivity spectra of shocked plagioclase for this study.

References

Alt, J. C., and R. Emmermann (1985), Geochemistry of hydrothermally altered basalts: Deep Sea Drilling Project Hole 504B, Leg 83, *Initial Rep. Deep Sea Drill. Proj., 83,* 249-262.

Alt, J. C., C. Lavern, D. A. Vanko, P. Tartarotti, D. A. H. Teagle, W. Bach, E. Zuleger, J. Erzinger, J. Honnorez, P. A. Pezard, K. Becker, M. H. Salisbury, and R. H. Wilkens (1996), Hydrothermal alteration of a section of upper oceanic crust in the eastern equatorial Pacific: A synthesis of results from site 504 (DSDP 69, 70, and 83, and ODP 111, 137, 140, and 148), *Proc. Ocean Drilling Prog. Scientific Results, 148,* 417-434.

Arslan, M., S. Kadir, and E. Abdioğlu and H. Kolayli (2006), Origin and formation of kaolin minerals in saprolite of Tertiary alkaline volcanic rocks, Eastern Pontides, NE Turkey, Clay Minerals, 41, 597-617, doi: 10.1180/0009855064120208.

Baccar, M. B., B. Fritz, and B. Madé (1993), Diagenetic albitization of K-feldspar and plagioclase in sandstone reservoirs: Thermodynamic and kinetic modeling, *J. Sedimentary Petrology, 63*, 1100 – 1109.

Baker, V. R., and D. J. Milton (1974), Erosion by catastrophic floods on Mars and Earth, *Icarus, 23,* 27-41.

Baker, V. R., M. H. Carr, V. C. Gulick, C. R. Williams, and M. S. Marley (1992), Channels and valley networks, *in Mars,* University of Arizona Press, Tucson, 493-522.

Bandfield, J. L. (2002), Global mineral distributions on Mars, *J. Geophys. Res., 107*, doi: 10.1029/2001JE001510.

Bandfield, J. L., V. E. Hamilton, and P. R. Christensen (2000), A global view of martian surface compositions from MGS-TES, Science, 287, 1626-1630.

Bandfield, J. L., V. E. Hamilton, P. R. Christensen, and H. Y. McSween, Jr. (2004), Identification of quartzofeldspathic materials on Mars, *J. Geophys. Res., 109*, doi:10.1029/2004JE002290.

Bibring, J.P., Y. Langevin, J. F. Mustard, F. Poulet, R. Arvidson, A. Gendrin, B. Gondet, N. Mangold, P. Pinet, F. Forget, and the OMEGA team (2006), Global mineralogical and aqueous Mars history derived from OMEGA/Mars Express data, *Science, 312,* 400 – 404.

Blum, A. E. and L. L. Stillings (1995), Feldspar dissolution kinetics, *In* A. F. White and S. L. Brantley eds., *Chemical Weathering Rates of Silicate Minerals, 31,* Mineralogical Society of America, 291-351.

Boles, J. R. (1982), Active albitization of plagioclase in Gulf Coast Tertiary, *Am. J. of Science, 282*, 165 – 180.

Bunch, T.E. Cohen, A.J. and Dence, M.R. (1967), Natural terrestrial maskelynite. *American Mineralogist, 52*, pp. 244-253.

Cann, J. R. (1969), Spilites from the Carlsberg Ridge, Indian Ocean, *J. of Petrology, 10,* 1-19.

Carr, M. H. (1984), Mars, In *The Geology of the Terrestrial Planets*, NASA Special Publication 469, 207-263.

Carr, M. H. (1996), *Water on Mars*, Oxford University Press, London.
Carr, M. H., L. S. Crumpler, J. A. Cutts, R. Greeley, J. E. Guest, and H. Masursky (1977), Martian impact craters and emplacement of ejecta by surface flow, *J. Geophys. Res., 82*, 4055-4065.
Carr, M. H., and J. W. Head III (2003), Oceans on Mars: An assessment of the observational evidence and possible fate, *J. Geophys. Res., 108*, doi:10.1029/2002JE001963.
Christensen, P. R., and H. J. Moore (1992), The Martian surface layer, in *Mars,* ed. By H. H. Kieffer et al., University of Arizona Press, 686-729.
Christensen, P. R., D. L. Anderson, S. C. Chase, R. N. Clark, H. H. Kieffer, M. C. Malin, J. C. Pearl, and J. Carpenter (1992), Thermal Emission Spectrometer experiment: Mars Observer mission, *J. Geophys. Res., 97*, 7719-7734.
Christensen, P. R., J. L. Bandfield, M. D. Smith, V. E. Hamilton, and R. N. Clark (2000a), Identification of a basaltic component on the martian surface from Thermal Emission Spectrometer data, *J. Geophys. Res.*, 105, E4, 9623-9642.
Christensen, P. R., J. L. Bandfield, R. N. Clark, K. S. Edgett, V. E. Hamilton, T. Hoefen, H. H. Kieffer, R. O. Kuzmin, M. D. Lane, M. C. Malin, R. V. Morris, J. C. Pearl, R. Pearson, T. L. Roush, S. W. Ruff, and M. D. Smith (2000b), Detection of crystalline hematite mineralization on Mars by the Thermal Emission Spectrometer: Evidence for near-surface water, *J. Geophys. Res., 105,* 9623 – 9642.
Christensen, P. R., J. L. Bandfield, V. E. Hamilton, D. A. Howard, M. D. Lane, J. L. Piatek, S. W. Ruff, and W. L. Stefanov (2000c), A thermal emission spectral library of rock-forming minerals, *J. Geophys. Res., 105*, E4, 9735 – 9739.
Christensen, P. R., J. L. Bandfield, V. E. Hamilton, S. W. Ruff, H. H. Kieffer, T. N. Titus, M. C. Malin, R. V. Morris, M. D. Lane, R. L. Clark, B. M. Jakosky, M. T. Mellon, J. C. Pearl, B. J. Conrath, M. D. Smith, R. T. Clancy, R. O. Kuzmin, T. Roush, G. L. Mehall, N. Gorelick, K. Bender, K. Murray, S. Dason, E. Greene, S. Silverman, and M. Greenfield (2001), Mars Global Surveyor Thermal Emission Spectrometer experiment: Investigation description and surface science results, *J. Geophys. Res., 106*, 23,823-23,871.
Christensen, P. R., J. L. Bandfield, J. F. Bell III, N. Gorelick, V. E. Hamilton, A. Ivanov, B. M. Jakosky, H. H. Kieffer, M. D. Lane, M. C. Malin, T. McConnochie, A. S. McEwen, H. Y. McSween, Jr., G. L. Mehall, J. E. Moersch, K. H. Nealson, J. W. Rice Jr., M. I. Richardson, S. W. Ruff, M. D. Smith, T. N. Titus, M. B. Wyatt (2003), Morphology and composition of the surface of Mars: Mars Odyssey THEMIS results, *Science, 300*, 2056-2061.
Christensen, P. R., M. B. Wyatt, T. D. Glotch, A. D. Rogers, S. Anwar, R. E. Arvidson, J. L. Bandfield, D. L. Blaney, C. Budney, W. M. Calvin, A. Fallacaro, R. L. Fergason, N. Gorelick, T. G. Graff, V. E. Hamilton, A. G. Hayes, J. R. Johnson, A. T. Knudson, H. Y. McSween, Jr., G. L. Mehall, L. K. Mehall, J. E. Moersch, R. V. Morris, M. D. Smith, S. W. Squyres, S. W. Ruff, M. J. Wolff (2004), Mineralogy at Meridiani Planum from the Mini-TES experiment on the Opportunity rover, *Science, 306,* 1733 – 1739.
Christensen, P. R., H. Y. McSween, Jr., J. L. Bandfield, S. W. Ruff, A. D. Rogers, V. E.

Hamilton, N. Gorelick, M. B. Wyatt, B. M. Jakosky, H. H. Kieffer, M. C. Malin, and J. E. Moersch (2005), Evidence for magmatic evolution and diversity on Mars from infrared observations, *Nature,* doi:10.1038/nature03639.

Coleman, N. M. (2003), Aqueous flows carved the outflow channels on Mars, *J. Geophys. Res., 108*, doi:10.1029/2002JE001940.

Corliss, J. B., J. A. Baross, and S. E. Hoffman (1981), An hypothesis concerning the relationship between submarine hot springs and the origin of life on Earth, in *Twenty-sixth International Geological Congress: Colloquium C4, Geology of Oceans* (X. Le-Pichon, J. Debyser, F. Vine eds.) Gauthier-Villars, Paris, France.

Cutts, J. A., and R. S. U. Smith (1973), Eolian deposits and dunes on Mars, *J. Geophys. Res., 73*, 4139-4154.

Deer, W. A., R. A. Howie, and J. Zussman (1997), An introduction to the rock-forming minerals, Addison Wesley Longman Ltd.

Easton, A. J. and C. J. Elliott (1977), Analysis of some meteorites from the British Museum (Natural History) collection, *Meteoritics, 12,* 409-416.

Fagents, S. A., K. Pace, and R. Greeley (2001), Origin of small volcanic cones on Mars, *LPSC XXXIII* (CD-ROM), Lunar & Planetary Inst., Houston, TX, abstract #1594.

Farmer, J. D. (1996), Hydrothermal systems on Mars: an assessment of present evidence, in *Evolution of Hydrothermal Ecosystems on Earth (and Mars?)*, 273-299, John Wiley, New York.

Farmer, J. (1998), Thermophiles, early biosphere evolution, and the origin of life on Earth: Implications for the exobiological exploration of Mars, *J. Geophys. Res.*, *103*, E12, 28,457-28,461.

Farmer, J. D., and D. J. Des Marais (1999), Exploring for a record of ancient martian life, *J. Geophys. Res.*, *104*(E11), 26977-26995.

Farrand, W. H., L. R. Gaddis, and S. Blundell (2001), Possible hydrovolcanic landforms observed in MOC NA imagery: A preliminary survey, *LPSC XXXII* (CD-ROM), Lunar & Planetary Inst., Houston, Texas, #1664.

Feely, K. C., and P. R. Christensen (1999), Quantitative compositional analysis using thermal emission spectroscopy: Application to igneous and metamorphic rocks, *J. Geophys. Res., 104,* 24,195 – 24,210.

Feldman, W. C., W. V. Boynton, R. L. Tokar, T. H. Prettyman, O. Gasnault, S. W. Squyres, R. C. Elphic, D. J. Lawrence, S. L. Lawson, S. Maurice, G. W. McKinney, K. R. Moore, and R. C. Reedy (2002), Global distribution of neutrons from Mars: Results from Mars Odyssey, *Science, 297*, 75-78.

Frey, H., J. H. Roark, K. M. Shockey, E. L. Frey, and S. E. H. Sakimoto (2002), Ancient lowlands on Mars, *Geophys. Res. Lett. 29,* doi:10.1029/2001GL013832.

Greeley, R. G., N. Lancaster, S. Lee, and P. Thomas (1992), Martian aeolian processes, sediments, and feature, *in Mars,* University of Arizona Press, Tucson.

Gulick, V. C. (1998), Magmatic intrusions and a hydrothermal origin for fluvial valleys on Mars, *J. Geophys. Res., 103*, E8, 19365-19387.

Hamilton, V. E. (1999), The effect of particle size on rock spectra in the thermal infrared: Implications for TES data analysis, *Lunar Planet. Sci.* [CD-ROM], *XXX*,

Abstract 2001.
Hamilton, V. E., and P. R. Christensen (2000), Determining the modal mineralogy of mafic and ultramafic igneous rocks using thermal emission spectroscopy, *J. Geophys. Res., 105*, 9717 – 9733.
Hamilton, V. E., P. R. Christensen, and H. Y. McSween, Jr. (1997), Determination of Martian meteorite lithologies and mineralogies using vibrational spectroscopy, *J. Geophys. Res., 102,* 25,593 – 25,603.
Hamilton, V. E., M. B. Wyatt, H. Y. McSween, Jr., and P. R. Christensen (2001), Analysis of terrestrial and martian volcanic compositions using thermal emission spectroscopy: 2. Application of martian surface spectra from the Mars Global Surveyor Thermal Emission Spectrometer, *J. Geophys. Res., 106*, 14733-14746.
Hamilton, V. E., P. R. Christensen, H. Y. McSween, Jr., and J. L. Bandfield (2003), Searching for the source regions of Martian meteorites using MGS TES: Integrating Martian meteorites into the global distribution of igneous materials on Mars, *Meteoritics & Planetary Sci., 38*, 871-885.
Hardie, L. A. (1983), Origin of $CaCl_2$ brines by basalt-seawater interaction: Insights provided by some of simple mass balance calculations, *Contrib. Mineral. Petrol., 82(2–3)*, 205– 213.
Hartmann, W. K., and D. C. Berman (2000), Elysium Planitia lava flows: Crater count chronology and geological implications, *J. Geophys. Res., 105*, 6, 15011-15025.
Hartmann, W. K., and G. Neukum (2001), Cratering chronology and the evolution of Mars, *Space Science Reviews, 96*, 165-194.
Hartmann, W. K., M. Malin, A. McEwen, M. Carr, L. Soderblom, P. Thomas, E. Danielson, P. James, and J. Veverka (1999), Evidence for recent volcanism on Mars from crater counts, *Nature, 397,* 586-589.
Hiesinger, H. and J. W. Head III (2002), Syrtis Major, Mars: Results from Mars Global Surveyor data, *LPSC XXXIII*, abstract #1063 (CD-ROM).
Hoefen, T. M. R. N. Clark, J. L. Bandfield, M. D. Smith, J. C. Pearl, P. R. Christensen (2002), Discovery of olivine in the Nili Fossae Region of Mars, *Science, 302,* 627-630.
Hunter, A. G., P. D. Kempton, and P. Greenwood (1999), Low-temperature fluid-rock interaction-an isotopic and mineralogical perspective of upper crustal evolution, eastern flank of the Juan de Fuca Ridge (JdFR), ODP Leg 168, *Chem. Geology, 155,* 3-28.
Hurowitz, J. A., S. M. McLennan, D. H. Lindsley, M. A. A. Schoonen (2005), Experimental epithermal alteration of synthetic Los Angeles meteorite: Implications for the origin of Martian soils and identification of hydrothermal sites on Mars, *J. Geophys. Res., 110,* doi:10.1029/2004JE002391.
Hurowitz, J. A., S. M. McLennan, N. J. Tosca, R. E. Arvidson, J. R. Michalski, D. W. Ming, C. Schröder, and S. W. Squyres (2006), In situ and experimental evidence for acidic weathering of rocks and soils on Mars, *J. Geophys. Res., 111,* doi:10.1029/2005JE002515.
Iiishi, K., T. Tomisaka, T. Kato, and Y. Umegaki (1971), Isomorphous substitution and infrared and far infrared spectra of the feldspar group, *Neues Jahrb. Mineral., 115,*

98-119.
Jakosky, B. M. (1986), On the thermal properties of Martian fines, *Icarus, 66*, 117-124.
Jakosky, B. M., and M. T. Mellon (2001), High-resolution thermal inertia mapping of Mars: Sites of exobiological interest, *J. Geophys. Res., 106*, 23887-23907.
Jeong, G. Y. (1998), Formation of vermicular kaolinite from halloysite aggregates in the weathering of plagioclase, *Clays and Clay Minerals, 46*, 270-279.
Johnson, J. R., and M. I. Staid (2005), Thermal infrared spectral deconvolution of experimentally shocked basaltic rocks using experimentally shocked plagioclase feldspar endmembers, *LPSC XXXVI,* Lunar and Planetary Institute (CD-ROM), Abstract # 848.
Johnson, J. R., F. Hörz, P. G. Lucey, and P. R. Christensen (2002), Thermal infrared spectroscopy of experimentally shocked anorthosite and pyroxenite: Implications for remote sensing of Mars, *J. Geophys. Res., 107,* doi:10.1029/2001JE001517.
Johnson, J. R., F. Hörz, and M. I. Staid (2003), Thermal infrared spectroscopy and modeling of experimentally shocked plagioclase feldspars, *American Mineralogist, 88,* 1575-1582.
Johnson, J. R., M I. Staid, T. N. Titus, and K. Becker (2006), Shocked plagioclase signatures in Thermal Emission Spectrometer data of Mars, *Icarus, 180*, 60-74.
Kieffer, H. H., J. S. C. Chase, E. Miner, G. Münch, and G. Neugebauer (1973), Preliminary report on infrared radiometric measurements from Mariner 9 spacecraft, *J. Geophys. Res., 78,* 4291-4312.
Kieffer, H. H., T. Z. Martin, A. R. Peterfreund, B. M. Jakosky, E. D. Miner, and F. D. Palluconi (1977), Thermal and albedo mapping of Mars during the Viking primary mission, *J. Geophys. Res., 82*, 4249-4292.
Klingelhöfer, G., R. V. Morris, B. Bernardt, C. Schröder, D. S. Rodinov, P. A. de Souza Jr., A. Yen, R. Gellert, E. N. Evlanov, B. Zubkov, J. Foh, U. Bonnes, E. Kankeleit, P. Gütlich, D. W. Ming, F. Renz, T. Wdowiak, S. W. Squyres, R. E. Arvidson (2004), Jarosite and hematite at Meridiani Planum from Opportunity's Mössbauer Spectrometer, *Science, 306,* 1740-1745.
Lanagan, P. D., A. S. McEwen, L. P. Keszthelyi, and T. Thordarson (2001), Rootless cones on Mars indicating the presence of shallow equatorial ground ice in recent times, *Geophys. Res. Let., 28*, 2365-2368.
Land, L. S. (1984), Frio Sandstone diagenesis, Texas Gulf Coast: A regional isotopic study, *in* McDonald, D. C. and R. C. Surdam eds., *Clastic Diagenesis: American Association of Petroleum Geologists Memoir 37,* 47 – 62.
Larsson, D., K. Grönvold, N. Oskarsson, and E. Gunnlaugsson (2002), Hydrothermal alteration of plagioclase and growth of secondary feldspar in the Hengill Volcanic Centre, SW Iceland, *J. of Volcanology and Geothermal Res., 114*, 275-290.
Lobitz, B., B. L. Wood, M. M. Averner, and C. P. McKay (2001), Use of spacecraft data to derive regions on Mars where liquid water would be stable, *Proceedings of the National Academy of Science, 98,* 2132-2137.
Lyon, R. J. P. (1965), Analysis of rock spectra by infrared emission (8-25 μm), *Econ.*

Geol., 60, 715-736.
Lyon, J. P., W. M. Tuddenham, and C. S. Thompson (1959), Quantitative mineralogy in 30 minutes, *Economic Geology, 54*, 1047-1055.
Malin, M. C., and K. S. Edgett (2000a), Evidence for recent groundwater seepage and surface runoff on Mars, *Science, 288,* 2330-2335.
Malin, M. C. and K. S. Edgett (2001), Mars Global Surveyor Mars Orbiter Camera: Interplanetary cruise through primary mission, *J. Geophys. Res., 106,* 23,429-23,570.
Malin, M. C. and K. S. Edgett (2003), Evidence for persistent flow and aqueous sedimentation on early Mars, *Science, 302*, 1931-1934.
Mangold, N., C. Quantin, V. Ansan, C. Delacourt, and P. Allernand (2004), Evidence for precipitation on Mars from dendritic valleys in the Valles Marineris area, *Science, 305,* 78 – 81.
McSween, H. Y., Jr. (1994), What we have learned about Mars from the SNC meteorites, *Meteoritics, 29,* 757-779.
McSween, H. Y., Jr. (2002), The rocks of Mars, from far and near, *Meteoritics and Planetary Science, 37,* 7-25.
McSween, H. Y. Jr. and A. H.Treiman (1998), Martian meteorites, *Rev. Mineral., 36,* 6-01-6-53.
McSween, H. Y., Jr., S. L. Murchie, J. A. Crisp, N. T. Bridges, R. C. Anderson, J. F. Bell III, D. T. Britt, J. Brückner, G. Dreibus, T. Economou, A. Ghosh, M. P. Golombek, J. P. Greenwood, J. R. Johnson, H. J. Moore, R. V. Morris, T. J. Parker, R. Reider, R. Singer, and H. Wänke (1999), Chemical, multispectral, and textural constraints on the composition and origin of rocks at the Mars Pathfinder landing site, *J. Geophys. Res., 104,* 8679-8715.
McSween, H. Y., R. E. Arvidson, J. F. Bell III, D. Blaney, N. A. Cabrol, P. R. Christensen, B. C. Clark, J. A. Crisp, L. S. Crumpler, D. J. Des Marais, J. D. Farmer, R. Gellert, A. Ghosh, S. Gorevan, T. Graff, J. Grant, L. A. Haskin, K. E. Herkenhoff, J. R. Johnson, B. L. Jolliff, G. Klingelhoefer, A. T. Knudson, S. McLennan, K. A. Milam, J. E. Moersch, R. V. Morris, R. Rieder, S. W. Ruff, P. A. de Souza Jr., S. W. Squyres, H. Wänke, A. Wang, M. B. Wyatt, A. Yen, J. Zipfel (2004), Basaltic rocks analyzed by the Spirit rover in Gusev Crater, *Science, 305*, 842-845.
McSween, H. Y., S. W. Ruff, R. V. Morris, J. F. Bell III, K. Herkenhoff, R. Gellert, K. R. Stockstill, L. L. Tornabene, S. W. Squyres, J. A. Crisp, P. R. Christensen, T. J. McCoy, D. W. Mittlefehldt, and M. Schmidt (2006), Alkaline volcanic rocks from the Columbia Hills, Gusev crater, Mars, *J. Geophys. Res., 111*, doi:10.1029/2006JE002698.
Mellon, M. T., B. M. Jakosky, H. H. Kieffer, and P. R. Christensen (2000), High-resolution thermal-inertia mapping from the Mars Global Surveyor Thermal Emission Spectrometer, *Icarus, 148*, 437-455.
Milam, K. A., H. Y. McSween, Jr., V. E. Hamilton, J. E. Moersch, and P. R. Christensen (2004), Accuracy of plagioclase compositions from laboratory and Mars spacecraft thermal emission spectra, *J. Geophys. Res., 109*, E04001,

doi:10.1029/2003JE002097.
Moersch, J. E., and P. R. Christensen (1995), Thermal emission from particulate surfaces: A comparison of scattering models with measured spectra, *J. Geophys. Res., 100,* 7465-7477.
Morad, S., M. Bergan, R. Knarud, and J. P. Nystuen (1990), Albitization of detrital plagioclase in Triassic reservoir sandstones from the Snorre Field, Norwegian North Sea, *J. Sedimentary Petrology, 60,* 411 – 425.
Mustard, J. F. and J. E. Hays (1997), Effects of hyperfine particles on reflectance spectra from 0.3 to 25 μm, *Icarus, 125,* 145-163.
Nash, D. B., and J. W. Salisbury (1991), Infrared reflectance spectra (2.2-15mm) of plagioclase feldspars, *Geophys. Res. Lett., 18*, 1151-1154.
Nayak, V.K. (1993), Maskelynite from the Indian impact crater at Lonar. Journal Geological Society of India, v. 41, pp. 307-312.
Neuhoff, P. S., T. Fridriksson, S. Arnórsson, and D. K. Bird (1999), Porosity evolution and mineral paragenesis during low-grade metamorphism of basaltic lavas at Teigarhorn, Eastern Iceland, *Am. J. of Science, 299,* 467-501.
Nyquist, L. E., D. D. Bogard, C. Y. Shih, A. Greshake, D. Stöffler, and O. Eugster (2001), Ages and geologic histories of Martian meteorites, *Chronology and Evolution of Mars, 96,* 105-164.
Pelkey, S. M., B. M. Jakosky, and M. T. Mellon (2001), Thermal inertia of crater-related wind streaks on Mars, *J. Geophys. Res., 106,* 23909-23920.
Perez, R. J. and J. R. Boles (2005), An empirically derived kinetic model for albitization of detrital plagioclase, *American Journal of Science, 305,* 312-343.
Ramsey, M. S. and P. R. Christensen (1998), Mineral abundance determination: Quantitative deconvolution of thermal emission spectra *J. Geophys. Res.*, *103*, 579– 596.
Ramseyer, K., J. R. Boles, P. C. Lichtner (1992), Mechanism of plagioclase albitization, *J. Sedimentary Petrology, 62,* 349-356.
Robertson, I. D. M., and R. A. Eggleton (1991), Weathering of granitic muscovite to kaolinite and halloysite and of plagioclase-derived kaolinite to halloysite, *Clays and Clay Minerals, 39,* 113-126.
Rogers, A. D. and P. R. Christensen (2007), Surface mineralogy of Martian low-albedo regions from MGS-TES data: Implications for upper crustal evolution and surface alteration, *J. Geophys. Res., 112*: doi:10.1029/2006JE002727.
Rosenbauer, R. J., J. L. Bischoff, and A. S. Radtke (1983), Hydrothermal alteration of greywacke and basalt by 4 molal NaCl, *Economic Geology, 78,* 1701-1710.
Ruff, S. W. (1998), Quantitative thermal infrared emission spectroscopy applied to granitoid petrology, Ph.D. dissertation, 234 pp. Ariz. State Univ., Tempe.
Ruff, S. W. and V. E. Hamilton (2001), Mineralogical anomalies in Mars Nili Patera caldera observed with Thermal Emission Spectrometer data, *Lunar Planet. Sci. XXXII*, abstract # 2186 (CD-ROM).
Ruff, S. W., and P. R. Christensen (2002), Bright and dark regions on Mars: Particle size and mineralogical characteristics based on Thermal Emission Spectrometer

data, *J. Geophys. Res., 107*(E12), 5127, doi:10.1029/2001JE001580.
Scott, D. H. and M. H. Carr (1978), Geologic map of Mars, USGS I-1083, 1:25,000,000, 1978.
Shikazono, N., M. Utada, and M. Shimizu (1995), Mineralogical and geochemical characteristics of hydrothermal alteration of basalt in the Kuroko Mine area, Japan: Implications for the evolution of a back arc basin hydrothermal system, *App. Geochemistry, 10,* 621-642.
Smith, J. V., and R. L. Hervig (1979), Shergotty meteorite: Mineralogy, petrology, and minor elements, *Meteoritics, 14,* 121-142.
Soderblom, L. A., R. C. Anderson, R. E. Arvidson, J. F. Bell, III, N. A. Cabrol, W. Calvin, P. R. Christensen, B. C. Clark, T. Economou, B. L. Ehlmann, W. H. Farrand, D. Fike, R. Gellert, T. D. Glotch, M. P. Golombek, R. Greeley, J. P. Grotzinger, K. E. Herkenhoff, D. J. Jerolmack, J. R. Johnson, B. Jolliff, G. Klingelhöfer, A. H. Knoll, Z. A. Learner, R. Li, M. C. Malin, S. M. McLennan, H. Y. McSween, D. W. Ming, R. V. Morris, J. W. Rice, Jr., L. Richter, R. Rieder, D. Rodionov, C. Schröder, F. P. Seelos IV, J. M. Soderblom, S. W. Squyres, R. Sullivan, W. A. Watters, C. M. Weitz, M. B. Wyatt, A. Yen, and J. Zipfel (2004), Soils of Eagle Crater and Meridiani Planum at the Opportunity rover landing site, *Science, 306*, 1723-1726.
Squyres, S. W., J. P. Grotzinger, R. E. Arvidson, J. F. Bell III, W. Calvin, P. R. Christensen, B. C. Clark, J. A. Crisp, W. H. Farrand, K. E. Herkenhoff, J. R. Johnson, G. Klingelhöfer, A. H. Knoll, S. M. McLennan, H. Y. McSween Jr., R. V. Morris, J. W. Rice Jr., R. Rieder, L. A. Soderblom (2004), In situ evidence for an ancient aqueous environment at Meridiani Planum, Mars, *Science, 306*, 1709-1714.
Squyres, S. W., A. H. Knoll, R. E. Arvidson, B. C. Clark, J. P. Grotzinger, B. L. Jolliff, S. M. McLennan, N. Tosca, J. F. Bell III, W. M. Calvin, W. H. Farrand, T. D. Glotch, M. P. Golombek, K. E. Herkenhoff, J. R. Johnson, G. Klingelhöfer, H. Y. McSween, A. S. Yen (2006), Two years at Meridiani Planum: Results from the Opportunity rover, *Science, 313*, 1403-1407.
Stakes, D. S., and P. Schiffman (1999), Hydrothermal alteration within the basement of the sedimented ridge environment of Middle Valley, northern Juan de Fuca Ridge, *Geol. Soc. Am. Bull., 3,* 1294–1314.
Stöffler, D., R. Ostertag, C. Jammes, G. Pfannschmidt, P. R. Sen Gupta, S. B., Simon, J. J. Papike, and R. H. Beauchamp (1986), Shock metamorphism and petrography of the Shergotty achondrite, *Geochim. Cosmochim. Acta, 50,* 889-913.
Stolper, E. M., H. Y. McSween, Jr., and J. F. Hays (1979), A petrogenetic model of the relationships among achondritic meteorites, *Geochim., Cosmochim., Acta, 43,* 589-602.
Strom, R. G., S. K. Croft, and N. G. Barlow (1992), The martian impact cratering record, In *Mars*, 383-423, University of Arizona Press, Tuscon.
Tanaka, K. L., D. H. Scott, and R. Greeley (1992a), Global stratigraphy, In *Mars*, 345-382, University of Arizona Press, Tuscon.
Tanaka, K. L., M. G. Chapman, and D. H. Scott (1992b), Geologic map of the

Elysium region of Mars, scale 1:5,000,000, U.S. Geol. Surv. Misc. Invest. Ser. Map., I-2147.

Tanokura, T., and H. Onuki (1990), Miocene metabasites of the Hanaoka area, northern Akita Prefecture, *Journal of Mineralogy, Petrology, and Economic Geology, 85*, 6, 257.

Thomas, P. and C. Weitz (1989), Sand dune materials and polar layered deposits on Mars, *Icarus, 81,* 185-215.

Thomson, J. L. and J. W. Salisbury (1993), The mid-infrared reflectance of mineral mixtures (7-14 μm), *Remote Sensing Env., 45*, 1-13.

Treiman, A. H. (2003), Geologic settings of Martian gullies: Implications for their origins, *J. of Geophys. Res., 108,* doi:10.1029/2002JE001900.

Walter, M.R., and D.J. Des Marais (1993), Preservation of biological information in thermal spring deposits: Developing a strategy for the search for fossil life on Mars, *Icarus, 101,* 129-143.

Wänke, H., J. Brückner, G. Driebus, R. Rieder, and I. Ryabchikov (2001), Chemical composition of rocks and soils at the Pathfinder site, *Space Science Reviews, 96*, 317-330.

White, A. F., A. E. Blum, M. S. Schulz, T. D. Bullen, J. W. Harden, and M. L. Peterson (1996), Chemical weathering rates of a soil chronosequence on granitic alluvium: I. Quantification of mineralogical and surface area changes and calculation of primary silicate reaction rates, *Geochem. et Cosmochim. Acta, 60,* 2533-2550.

White, A. F., T. D. Bullen, M. S. Schulz, A. E. Blum, T. G. Huntington, and N. E. Peters (2001), Differential rates of feldspar weathering in granitic regoliths, *Geochem. et Cosmochimica Acta, 65*, 847-869.

Wright, S. P., J. R. Johnson, P. R. Christensen (2004), Thermal emission spectra of impact glass and shocked Deccan basalt from Lonar crater, India and implications for remote sensing of Mars, *LPSC XXXV,* Lunar and Planetary Institute, Houston, TX (CD-ROM), Abstract # 2072.

Wyatt, M. B., and H. Y. McSween Jr. (2002), Spectral evidence for weathered basalt as an alternative to andesite in the northern lowlands of Mars, *Nature, 417*, 263-266.

Wyatt, M. B., V. E. Hamilton, H. Y. McSween, Jr., P. R. Christensen, and L. A. Taylor (2001), Analysis of terrestrial and Martian volcanic compositions using thermal emission spectroscopy: 1. Determination of mineralogy, chemistry, and classification strategies, *J. Geophys. Res., 105*, 14,711 – 14,732.

Zierenberg, R. A., P. Schiffman, I. R. Jonasson, R. Tosdal, W. Pickthorn, and J. McClain (1995), Alteration of basalt hyaloclastite at the off-axis Sea Cliff hydrothermal field, Gorda Ridge, *Chem. Geology, 126*, 77-99.

Appendix for Part 4

Table 12. Spectral endmembers (and their bulk chemistries) used in this study. Not included are the TES atmospheric and surface dust endmembers.

Sample	Mineral Name	Notes	Collection	SiO_2	Al_2O_3	FeO (Fe_2O_3)	MnO	MgO	CaO	Na_2O	K_2O	TiO_2	Total	An
WAR-0235	albite		ASU	68.3	20	0.33	0.01	0.04	0.01	11.5	0.02	0.00	100	<1
WAR-0244	albite		ASU	69.2	18.2	0.24	0.01	0.01	0.38	10.2	0.66	0.00	98.9	2
WAR-0612	albite		ASU	67.2	19	0	0.02	0.4	0.35	9.26	0.18	0.00	96.4	2
5851	albite	1,2,3,4,5,6	UT	67.9	19.9	0	0.02	0.02	0.63	9.71	0.27	0.00	98.5	2
WAR-5851	albite	7	ASU	63	19.7	5.51	0.02	0.47	1.37	8.5	0.22	0.00	98.8	8
BUR-060D	oligoclase	10	ASU	63.5	22.5	0.21	0.01	0.01	3.36	9.21	0.6	0.00	99.4	15
BUR-060	oligoclase		ASU	60.4	21.9	4.16	0.08	0.06	3.24	9.37	0.79	0.00	100	16
WAR-5804	oligoclase	7	ASU	62	24	0.04	0	0	4.74	9.03	0.5	0.00	100	22
WAR-3680	oligoclase		ASU	63.5	22.7	0.03	0.13	0.44	4.94	7.76	0.63	0.00	100	25
WAR-0234	oligoclase		ASU	60.8	22.1	0	0.02	0.85	5.37	6.71	0.91	0.00	96.8	29
BUR-240	andesine	7	ASU	53.9	27.1	0.53	0.01	0.07	9.51	5.55	0.34	0.00	97	48
WAR-3080A	andesine		ASU	53.4	26.3	1.5	0.03	0.65	9.62	4.94	1.2	0.00	97.6	48
WAR-0024	andesine		ASU	56.4	24.6	0.06	0.07	2.51	9.38	4.67	0.76	0.00	98.5	50
4512A-L	labradorite	1,2,3,5,6	UT	54.2	24.4	2.16	0.05	1.32	9.8	4.34	1.3	0.00	97.6	51
0022b	labradorite	1,2,3,5,6	UT	54.8	26.5	1.1	0.03	0.24	10.4	4.02	0.47	0.00	97.6	53
WAR-4524	labradorite	7, 8, 9	ASU	52.6	27.7	2.5	0.02	0.14	10.9	5.01	0.42	0.00	99.3	53
WAR-1384	labradorite	8,9,10	ASU	51.3	30.9	0.32	0.03	0.5	11.8	3.64	0.26	0.00	98.8	63
WAR-RGAND01	labradorite	7	ASU	49.9	28	3.09	0.03	0.68	13	3.46	0.22	0.00	98.4	67
SS	labradorite	2,3,6	UT	50.9	29.8	0.3	0.02	0.15	13.4	3.42	0.14	0.00	98.1	68
WAR-5859	bytownite		ASU	48.4	31.5	1.56	0.01	0.26	14.7	2.89	0.09	0.00	99.4	73
1382a	bytownite	3,4,10	UT	49.1	30.4	0.5	0.04	0.45	14.5	2.86	0.2	0.00	98.1	73
WAR-5759	bytownite	8	ASU	41.5	29.5	9.2	0.03	2.69	15.4	1.13	0.08	0.00	99.5	88
BUR-340	anorthite	7,10	ASU	43.2	35.6	0.54	0.01	0.39	17.6	0.84	0.01	0.00	98.2	92
BUR-4120	plutonic Quartz		ASU	100.00	0.00	0.00	0.00	0.00	0.00	0.00	0.00	0.00	100.00	
HS-9.4	orthopyroxene Mg_{90}		ASU	57.87	0.99	6.88	0.17	34.86	0.67	0.00	0.00	0.02	101.46	
NMNH-93527	orthopyroxene Mg_{77}		ASU	51.84	5.28	13.79	0.23	26.76	1.46	0.07	0.00	0.35	99.79	
DSM-HED01	hedenbergite	9	ASU	49.96	0.06	14.14	7.99	4.32	22.80	0.11	0.00	0.01	99.39	
WAR-6474	augite (low-Ca)		ASU	50.60	2.35	12.58	0.30	9.96	21.13	2.00	0.00	0.18	99.10	
NMNH-9780	augite (low-Ca)		ASU	51.00	1.55	16.52	0.46	9.42	20.49	0.33	0.02	0.20	99.99	
WAR-RGFAY01	fayalite		ASU	31.11	0.00	59.75	1.30	7.71	0.09	0.00	0.00	0.06	100.02	

Table 12 (continued)

Sample Name	Mineral	Notes	Collection	SiO_2	Al_2O_3	FeO (Fe_2O_3)	MnO	MgO	CaO	Na_2O	K_2O	TiO_2	Total	An
None	K-rich glass		ASU	77.87	12.55	0.00	0.00	0.00	0.00	3.90	5.67	0.00	99.99	
None	pure silica glass		ASU	99.99	0.00	0.00	0.00	0.00	0.00	0.00	0.00	0.00	99.99	
WAR-4119	ilmenite		ASU	0.01	0.01	48.05	0.21	3.13	0.01	0.00	0.01	47.81	99.24	
HS 116.4B	actinolite		ASU	54.7	1.53	6.96	0	0.16	21.33	11.2	1.03	0.08	100.6	
WAR-5474	muscovite		ASU	43.8	33.4	2.36	0.00	0.06	0.22	0.01	0.69	9.30	90.0	
BUR-840	biotite		ASU	39.0	11.2	19.7	0.00	0.80	14	0.51	0.53	8.80	97.5	
BUR-3460	microcline		ASU	63.5	19.1	0.13	0.00	0.01	0.01	0.16	2.77	12.0	18.4	
BUR-2600	hematite		ASU											
BUR-1690	serpentine		ASU	38.7	1.15	8.81	0.00	0.15	39.1	0.04	0.01	0.01	100.6	
BUR-3460A	microcline		ASU	64.2	19.1	0.17	0.00	0.01	0.01	0.02	3.12	13	100.2	
WAR-0579	anorthoclase		ASU	62.9	19.9	0.30	0.00	0.04	1.01	2.64	5.77	4.32	98.2	
ML-S9	gypsum		ASU											
ML-S6	calcite		ASU											
C27	calcite		ASU	0.00	0.00	0.00	0.00	0.26	56.48	0.00	0.00	0.00	99.9	43 wt% CO_2
C28	dolomite		ASU	0.00	.0.00	0.54	0	20.64	30.14	0	0.00	0.00	100.0	49 wt% CO_2
Swa-1	Fe-smectite		ASU											
Imt-2	illite		ASU	55.1	22.0	6.62	0.00	0.00	2.80	0.02	0.08	8.04	100.0	
WAR-1924	chlorite		ASU	28.7	19.3	7.20	0.00	0.14	30.5	0.01	0.01	0.01	85.9	
WAR-5108	Nontronite		ASU	N/A	N/A	N/A	N/A	N/A	N/A	N/A	N/A	N/A	N/A	

Table 13. Percentages of all TES spectra modeled as solid solution plagioclase compositions by surface type and globally (total for dust-free regions). Results indicate that labradorite and bytownite comprise the largest proportion of emissivity spectra analyzed in this study.

Solid solution composition	Surface type 1 average %	Surface type 2 average %	Global %
albite (An_{0-10})	2	8	5
oligoclase (An_{10-30})	4	7	6
andesine (An_{30-50})	12	15	14
labradorite (An_{50-70})	49	34	42
bytownite (An_{70-90})	25	20	20
anorthite (An_{90-100})	7	16	12

Table 14. Average plagioclase compositions for Mars. Averages were determined by calculating the average from average plagioclase compositions for all TES spectra used in this study.

Surface type / region	Anorthite Content
Surface type 1	An_{62}
Surface type 2	An_{59}
Total Mars	An_{61}

Table 15. Plagioclase compositional variation for selected regions on Mars.

Surface type/region	Average An	% of TES data					
		ab	ol	and	lab	by	an
Surface type 1							
Hesperia Planum	63	2	3	12	48	29	7
Noachis Terra	61	3	5	13	50	22	8
Solis Planum	60	2	5	17	47	24	6
Syrtis Major	63	1	3	14	50	25	7
Terra Sirenum	61	3	4	14	51	22	7
Surface type 2							
Acidalia/Chryse Planitia	61	6	6	14	36	21	17
Arcadia Planitia	58	10	7	18	30	22	14
Utopia Planitia	58	10	7	16	32	21	17
Global	61	5	6	14	42	20	12

Table 16. Reported anorthite variations and RMS errors for deconvolutions of shocked bytownite and albite used in *Johnson et al.* [2003].

Sample					
Bytownite (An_{75})		chips (2-10 mm)		powder (<20-30μm)	
		ΔAn	RMS	ΔAn	RMS
	average	5	0.005	18	0.006
	1 σ std. dev.	3	0.002	9	0.002
	maximum	12	0.008	27	0.011
	minimum	2	0.002	8	0.004
Albite (An_2)		chips (2-10 mm)		powder (<20-30μm)	
		ΔAn	RMS	ΔAn	RMS
	average	32	0.006	28	0.011
	1 σ std. dev.	18	0.002	10	0.005
	maximum	65	0.010	38	0.021
	minimum	9	0.004	6	0.004

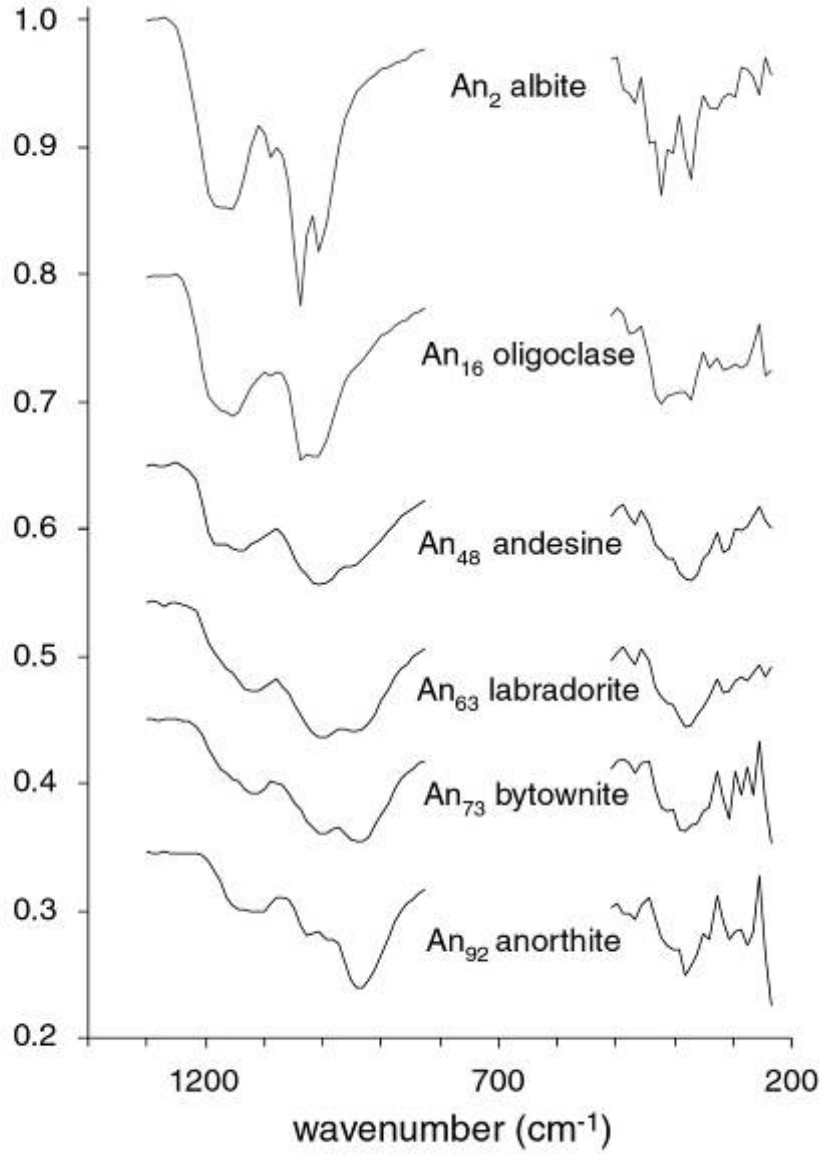

Figure 24. Thermal emission spectra of some plagioclase compositions at TES spectral resolution (10 cm^{-1} sampling) between ~1300-200 cm^{-1}. All spectra (except albite) are variably offset (1-2 in emissivity) for clarity. The region centered at ~667cm^{-1} has been excluded because of a prominent atmospheric CO_2 absorption (from *Christensen et al.,* 2001 and *Milam et al.*,2004].

Figure 25. Plagioclase compositional map (cylindrical projection) showing TES spectra (red) modeled with average plagioclase compositions between An_{1-10} (albite). Gray areas in the lower half of this figure represent areas where data was not selected for use in this study or modeled no percentage of albite in deconvolutions. Only <4% of spectra used in this study modeled no plagioclase.

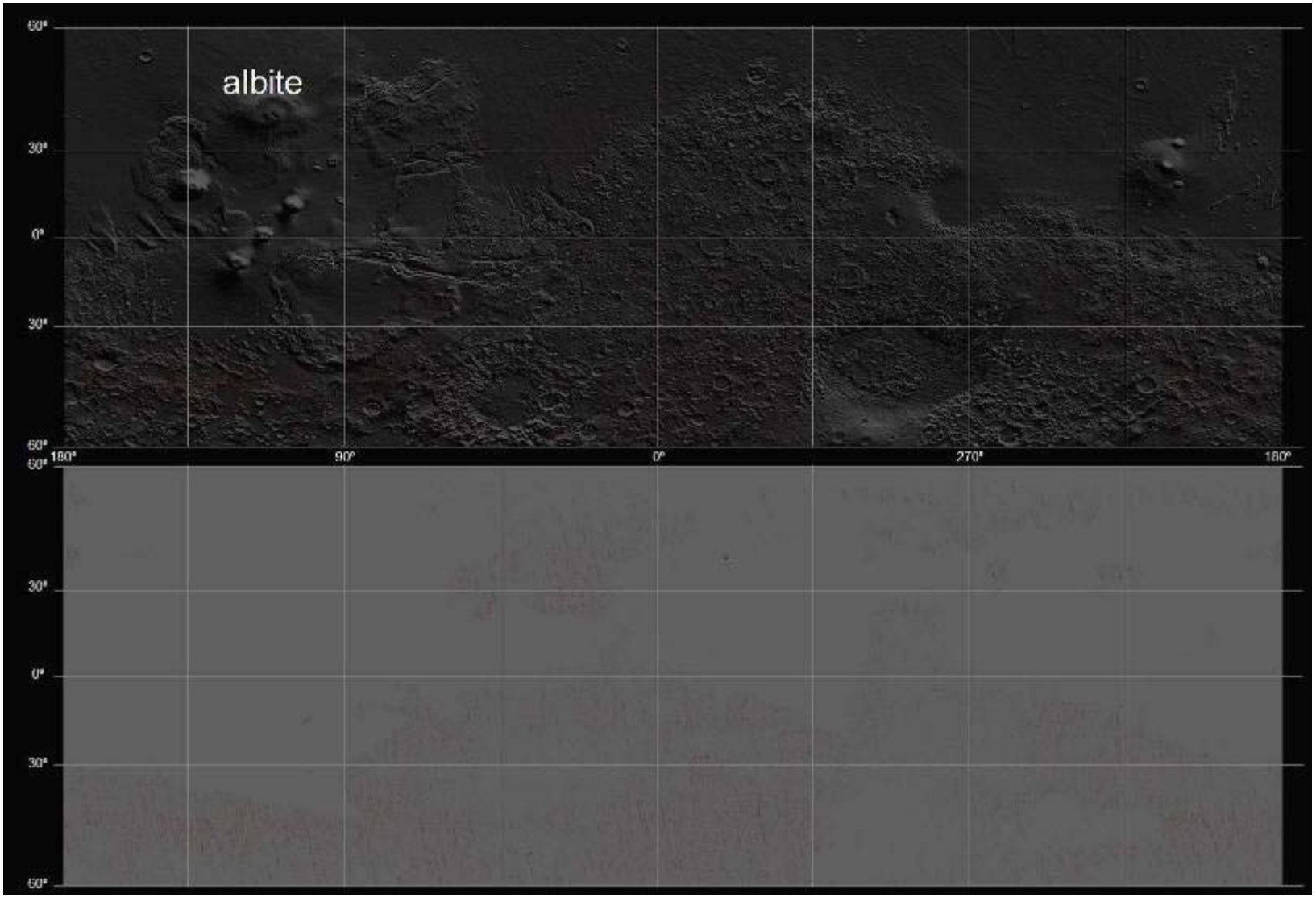
albite
60°
30°
0°
30°
60°
180°
90°
0°
270°
180°

Figure 26. Plagioclase compositional map (cylindrical projection) showing TES spectra (orange) modeled with average plagioclase compositions between An_{10-30} (oligoclase). Gray areas in the lower half of this figure represent areas where data was not selected for use in this study or modeled no percentage of oligoclase in deconvolutions. Only <4% of the data used in this study modeled no plagioclase.

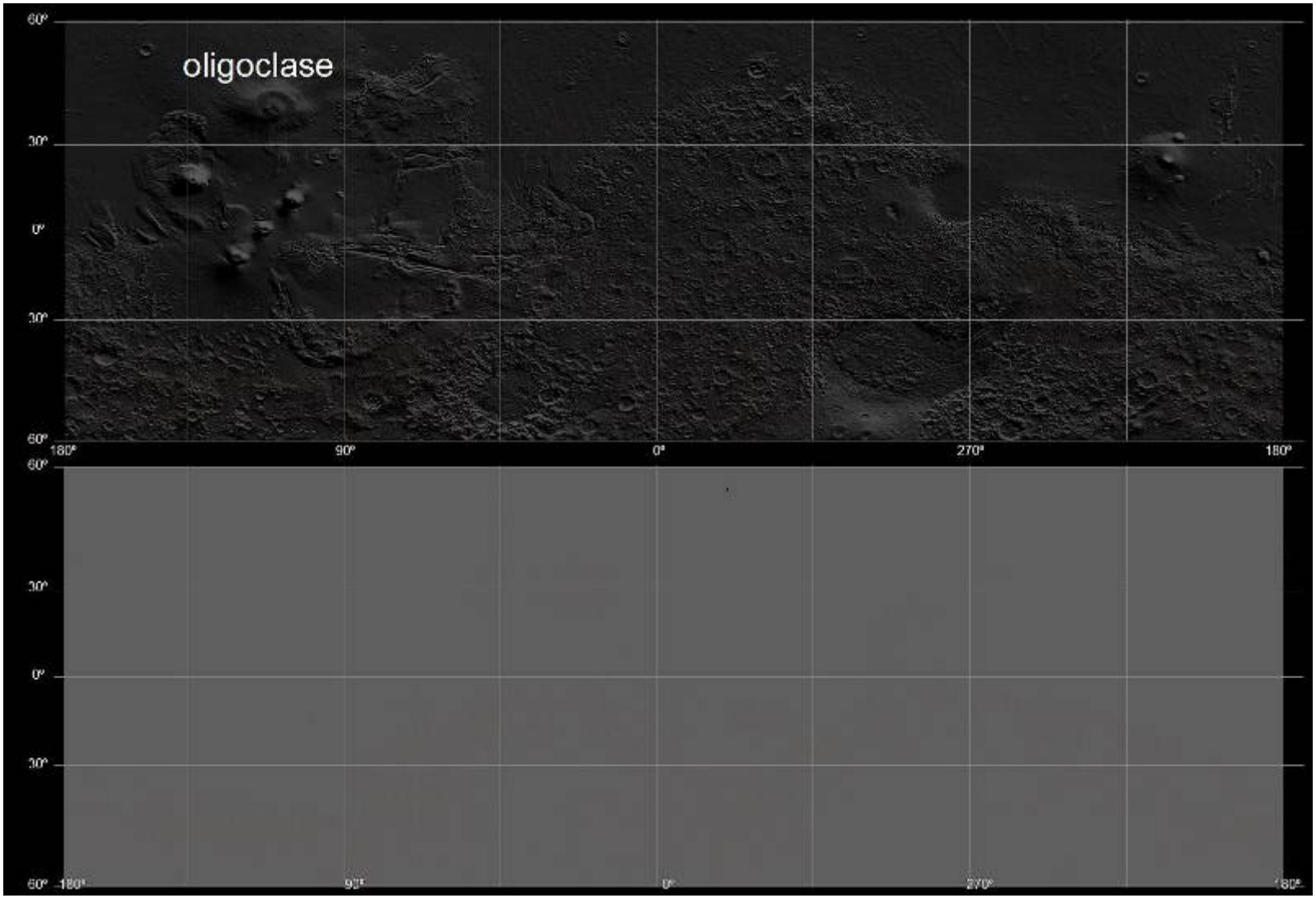
oligoclase
60°
30°
0°
30°
60°
180°
90°
0°
270°
180°

Figure 27. Plagioclase compositional map (cylindrical projection) showing TES spectra (light blue) modeled with average plagioclase compositions between An_{30-50} (andesine). Gray areas in the lower half of this figure represent areas where data was not selected for use in this study or modeled no percentage of andesine in deconvolutions. Only <4% of the data used in this study modeled no plagioclase.

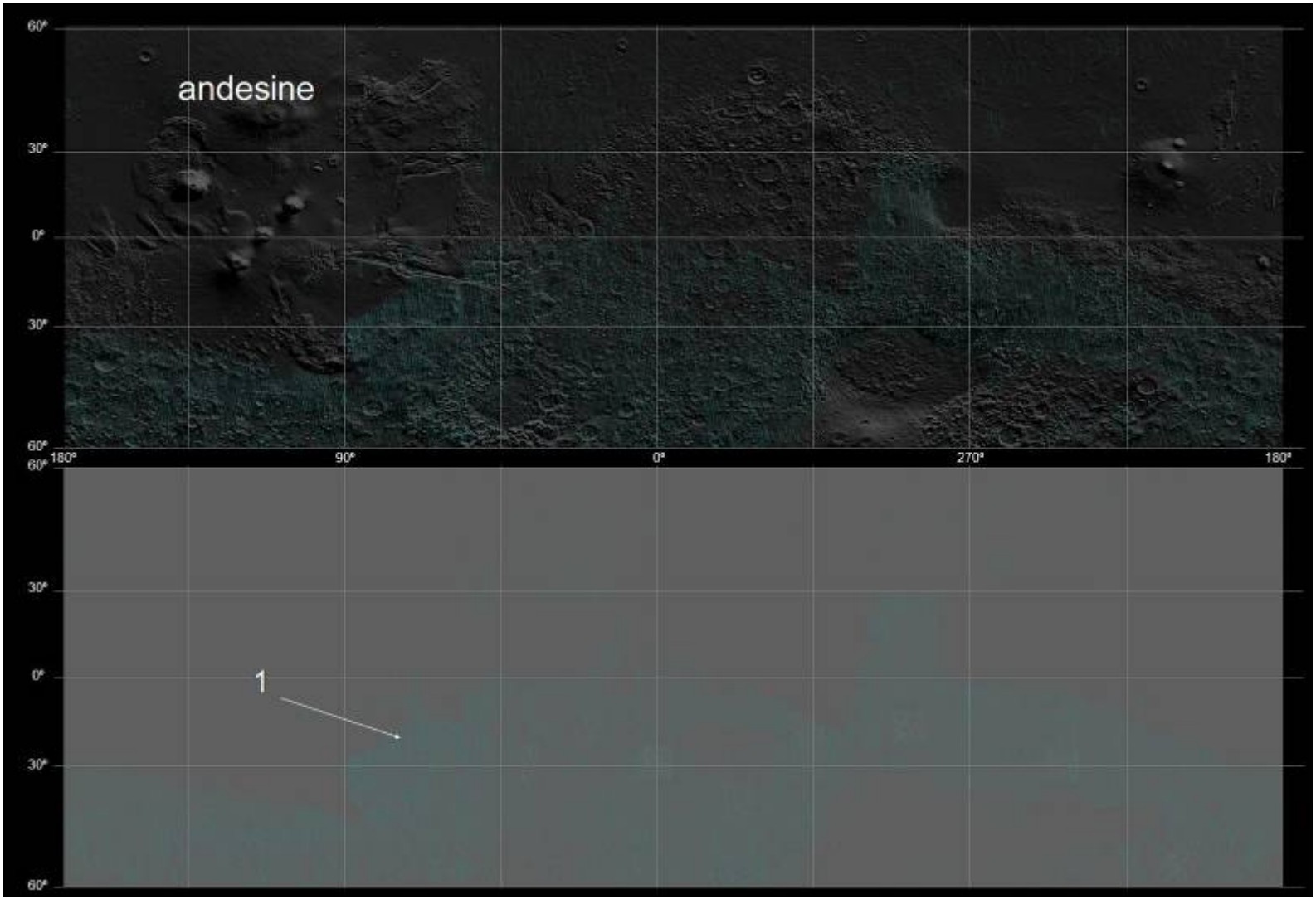
andesine
60°
30°
0°
30°
60°
180°
90°
0°
270°
180°
1

Figure 28. Plagioclase compositional map (cylindrical projection) showing TES spectra (aqua) modeled with average plagioclase compositions between An_{50-70} (labradorite). Gray areas in the lower half of this figure represent areas where data was not selected for use in this study or modeled no percentage of labradorite in deconvolutions. Only <4% of the data used in this study modeled no plagioclase.

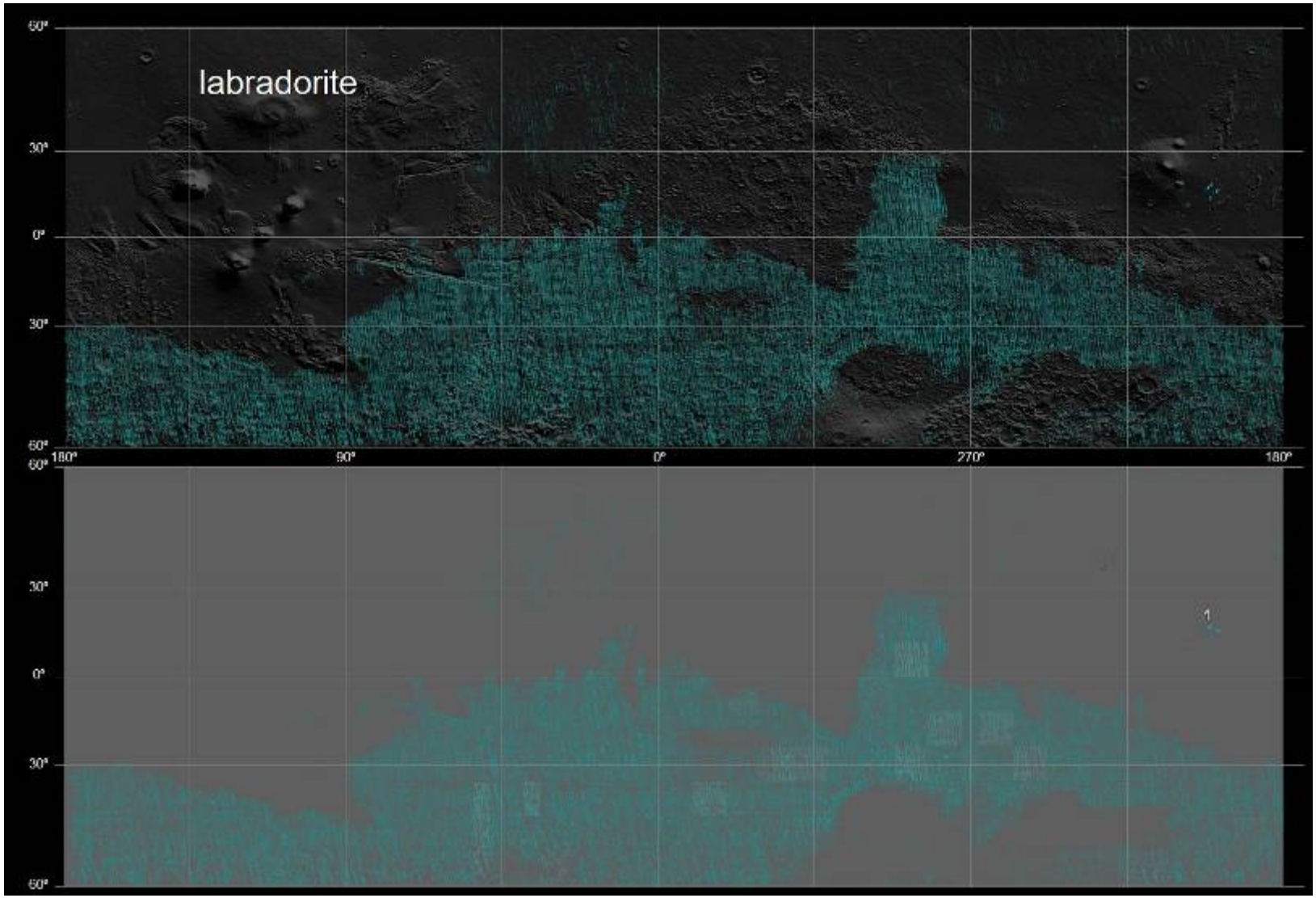
labradorite
60°
30°
0°
30°
60°
180°
90°
0°
270°
180°

Figure 29. Plagioclase compositional map (cylindrical projection) showing TES spectra (blue) modeled with average plagioclase compositions between An_{70-90} (bytownite). Gray areas in the lower half of this figure represent areas where data was not selected for use in this study or modeled no percentage of bytownite in deconvolutions. Only <4% of the data used in this study modeled no plagioclase.

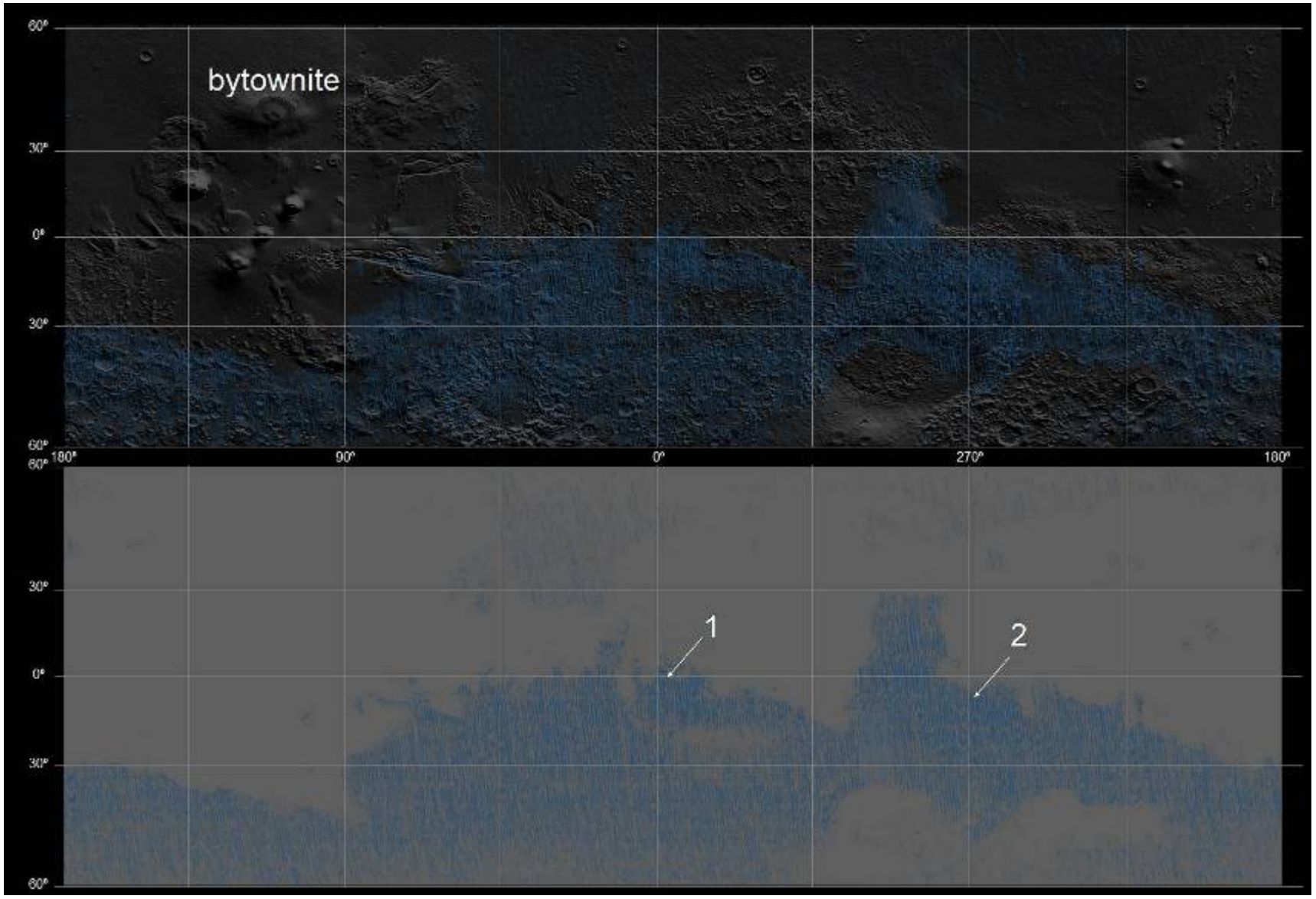
bytownite
60°
30°
0°
30°
60°
180°
90°
0°
270°
180°
1
2

Figure 30. Plagioclase compositional map cylindrical projection) showing TES spectra (dark blue) modeled with average plagioclase compositions between $An_{90\text{-}100}$ (anorthite). Gray areas in the lower half of this figure represent areas where data was not selected for use in this study or modeled no percentage of anorthite in deconvolutions. Only <4% of the data used in this study modeled no plagioclase.

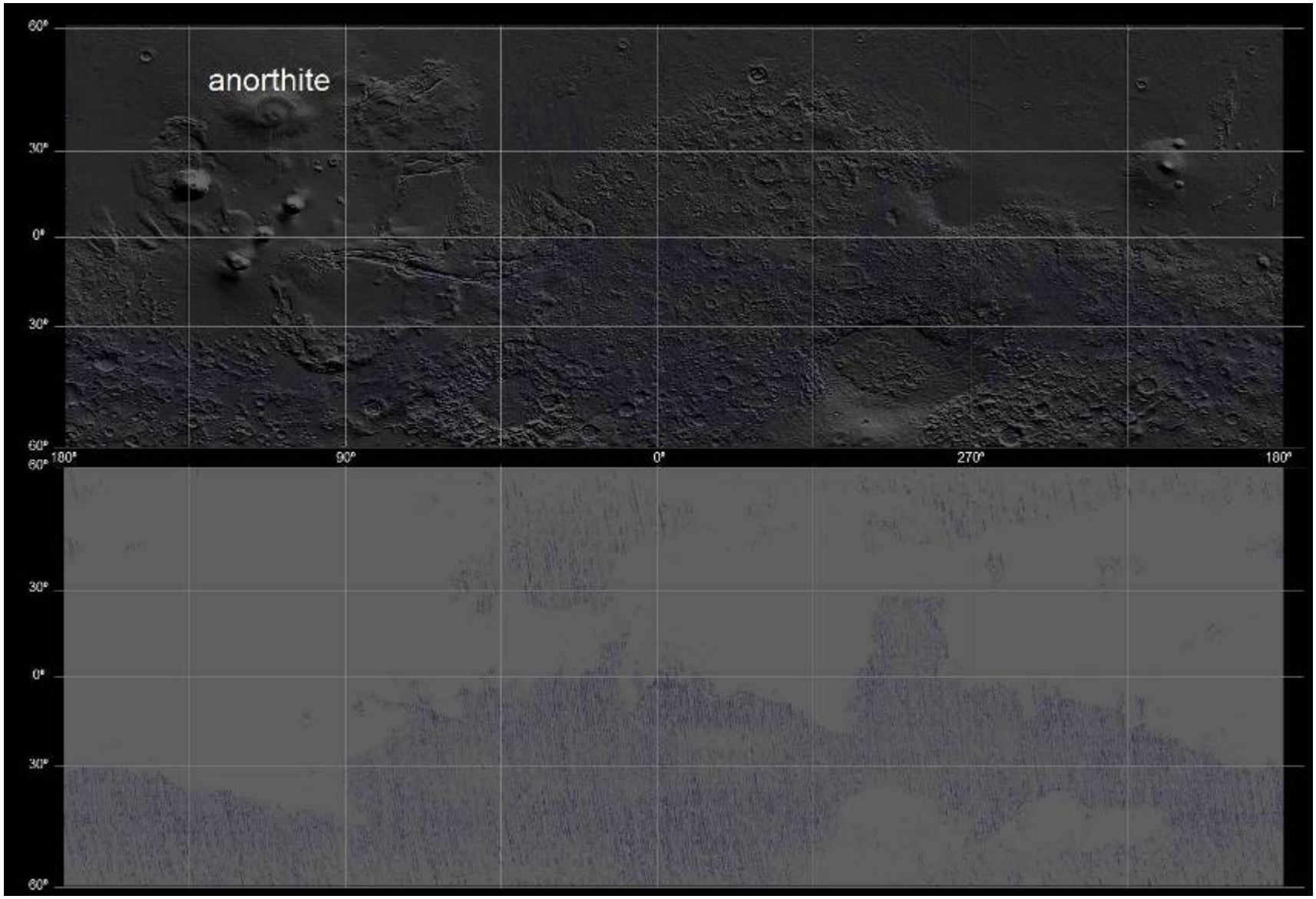
anorthite
60°
30°
0°
30°
60°
180°
90°
0°
270°
180°

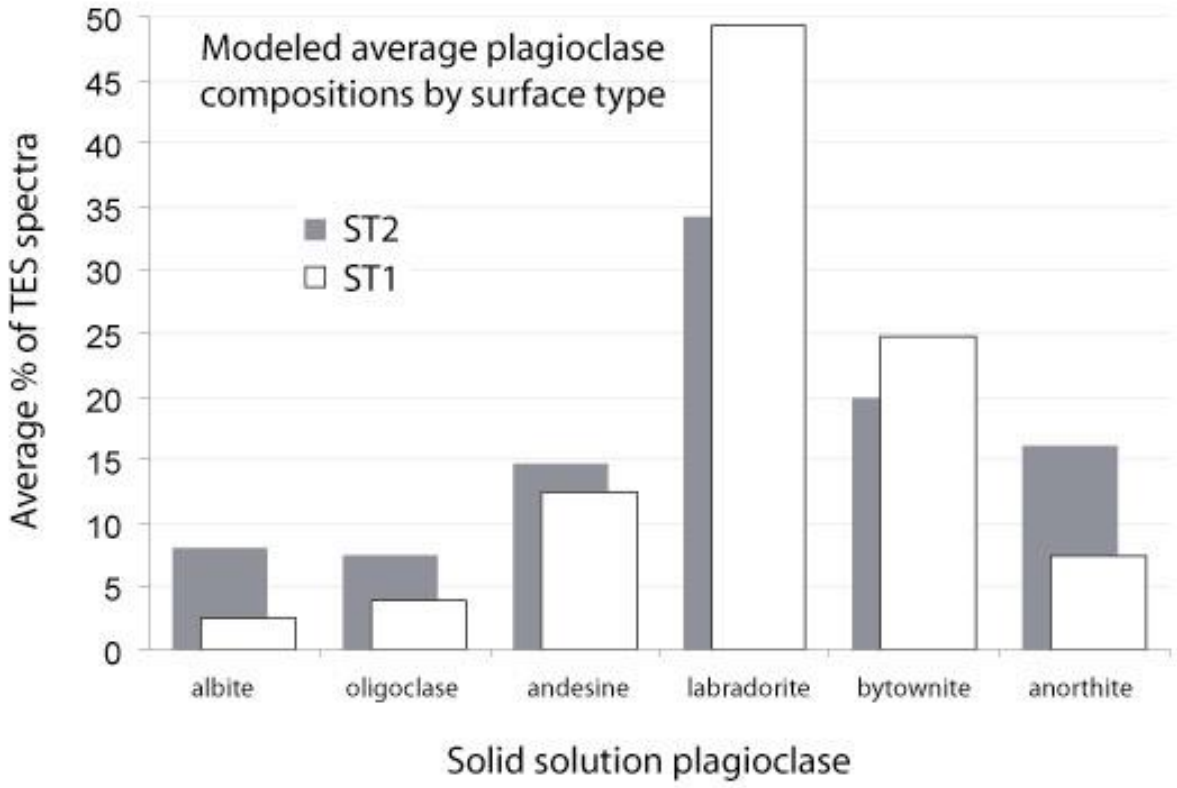

Figure 31. Bar diagram depicting the percentages of TES observations modeled as various solid solution compositions by surface type. These global averages show that both surface types are dominated by labradorite and bytownite, with albite being the least commonly modeled average plagioclase composition.

Figure 32. Plagioclase compositional data for Syrtis Major (top), showing plagioclase compositions $<An_{50}$ (light blue) vs. $>An_{50}$ (dark blue). Plagioclase compositions are averaged for each 10° x 10° quadrant. The dashed line represents the approximate visual boundary between relatively calcic ($>An_{63}$) and sodic (An_{60}) regions. Non-colored areas represent regions where data was not used in this study or did not model plagioclase in any percentage. The bottom image shows an overlay of average plagioclase compositions and the boundary overlain on a MOLA shaded relief image.

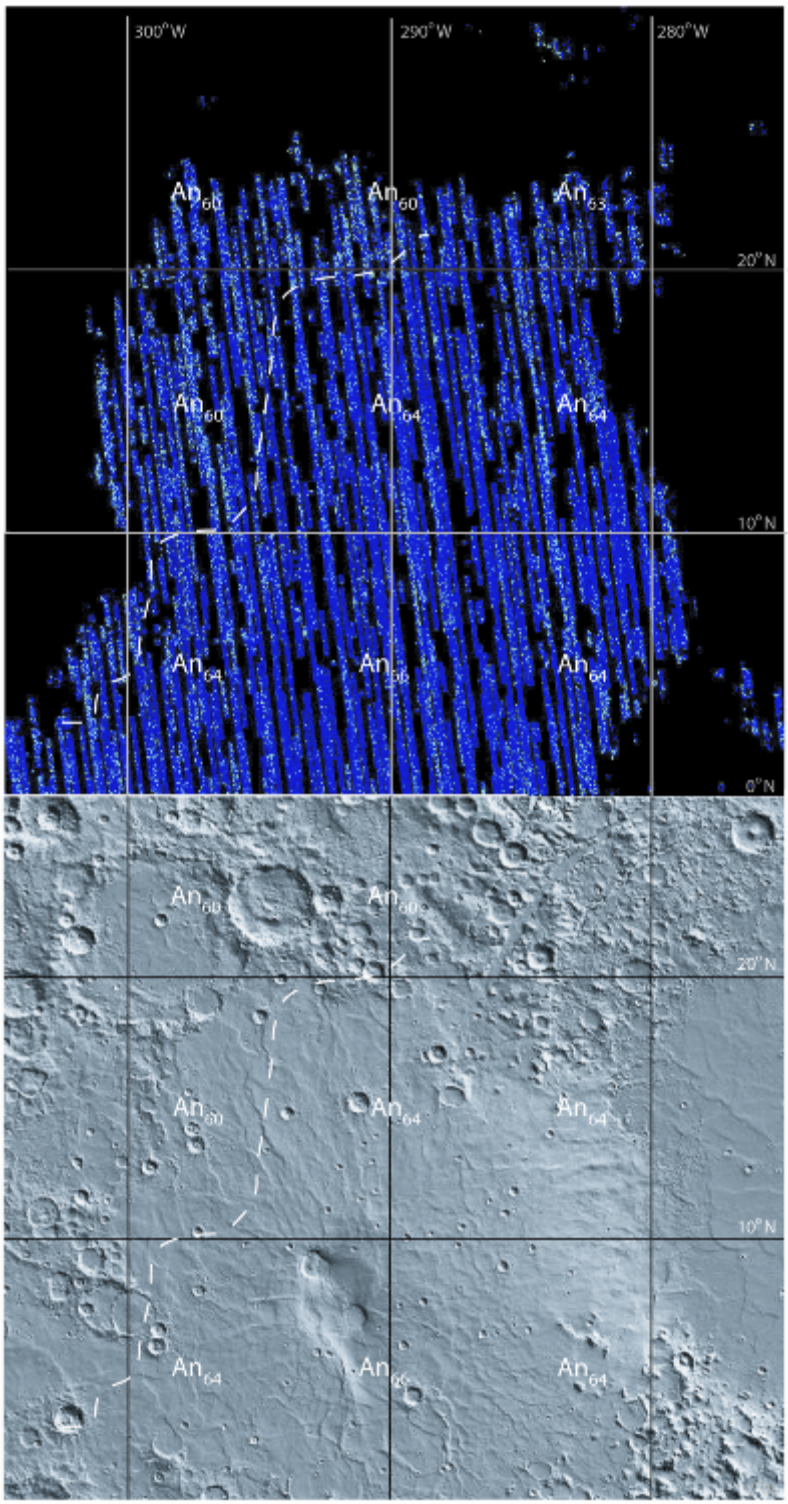
300°W
290°W
280°W
20°N
10°N
0°N
An60
An64

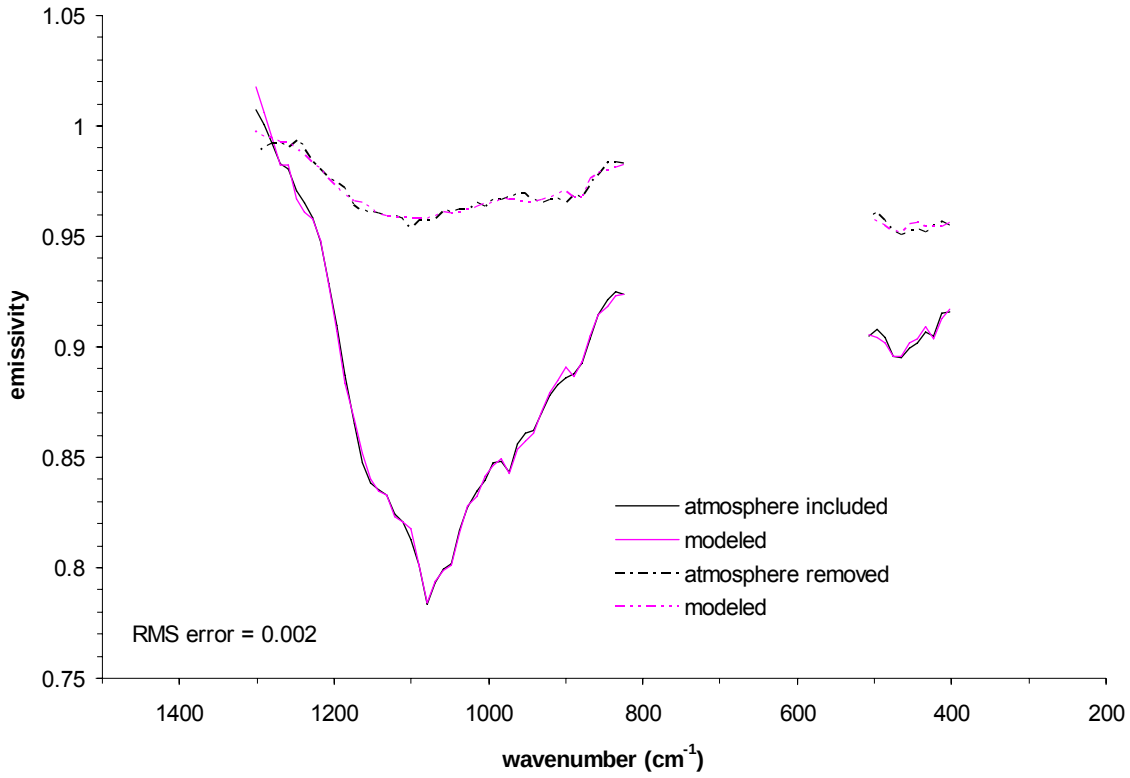

Figure 33. Actual (black) vs. modeled (purple) average TES emissivity spectrum for the Opportunity landing site. Solid lines are spectra with the atmospheric component included, while dashed line spectra have atmospheric components removed.

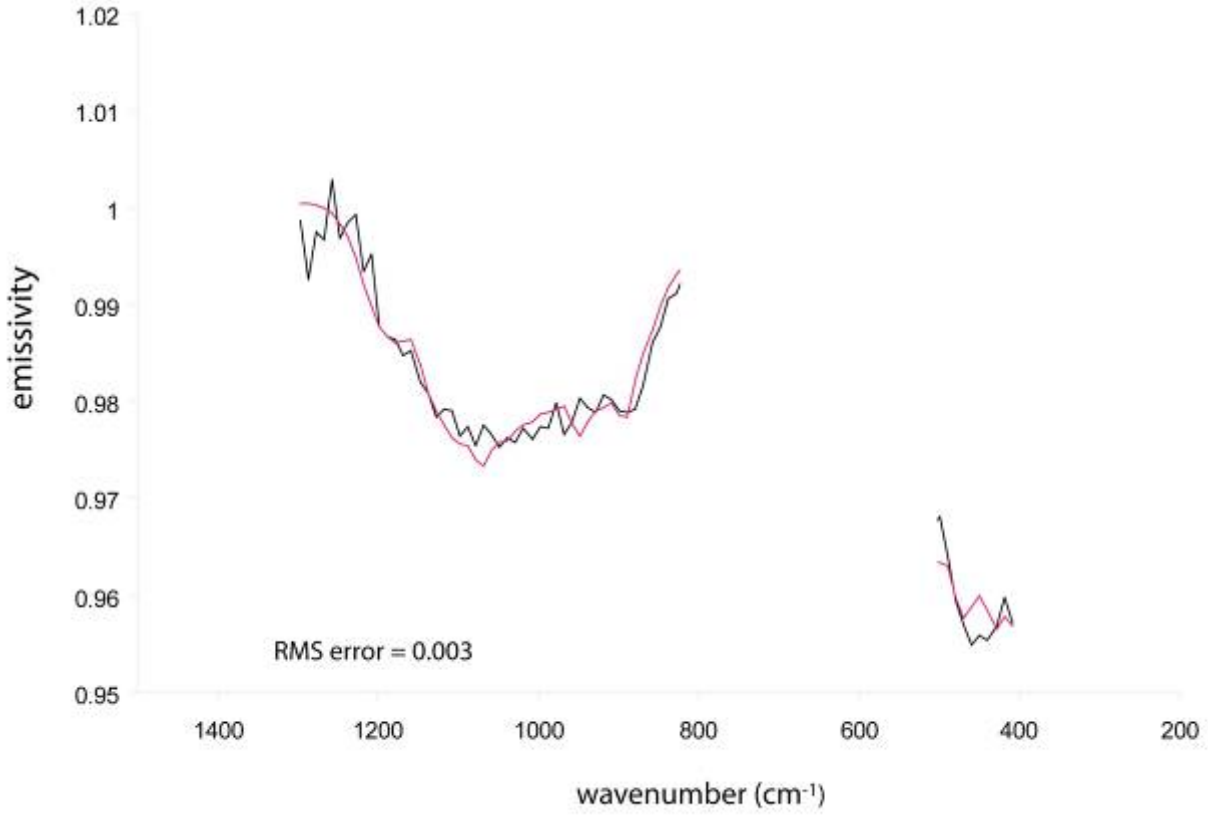

Figure 34. Actual (black) vs. modeled (purple) Mini-TES emissivity spectrum representing the basaltic, hematite-rich sands of Meridiani Planum. The actual spectrum is an average of 90 Mini-TES observations on sol 90 collected by the Opportunity rover during its traverse from Fram to Endurance craters. The spectrum has been corrected for downwelling atmospheric radiance and may also be found in *Christensen et al*. [2004]. The modeled anorthite content from this deconvolution of the Mini-TES spectrum is An_{58}.

Figure 35. Martian plagioclase compositions reported by sample-, rover-, and orbital-based studies. Martian meteorites display the widest (and most precise) compositional ranges for plagioclase because geochemical analyses represent the full range of zoning within given samples. APXS values represent the average normative values for each sample analyzed and orbital studies average plagioclase in many samples over the spatial footprint of the TES instrument. Overall, these ranges are more sodic compared to rover (APXS) and orbital studies. Meteorite data are from the *Mars Meteorite Compendium* [2006], Gusev data are from *McSween et al.* [2004], and Pathfinder data are from *Wänke et al.* [2001]. TES-derived average plagioclase and Meridiani values are from this study.

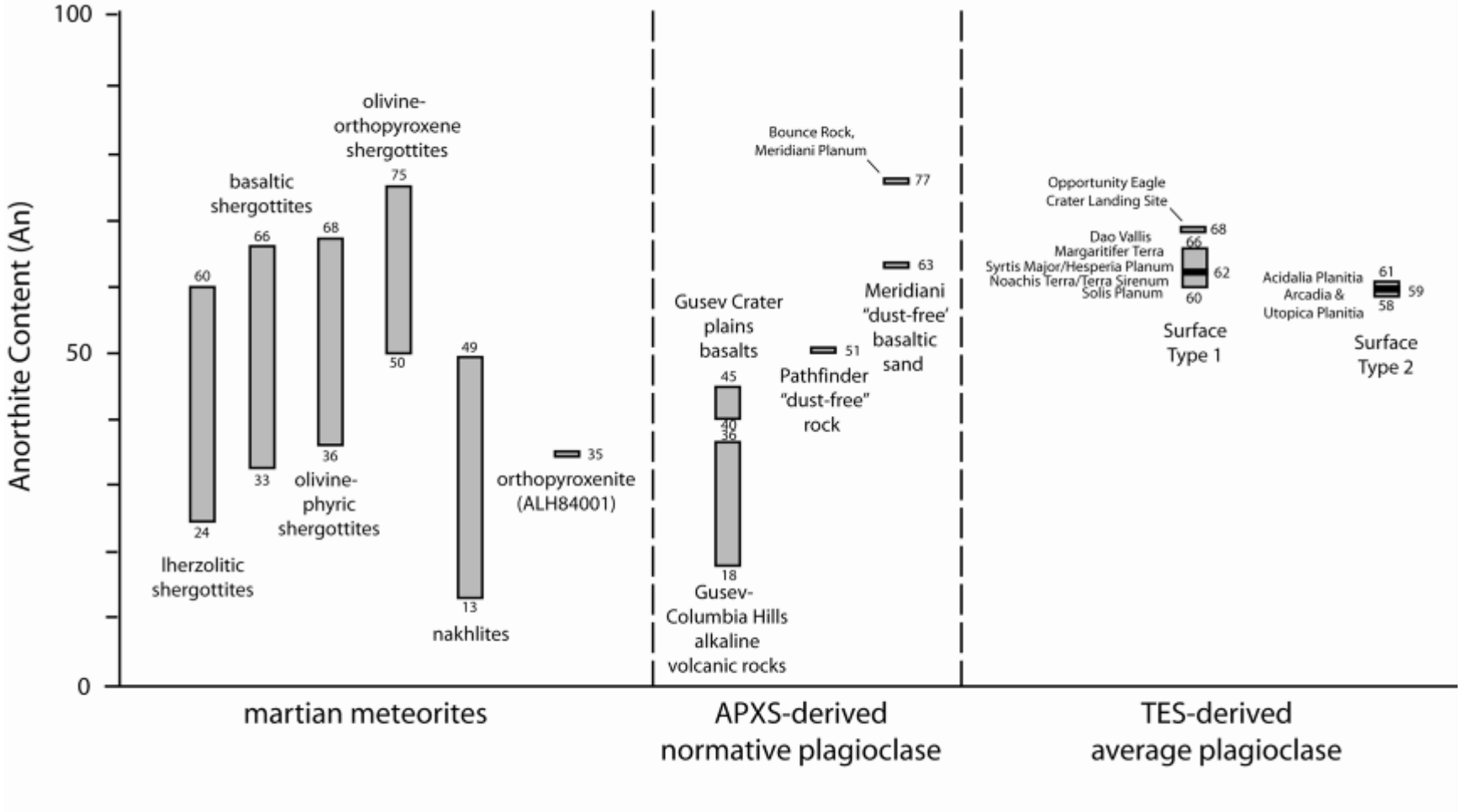
Anorthite Content (An)
100
50
0
olivine-
orthopyroxene
shergottites
basaltic
shergottites
75
66
68
60
50
36
33
24
olivine-
phyric
shergottites
lherzolitic
shergottites
49
13
nakhlites
35
orthopyroxenite
(ALH84001)
martian meteorites
Bounce Rock,
Meridiani Planum
77
63
Meridiani
"dust-free"
basaltic
sand
Gusev Crater
plains
basalts
51
Pathfinder
"dust-free"
rock
45
40
36
18
Gusev-
Columbia Hills
alkaline
volcanic rocks
APXS-derived
normative plagioclase
Opportunity Eagle
Crater Landing Site
68
Dao Vallis
Margaritifer Terra
Syrtis Major/Hesperia Planum
Noachis Terra/Terra Sirenum
Solis Planum
66
62
60
Surface
Type 1
Acidalia Planitia
Arcadia &
Utopica Planitia
61
59
58
Surface
Type 2
TES-derived
average plagioclase

Figure 36. Representative sampling of results from this study showing (a) lambert albedo vs. ΔAn, (b) % of atmospheric spectral endmembers modeled in deconvolutions vs. ΔAn, (c) % of surface dust modeled in deconvolutions vs. An, (d) dust cover index vs. ΔAn, and (e) RMS error vs. temperature, and (f) temperature vs. ΔAn for southeastern Syrtis Major (between 0-10º N and 275-285ºW.

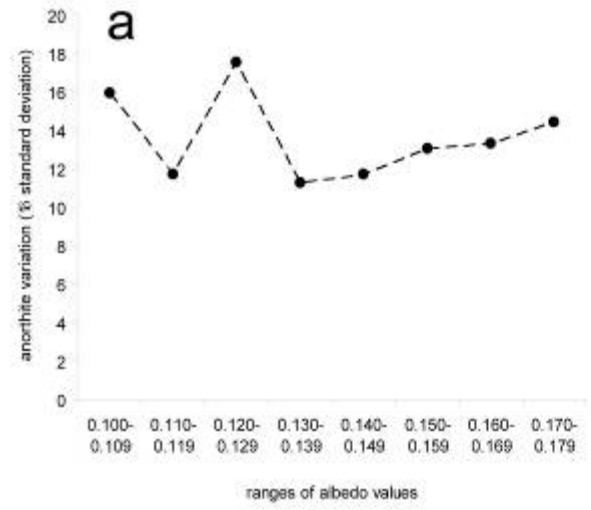
a
anorthite variation (1δ standard deviation)
20
18
16
14
12
10
8
6
4
2
0
0.100-0.109
0.110-0.119
0.120-0.129
0.130-0.139
0.140-0.149
0.150-0.159
0.160-0.169
0.170-0.179
ranges of albedo values

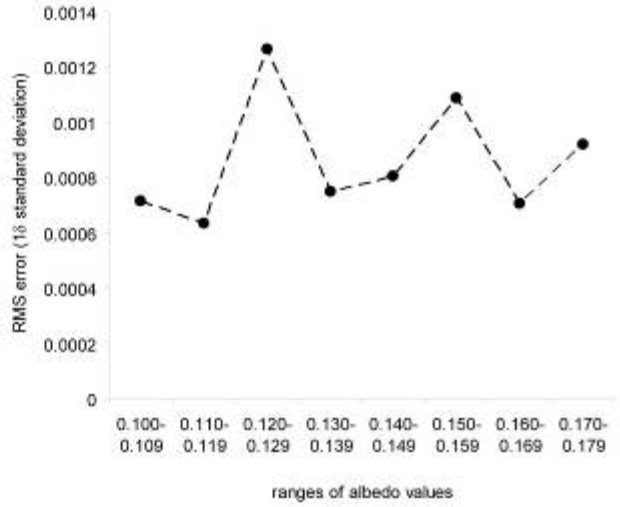
RMS error (1δ standard deviation)
0.0014
0.0012
0.001
0.0008
0.0006
0.0004
0.0002
0
0.100-0.109
0.110-0.119
0.120-0.129
0.130-0.139
0.140-0.149
0.150-0.159
0.160-0.169
0.170-0.179
ranges of albedo values

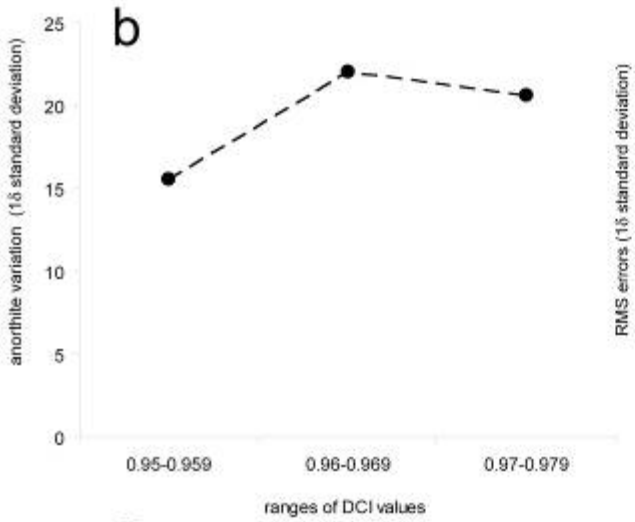
b
anorthite variation (1δ standard deviation)
25
20
15
10
5
0
0.95-0.959
0.96-0.969
0.97-0.979
ranges of DCI values

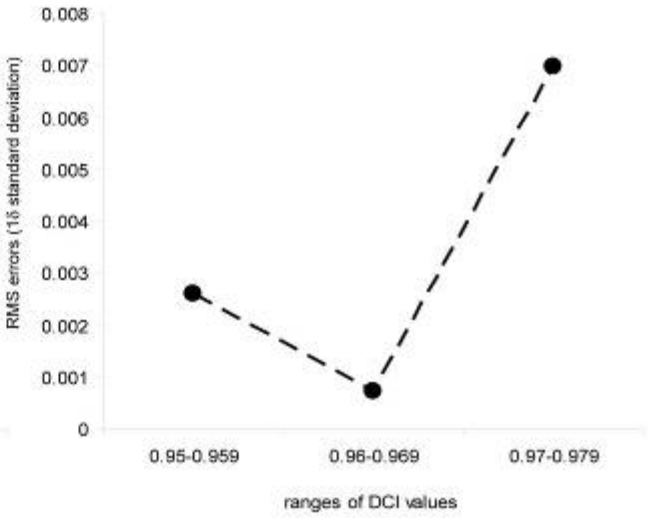
RMS errors (1δ standard deviation)
0.008
0.007
0.006
0.005
0.004
0.003
0.002
0.001
0
0.95-0.959
0.96-0.969
0.97-0.979
ranges of DCI values

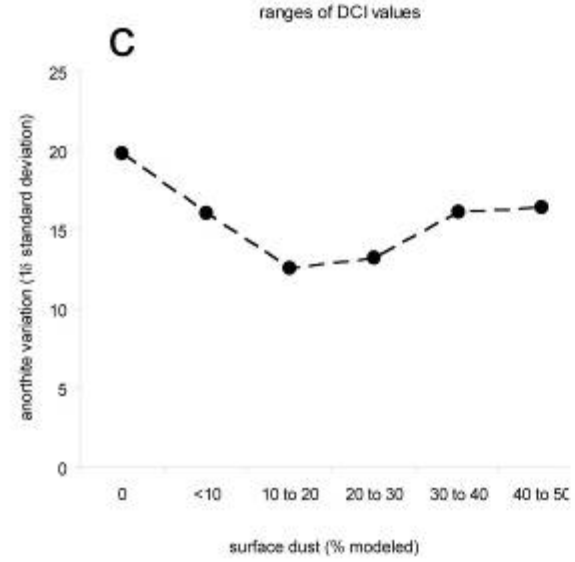
c
anorthite variation (1δ standard deviation)
25
20
15
10
5
0
0
<10
10 to 20
20 to 30
30 to 40
40 to 50
surface dust (% modeled)

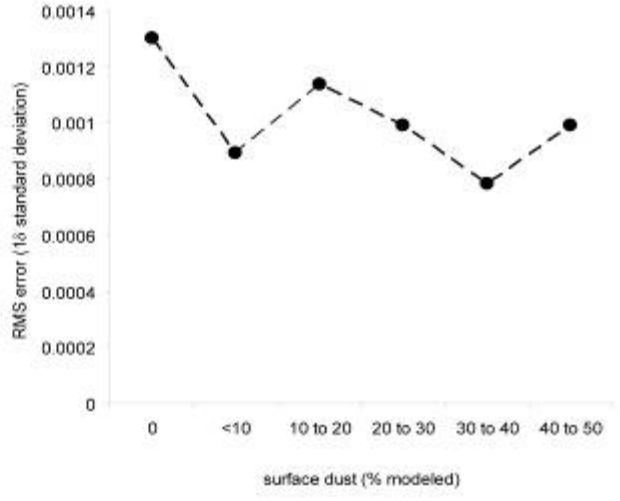
RMS error (1δ standard deviation)
0.0014
0.0012
0.001
0.0008
0.0006
0.0004
0.0002
0
0
<10
10 to 20
20 to 30
30 to 40
40 to 50
surface dust (% modeled)

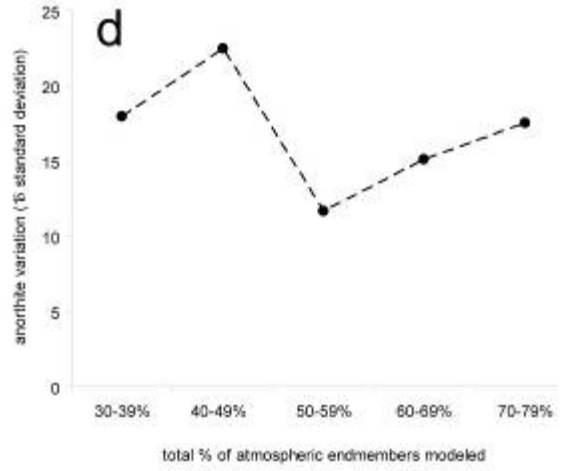
d
anorthite variation (1δ standard deviation)
25
20
15
10
5
0
30-39%
40-49%
50-59%
60-69%
70-79%
total % of atmospheric endmembers modeled

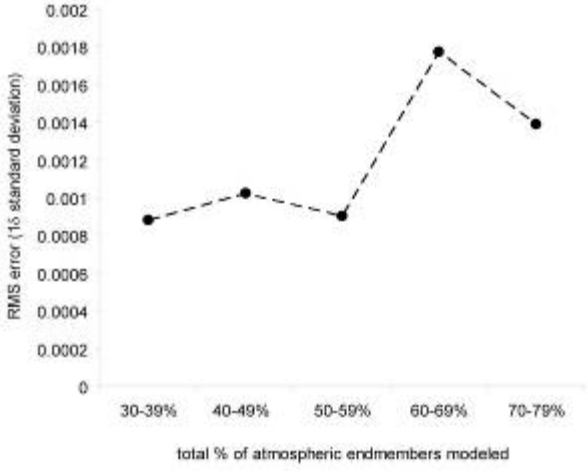
RMS error (1δ standard deviation)
0.002
0.0018
0.0016
0.0014
0.0012
0.001
0.0008
0.0006
0.0004
0.0002
0
30-39%
40-49%
50-59%
60-69%
70-79%
total % of atmospheric endmembers modeled

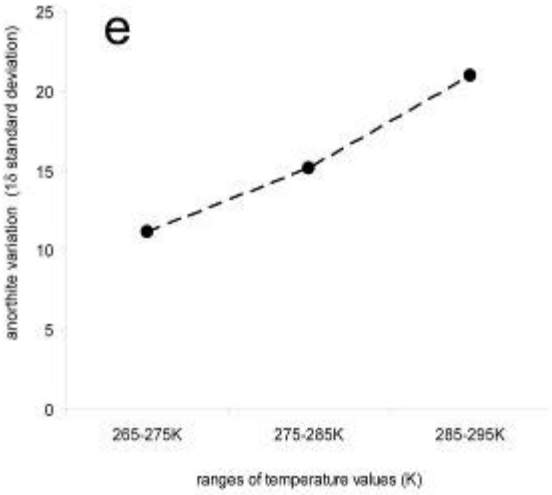
e
anorthite variation (1δ standard deviation)
25
20
15
10
5
0
265-275K
275-285K
285-295K
ranges of temperature values (K)

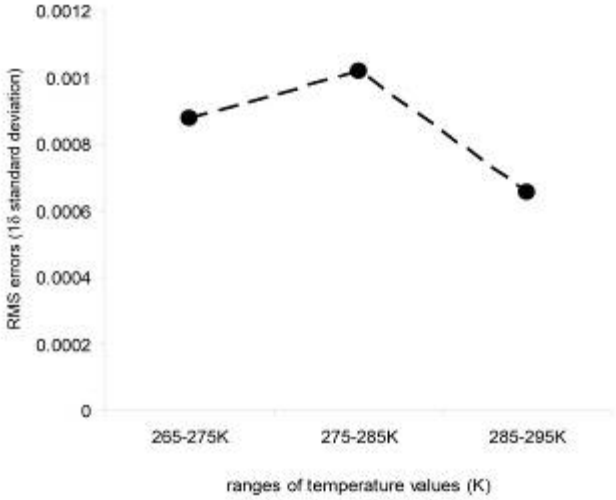
RMS errors (1δ standard deviation)
0.0012
0.001
0.0008
0.0006
0.0004
0.0002
0
265-275K
275-285K
285-295K
ranges of temperature values (K)

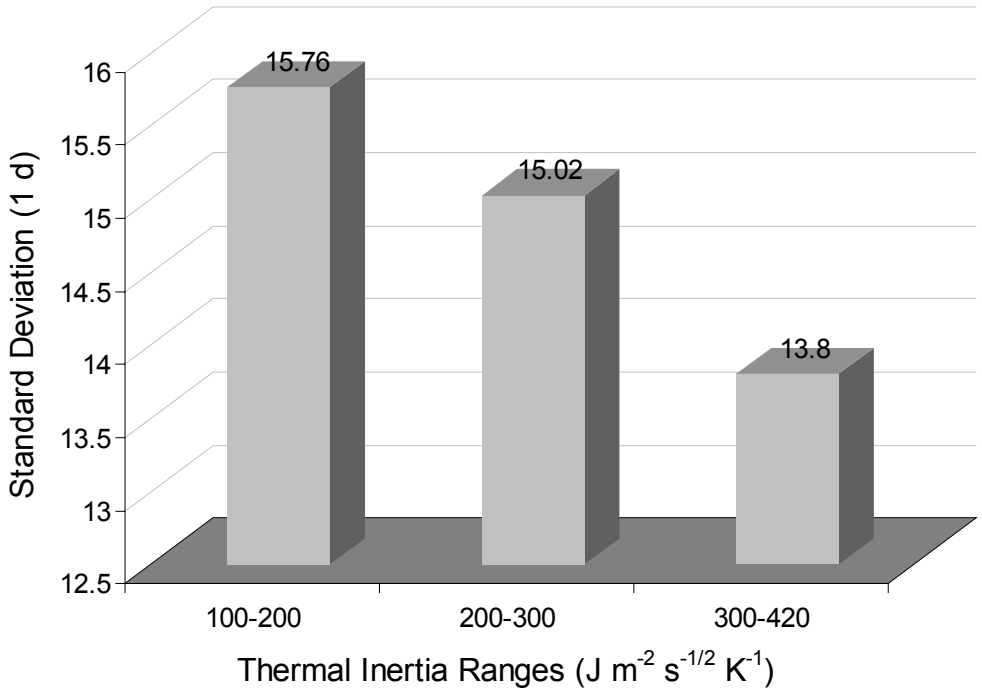

Figure 37. Bar diagram showing 1 σ standard deviations in average anorthite contents for selected TES observations for nine 10˚ x 10˚ areas on Mars per ranges in TI values. TI values corresponding to 100-199, 200-299, 300-420 J m^{-2} $s^{-1/2}$ K^{-1} represent approximate grain size ranges of 10-110 (silt to very fine sand), 110-1000 (very fine sand to coarse sand), and 1000-1300 μm (very coarse sand) respectively. Thermal inertia values >420 J m^{-2} $s^{-1/2}$ K^{-1} (not shown here) correspond with even lower standard deviations in average plagioclase compositions, but are independent of particle size [*Jakosky*, 1986].

Main Appendices

Appendix A. Precursory study of the effects of added noise at varying temperatures on our ability to model plagioclase compositions in thermal emissivity spectra at TES spectral resolution (10 cm^{-1} sampling).

Purpose and Methods

As a precursory examination into the potential effects of added noise at varying temperatures on our ability to accurately model plagioclase compositions in thermal emissivity spectra at TES spectral resolution (10 cm^{-1} sampling), we have re-examined laboratory-measured spectra from Chapter 2 of this volume. The description of sample acquisition and collection of emissivity spectra may be found there.

For this work, we degraded laboratory spectra collected from 2000-200 cm^{-1} at 2 cm^{-1} intervals to TES spectral resolution (10 cm^{-1} sampling). Both multi-component and multi-phase coarse-grained sand mixture spectra from Chapter 2 were utilized.

Each TES-resolution thermal emission spectrum was multiplied by planck blackbodies generated for temperatures ranging from 140-300 K, a range that represents surface temperatures on Mars over which TES has collected data. Blackbodies were produced at 10 K temperature intervals, with the exception of 265 K – our cut-off temperature for TES data selection for the main part of this study.

Twenty noise spectra were produced over 1300-400 cm^{-1} by randomly generating positive and negative numbers with a Gaussian distribution about the noise-equivalent spectral radiance values (NESR) derived from space observations from ock 2000 to 2500 of the TES instrument onboard Mars Global Surveyor (Figure A.1, data provided by J. Bandfield). TES ran at a fairly constant T throughout the mission and NESR values for ocks 2000-2500 are a fair representation of instrumental conditions (*J. Bandfield, pers. comm.,* 2006]. Because all of the randomly-generated noise spectra showed no major excursions from the average, we chose six of the noise spectra (Figure A.2) to be added to multi-phase emissivity spectra. Each of the six noise spectra was generated for NESR values from detectors 1 through 6. For additional comparison, we also chose two of the noise spectra (#3 and #6 from Figure A.2) to be added to each of the fifteen multi-component mixtures (III-A through V-E). Once the noise was added, radiance values were then converted back to emissivity. Representative examples of noise-added emission spectra for multi-phase mixtures are shown in Figure A.3.

Multi-phase mixture spectra were deconvolved using the same multi-phase spectral libraries as outlined in Chapter 2. These endmember sets included common mafic-intermediate igneous rock mineral phases without secondary minerals because of the lack of alteration or weathering in our controlled mixtures. Each library also excluded plagioclase with compositions matching those of spectral endmembers to those actually present in Mars spectra. Spectral libraries used to model multi-component mixtures included plagioclase only and likewise excluded spectral endmembers whose compositions matched those in each sand

mixture. Spectra were deconvolved over the spectral range of 1300-400 cm^{-1} to be directly comparable to previous studies (*Wyatt et al.,* 2001; *Milam et al.,* 2004; and Chapter 2 of this volume), but excluding the range 807-525 cm^{-1} that includes a prominent atmospheric CO_2 absorption feature present in actual TES spectra.

Results and Discussion

Results indicate that our selection of TES data at temperatures > 265 K (corresponding to signal-to-noise ratios (SNRs) > 245) avoided most of the degraded accuracy in deriving anorthite contents (represented by ΔAn) and in modeling spectra (reflected in RMS errors). Most plagioclase compositions (to within 1 σ standard deviation) can be modeled with accuracies comparable to previous work (*Milam et al.,* [2004] and Chapter 2 of this volume) at temperatures > 180-200K (in multi-component and multi-phase sand mixtures (Figure A.4; Table A.1) and SNR ratios > 23-45. Previous studies modeled plagioclase compositions at multiple resolutions in both multi-component and multi-phase mixtures to within ΔAn = 6. Similar accuracy can be achieved at temperatures > 180-200K (SNRs > 23-45) in noisy spectra (Figure A.4; Table A.1). However, below 180-200K, accuracy is degraded significantly and varies more (by as much as 50 An). Thus, noise does not become an issue for deriving anorthite contents until ~180-200 K.

The quality of the spectral fit between measured and modeled spectra, however, rapidly degrades at temperatures lower than 180-200K (SNRs > 23-45). RMS errors (Table A.2), which are a quantitative measure of the overall spectral fit between measured and modeled spectra, became worse (below 0.006) at temperatures < 255K (corresponding to SNR ~ 200; Figure A.5). This indicates added noise does affect the overall spectral fit of the modeled spectrum in each deconvolution at much higher temperatures than the 180-200 K minimum for deriving ΔAn.

It is important to note, that while 1 σ modeled ΔAn values in noisy spectra (at T's > 265K; SNR > 245) at TES spectral resolution in multi-component mixtures are comparable to those from *Milam et al.* [2004] and Chapter 2 (ΔAn =6), anorthite variations in multi-phase mixtures are slightly worse (ΔAn =10). While these values represent the majority of results, absolute ΔAn values (for a single deconvolution) can vary by as much as 14 An and 30 An in multi-component and multi-phase mixtures respectively at temperatures > 265 K (SNR > 245). Multi-phase mixtures are much more analogous to complex physical mixtures on the surface of Mars. Thus, the introduction of noise even at higher temperatures may introduce at least 4 An of additional error (10 An (noisy multi-component results) – 6 An (previously-reported accuracies)) in most deconvolutions, but some deconvolutions of TES data to produce global compositional maps may result in inaccuracies in modeled plagioclase compositions by as much as 30 An. This could potentially result in a misclassification of average plagioclase compositions for some TES observations. For deconvolutions in TES-simulated noisy spectra at temperatures > 265 K, the percentage of anorthite variations > 10 (which could result in a misclassification of solid solution plagioclase) was 5 and 38% for

multi-component and multi-phase mixtures respectively. The latter number is likely most applicable for actual TES observations used in plagioclase compositional maps considering that the Martian surface in almost all instances is a mixture of multiple mineral phases. The percentages are much worse for deconvolutions of noisy multi-phase spectra at temperatures < 265 K (SNR < 245), with 63% of deconvolutions producing anorthite variations > 10 An.

Summary

This precursory examination indicates that most (to within 1 σ standard deviation) anorthite contents from TES resolution spectra can be modeled to within 10 An of measured plagioclase compositions when noise is added at varying temperatures. However, in approximately one third of our deconvolutions at temperatures > 265 K (SNR> 245) produce ΔAn values > 10, which could result in a misclassification of average plagioclase compositions in a given TES observation.

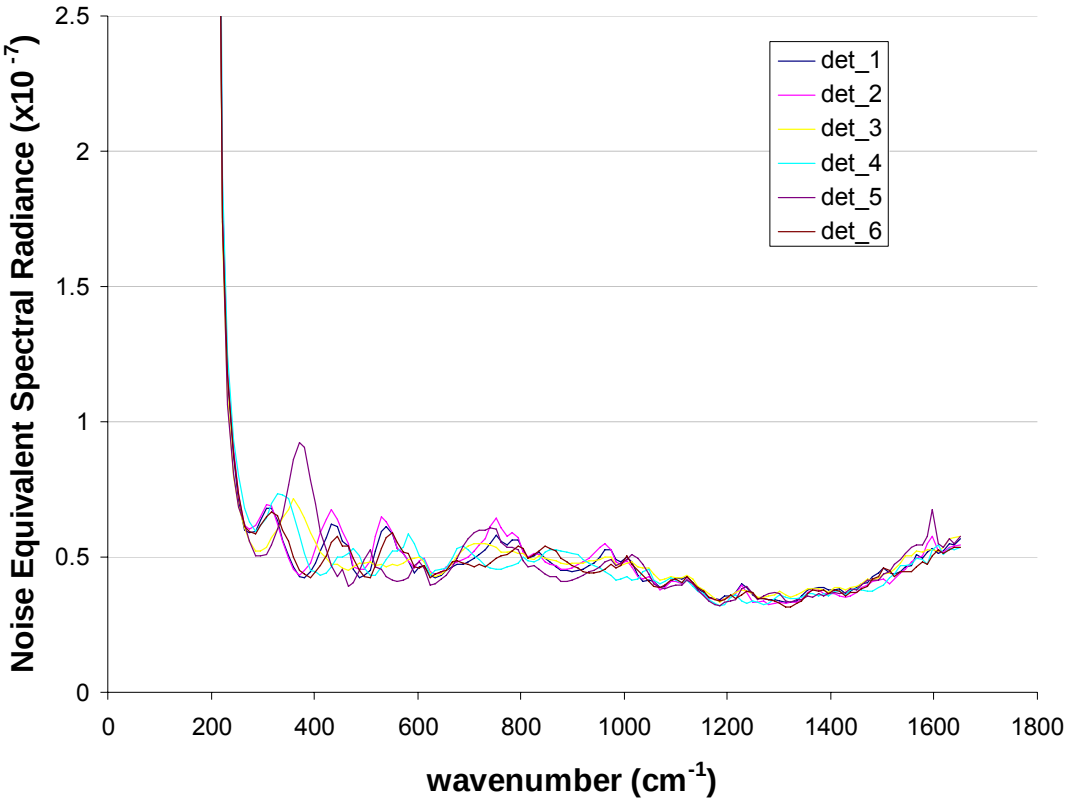

Figure A.1. Noise equivalent spectral radiance (NESR) values for the Thermal Emission Spectrometer (TES) derived from space observations from ock 2000 to 2500 for all six detectors (provided by J. Bandfield). Radiance units are W cm^{-2} sr^{-1} cm^{-1}.

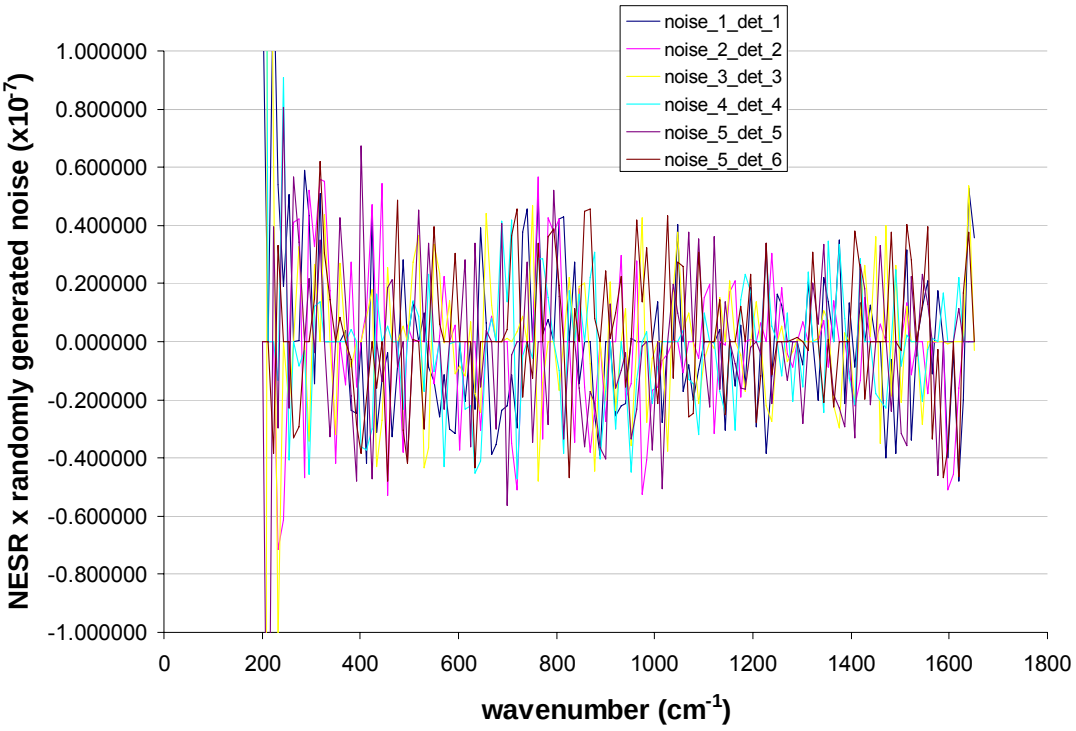

Figure A.2. Randomly generated noise using the NESR values for detectors 1-6 for ocks 2000 – 2500. These six noise spectra were then added to radiance values for multi-phase and multi-component mixtures.

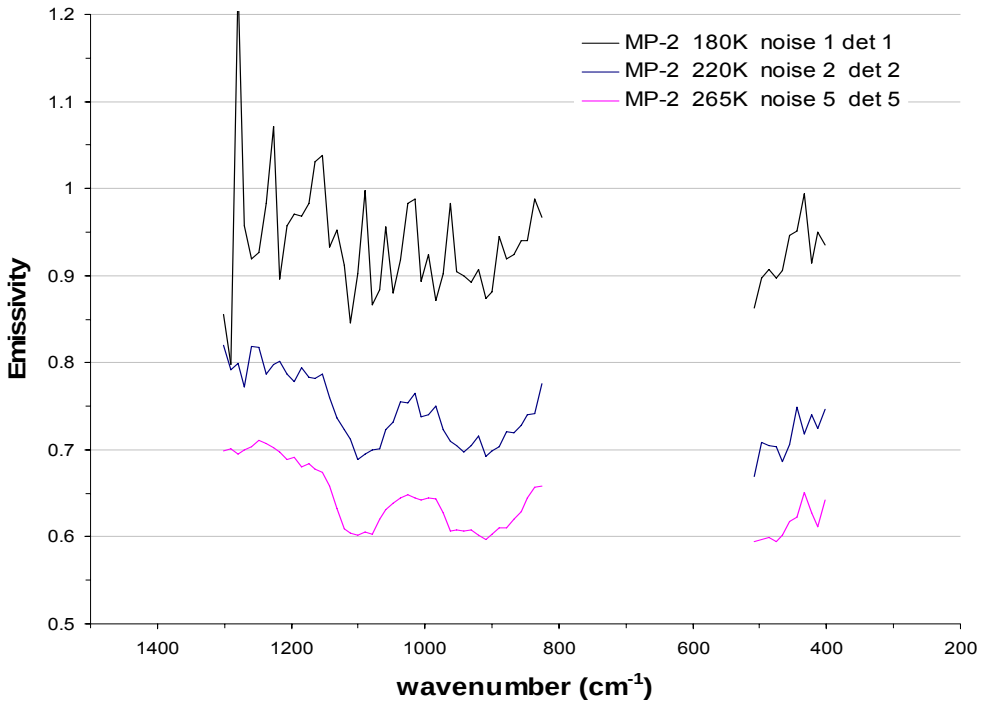

Figure A.3. Representative multi-phase mixture emissivity spectra for mixture MP-2 with noise added at three different temperatures. Thermal emission spectra at 220K and 265K were offset for clarity.

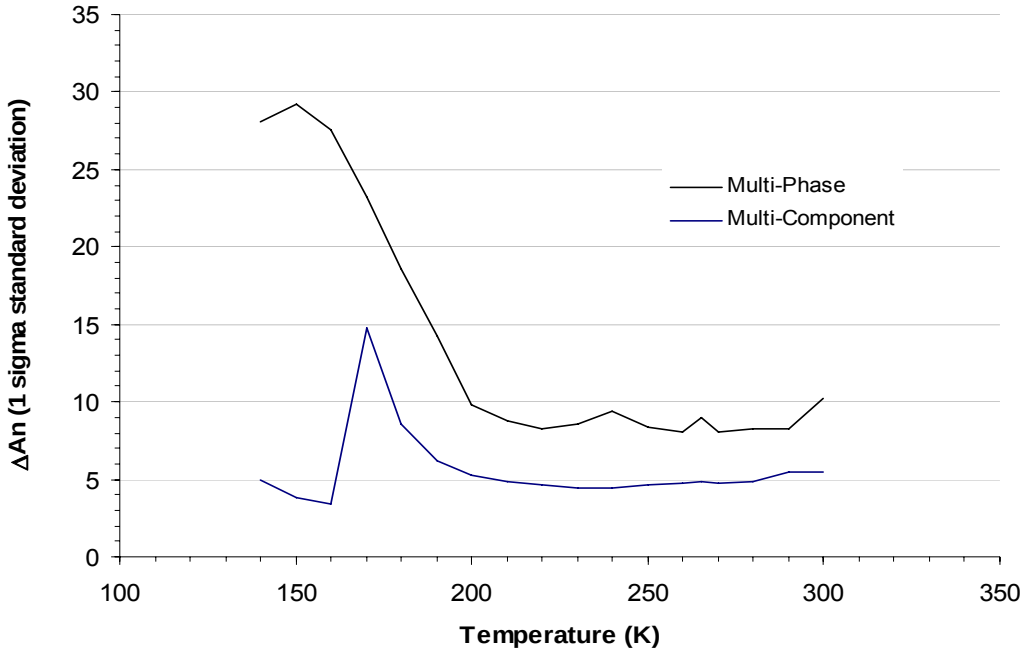

Figure A.4. Anorthite variation (1 σ std. dev.) for multi-phase and multi-component mixture deconvolutions vs. temperature (K). ΔAn begins to degrade for both sets of mixtures in the 180-200K range.

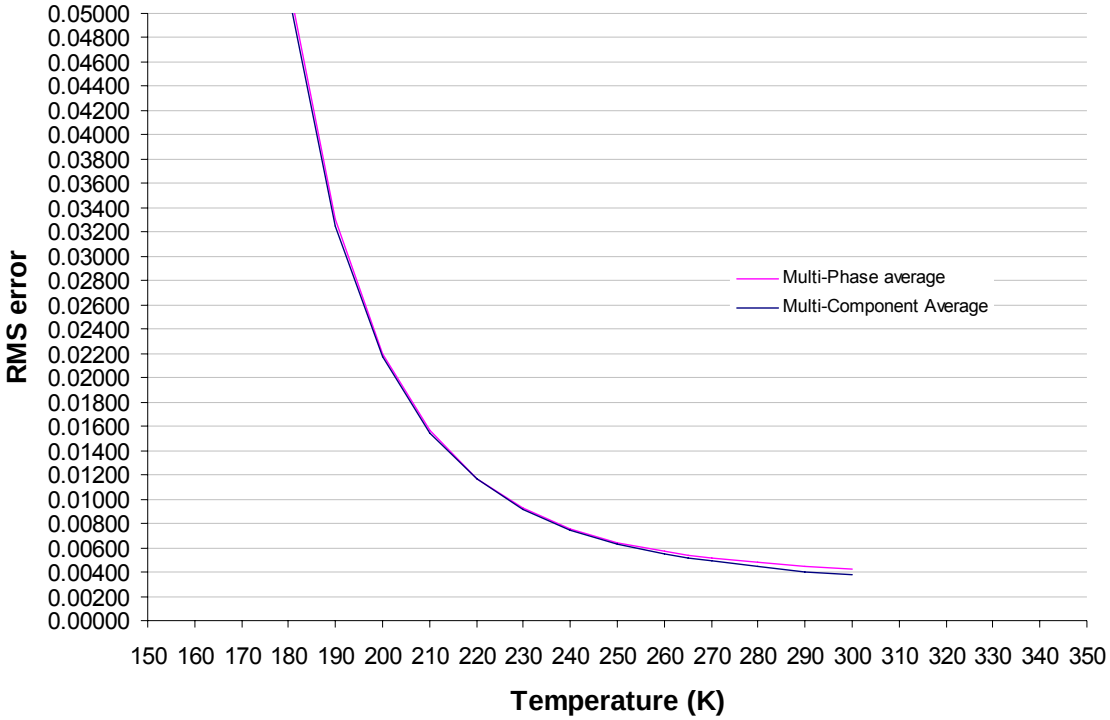

Figure A.5. Average RMS error values for deconvolutions of "noisy" multi-phase and multi-component mixtures.

Table A.1. Anorthite variation (ΔAn) resulting from linear deconvolutions of multi-phase and multi-component mixtures with added noise at varying temperatures.

		Multi-Phase				Multi-Component			
T(K)	SNR	max.	min.	avg.	std. dev.	max.	min.	avg.	std. dev.
140	4	33	-28	4	28	52	36	42	5
150	6	48	-31	-2	29	23	11	15	4
160	10	48	-25	7	28	16	5	9	3
170	15	48	-25	11	23	16	-36	-2	15
180	23	48	-22	12	19	16	-19	0	9
190	33	37	-19	12	14	12	-13	0	6
200	45	37	-2	13	10	10	-11	-1	5
210	62	37	-1	15	9	9	-10	-1	5
220	83	37	4	14	8	8	-10	-2	5
230	109	37	2	13	9	7	-11	-2	4
240	140	37	1	12	9	7	-10	-2	4
250	177	33	1	11	8	7	-10	-2	5
260	221	31	1	10	8	8	-11	-2	5
265	245	30	-4	9	9	8	-11	-2	5
270	271	30	0	10	8	8	-11	-1	5
280	328	29	-2	9	8	8	-10	-1	5
290	394	28	-3	9	8	14	-10	-1	5
300	467	33	-3	9	10	14	-10	-1	5

Table A.2. RMS errors resulting from linear deconvolutions of multi-phase and multi-component mixtures with added noise at varying temperatures.

	Multi-Phase Total				Multi-Component Total			
T(K)	Maximum	Minimum	Average	Stdev	Maximum	Minimum	Average	Stdev
140	1.07983	0.70588	0.82777	0.13398	0.90579	0.71590	0.81218	0.09457
150	0.39166	0.31354	0.34291	0.02979	0.36585	0.31287	0.34020	0.02505
160	0.19105	0.15053	0.16774	0.01536	0.17914	0.14878	0.16421	0.01412
170	0.10119	0.08062	0.09050	0.00760	0.09663	0.08076	0.08854	0.00720
180	0.05769	0.04810	0.05277	0.00371	0.05614	0.04780	0.05179	0.00349
190	0.03556	0.03000	0.03306	0.00190	0.03498	0.03028	0.03246	0.00172
200	0.02367	0.01963	0.02196	0.00114	0.02326	0.02058	0.02175	0.00079
210	0.01843	0.01393	0.01571	0.00096	0.01648	0.01486	0.01546	0.00034
220	0.01323	0.01042	0.01166	0.00070	0.01296	0.01108	0.01163	0.00040
230	0.01115	0.00812	0.00923	0.00086	0.01089	0.00841	0.00914	0.00050
240	0.00981	0.00644	0.00756	0.00086	0.00954	0.00667	0.00747	0.00061
250	0.00802	0.00533	0.00643	0.00071	0.00862	0.00551	0.00630	0.00068
260	0.00734	0.00457	0.00570	0.00075	0.00798	0.00472	0.00549	0.00072
265	0.00707	0.00429	0.00541	0.00074	0.00772	0.00442	0.00517	0.00073
270	0.00684	0.00418	0.00518	0.00074	0.00751	0.00417	0.00489	0.00073
280	0.00646	0.00383	0.00479	0.00070	0.00716	0.00371	0.00444	0.00074
290	0.00621	0.00358	0.00450	0.00069	0.00539	0.00335	0.00402	0.00050
300	0.00562	0.00340	0.00425	0.00061	0.00514	0.00306	0.00373	0.00048

Appendix B. Plagmap IDL code v.3.0.

```
;       *** PLAGMAP.pro v.3.0 ***
; *** by Keith A. Milam, Jen Piatek ***
;    *** University of Tennessee ***


; *** PURPOSE ***
; This program is designed to read in modeled endmember percentages from a
deconvolution
; of TES data, calculate the average anorthite content (An) for each TES pixel, and
; produce a color-coded map of plagioclase compositions for areas of interest on Mars.

     pro plagmap3, event

; *** INPUT FILE AND READ THE FIRST 23 UNMIX RESULTS ***
; Here the user selects unmixed TES file that they wish to use to map.  For this program,
; the endmember library used is assumed to contain all available plagioclase spectral end-
; members.  As of 04.05.06, there are 23 available endmembers.

    Result = DIALOG_MESSAGE ("Caution: Does unmixed file contain all plag endmembers
(23 as of 04.05.06) in ascending order of An content at the beginning of file?", /QUESTION,
/DEFAULT_NO, DISPLAY_NAME="Caution!")
    if Result eq 'no' then return
    if Result eq 'yes' then begin
      envi_select, FID=myfid, DIMS=mydims, pos=mypos, title='Please select atm-corrected,
unmixed data set'
      rows = DIMS[2] + 1
      cols = DIMS[4] + 1
      bands = 23
      data = fltarr(rows, cols, bands)
      b = 0
      mydims = [-1,0,ns-1,0,nl-1]
      for b=0, bands-1 do begin
        data[*,*,b] = envi_get_data(FID=myfid, DIMS=mydims, pos=b)
      endfor
    endif
    print, "File read in."

; *** RE-WEIGHT THE UNMIXED PLAG RESULTS ***
; Here each of the reported percentages are multiplied by 0.01 so that the total is less than 1.

    data = data * 0.01
```

```
; *** ADD & NORMALIZE RE-WEIGHTED PLAG RESULTS ***
; Here all the re-weighted unmixing results are summed and normalized to equal 1.0.

    print, "Adding and normalizing results. . ."
    sum = TOTAL(data,3)
    plag_ind = WHERE(sum gt 0.0)
    n_factor = fltarr(rows, cols)
    n_factor[plag_ind] = 1.0/(sum[plag_ind])
    for b1 = 0, bands-1 do begin
      plag_norm[*,*,b1] = data[*,*,b1]*n_factor
    endfor

; *** MULTIPLY EACH SPECTRAL ENDMEMBER BY ITS RESPECTIVE ANORTHITE CONTENT
***
; Here the normalized endmember percentages are multiplied by each endmember's
respective
; anorthite content (An), found in an integer array (An_value). For this algorithm, it is
; assumed that the plagioclase spectral endmembers are not only at the beginning of your
; spectral library, but also placed in ascending An.

    An_values = [1, 2, 2, 2, 8, 15, 16, 22, 25, 29, 48, 48, 50, 51, 53, 53, 63, 67, 68, 73,
73, 88, 92]
    plag_An = fltarr[rows, cols, bands]
    print, "Multiplying each spectral endmember by its anorthite content. . ."
    for b2 = 0, bands-1 do begin
      An_rc = plag_norm[*,*,b2] * An_values[b2]
    endfor

; *** PRODUCE AN AVERAGE ANORTHITE CONTENT FOR EACH PIXEL ***
; This step sums the running count of modeled An numbers to produce an average
; plagioclase composition for each pixel.

      print, "Producing an average anorthite content for each pixel. . ."
      An_avg = TOTAL(An_rc, 3)

; *** PRODUCE BLACK & WHITE AND COLOR PLAGIOCLASE COMPOSITIONAL MAPS ***
; This routine reads in the average plagioclase composition for each TES pixel and assigns
; an RGB color to that pixel.  What results is a color-coded plagioclase compositional map
; for a given region of interest.

   plagmap = fltarr(rows, cols, 3)
   print, "Producing a plagioclase composition map for the selected scene. . ."
   for r = 0, rows-1 do begin
     for c = 0, cols-1 do begin
```

```
        tmp1 = WHERE((An_avg gt 0.0) and (An_avg le 10.0))
        tmp2 = WHERE((An_avg gt 10.0) and (An_avg le 30.0))
        tmp3 = WHERE((An_avg gt 30.0) and (An_avg le 50.0))
        tmp4 = WHERE((An_avg gt 50.0) and (An_avg le 70.0))
        tmp5 = WHERE((An_avg gt 70.0) and (An_avg le 90.0))
        tmp6 = WHERE((An_avg gt 90.0) and (An_avg le 100.0))
        tmp7 = WHERE(An_avg gt 100.0)
        plagmap[tmp1,*] = [144,252,255]
        plagmap[tmp2,*] = [0,235,255]
        plagmap[tmp3,*] = [0,197,255]
        plagmap[tmp4,*] = [0,121,255]
        plagmap[tmp5,*] = [0,0,220]
        plagmap[tmp6,*] = [0,0,160]
        plagmap[tmp7,*] = [255,255,0]
      endfor
    endfor
    print, "Finished."

; *** WRITE OUT FILES ***
; The following writes out the black-and-white plagioclase compositional map
; with the average An for each pixel and the color plagioclase compositional
; map.  Note, change the filename immediately after processing to avoid writing
; over files.  I'll fix this later.

envi_write_envi_file, An_avg, data_type=4, nb=1, nl=cols, ns=rows, offset=0,
bnames=['Average An'], out_name='plagmap_bw.img'
envi_write_envi_file, plagmap, data_type=2, nb=3, nl=cols, ns=rows, offset=0,
bnames=['Average An'], out_name='plagmap_rgb.img'

end
```

Appendix C.

To examine the effects of modeling compositions of shocked plagioclase, we deconvolved shocked albite and bytownite emissivity spectra (from *Johnson et al.* [2002; 2003]) with the unshocked plagioclase (Table 12) and blackbody from the spectral library used in our global deconvolutions. Both feldspars under study had been experimentally shocked over various intervals beginning with 17 GPa and ranging up to ~ 56 GPa [*Johnson et al.* 2002, 2003]. Emissivity spectra (1667 – 200 cm^{-1}) were collected for larger grain sizes (2-10 mm) and "powders" (< 20-30 μm). Spectra for both feldspars at all shock pressures and grain sizes were degraded to the spectral sampling of the TES instrument (band passes at 10 cm^{-1} over 1667 – 200 cm^{-1}) and unmixed per the same procedures above using a linear deconvolution technique [*Ramsey and Christensen*, 1998] over a wavenumber range of 1300 – 400 cm^{-1} (excluding the range 825 – 507 cm^{-1} centered around a prominent CO_2 atmospheric absorption present in TES spectra). The spectral resolution and wavenumber range was chosen so that results could be directly compared to our processing of TES data to produce plagioclase compositional maps and for comparison previous studies [*Milam et al.*, 2004;, in review]. Modeled average plagioclase compositions of albite and labradorite at various shock pressures and grain sizes are reported in Table 16.

Table 16 clearly shows that shock does not affect our ability to model average compositions in coarse-grained calcic plagioclase. Variation in anorthite content between measured and modeled plagioclase compositions, or ΔAn, in shocked bytownite is virtually identical to those reported for sand mixture spectra from previous studies [*Milam et al.*, 2004; 2007-in review], with ΔAn_{max} = 12 and the ΔAn (1σ std. dev.) = 3. RMS errors ranged from

0.002 – 0.008 in all deconvolutions. There is no apparent degradation in modeling the average plagioclase composition in coarse bytownite with increasing pressure, although there is a slight degradation in RMS error. So for calcic plagioclase, the spectral library used in this study was sufficient for modeling all spectral features of coarse calcic plagioclase with reasonable accuracy. In shocked albite, however, $\square An_{max} = 27$, while $\square An_{1\square} = 9$. RMS errors ranged from 0.004 – 0.01. While RMS error degraded with increasing shock pressure in albite, $\square$An did not vary along any noticeable trend. The implication is that in regions with shocked calcic ($\sim An_{75}$) plagioclase, our approach to spectral deconvolution is sufficient to modeling plagioclase compositions from TES emissivity spectra. In regions dominated by shocked albite, however, our ability to derive the average plagioclase composition may be significantly degraded. Regional-scale sodic plagioclase have not been detected on Mars and similarly, older (more highly-shocked) terrain on Mars does not show evidence of wider variations in modeled plagioclase compositions

These are only two endmembers of a continuous solid solution series, however. Derived plagioclase compositions in shocked samples of intermediate compositions have yet to be examined. Thermal emission spectra of shocked Martian meteorites, however, may serve to fill in the compositional gaps in our knowledge. We also applied the same processing techniques to the emissivity spectra of two basaltic shergottites, Zagami and EETA79001 (used in *Hamilton et al.,* 1997 and provided courtesy of V. Hamilton). Zagami and EETA79001 contain maskelynite with measured compositions of An_{43-57} and An_{50-68} respectively [*Stolper et al.,* 1979]. Deconvolutions of these spectra with our endmember set (Table 12 – minus atmospheric endmembers) reveal that modeled average plagioclase

compositions (Figure A.3.1.) are well within the reported ranges for both meteorites [*Stolper et al.,* 1979]. This suggests that highly shocked intermediate plagioclase can also be adequately modeled with spectral libraries that do not include shocked feldspars.

Figure A.3.1. Measured (black) vs. modeled (purple) emissivity spectra for two common basaltic shergottites, Zagami and EETA79001. Spectra have been degraded to TES spectral resolution and deconvolved over 1300-400 cm^{-1}, excluding the region (507-825 cm^{-1}) centered around the prominent CO_2 atmospheric absorption (~ 667 cm^{-1}). Measured plagioclase compositional ranges for each meteorite along with modeled values and RMS errors for each deconvolution are also shown.

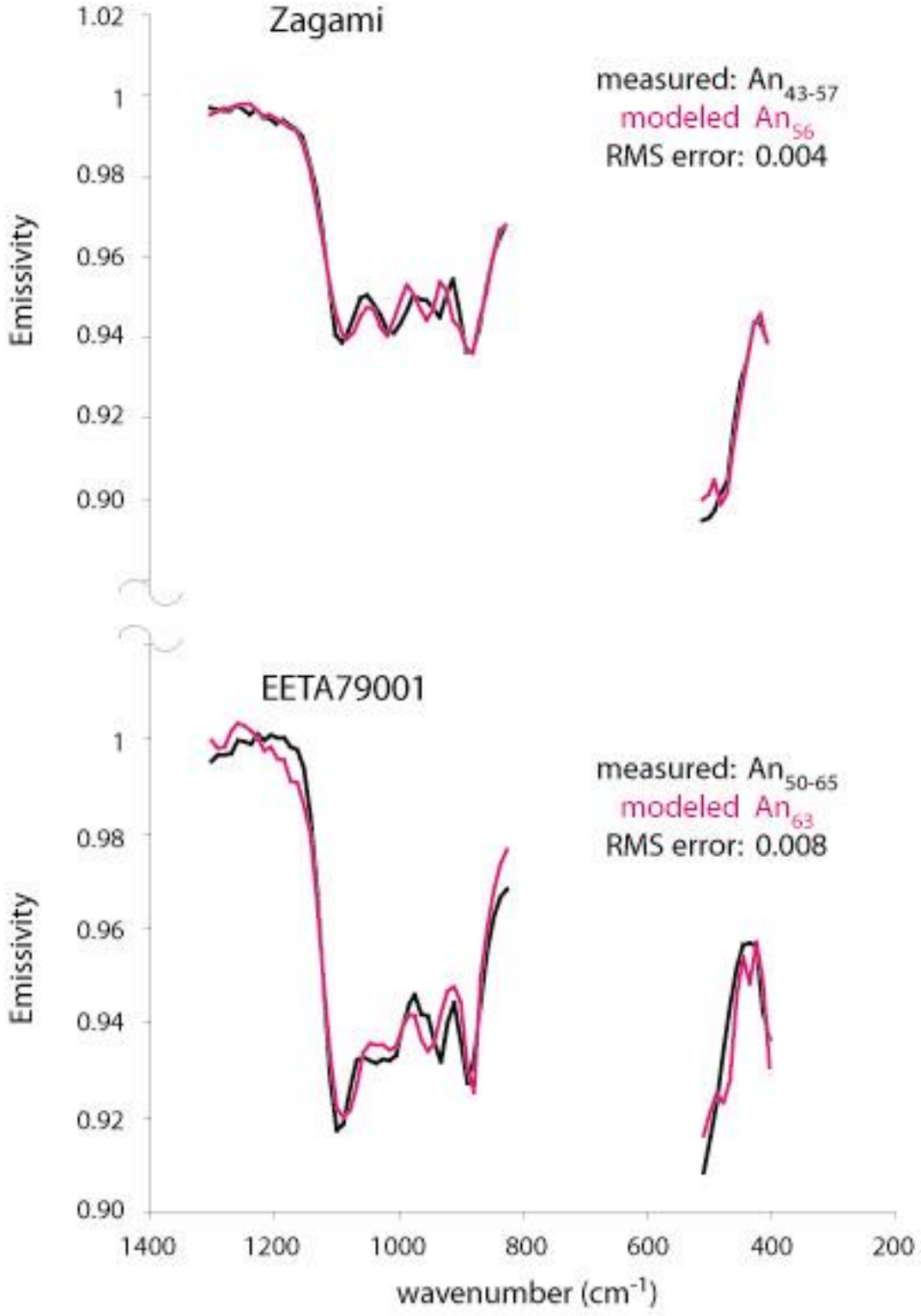
Zagami
measured: An43-57
modeled An56
RMS error: 0.004
EETA79001
measured: An50-65
modeled An63
RMS error: 0.008
Emissivity
1.02
1
0.98
0.96
0.94
0.92
0.90
1400
1200
1000
800
600
400
200
wavenumber (cm-1)

Vita

Keith Alan Milam was born on December 28, 1974 in Bowling Green, Kentucky to Kenneth and Millie Milam. He lived most of his early life outside the city limits in the small community of Rockfield, Kentucky. At an early age he was fascinated by space exploration and science. At Rockfield Elementary School, Keith was inspired by the enthusiasm of his seventh grade science teacher, Stan Peterie. It was during this time that he attended Space Academy in Huntsville, Alabama . . . three times. At Warren Central High School, Keith's interest in space was bolstered by the incredible teaching methods of Doug "Dr. J." Jenkins, the high school physics teacher.

After graduation from high school in May, 1992, Keith attended nearby Western Kentucky University. At Western, he fell in love with geology and found his true calling in planetary geology. Although attending primarily a teaching college, Keith was encouraged to do original research by the late Dr. Deborah Kuehn. He earned his B.S. in geology in 1997 and continued to work at the American Cave Museum in Horse Cave, Kentucky where he was soon promoted to educational coordinator and staff geologist. Keith worked there several years and later as a park ranger at Mammoth Cave National Park before attending graduate school at the University of Tennessee in the Fall of 1999.

Keith worked under Harry Y. McSween, Jr. to earn his M.S. in geology in 2002 for his initial laboratory studies of thermal emissivity spectra of plagioclase feldspar and its application to Mars spacecraft data. He decided to stay on at the University of Tennessee to continue work with Mars Global Surveyor and Mars Odyssey data and to join the Mars Exploration Rover science team as a student collaborator, science theme group member and lead, and a payload downlink lead for the Miniature Thermal Emission Spectrometer instrument. Keith successfully completed the requirements for his doctoral degree during the spring of 2007.

Keith is currently employed as an assistant professor of planetary geology in the Department of Geological Sciences at Ohio University.